COMPRESSIVE RESPONSE OF NOTCHED COMPOSITE-HONEYCOMB SANDWICH PANELS

by

Michael Garcia-Lopez Toribio

B. S., Mechanical Engineering
United States Naval Academy (1997)

Submitted to the Department of Aeronautics and Astronautics in Partial
Fulfillment of the Requirements for the Degree of

Master of Science
in Aeronautics and Astronautics

at the

Massachusetts Institute of Technology
June 1999

© 1999 Massachusetts Institute of Technology
All rights reserved

Signature of Author ....
Department of Aeronautics and Astronautics
May 7, 1999

Certified by .... ν ....
S. Mark Spearing
Esther and Harold E. Edgerton
Associate Professor of Aeronautics and Astronautics
Thesis Supervisor

Accepted by ....
Jaime Peraire
Associate Professor of Aeronautics and Astronautics
Chairman, Department Graduate Committee
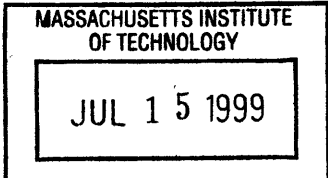
COMPRESSIVE RESPONSE OF NOTCHED COMPOSITE-HONEYCOMB SANDWICH PANELS

by

Michael Garcia-Lopez Toribio

Submitted to the Department of Aeronautics and Astronautics
on May 7, 1999 in Partial Fulfillment of the
Requirements for the Degree of Master of Science in
Aeronautics and Astronautics

ABSTRACT

Experimental and numerical work was conducted to understand better the compressive response of notched composite sandwich panels. The quasi-static uniaxial compressive response of notched (circular through hole) E-glass/epoxy-Nomex™ sandwich panels were studied experimentally. Two different woven fabric architectures were examined. The key failure mechanism was observed to be linear damage zones (LDZs) emanating from the notch tip (in both materials). LDZ's behaved in a macroscopically similar manner to a bridged crack under tensile loading, and were characterized by semi-stable propagation. Cross-sectioning studies revealed the key damage mechanisms operating within the LDZ. Progressive cross-sections indicated that individual fiber microbuckling led to out-of-plane warp tow kinking. The LDZ *wake* was characterized by kinking in all warp tows and transverse tow splitting. Strain gages were used to measure the *in situ* damage zone tractions as the LDZ propagated across the width of the specimen; a softening trend was observed.
   Consistent with observations, a two parameter linear strain softening traction law was used to model the LDZ constitutive behavior. The traction law was treated as a material property. The damage zone modeling (DZM) framework was investigated to determine its validity, specifically its ability to predict three experimentally observed phenomena: the notched strength, local strain distribution, and LDZ growth characteristics. A self-consistent physically-based model should be able to predict all three phenomena. Two models were created in order to interrogate the DZM. The damage growth model was used to determine the ability of the DZM to predict the LDZ growth behavior and notched strength. A finite element model that used discrete nonlinear springs in the wake of the LDZ to model the LDZ as a continuous spring, was implemented to determine if the DZM could predict the local strain distribution. Results showed that the current traction law provided excellent agreement with the phenomenon used to calibrate the traction law, for all specimen sizes. Extension of predictive power to other phenomena resulted in weaker correlations. The modeling framework and methodology established provide a robust tool for investigating the potential of adding physical bases to the DZM.

Thesis Supervisor: S. Mark Spearing
Title: Esther and Harold E. Edgerton Associate Professor of Aeronautics and
    Astronautics

Acknowledgments

I really want to extend a heartfelt thank you to all of you who made this possible- the people make it worth it. If I forget to mention someone, I'm sorry, but you know I didn't do it on purpose.

The first thanks goes out to my advisor, Professor Spearing. Thanks Mark, first for trusting me to begin this project, then for guiding me through it, and finally for the perseverance. Thanks to the other professors in TELAC who enjoy helping students: Professor Lagace, Professor Cesnik, Professor Dugundji, and Professor McManus. Thanks also to Deb and Ping and especially Liz Zotos for getting me in here!

And thank you to those who also helped on the technical stuff: Michael Abruzzese, Jee Bang, Ariela Gruszka, Staci Jenkins, John Kane, Seth Kessler, Professor Link (USNA), Eric Martin (SDRC), Thad Matuszeski, Jose Mirazo, Lenny Rigione, Catherine and Wynn Sanders, Yong Shi, and Dong-Jin Shim.

I want to thank *all of the students* in TELAC. Especially "the *micky-ficky* man, big booooy!!!!" Jose Mirazo. Thanks for everything my friend, and I'll see you in Spain? Also the ones who helped to focus on things other than work: Dennis Burianek (Pole Position); Tom Reynolds, Troy Hacker, Mevlut Oenkal, and Jason Richards (all for IM football); Brian Wardle (the squat rack); DJ (Dodgers?); Gordon Maahs (Wachusett). Thanks also to Cyrus Jilla.

And I can't forget John & Gina Raimondo. Thank you for trying to round me out. The Obandos (and Pam, of course), thank you for everything, I appreciate it!

And finally, the best for last. With love, respect, and in prayerful thanksgiving, I thank my family. *All* of you are a constant inspiration for me, thank you, I love you, and this is for you.

A special thanks to my spiritual director Father Wright, O. M. V., and all the Oblates at the St. Francis Chapel at the *Pru*, and the Franciscans at St. Anthony's Shrine downtown. Thank you all for helping to show me what is most important in life.

"O give thanks to the LORD, for he is good, for his steadfast love endures forever." Ps 118:29
"For God alone my soul waits in silence, for my hope is from him. He alone is my rock and my salvation, my fortress; I shall not be shaken. On God rests my deliverance and my honor; my mighty rock, my refuge is in God." Ps 62:5-7
"And those who know your name put their trust in you, for you, O LORD, have not forsaken those who seek you." Ps 9:10
"'Come to me, all you that are weary and are carrying heavy burdens, and I will give you rest. Take my yoke upon you, and learn from me; for I am gentle and humble in heart, and you will find rest for your souls. For my yoke is easy, and my burden is light.'" Mt 11:28-30
"Jesus said to them, 'I am the bread of life. Whoever comes to me will never be hungry, and whoever believes in me will never be thirsty...'" Jn 6:35
"Just then a lawyer stood up to test Jesus. 'Teacher,' he said, 'what must I do to inherit eternal life?' He said to him, 'What is written in the law? What do you read there?' He answered, 'You shall love the Lord your God with all your heart, and with all your soul, and with all your strength, and with all your mind; and your neighbor as yourself.' And he said to him, 'You have given the right answer; do this, and you will live.'" Lk 10:25-28
"And this is what he has promised us, eternal life." 1 Jn 2:25
"'And this is eternal life, that they may know you, the only true God, and Jesus Christ whom you have sent.'" Jn 17:3
"...'Amen! Blessing and glory and wisdom and thanksgiving and honor and power and might be to our God forever and ever! Amen.'" Rev 7:12

Thank you God. Without You, I am nothing.

Foreword

Table of Contents

List of Figures

List of Tables

Nomenclature

F_h^s hole correction factor for remote stress case

F_w^s finite width correction factor for remote stress case

F_o^s orthotropic correction factor for remote stress case

F_h^σ hole correction factor for crack traction case

F_w^σ finite width correction factor for crack traction case

F_o^σ orthotropic correction factor for crack traction case

G_{ss} energy per unit area dissipated by crack propagation in steady state

K_0 fracture toughness

K_s corrected stress intensity factor due to remote stress

K_∞^s uncorrected stress intensity factor due to remote stress

K_σ corrected stress intensity factor due to crack tractions

K_∞^σ uncorrected stress intensity factor due to crack tractions

S remote applied stress

V_s crack opening profile due to remote stress

V_σ crack opening profile due to tractions

a actual half crack length in Dugdale analysis

d total crack length plus hole diameter

f_i short crack segment distance

g_i long crack segment distance

r radius

v crack opening displacement

v_c maximum crack opening displacement

w facesheet half width

x distance along crack measured from hole center

x_t middle crack segment distance

ρ Dugdale plastic zone size

σ stress on crack face (traction)

σ_c maximum traction

σ_{YS} yield stress

CHAPTER 1

INTRODUCTION

Advanced composites are currently used as standard materials in several industries, such as aerospace, sporting goods, and automotive. Due to their structural performance advantages [1-3] (e.g. tailorability of material properties, specific strength and stiffness), composites have replaced traditional metallic components and have become established as the materials of choice in some cases. Notwithstanding the current widespread usage of composites, many possible avenues of application remain unexplored. Arguably, composites' full potential, particularly in the aerospace industry, has yet to be realized.

In the aerospace industry, the design process is increasingly driven by economic considerations. To this end, composite materials have been introduced into aircraft design to reduce weight, and hence reduce fuel costs. An example of this can be found in composite sandwich structures. Composite-honeycomb sandwich panels utilize the high intrinsic bending stiffness of sandwich structures to enhance laminated composites as structural components, which by themselves are characterized by a relatively low bending stiffness. The overall weight is kept to a minimum due to the very low density of core materials. Currently, applications of honeycomb-cored composite sandwich structures range from helicopter rotor blades to secondary structures in commercial and military aircraft [4].

The incorporation of advanced composites into aircraft primary

structures has been delayed for several reasons, including a lack of understanding, by comparison to metals, of their damage tolerance [5]. In particular, the poor performance of sandwich structures subject to severe impact loading has been a recurrent concern. This shortcoming for composite sandwich panels is a specific instance of more general limitations in the design methodology for composite structures.

Currently, the composite design process relies on a multitude of coupon-level tests to obtain a database with which to pass strength data on to progressively larger, more complex structural components. This translates into two undesirable results. First, the large amount of testing requires an equivalently large capital investment. Second, this building block type design approach does not utilize mechanism-based (or "physically-based") failure prediction models, which effectively forces the reliance on empiricism and increases the design/production time. The desire is to utilize mechanism-based models within the damage tolerant design approach to reduce costs and reduce the time within which advanced composites can be reliably and better implemented in aerospace applications [6].

Two overarching issues are addressed by the present work which result from considerations relating to the damage tolerant design approach currently used in the aerospace industry. The first issue addresses the fact that composite sandwich structures are currently in use, and the fact that mechanism-based failure prediction models do not exist. In order to apply a damage tolerant design approach, these types of models must exist [6] for any material susceptible to damage and time-dependent damage growth. The second issue addresses composites', and in the present investigation, composite sandwich panels', lack of realized potential. For example, primary structures are currently composed of metals which are heavier than composite

materials. It should be noted that mechanism-based modes *do* exist for metals; i.e. their damage tolerance is relatively well understood [5].

The objective of the present work is to investigate the potential for adding physical bases to the damage zone modeling (DZM) framework applicable to sandwich structures under compression. Both experimental and numerical work are conducted to this end. The experimental study focuses on characterizing the key failure mechanisms resulting from the compressive loading of notched sandwich panels with glass fiber/epoxy facesheets. The numerical study is an investigation of the DZM. Specifically, experimental observations are applied to the DZM to assess the potential of implementing the model as a design tool for the damage tolerance of sandwich panels. This work was conducted in parallel with a similar approach applied to sandwich panels with graphite/epoxy facesheets [7].

The present work is arranged as follows. Chapter 2 presents an overview of the literature pertaining to compressive tests. Previous work on test fixtures, failure mechanisms, and modeling approaches are discussed which relate to unnotched and notched unidirectional and woven composites and sandwich panels. In chapter 3, a description of the experimental procedure used in the present work is presented. The procedures governing the compression tests and damage evaluation techniques are included. Chapter 4 presents the modeling framework and details of the analysis applied to the present case. In chapter 5, the results from the experimental and analytical investigation are presented. A discussion of the results and their correlation with the modeling is presented in chapter 6, followed by conclusions from the present study and recommendations for future work in chapter 7.

CHAPTER 2

LITERATURE REVIEW

This chapter begins by reviewing established compression test methods and fixtures used for composite laminates and composite sandwich panels. Then, the key compressive damage mechanisms observed in both laminates and sandwich panels of different materials and fiber architectures are reported. Finally, a summary of laminate and sandwich panel compressive strength prediction models, is presented.

2.1   Compression Testing Methods

Several test methods and associated testing fixtures exist for both composite laminates and sandwich panels. In general, these tests have been developed either to determine the material properties of a given composite, such as modulus or compressive strength, or to assess a specimen's specific compressive response in a damaged condition, in order to assess its damage tolerance. This latter purpose reflects the observation [8] that the compressive loading response is generally more critical than the tensile loading response for damage tolerant considerations.

2.1.1 Laminates

The compressive response of composite laminates has been studied extensively over the past 35 years. This has facilitated the emergence of standardized compressive testing methods such as ASTM Standards

D3410/D3410M [9] and D695 [10]. The fixtures used in the test procedures are either designed to introduce the compressive load via shear (e.g. the Celanese and IITRI fixtures specified in D3410) or end loading (e.g. D695). Shear loading is accomplished through indirect load transfer from wedge grips, usually by loading tabs which are bonded to the laminate on either side and on both ends. Several unacceptable failure modes are discussed in D3410, such as delamination of loading tabs, through-thickness laminate failures within the gripped areas, end crushing, and delamination occurring within the gripped areas. This leads to the conclusion that the alignment and load introduction characteristics are critical in obtaining allowable compressive failure modes. The end loading method, while presented as a standard for use with rigid plastics only, is commonly used with modifications (sometimes termed "modified ASTM D 695 test methods") on composites and utilizes a supporting jig or anti-buckling guide to prevent global buckling of the laminate. Experiments have shown that test sections larger than those specified by the standards could be used with the fixtures, as long as global buckling was avoided [11]. Furthermore, either loading scheme, shear or end loading, can be used to obtain valid compressive strength results [11]. A finite element study [12] suggested that a combined loading scenario would alleviate problems arising from stress concentrations in both the shear and end loaded fixtures; thus fixtures have been designed to transfer compressive load to the laminate via combined shear and end loading, with similar strength results as obtained with standard fixtures [13]. A test apparatus which introduces uniform compressive loading, avoids unwanted failure modes (such as brooming), and introduces the least stress concentration into the test specimen is most desirable.

2.1.2 Sandwich Panels

Using the fixtures referred to above in order to suppress out-of-plane buckling failures during compression tests can inhibit failure modes which could occur in real applications. To circumvent this problem, shear loaded composite-honeycomb sandwich panels have been investigated and identified as valid test specimens for the compressive response of thin laminates [14]. The sandwich structure allows for investigation of thin laminates with a much larger test section than would be possible with a similar laminate using standard methods. The sandwich construction prevents unwanted failure modes, such as general column buckling of the laminate. Standardized sandwich panel test methods include fixtures using four point bending tests [15] and edgewise loading [16], which uses lateral supports near the specimen ends.

In an effort to avoid general buckling, the novel mini sandwich column, which consists of facesheets surrounding a neat resin core, was tested in standard laminate fixtures [17, 18]. These specimens yielded compressive strengths that approached their tensile strengths, which leads to the conclusion that this test method may not be sufficiently conservative for design purposes. Furthermore, it has been noted that the stability attained in these tests is not representative of in-service conditions [19].

The applicability and usefulness of test specimens and fixtures with regard to how the apparatus represents an actual structural component is an important assessment, especially if the intent of the test is to simulate actual loading conditions (as opposed to determining compressive failure mechanisms in general). For example, using a test fixture with simply supported boundary conditions and very slender sandwich panels [20] is not representative of the conditions seen by aircraft secondary structures, but may be suitable for other

purposes. It should be noted, however, that values for composite compressive strengths vary for identical tests using the same fixture, and vary also from fixture to fixture [21].

2.1.3 Summary

By comparing the various test methods available, the most appropriate test can be determined for a given application. Comparative studies lead to the conclusion that the best test method to use in a particular case has certain characteristics [22]. First, the fixture must be adequately suited to geometrically accommodate the specimen and allow the possibility for all of the relevant failure modes to occur. Second, the fixture must introduce as small a stress concentration as possible. Finally, the test fixture should be of least cost to fabricate. Generally speaking, the shear loaded configurations are more attractive because they prevent the invalid failure modes that are prone to occur with the end loaded method; e.g. splitting and brooming. However, end loaded configurations are cheaper and easier to use.

2.2   Compressive Damage Mechanisms in Laminates

The damage tolerant design philosophy is based on the knowledge of the performance and longevity of damaged structures. The ability to obtain the residual strength or the life expectancy of structural components based on interpolation of data can be achieved without explicit information about the controlling damage mechanisms. However, a more detailed characterization of specific damage occurring at the coupon level is essential in order to establish mechanism-based models. Therefore, the first step in creating predictive models with truly physical bases is understanding the critical damage mechanisms, which is the focus of this section. A good review of compressive

failure mechanisms of composite materials is available in reference [8]. This review, however, does not cover all of the experimentally observed damage modes for both tape and woven fiber architectures in unnotched and notched composite laminates. Therefore, the following review is presented. Unless otherwise noted, compression loading techniques for the reported results are either performed using standardized procedures or similar techniques utilizing shear or end loading methods.

2.2.1 Compressive Damage Mechanisms in Unidirectional Composite Laminates

The majority of experimental studies relating to the compressive response of composite laminates has been focused on those consisting of unidirectional tape architectures, as opposed to woven fabrics. Laminates of both unidirectionally and multidirectionally aligned fibers are common test specimens, and many different material systems have been tested successfully.

The literature on unidirectional laminates is extensive. Unnotched carbon/epoxy laminates have been shown to fail by shear crippling [23, 24]. In most cases this is a sudden event with very little or absolutely no subcritical damage growth prior to catastrophic failure. The suddenness of failure requires that damage characterization, which consists of determining which specific failure mechanisms lead to final failure, is generally performed after the specimen has failed, i.e. by a *post-mortem* inspection. Shear crippling is a term commonly used (at the fiber length scale) to describe a kink band failure that results in fiber misalignment from an initially straight fiber. Kink bands refer to failure mechanisms resulting from fiber microbuckling, where single fibers break in two places along their length to form a ligament, and rotate with

similar adjacent ligaments to form a band. Kink bands usually have distinct widths and characteristic inclination angles and ligament rotation angles. Figure 2.1 illustrates the common microbuckling damage mechanisms. However, kink band formation is not limited to constant band widths, or to a single band, as will be discussed later, and both in and out-of-plane kink bands can occur. Experimental evidence supports the theory that the fiber/matrix interface plays a large role in fiber microbuckling of unnotched carbon/epoxy laminates; degraded interfaces due to temperature effects lead to out of plane microbuckling [25]. Notched (open hole) carbon/polymer laminas embedded between transparent polymer sheets for stability exhibited kink bands along with delamination [26]. Interestingly, the presence of a stress raiser, in this case a hole, did not lead to a different failure mode from that observed in unnotched specimens.

Shear crippled zones consisting of fiber microbuckling and kink bands are not exclusive to carbon/epoxy based unidirectional laminates. Several other material systems have been found to exhibit similar damage mechanisms. Unnotched E-glass/epoxy laminates tested in a novel flexure device failed via fiber microbuckling and delamination [27]. Kevlar fiber-reinforced composites were also found to exhibit this trend; fiber microbuckling and fiber kinking were the dominant failure mechanisms in unnotched Kevlar/epoxy specimens [28, 29]. Kink band formation is not limited to very high strength (including Kevlar) fiber composites. Model composite specimens consisting of glass, copper, or wheat flour fibers in a wax matrix failed due to microbuckling as well, which led to kink bands [30]. Although less applicable to advanced composite structures, other model composites have been tested to illustrate other possible compressive failure mechanisms; glass/silicone composites failed due to elastic microbuckling (note that all reported

Possible Kink Band Formation Patterns

Kink Band
Inclination β

Fiber
Rotation φ

Kink
Width w

Shear Crippling Due To Fiber Misalignment
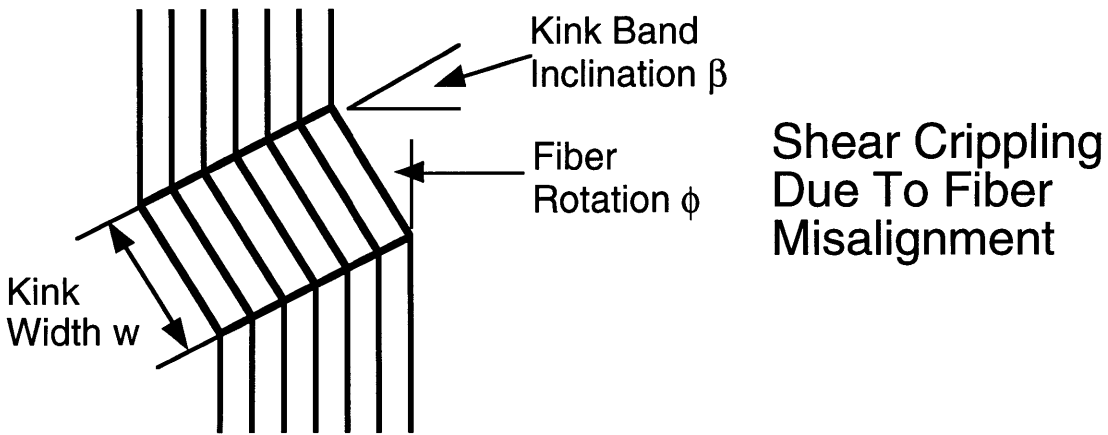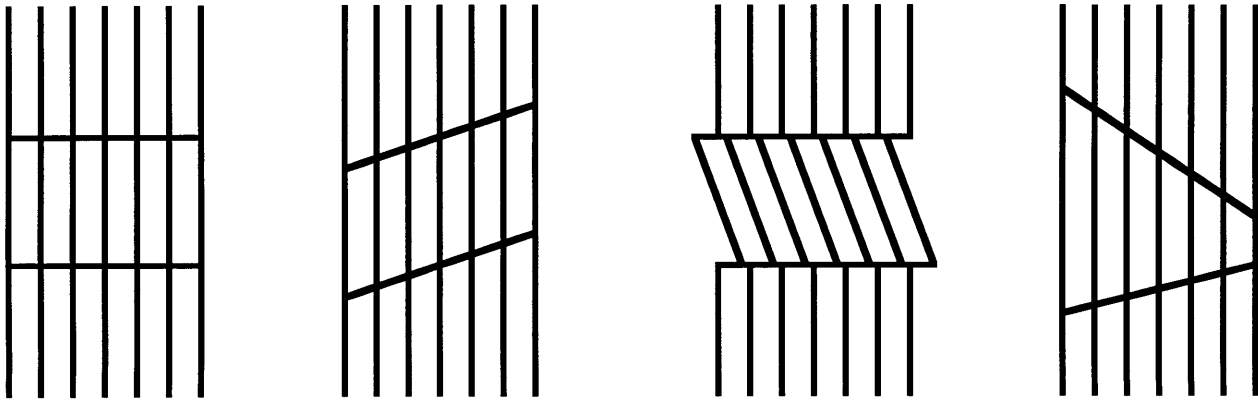
Multiple Kink Bands

Pure Microbuckling

Symmetric   Asymmetric
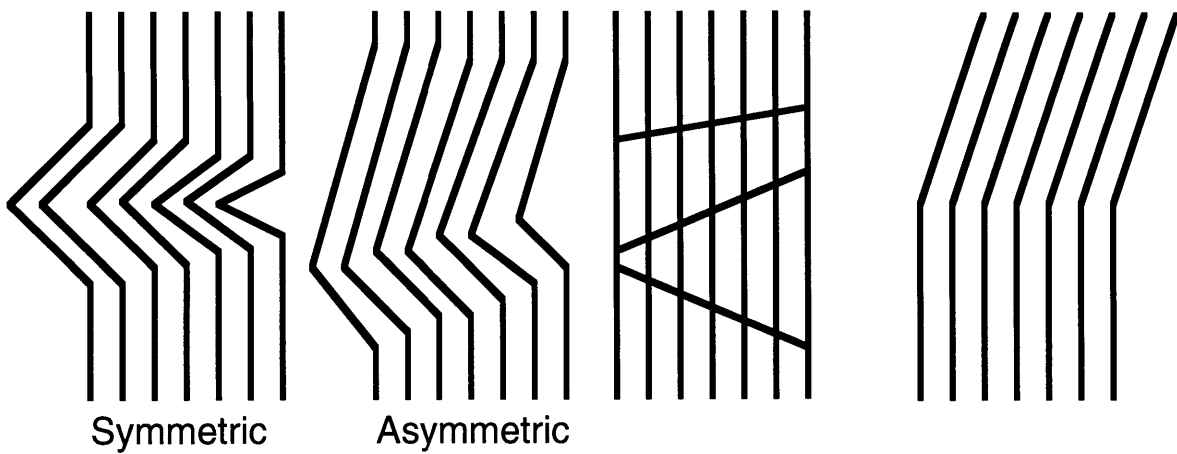
Figure 2.1   An illustration of some possible local modes of failure resulting from fiber microbuckling.

microbuckling is assumed plastic unless otherwise noted), wood/wax specimens suffered fiber crushing, and spaghetti/wax specimens failed due to matrix failure [30].

Interesting work has been done in the area of post-microbuckling analysis. Relatively thick unidirectional specimens exhibited a kink band failure which suddenly traversed the coupon: a shear crippling compressive failure. However, the specimen still possessed a notable load carrying capability. After a significant load drop, the edges/boundaries of the kink band propagated axially, increasing the width of the kink band. This mechanism was called "band width broadening". It was observed in notched (edge slit) carbon/PEEK composites and the band broadening was described as "propagating fiber bends" [31]. Band width broadening was found to occur in the same material by "micro-kink gliding" a process by which the advancing bends occurred in specific widths characterized by a propagating micro-kink band [32]. Tests done on side-indented carbon/PEEK composites indicated that the broadening was due to successive bends and breaks at the kink band boundaries [33]. The band broadening mechanism has not been reported in structures other than thick composites, because thin laminates will not retain as much load carrying capability after initial failure. Although new features of kink bands were addressed, the relevance of this work is limited to applications that incorporate thick composites, and/or ones in which post-failure compressive response is important.

Transverse kink band propagation has also been observed in thick laminates. Compression tests on center notched carbon/epoxy [34] and dented edge notched carbon/epoxy [35, 36] and carbon/PEEK [37] unidirectional laminates revealed that "damage zones" consisting of kink bands formed at the edge of the notch. The damage zone continues to propagate away from the

notch tip in a steady state manner under increased end-shortening. The panels used in these studies were thinner than those in which the band broadening mechanism was reported (3mm thick compared to 6mm thick specimens).

The failure modes that unidirectional composite laminates undergo may not be indicative of in-service damage likely to be exhibited by structural components because multidirectional composites are typically used for structural applications. However, in some cases the same damage mechanisms are observed in multidirectional laminates. Damage zones (also called crush zones, or in the present work, linear damage zones- LDZs) propagating from open holes in a similar manner as previously described for notched unidirectional composites were observed in thick carbon/PEEK and carbon/epoxy multidirectional laminates [38-41]. These crush zones initiate at the hole edges by fiber microbuckling of the 0° plies and/or out-of-plane shear crippling. The shear crippled zone extended through the thickness of the specimen and propagated away from the hole with increased loading. The 0° plies at the surface tended to fail by out-of-plane shear crippling, while the 0° plies located towards the middle of the laminate failed by kink band formation in which the fibers remained aligned above and below the kink bands. Multiple kink bands were observed, along with symmetric and asymmetric fiber microbuckling. Local deformation and delaminations also were found in the damage zone. It was postulated that such damage mechanisms must occur to accommodate the large deformations associated with fiber rotation and buckling. Similar results were obtained for thick carbon/epoxy multidirectional laminates with open holes [42-44]. Fiber microbuckling of the 0° plies into the hole was the initial failure mode. Additional damage included matrix cracks and delamination.

A study on thick, open hole, center-notched, and single edge-notched

carbon/epoxy laminates reported "plastic" deformation along with delamination and microbuckling of the 0° plies as the failure mechanisms, but did not mention damage zone propagation [45]. Unnotched multidirectional carbon/epoxy and S-glass/epoxy laminates have also been shown to fail by kink band formation in conjunction with delaminations [46]. The compressive response of E-glass/epoxy cross-ply laminates was studied in a novel flexure device [27]. Microbuckling and delamination were the key damage mechanisms observed in unnotched specimens. Fiber microbuckling initiated kink band shear crippling failures in unnotched angle-ply carbon/epoxy and carbon/PEEK laminates [47]. The same laminates containing a center hole were also found to fail due to fiber microbuckling. However, stable microbuckle zone growth was observed prior to ultimate failure. Accompanying damage included splitting in 0° plies and delamination between 0° and 45° plies.

For both unidirectional and multidirectional laminates, fiber microbuckling and kink band formation seem to be the key damage mechanisms. The majority of the compression tests have been accomplished using relatively thick laminates. The literature has reported propagating damage zones (also referred to as crush zones or linear damage zones-LDZs) consisting primarily of kinked fibers in thick notched laminates. However, LDZs have not been reported thus far in thin (two or three ply) notched laminates.

2.2.2 Compressive Damage Mechanisms in Woven Composite Laminates

Well established textile industry technologies have been applied to composites; two and three-dimensional composite laminates utilizing different weave types have been developed. Although generally more expensive than

unidirectional tape prepregs, woven prepregs offer substantial payoffs, such as greater pliability/drapability in uncured form, ease of handling, and multidirectional support (better out-of-plane properties) [48]. Unfortunately, the presence of fiber bundle crimp in woven composites presents a disadvantage when compared to unidirectional tape architectures. Crimp and other imperfections may contribute to both the early initiation and change the mode of the controlling damage mechanisms. It should be noted that sandwich structures with two and three ply woven E-glass composite laminate facesheets were used in the present work.

Two and three-dimensional woven composites consist of a woven architecture of fiber bundles. Bundles are either referred to as tows (untwisted, or straight fiber bundles) or yarns (twisted fiber bundles). When a two-dimensional ply is created, bundles are laid in longitudinal and transverse directions. The bundles oriented in the longitudinal direction are referred to as warp bundles. The bundles running in the transverse direction are referred to as weft, fill, or woof bundles. One woven ply is generally referred to as $[\theta_1/\theta_2]$. Three-dimensional composites have a similar nomenclature. For example, [0/90] generally refers to the 0° stuffers, or warp bundles, the 90° fillers, or weft bundles, and some sort of interlocking fiber system (the out-of-plane direction). Woven composites may be manufactured in several different ways; e.g. weaving, stitching, braiding, or knitting [49].

The compressive response of nine ply [0/90] and [-45/+45] five-harness satin weave carbon/epoxy laminates was observed using both compression and bending fixtures [50]. The damage found in the [-45/+45] specimens consisted of matrix cracking in the fiber directions followed by transverse yarn fiber failure and delamination. Fiber microbuckling occurred near the crossovers, where fiber misalignment is the greatest. Delamination propagated in the fiber

direction. The [0/90] specimens failed macroscopically by transverse shear. Fiber microbuckling in the out-of-plane direction of warp yarns, as well as propagation of matrix cracks, preceded ultimate failure. Laminates tested in the bending fixtures exhibited fiber kinking, propagating transverse matrix cracks, and interlaminar microcracking.

Twenty ply [0/90] and quasi-isotropic eight-harness satin weave carbon/carbon specimens, in both low and high initial crack (void) densities were studied [51]. In these specimens, material imperfections included thermally induced microcracking, a consequence of carbonization cycles, and fiber bundle crimp. In both specimens, ultimate failure occurred suddenly with no observable initial damage. The low crack density samples developed a through-thickness shear band, which was the result of fiber microbuckling and fiber kinking. The out-of-plane shear band developed after local bundle microbuckling in the vicinity of the crimps resulted in kink band formation in each warp bundle. Delaminations coalesced with the kink bands to form a large scale shear fault. Local microbuckled regions were found to contain multiple kink bands. Failure of high initial crack density specimens, on the other hand, was controlled by the axial microcracks. Upon loading, delaminations began at the cracks. Catastrophic failure occurred when a delamination suddenly extended the entire length of the specimen. No local buckling instabilities were found, supporting the theory that failure is imperfection sensitive.

Twelve ply [0/90] five-harness satin weave carbon/epoxy laminates were also found to fail without warning [47]. The primary damage mechanism was microbuckling of the warp tows. Kink bands were also observed. Matrix failure occurred on a plane oriented at 45° to the loading axis. The initial damage mechanism for central hole laminates of the same material was

microbuckling at the edge of the hole. Stable microbuckle zone growth was observed; increased loading promoted damage growth, until a critical damage length and maximum load was reached, resulting in catastrophic failure. Therefore, not only were similar damage mechanisms found to be operating in both notched woven fiber composites and notched tape laminates, but transverse propagation of a kink band dominated damage mode was also found in both cases.

Six ply [0/90] five-harness satin weave carbon/epoxy laminates and twenty-four ply [0/90] E-glass/epoxy laminates were found to exhibit the same compressive failure mechanisms [52]. The laminates failed due to fiber and matrix shear failure along a plane 45° to the loading axis. Splitting was also observed. However, no damage zone propagation was observed prior to catastrophic failure.

Three-dimensional woven and stitched composites offer the added quality of higher out-of-plane strength and delamination resistance when compared to two-dimensional composites [53], as well as better notch insensitivity and damage tolerance [49]. Fairly detailed compressive failure mechanism analysis was performed on three-dimensional [0/90] carbon/graphite samples [54]. These samples contained several material imperfections due solely to fabrication processes, including bundle fractures, matrix porosity, and fiber curvature. The warp bundles suffered the most damage, which was generally confined to fiber kinking. On a given specimen, multiple in and out-of-plane kink bands formed along the bundle. While individual fiber fracture characterized kink band boundaries, little matrix fracture at the boundaries were found. However, matrix voids were observed to be located at the intersection of the matrix with kink band boundaries. Kink bands were found to terminate at locations where previous defects were

located, such as voids or other kink bands. Some kink bands did not propagate the full width of fiber bundles. These gave an indication of the sequence of kink band formation. Specifically, it was noticed that significant fiber bending preceded fiber microbuckling, which in turn established kink band boundaries. Furthermore, for a given kink band, the individual fiber ligament lengths can vary significantly, although the inclination and boundary orientation angles are consistent. Typically, a kink band width is established because individual fiber ligament lengths within the kinked region are similar.

Three dimensional [0/90] carbon/carbon and carbon/S-glass woven composites and forty-eight ply quasi-isotropic carbon/carbon, carbon/S-glass, and carbon/Kevlar stitched laminates were found to vary considerably in compression failure mechanisms [53]. The stitched laminates failed in a brittle manner as compared to the woven specimens. Failure was due to a shear band failure through the thickness of the specimen. The shear band consisted of a kink band accompanied by delamination. The woven composites, in the same specimen configuration, exhibited widespread buckling and debonding. Detailed investigations showed that the woven composites were not affected by fabrication-induced material defects. Instead, cracks developed between warp tows and the matrix, as a result of debonding. Buckling of the straight warp stuffers followed, and kink bands were found throughout the test section at different locations. Matrix cracks were also found. Instead of sudden shear band failure, failure occurred by progressive fiber kinking. Observations were made with regard to factors influencing kink band formation, including geometrical flaws and location of the misaligned warp stuffers. Although the extent of damage was found to differ in woven and stitched composites, the key damage mechanism in all materials was kink band formation.

Both lightly (four ply) and heavily (four or six ply) compacted three-

dimensional [0/90] carbon/epoxy and S-glass/epoxy composites with various interlocking architectures were found to fail in compression predominantly by kink band formation in warp tows [49]. The lightly compacted specimens were similar to those previously tested in [53]; partial delaminations also contributed to failure. In heavily compacted specimens, which were half as thick, delamination was more prominent. In these cases, it seemed as if kink band formation was caused by delaminations. As before, comparisons between specimens with different imperfections resulted in similar damage mechanisms.

These findings for the compressive damage mechanisms agree well with results for five ply three-dimensional [0/90] carbon/epoxy laminates, where failure was characterized by kink band formation in the warp stuffers [47].

2.2.3 Summary

The key compressive damage mechanisms observed in notched laminates were fiber microbuckling and fiber kinking. Other possible damage mechanisms included matrix cracking, delamination, and splitting. Experiments have shown that similar compressive responses were obtained for notched laminates made from unidirectional tape and from woven fiber architectures. However, all of these results are indicative of thick laminates. No experimental evidence exists in the literature which reports the propagation of a kink band-dominated damage zone as the compressive failure mechanism for thin laminates.

2.3 Compressive Damage Mechanisms in Sandwich Panels and Other Structures

Composite sandwich constructions have been used in the aerospace

industry for applications in both civilian and military airplanes, missiles, and spacecraft [55]. Their advantages of high bending stiffness and low weight exist because thin composite facesheets are used [56]. The compressive properties of composite laminates can be employed without failure occurring as a result of a global instability, as would be observed in a very slender structure such as a thin laminate by itself. Although part of the intention of using sandwich panels includes avoiding instabilities, several buckling-related behaviors can still occur, such as shear crimping, facesheet wrinkling, and facesheet dimpling [55, 56]. Several possible buckling failure modes are shown in figure 2.2.

One very important issue arises from the literature regarding the compressive response of sandwich structures. A majority of the work focuses on characterizing the damage mechanisms and damage tolerance which arise as a result of post-impact compression. In service, sandwich structures are susceptible to a variety of impact events such as a hailstone strike or a tool drop, which in turn causes damage to the sandwich panel. The present work utilizes circular holes, in one sense, as an idealization of the damage incurred by such impact events. Therefore, failure mechanisms arising from post-impact compression are relevant to this work.

It should be noted that static and dynamic impact tests are performed on specimens to yield a representation of damage that might be incurred in service. Although simplifications exist (e.g. using a hole to represent impact damage) as cost-effective alternatives to actually impacting the specimen, the distinction between the actual case (impact) and the idealized case (hole) based on experimental observations needs to be addressed. It has been shown that impactor size cannot be used as the metric with which to measure hole size, since compressive strengths for impacted carbon/epoxy laminates are less

General Buckling

Shear Crimping

Facesheet Wrinkling

ADHESIVE BOND FAILURE

CORE COMPRESSION FAILURE

Facesheet Dimpling

FACES BUCKLE INTO CORE CELLS

HONEYCOMB CORE
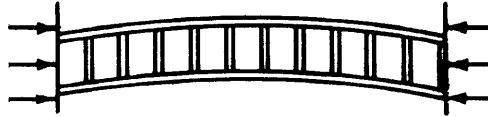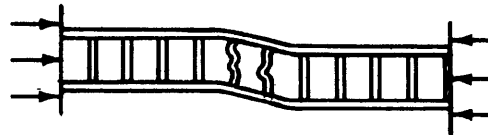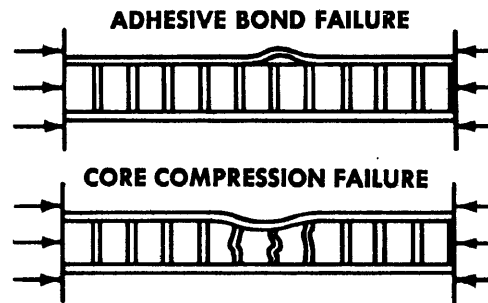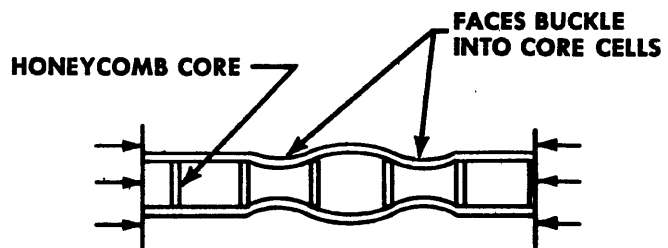
Figure 2.2   Possible instabilities in sandwich structures [56].

than those with holes of the same diameter of the impactor [57]. The amount of visible damage resulting from impact is also not a reliable metric, since impact events can cause externally invisible sub-surface damage [58, 59]. This fact, along with the difference in failure mechanisms observed in both impacted and notched sandwich panels loaded in compression (as will be discussed later), is important when assessing the overall effectiveness of using notches as representative damage [60]. However, the determination of the effectiveness of notches in accomplishing this task is beyond the scope of this work.

2.3.1 Compressive Damage Mechanisms in Sandwich Panels with Unidirectional Facesheets

Unnotched sandwich panels with [+45/-45/0]$_S$ (the layup represents one facesheet, and the sandwich panel is symmetric about its centerline) carbon/epoxy facesheets and various core materials and thicknesses exhibited failure modes that varied with core type [61-63]. All cores were 9.6mm thick or less. Measurements of out-of-plane facesheet displacement during testing indicated that a general buckling instability at least partially contributed to most of the observed failure modes. Panels with aluminum honeycomb cores failed due to facesheet fracture across the width of the specimen. Widespread facesheet debonding characterized by large bulges was the main failure mode in panels with Nomex^{TM} cores, although some specimens failed due to facesheet fracture accompanied by delamination. No facesheet damage was found in the majority of specimens with foam cores. Instead, the foam core fractured across its width. Accompanying damage included through-thickness facesheet fracture and delamination.

A common practice when testing unnotched sandwich panels involves

using a material such as epoxy to mount the ends of the specimen (also known as "potting") to prevent end failures. However, such fixtures can cause stress concentrations and failure modes of their own. For example, potted specimens with twelve ply multidirectional carbon/epoxy quasi-isotropic facesheets surrounding a 19mm thick glass-reinforced phenolic honeycomb core were characterized by a brooming failure near the potting compound, which included facesheet fracture, fiber splitting, and delamination [60]. The same specimens having a center end-rounded slit in either one or both facesheets failed by facesheet fracture. Fiber splitting was also observed to have occurred from the slit tip in the outer ply in the fiber direction.

2.3.2 Compressive Damage Mechanisms in Sandwich Panels with Woven Fiber Facesheets

Unnotched sandwich panels consisting of plain weave carbon/epoxy facesheets in [0/90] or [+45/-45] orientations and Nomex™ honeycomb cores were found to exhibit failure modes caused by buckling. Specimens with cores of either 9.5, 17.4, or 25.4mm thickness failed due to facesheet fracture or core failure [64]. Facesheet fracture was not acknowledged as a valid failure mode because it occurred due to the stress concentrations near the ends of the specimens. Buckling of facesheets was observed to occur when facesheets separated from the core material as a result of core tearing. Note that core tearing did not involve damage to the adhesive bond between the facesheet and the core. Sandwich panels also failed due to buckling as a result of core shear failure. This mode was characterized by global shear crippling. Unnotched [0/90] specimens with 25.4mm core thicknesses also exhibited facesheet fracture in combination with core tearing, but buckling was not observed to be the failure mechanism [4]. Facesheet fracture occurred in both facesheets,

but on one side, the core material tore in a location underneath the fracture site. The opposite side showed minimal core damage or none at all. Similar results were found in sandwich panels with [+45/-45] facesheets. The only difference was that facesheet fracture occurred in the fiber angle directions. Both facesheets failed, and the line of fracture was continuous, oriented in either a straight or triangle wave manner.

Different failure mechanisms were observed in notched specimens with 25.4mm thick cores [65]. Specimens had a circular hole in the center of one facesheet. [0/90] specimens suffered facesheet fracture in both facesheets with core tearing accompanying fracture on one side. Sandwich panels with [+45/-45] facesheets fractured along the fiber orientation angles. Through-thickness facesheet damage was not detected, which led to the conclusion that failure began between plies. Core tearing and bulges in both facesheets were also observed, but were not attributed to buckling instabilities because audible damage events along with cracks visible on the surface ply occurred prior to catastrophic failure. Facesheet fracture at a location other than through the hole was also observed.

Unnotched woven Kevlar specimens failed due to facesheet wrinkling, which caused full width facesheet fractures [66]. Facesheet wrinkling was also observed in carbon/epoxy specimens with two to four plies in assorted orientations and various 25.4mm thick honeycomb cores [67]. These findings lead to an important conclusion arising from the literature. The discrepancy which exists in describing failure mechanisms makes it difficult to specify the exact precursor to failure. For example, although facesheet fracture may be the ultimate failure mode, in many cases no information is found as to the damage mechanisms causing fracture. In this case, facesheet wrinkling was found to be the key damage mechanism. Whether or not facesheet fracture or

other damage modes are due to different failure mechanisms or are failure mechanisms in themselves is in many cases not documented in the literature.

2.3.3 Compressive Damage Mechanisms in Impacted Sandwich Structures

As mentioned before, testing of impacted sandwich panels attempts to capture damage modes that would be incurred from in-service impact events. To accomplish this, different fixtures may be used, as well as static or dynamic impact. Plain weave carbon/epoxy facesheets with two ([+45/-45] and [0/90]) and three ([0/90/-45]) ply facesheets and various Nomex core thicknesses up to 25.4mm were subjected to static indentation or dynamic impact [64]. Damage occurred as a result of the impact event, and was characterized by a "dimple". Compressive residual strength tests revealed that the key damage mechanism in both indented and impacted specimens was growth of the dimple. The dimple grew in area and length, primarily in a direction perpendicular to the loading direction. Dimple propagation continued until it completely traversed the facesheet, causing catastrophic facesheet fracture. The core tearing that accompanied facesheet fracture was indicative of buckling, since the thickness of the core still connected varied along the facesheet. Therefore, although dimple propagation was the observable damage mechanism (the red herring), facesheet wrinkling was the cause of failure.

Other compressive failure mechanisms were also observed in [0/90] and [+45/-45] plain weave carbon/epoxy specimens [4]. [0/90] panels with initial damage from static indentation or damage from simulated core damage (an initially crushed core) and static indentation had significant transverse dimple propagation prior to ultimate failure. The dimple did not extend across the full width of the damaged facesheet in all cases. When the dimple did cross the

entire facesheet, a full width facesheet fracture was accompanied by core tearing and core crushing, along with distinct facesheet bulges at the location of core tearing. Dimple propagation, facesheet fracture, core tearing, and core crushing were also observed in similarly impacted/damaged [+45/-45] panels. However, panels with simulated facesheet damage (resulting from very narrow cuts made with a Dremel® Moto-Tool®) failed due to stable damage propagation. Facesheet fractures extended from the tips of the slits in a stable manner along the fiber orientation angles. Fracture lines were either straight or oriented in a triangle wave pattern. Ultimate failure occurred instantaneously, with fracture lines extending the full width of the facesheet. Other material systems, such as impacted sandwich panels with woven Kevlar facesheets have exhibited stable dimple growth as well [66].

2.3.4 Compressive Damage Mechanisms in Other Structures

Carbon/PEEK structures in circular rod and ring structures tested in compression failed due to sudden fracture [68]. Rods that had non-uniform cross-sections broke into two pieces upon failure. Rings fractured at one location on a line at a small angle to the loading direction. Circular rods that had uniform cross-sections, however, developed kink bands. Multiple kink bands were observed, and they were found to increase in number with further end-shortening [68, 69].

2.3.5 Summary

Both unnotched and notched composite-honeycomb sandwich panels with either unidirectional tape or woven fiber architectures generally failed due to facesheet fracture. Stable growth of a kink band-dominated damage zone, as reported for thick laminates, was not observed. However, stable growth of an impact-induced dimple did occur. In both cases, increased end shortening

resulted in stable damage propagation in a direction perpendicular to the loading direction. Studies involving the compressive response of sandwich panels do not report fiber microbuckling or fiber kinking as damage mechanisms which contribute to the ultimate failure mode, as was the case with laminates. This may be due to the fact that the majority of sandwich panel work was done on panels having thin facesheets.

2.4   Compressive Failure Prediction Techniques for Laminates

Methods for predicting the compressive behavior of laminates, particularly the strength, have been developed. Techniques exist that attempt to model failure at the individual fiber length scale, as well as those that either generalize the composite's local response into a cohesive zone or ignore physical damage mechanisms completely. The present work is concerned with the type of modeling commonly referred to as damage zone modeling (DZM), which is also referred to as cohesive zone modeling (CZM). It is beyond the scope of this work to describe the other modeling techniques in detail. However, this section will present a brief review of the more common failure prediction models.

2.4.1 Micromechanics Models

An extensive literature exists on micromechanics-based compressive strength models. These models, for the most part, attempt to describe the behavior of a compressively-loaded composite laminate by modeling buckling of the fibers. A vast number of techniques, mostly refinements of earlier modeling efforts, have been developed. Laminate failure is generally regarded as occurring as a result of fiber microbuckling [23, 24, 27, 70-78], kink band formation [46, 54, 79-87], kink band propagation or kink band width

broadening [31, 32, 88, 89], or other damage mechanics approaches [90-92]. The large number of models in the literature gives an indication of the subtleties involved in modeling this problem. Factors that have real physical effects on the strength of composites, such as initial waviness, nonlinearity, or stochastic variables may or may not be incorporated into a single micromechanics model. Therefore, similar models may differ by the incorporation of just one of these factors. The goal then becomes to discover which modeling parameters provide the best agreement with experimental results. The majority of the previous work assumes that the composite laminate is unidirectional, and applying these models to multidirectional composites involves greater complexity and more assumptions. Micromechanics models have been developed, however, for woven fiber architectures [93]. Notwithstanding, the analyses can be cumbersome to implement and refine, while still lacking the ability to capture key damage mechanisms, such as the propagation of a kink band-dominated zone in a woven fabric composite. It should be noted that finite element models focusing on fiber microbuckling have also been utilized [24, 68, 69, 94-97].

2.4.2 Stress-Based Models

Two related notched strength models, the point and average stress criteria (PSFC and ASFC, respectively) [98], are among the most widely used stress-based failure prediction models. They were originally developed as failure stress correlative models of circular-notched laminates under tensile loading, with no distinction between unidirectional or multidirectional layups.

Analysis of the stress distribution around a circular hole in a laminate subjected to a remote tensile stress indicates that regions of high stress exist only in the vicinity of the hole. The effect of hole size on strength was explained

by the assumption that plates with larger holes have a greater probability of having flaws within the higher stress area; i.e. as the hole size increases the strength decreases. Since composite laminate failure typically occurs in a brittle fashion, failure is presumed to initiate at a location of a flaw in the material. The area of this high stress region at the notch tip increases with hole size. The stress-based failure criteria states that a notched laminate will fail when the stress acting at a characteristic distance (PSFC) or when the average stress acting at a characteristic distance (ASFC) equals the unnotched laminate strength. The critical distances are assumed to be material properties. The most convincing physical argument comes from the PSFC, which postulates that the characteristic distance is equal to the distance over which a flaw exists such that when subjected to the critical stress, failure will occur. In application, these criteria are effectively two parameter fitting models, and the characteristic distance that is chosen is the one that best fits the experimental data. However, the characteristic distances are not indicative of material properties, since they tend to vary with notch size.

Other stress-based failure prediction techniques, using the same framework as the PSFC and ASFC, were created by incorporating parameters such as a notch sensitivity factor in an effort to obtain better strength predictions [99]. In reality, the correction factors simply become a replacement fitting parameter at best, and at worst an additional fitting parameter. Other failure criteria based on the stress distribution around a notch for unnotched and notched multidirectional laminates have been developed for the tensile loading case, but have not been as widely used as the PSFC or ASFC.

The extension of the ASFC to notched laminates loaded compressively

has been accomplished via a single assumption: application in compression is just as allowable as application in tension [100]. The model has not been utilized as much for notched compressive strength predictions, but it has been used in conjunction with a fracture mechanics analysis [42, 43]. The PSFC has also been used [41]. Notwithstanding these examples the application of these stress-based models to notched composites under compression is very limited, compared to their use for the tensile loading case.

2.4.3 Fracture Mechanics-Based Models

The use of linear elastic fracture mechanics (LEFM) concepts, specifically with regard to isotropic materials, requires that certain assumptions are made. These assumptions include: the presence of a pre-existing flaw, tensile loading (mode I), self-similar crack growth, and a crack as the only damage mechanism. Application of LEFM to composite materials requires a few more assumptions to validate their usage. For example, the composite is assumed to have a fracture toughness, and the damage, which in itself can be comprised of many types of individual damage mechanisms, is assumed to propagate in a collinear manner with the damage zone dimensions being small compared to specimen geometry dimensions [101]. The application of LEFM concepts to notched composite laminates began with the analysis of tensile loading cases with the inherent flaw criterion (also referred to as the fictitious crack model) [102]. As with the stress-based models, no distinction was made between unidirectional and multidirectional layups. Despite the attempt at introducing a physical basis, the analysis reduces to a fitting exercise; the length of the inherent flaw located at the notch tip, referred to as the "intense energy region," is treated as a variable parameter, much like the characteristic distances of the PSFC and ASFC. By adjusting the length,

the best prediction can be made with regard to experimental strength results.

Another widely used notched strength model, known as the Mar-Lin correlation [103, 104], is derived from an LEFM framework and is very similar to the inherent flaw criterion. The model utilizes the notch size, a fracture parameter, and an exponent which describes the order of the singularity of the crack. Although the fracture parameter can be determined experimentally, as with the unnotched strength in the previous models, the exponent is determined empirically.

Fitting within bounds provided by experimental results provides a good "prediction" of notched strength, both with the stress-based failure criteria and with the fracture mechanics-based models. The predictive power, or the ability to extrapolate strength prediction to other geometries and even to other layups, is not addressed by these models. While it is generally accepted that these models are quite good at "predicting" based on interpolation, effective extrapolation remains a goal of strength modeling. Currently, the aforementioned models are seldomly used.

2.4.4 Damage Zone Models

One other major modeling framework exists that originated from modeling laminates under tensile loading conditions. The basic idea behind damage zone modeling in composites (also referred to as cohesive zone modeling) is that all of the damage mechanisms (such as matrix cracks, fiber breaks and pull-out, and delaminations) contained in a damage zone emanating from the tip of a notch in a composite material under tensile loading are lumped together and treated as a bridged crack. The damaged material is idealized as a single crack with a distributed traction acting on the faces of the crack, which represents the constitutive behavior of the damage zone. The traction

law is the relationship between the "bridging" stress on the crack face and the crack opening displacement, and it is assumed to be a material property. The damage zone modeling framework originated with the Dugdale approach for metals [105], and hence these analyses, which in practice can be very different from the original model, are typically referred to as "Dugdale-type" models. Early application of the model to notched multidirectional laminated composites in tension required the use of a finite element analysis and resulted in the Damage Zone Model (DZM) [106-109]. These analyses differed from the Dugdale approach in that a fracture mechanics criterion for crack propagation was not used. The finite element model calculated the tractions, crack opening displacement, and applied load as the crack length was increased. Fracture was assumed to occur when an increase in crack length did not produce an increase in applied load. A similar model, the Damage Zone Criterion (DZC), utilizing both the DZM and a stress-based failure criterion, allowed for simplification of the DZM while still using a Dugdale-type approach [110]. Other cohesive zone models have been developed, such as the Effective Crack Growth Model (ECGM) [111, 112], which differ in detail from the DZM or DZC but still adhere to the basic concepts of damage zone modeling; i.e. the damage zone is simplified to a bridged crack subject to a traction law.

The use of damage zone modeling has been successfully extended to thick (greater than two or three plies) notched composites under compressive loading, with unidirectional [34-37] and multidirectional [38-44] layups. The rationale behind this is that in certain cases compression-loaded laminates develop damage zones which initiate and subsequently propagate from the notch tips. Microscopically, these damage zones are dominated by kink bands. Macroscopically, however, they look and behave as cracks in tension. After initiation, the kink band zone continues to propagate in a direction

approximately perpendicular to the loading direction with further end shortening, which is macroscopically similar behavior to cracks growing in tension. Although the DZC has been applied to notched multidirectional laminates [113], the models used to obtain compressive strengths differ in application to the DZM or the DZC. Since the present work utilizes a damage zone modeling analysis, the details regarding the application and physical bases of the damage zone model will be discussed in chapter four.

2.4.5 Summary

Several modeling approaches have been developed to predict the compressive failure strength of notched composite laminates. Micromechanics models, along with the stress-based and fracture-based failure criteria, have shown some levels of success. Two discrepancies exist among these models which limit their effectiveness as physically-based predictive models. The first discrepancy deals with empiricism. The practice of fitting to experimental data found in strength prediction models is associated with almost all current failure prediction models. The true predictive capability of a model that is calibrated on a data set is actually quite strong if "predictive" is taken to mean interpolation within the bounds of the data used to calibrate the model. The model can predict notched strength for a given material type and configuration once a significant amount of testing has been accomplished. These failure prediction models may be thought of as an extreme case of problem simplification, a goal of modeling in general [114]. However, in order to advance the modeling efforts, sound, physically-based models must continue to be developed. Understanding the key damage mechanisms is a prerequisite to creating physically-based models, which are required to successfully apply a damage tolerant design approach.

The second discrepancy concerning the first three classes of models discussed is their inability to characterize the type of compressive damage mechanism observed in thick notched composite laminates (and in the present work, thin facesheets in composite-honeycomb sandwich panels): stable propagation of a linear damage zone prior to catastrophic failure. Damage zone models possess this capability. In theory, they can predict the ultimate failure load, damage propagation, and the local strain distribution.

2.5 Compressive Failure Prediction Techniques for Sandwich Panels

A variety of sandwich panel compressive strength models exist. Models either focus on the entire sandwich panel or only on the facesheets. Treating the facesheets as independent entities can be justified in cases characterized by even load distribution between both facesheets with negligible bending effects. Furthermore, failure of one facesheet should not be significantly affected by the core. In such cases, it may be appropriate to apply compressive strength models derived for use in laminates. When the entire sandwich structure is analyzed, the core is taken into account, and strength predictions vary depending on the instability being modeled (some types of instabilities that can occur in sandwich panels [115] were mentioned previously). When the facesheets are treated as separate entities, stress-based [65] and fracture mechanics-based [4, 60, 64] models can be used. Furthermore, other models have been developed in order to accommodate dimple propagation observed in post-impacted panels [4, 60]. No work, and hence no modeling, has been done on notched sandwich structures which fail due to propagating damage zones.

2.6 Summary

The key compressive damage mechanisms observed in both unnotched and notched unidirectional and multidirectional laminates, both with unidirectional tape and woven fiber architectures, is fiber microbuckling and fiber kinking. Fiber kink bands are a local instability typically characterized by several buckled fiber ligaments which cooperatively align together to form a band with a distinct width which is oriented along specific angles. The kink band failure mechanism has, for the most part, not been reported in composite-honeycomb sandwich panels. Propagating damage zones consisting primarily of kink bands are the principal failure mechanisms observed in thick laminates. Several compressive strength models exist to predict both the unnotched and residual strength of composite laminates. Damage zone models have been used successfully in instances where the failure mechanism is a propagating damage zone. The present work applies damage zone modeling to thin facesheet notched composite-honeycomb sandwich panels, which fail due to a propagating kink band dominated linear damage zone (LDZ).

CHAPTER 3

EXPERIMENTAL PROCEDURES

This chapter begins by describing the materials used in the experimental study. Then, the procedures used to fabricate the sandwich panels are discussed. The compression testing method utilized is discussed, as well as the procedures used to detect and characterize damage.

The materials were supplied by the Structural Methods and Allowables Group (SMA) at The Boeing Company. Material dimension values or material properties denoted as "nominal" refer to the values listed in the material data sheet provided by Boeing.

3.1 Materials

The test materials provided by Boeing are considered proprietary; i.e. any information aside from that listed on the material data sheet is either unknown or cannot be divulged.

The test specimens were notched E-glass/epoxy-Nomex™ honeycomb sandwich panels. The sandwich structure consisted of a hexagonal honeycomb core surrounded on both sides by composite facesheets. The core material, nominally 25.4 mm thick with a density of 48.055 kg/m³, was reduced to a thickness of 24.7 mm and 25.1 mm (for M4 and M5 materials, respectively) due to manufacturing procedures. All notches were centrally located circular holes drilled through the entire specimen thickness.

It is speculated that the sandwich panels were co-cured, because of the

"dimpling" observed on one facesheet which caused it to have a rough texture. In contrast, the other facesheet of the sandwich panel was smooth. The smoothness was probably due to the use of a metal caul plate during the curing process. The smooth facesheet was designated as the "front" side, and the rough facesheet was designated as the "back" side.

The woven facesheets were composed of E-glass fibers and epoxy matrix. No information was given for the epoxy material, or for the specific weave types. It is assumed that the same fibers were used in each facesheet type for both the warp and weft tows; no weft tow information was provided and nominal elastic moduli in the warp and weft directions were equal. It should be noted (and will be discussed later) that the exact value of material properties other than E_1 do not significantly affect the test procedures or subsequent modeling. Two facesheet material systems were used in the sandwich panels: "A-series" or "M4" panels, and "B-series" or "M5" panels. M4 and M5 refer to the material designations used by Boeing SMA. Both facesheet material systems were composed of multiple plies of E-glass fiber bundles arranged in a [0/90] configuration, with 0° being the warp and loading direction. Each ply was composed of a two-dimensional weave consisting of 0° warp bundles and 90° weft bundles. In order to determine the weave type, facesheet samples approximately 25 mm x 38 mm were cut out of a specimen from each material type using a Dremel® Moto-Tool® with an emery cut-off wheel (attachment #409). The epoxy was burned off the sample using a propane torch and the weaves examined under an optical microscope.

M4 sandwich panel facesheets consisted of two plies of eight-harness satin weave. A cross-sectioning method (discussed later) was used to determine the number of fibers per bundle, which was found to be approximately 800. An exact number could not be obtained, since the

photograph quality along with the polishing process may have obscured a few fibers. After the epoxy was burned off, the bundle width was measured to be 0.508 mm for both warp and weft fiber bundles (all dimension measurements were taken using a caliper with a resolution of 0.0127 mm unless otherwise indicated). Figure 3.1 illustrates both the "warp" and "weft" side of one M4 ply. For a satin weave, warp tows will be more visible on one side of a ply, while on the other side the weft tows will be more visible. Hence the designation of "warp" and "weft" sides. The stacking arrangement was, beginning from the smooth side: weft(facing out on smooth side)/warp, weft/warp, core, warp/weft, and weft/warp(facing out on rough side). Both a warp on weft interface and a warp on warp interface were used, resulting in an "unbalanced" sequence. The nominal thickness of the M4 facesheets was 0.4826 mm. Since the woven fiber architecture along with the co-cure procedure resulted in varying thicknesses at any given point on the laminate, it was impossible to obtain an exact value for facesheet thickness. Therefore, the average value for measured facesheet thickness was determined to be approximately equal to the nominal value (0.483 mm). The nominal facesheet thickness was used in all calculations.

M5 sandwich panel facesheets consisted of three plies of four-harness satin weave. Figure 3.2 illustrates both sides of one ply. Warp and weft tows consisted of approximately 200 fibers per tow. The bundle width, measured after the epoxy was burned off, was 0.381 mm. The stacking arrangement was, beginning from the smooth side: weft/warp, warp/weft, weft/warp, core, weft/warp, warp/weft, weft/warp. The average measured facesheet thickness for the M5 facesheets was 0.284 mm. Table 3.1 summarizes M4 and M5 facesheet material properties.

Warp Side   Weft Side

Warp Tows

Weft Tows

Loading
Direction
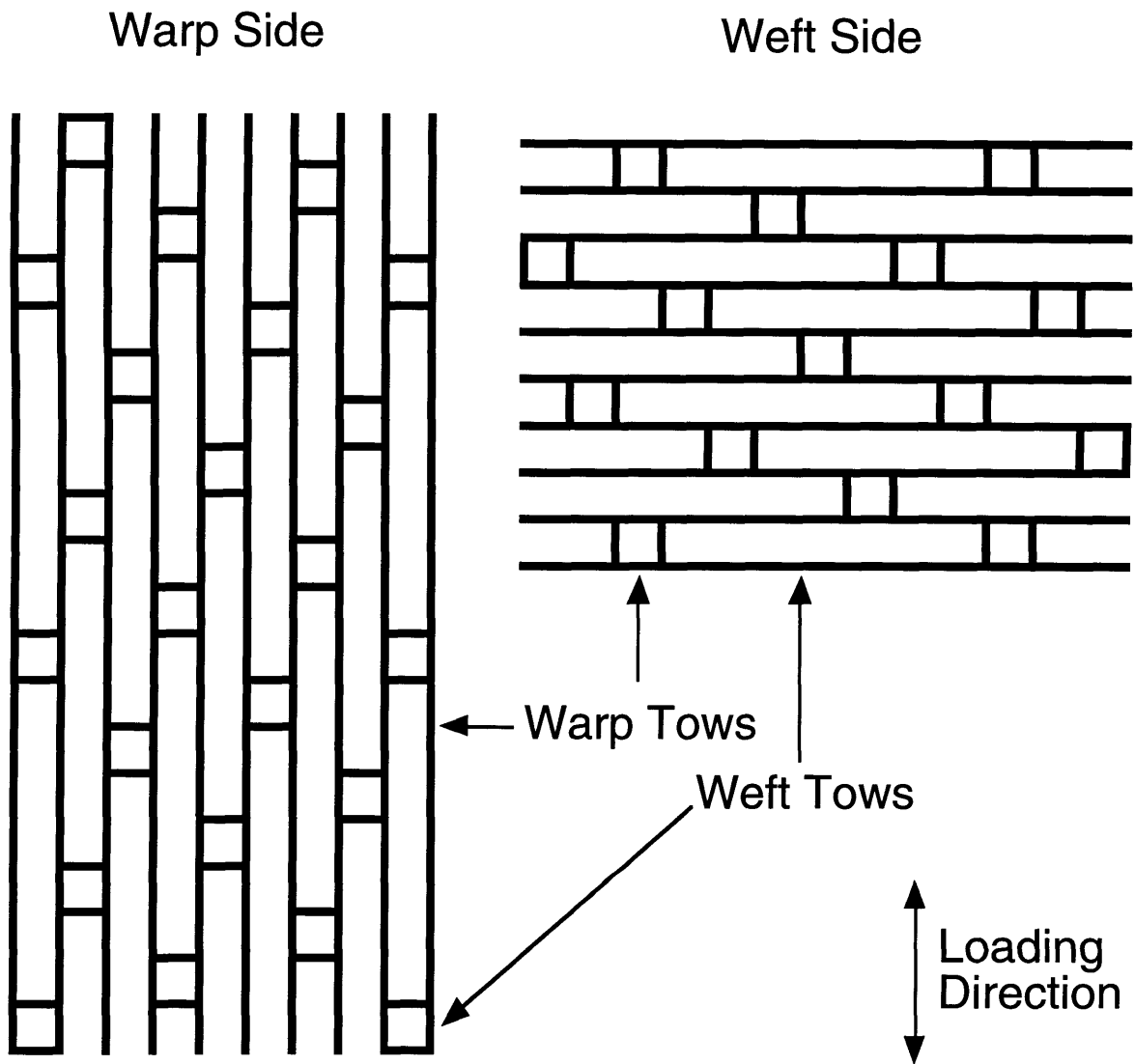
Figure 3.1   An illustration showing both sides of one M4 eight-harness satin
weave ply. The warp side shows nine warp tows. The weft side
shows nine weft tows.

Warp Side　　　　　　Weft Side

Warp Tows

Weft Tows

Loading
Direction
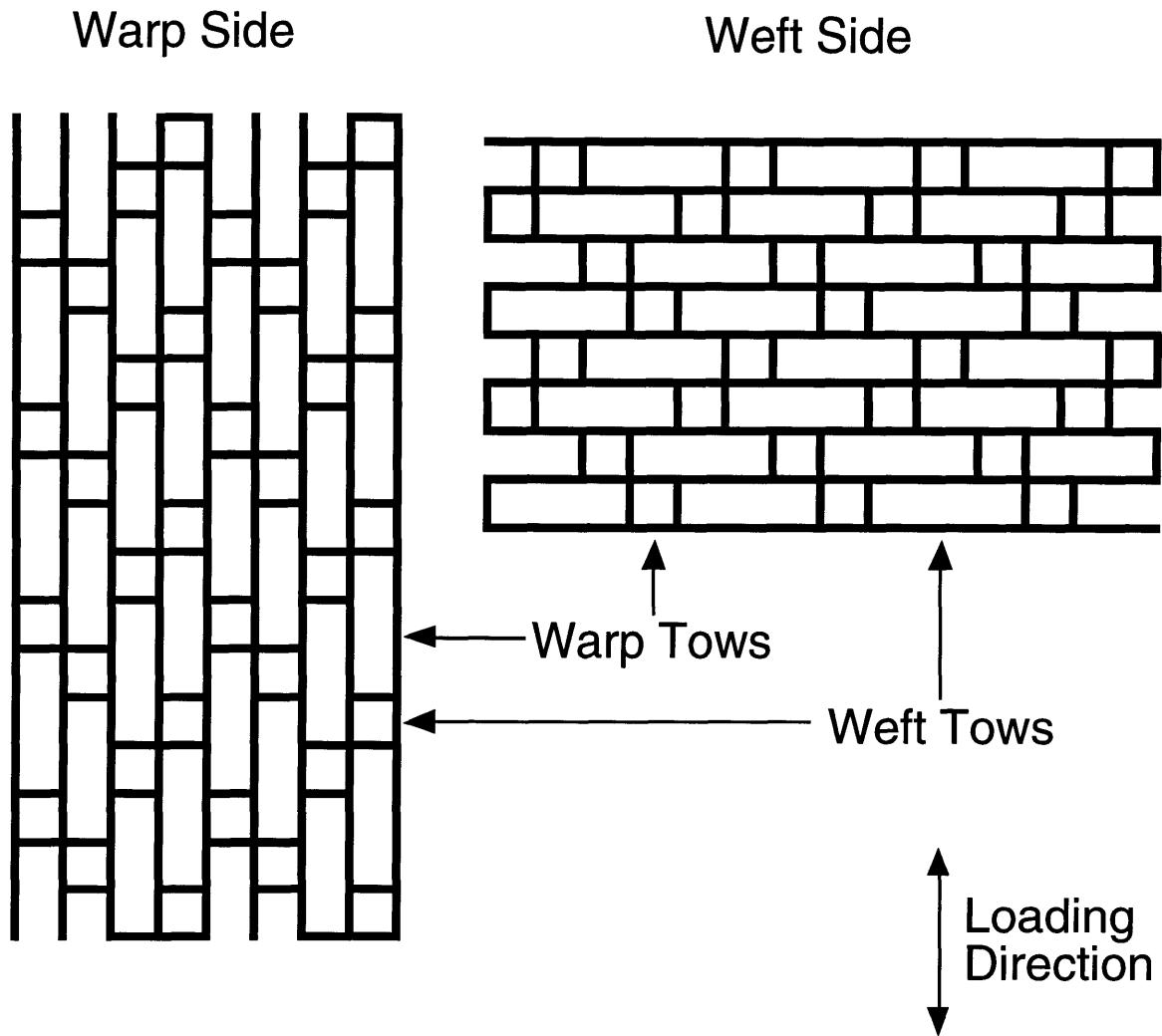
Figure 3.2　　An illustration showing both sides of one M5 four-harness satin
weave ply. The warp side shows eight warp tows. The weft side
shows eight weft tows.

Table 3.1   Material Properties

Material	E_1	E_2	G_{12}	v_{12}
M4	22.1 GPa	22.1 GPa	3.79 GPa	0.11
M5	22.1 GPa	22.1 GPa	3.79 GPa	0.11

3.2 Manufacturing

This section discusses the procedures used to cut the sandwich panels down to specified coupon sizes. The procedure used to notch the specimens, as well as the damage incurred from machining, is also discussed.

3.2.1 Machining

The sandwich panels were manufactured and delivered by Boeing SMA. They arrived in two large panels that were approximately 927 mm long by 406 mm wide, with one panel for each material system. The panels were already cut such that the 0° fiber direction was oriented parallel to the long edge of the panels.

Each panel was then cut into smaller test specimens using a diamond impregnated blade mounted on a Bridgeport® EZTrack® milling machine. The machining was done under contract at the MIT Central Machine Shop. The milling machine was set up to make long cuts. The 254 mm diameter diamond coated blade was oriented such that it cut parallel to the floor. The cuts were made with the blade spinning at 1600 rpm. The nominal specimen sizes for the small, medium, and large specimens were 50.8 mm x 152.4 mm, 101.6 mm x 304.8 mm, and 203.2 mm x 406.4 mm., respectively. The longer dimension corresponds to the edge parallel to the 0° fiber direction and loading axis.

The center of each specimen was located by drawing lines across each smooth facesheet from opposing corners. This center point was then intersected twice using a square, in order to provide a reference for a standard circular template. Holes with diameters of 12.7 mm, 25.4 mm, and 50.8 mm were then drawn at the center of the facesheet of the small, medium, and large specimens, respectively. Diamond impregnated core drill bits were used to cut

holes through the entire thickness of each sandwich panel. A scrap fiberglass or wood panel was placed under the sandwich panel in order to prevent damage from occurring due to the exit of the drill bit. Measured sandwich panel dimensions can be found in Appendix A.

A simple numbering scheme was used to keep track of the specimens. Each specimen was assigned a five digit code. The first letter represented the material system used, and was either "A" for M4 or "B" for M5. The second letter represented the specimen size, with "A", "B", and "D" for small, medium, and large panels, respectively. The last letter corresponded to the hole size, with "A", "B", and "C" for 12.7 mm, 25.4 mm, and 50.8 mm diameter holes, respectively. The fourth digit was a number, which simply represented different panels of the same configuration which were otherwise identical. The last number was used to indicate the compression test number. For example, ADC2_1 represents the first compression test of the second M4 203.2 mm x 406.4 mm sandwich panel that contained a 50.8 mm diameter hole.

3.2.2 Damage Incurred From Machining

As described in chapter 2, damage in compressively loaded notched laminates originates at the notch tips. Therefore, it was necessary to check for damage around the holes as a result of the machining process. A sample facesheet that was drilled in the same manner as described above was used to determine if any machining-induced damage occurred. Inspection of the hole edges with an optical microscope revealed very little damage, so inspection was omitted for subsequent specimens. Some broken fibers were observed at the surface of the laminates, but no significant damage could be found (in comparison with key damage mechanisms described later). No through-thickness damage was found.

Aside from optical microscopy, X-radiography was also used to characterize any machining induced damage. The Scanray® Torrex 150D X-Ray Inspection System was used. A hole was drilled into a facesheet, and then the portion of the facesheet containing the hole was cut out. The core was removed with a razor blade. An X-radiograph was taken of the specimen, with a magnification factor of about one. Then, a dye penetrant was applied with a syringe to the entire hole edge, with a soaking time of approximately twenty minutes. An X-radiograph was taken of the dye enhanced specimen. Typically, damage such as matrix cracks or delaminations would appear as dark areas on an X-radiograph. No observable damage was found, as shown in figure 3.3. Any dye absorption detected was due to the small amount of honeycomb left on the facesheet. The magnification factor was determined to be sufficient, since visual detection was enough to determine the initiation of a linear damage zone (discussed in chapter 5).

3.3 Strain Gages

Strain gages were used for two purposes. First, they were used to determine the far field strain response, to determine the relative bending of the sandwich panel that occurred during the test. Second, they were used to measure the strain field near the LDZ, which gave an indication of the load carrying capability of the damage zone.

Figure 3.4 illustrates the position of the far field strain gages. The far field gages were placed in a back-to-back configuration, so that the back gage (rough side) was directly opposite the front gage (smooth side). Measurements Group® strain gages (EA-06-125AD-120) were used on all specimens in the far field position. Strain gage application procedures followed Measurements Group® Instruction Bulletin B-127-13 as a guide.
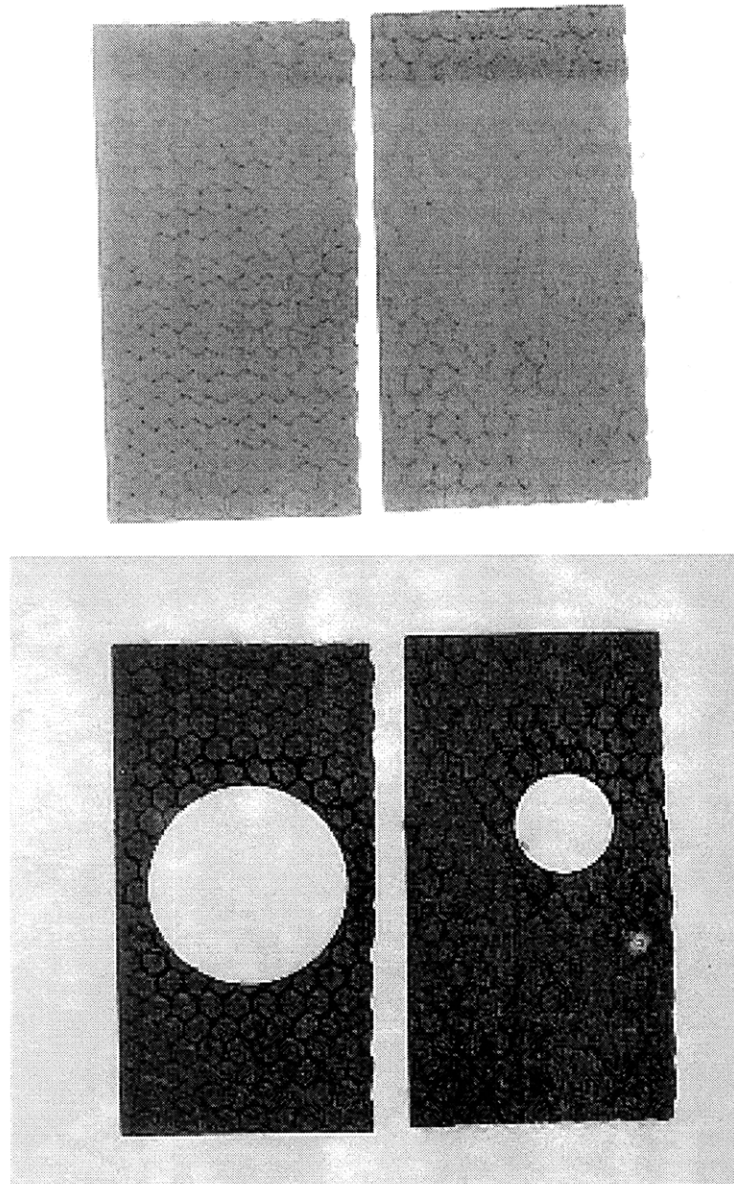
Figure 3.3   X-radiographs before and after machining. The honeycomb core cells are accentuated due to dye penetrant absorbtion.

#1   #2

Equal

Equal

Rough

Smooth
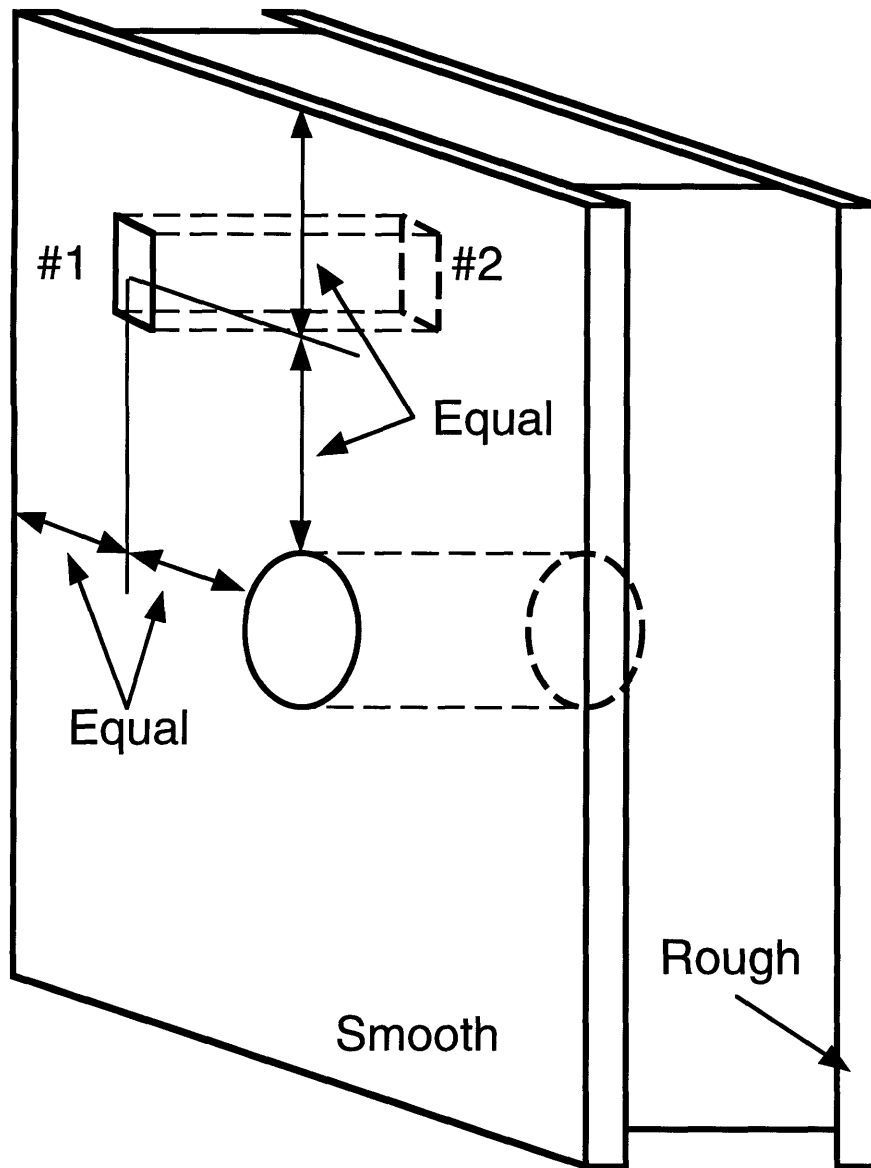
Figure 3.4   The far field strain gages are place in a back-to-back configuration on the front and back facesheets. Figure not drawn to scale.

In all tests but one, local strain gages were placed on a specimen after the damage initiation test. Once an LDZ was initiated, the load was immediately removed from the specimen, and local strain gages were placed in an array along a line perpendicular to the loading direction.

Although preliminary tests done on scrap material established the LDZ as the key failure mechanism, it was uncertain how far across the net section a linear damage zone would propagate prior to catastrophic failure. The net section refers to the areas on either side of a hole between the point on the hole's horizontal diameter and the edge of the facesheet. Therefore, about half of the test specimens had local gages placed further away from the hole edge, in the case that the LDZ would propagate in a stable manner near the edge of the facesheet. Figure 3.5 illustrates this local strain gage configuration. Gages that were placed in this configuration are referred to as L2X, where X indicates the gage number, as shown in figure 3.5. In all B-series specimens and one A-series specimen (ADC2), the first local gage was placed closer to the hole, and adjacent local gages were placed side-by-side, as shown in figure 3.6. Gages that were placed in this configuration are referred to as L1X, where X indicates the gage number, as shown in figure 3.6. One specimen (BAA4) had local gages attached prior to damage initiation. This was done to determine if the same type of toughening behavior would be found during a continuous test to failure, as was found with the interrupted tests. The strain gage positioning for all sandwich panels can be found in Table 3.2.

Special attention was needed when applying local strain gages, so that the adhesive did not flow near the LDZ. Any foreign material introduced into the LDZ could have affected its characteristics. A strip of black electrical tape was first applied on the damaged net section in a direction perpendicular to the loading direction. The tape was placed such that one edge was parallel and

Radius R (mm)	6.35	12.7	25.4
Distance D (mm)	5.08	7.62	7.62
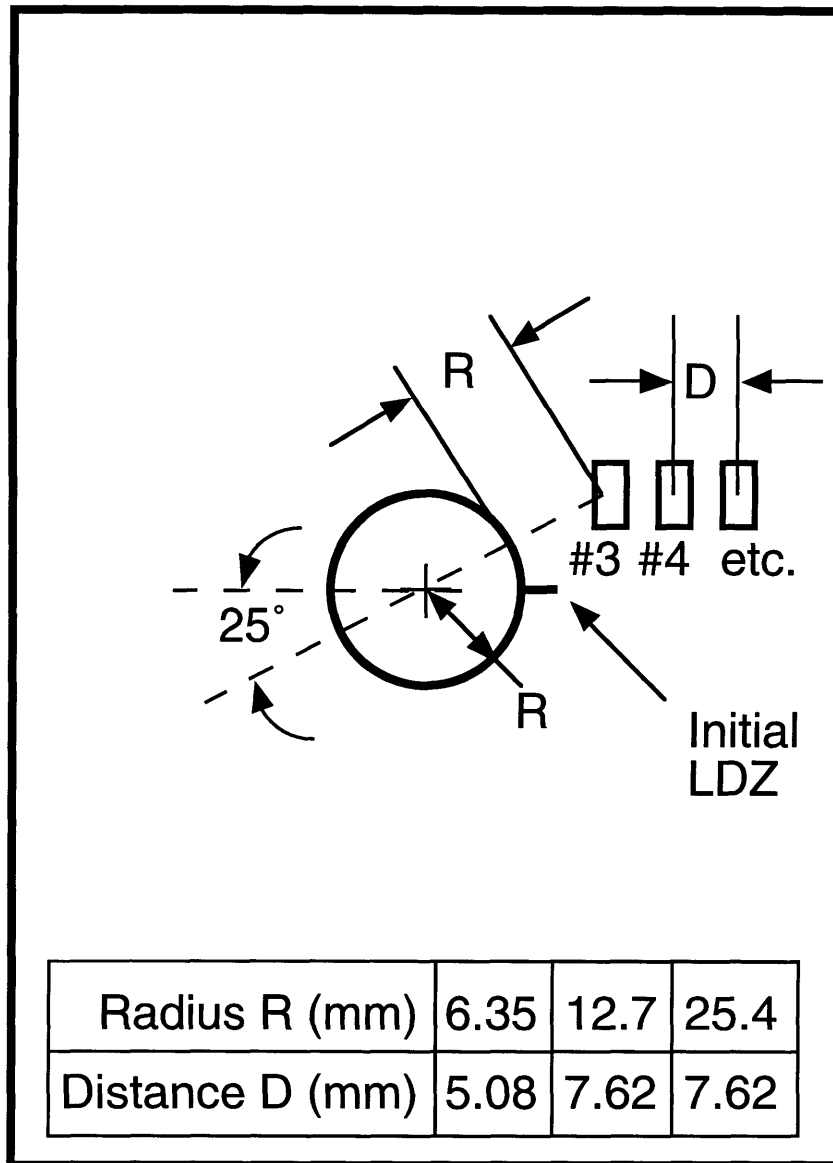
Figure 3.5   Local strain gage positioning for A-series specimens (i.e. L2X). The local strain gages on specimen ADC2 were placed as shown in figure 3.6. Strain gages are numbered in ascending order beginning with the gage nearest to the hole. Figure not drawn to scale.

Tangent to
Hole Edge

Hole

#3 #4 etc.

2.54mm

Initial
LDZ
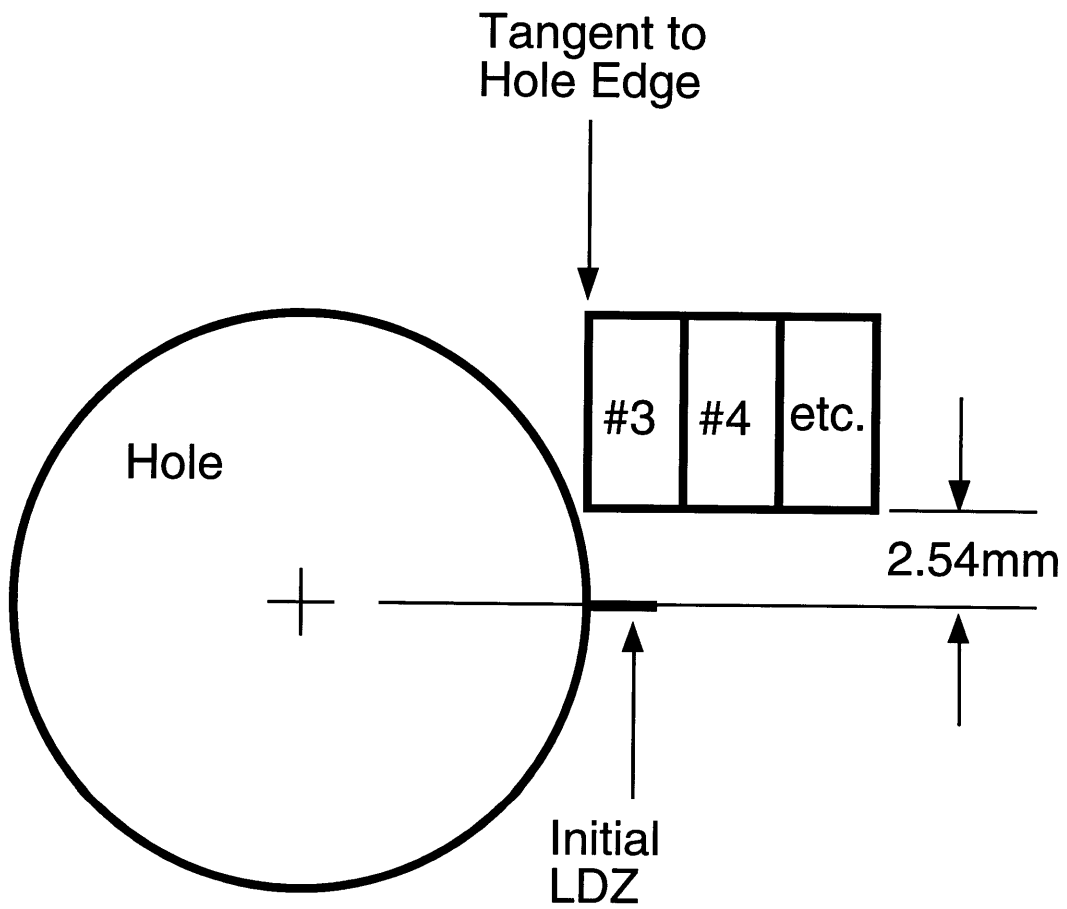
Figure 3.6   Local strain gage configuration for B-series specimens (i.e. L1X).
Specimen ADC2 was also gaged in this manner. Strain gages
are numbered in ascending order beginning with the gage
nearest to the hole. Figure not drawn to scale.

Table 3.2   Strain Gage Positioning

Specimen	Local Strain Gage Positions						
	L11	L12	L13	L14	L21	L22	L23
AAA1					BL	BL	BL
AAA2					BR	BR	BR
AAA3*							
AAA4					BL	BL	BL
ABB1					BL	BL	BL
ABB2					BL	BL	BL
ABB3					BL	BL	BL
ABB4					BR	BR	BR
ADC1					FL/FR	FL/FR	FL/FR
ADC2	BR	BR	BR	BR			
BAA1	BR						
BAA2	BL/BR	BL/BR					
BAA3**							
BAA4	ALL						
BBB1**							
BBB2†							
BBB3	BR	BR			BR		
BBB4	BL/BR	BL/BR					
BDC1	BR	BR	BR		BR		
BDC2	BL	BL	BL	BL	BL		

*   No stable LDZ growth after initiation
** Cross-sectioned after LDZ initiation
†   Tested at Instron

adjacent to the location of the local strain gages' lower edges, as shown in figure 3.7. Then, the local strain gages were applied in the usual manner. EA-06-125AD-120 strain gages were used in the local positions, except for on the AAA specimens, where EA-06-013DE-120 gages were used. These smaller gages were not used on any other specimens due to the difficulty associated with soldering wires to their terminals.

3.4 Compression Testing

This section describes the test equipment used. The test and alignment verification procedures are also discussed.

3.4.1 Test Apparatus

Compression tests were performed on a 500 kN MTS® load frame equipped with 216 mm diameter compression patens. The bottom platen was rigid. The top platen was self aligning. The load frame was controlled by an Instron® 8500 Plus digital control panel. Loading data was obtained via a 50 metric ton MTS® load cell. Analog load and strain gage data outputs were fed into a Macintosh® IIx computer running the LabView® 2.0.6 data acquisition program. The data acquisition rate was 2 Hz, although a few initial tests (prior to damage initiation) were performed at 1 Hz. Figure 3.8 shows the test setup.

3.4.2 Compression Test Procedure

The specimen to be tested was oriented such that the 0° fiber direction was parallel to the loading axis of the testing machine. The upper platen was aligned by hand if it did not appear to be aligned. Only a rough alignment was necessary, since the self aligning platen would automatically adjust and align itself to the specimen. The specimen was placed in the center of the lower platen. This was accomplished by using the concentric grooves in the platen

Strain Gages

Hole

#3 #4 etc.

+

Electrical Tape
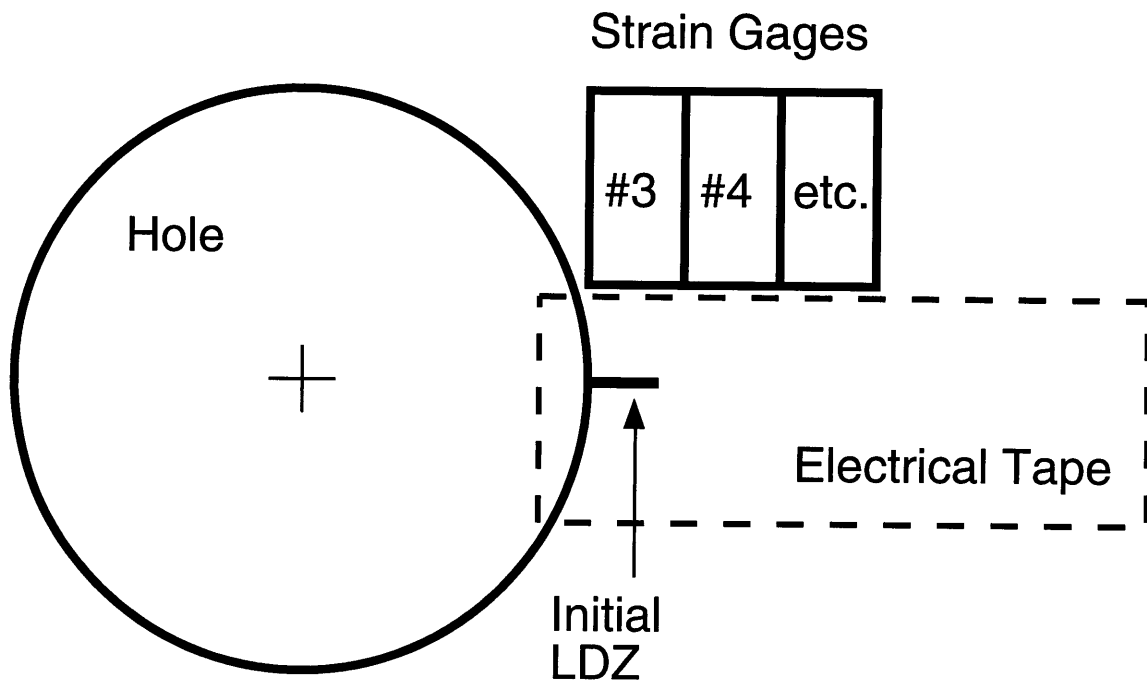
Initial
LDZ

Figure 3.7   Electrical tape is placed over the initial LDZ and along the line in
which it will propagate. Minimal pressure is exerted on the
facesheet when applying the tape. Figure not drawn to scale.
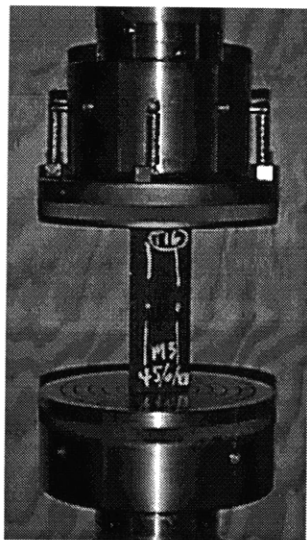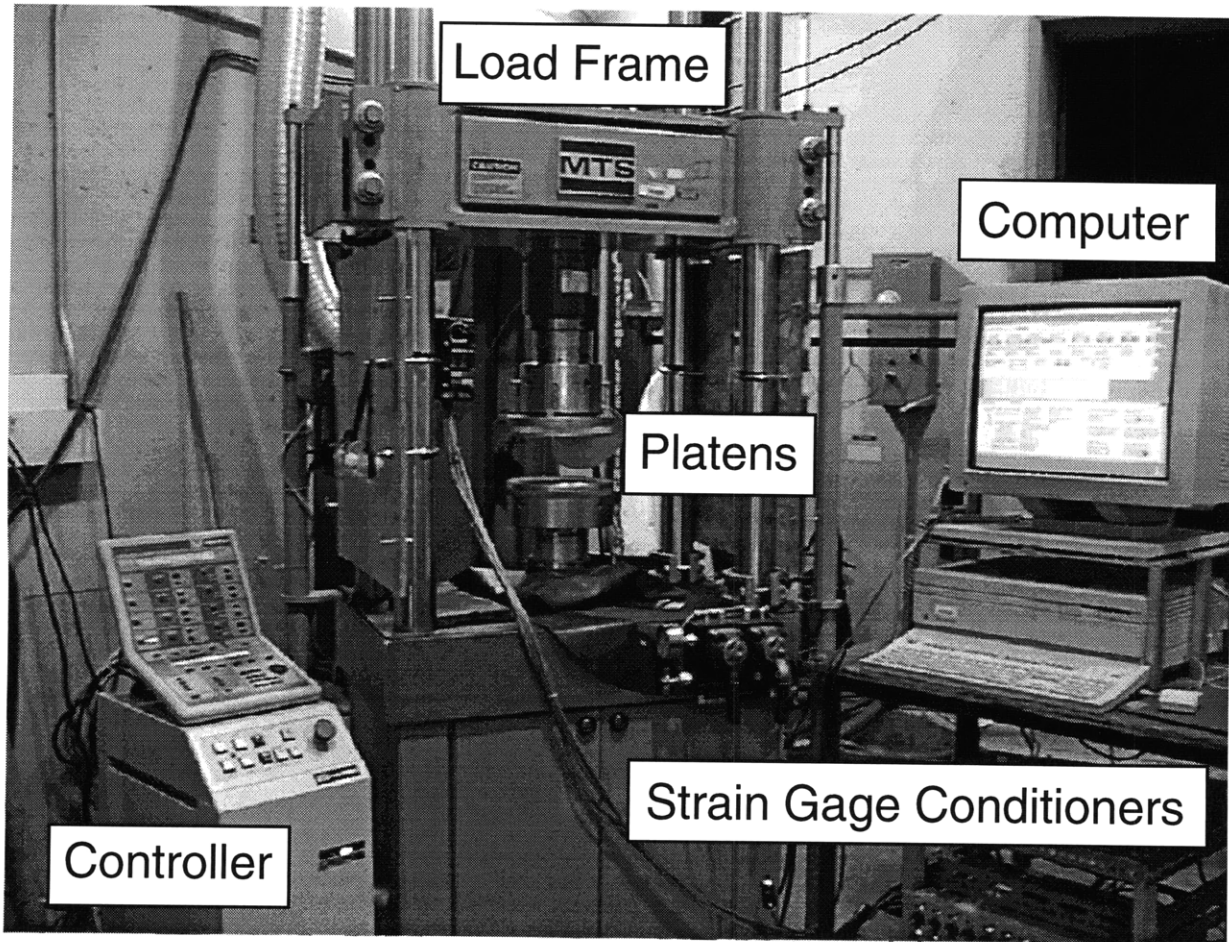
Figure 3.8   A picture showing the components of the test apparatus.

as a reference. The vertical alignment of the specimen was verified by using a square. However, it was found that pressing the sandwich panel against the lower platen with even pressure on both facesheets was sufficient to align the specimen vertically. Once the specimen was situated on the lower platen by hand, the lower platen was moved upwards until the specimen made contact with the upper platen. At that point, the specimen could be released because the platens remained in a position to hold the specimen in place.

The next step was to properly calibrate the strain gages and perform an initial alignment check. The lower platen was slowly moved upwards by using the manual stroke control button on the control panel until the compressive load was approximately 875 N, and then the platens were held at that position. The far field strain gage readings were compared in order to determine if the load was being distributed evenly in both facesheets. If the strain readings were not the same, then the upper platen was slowly moved by hand until both far field strain gages were reporting the same strain. If there was less strain (and therefore less load) in the front facesheet, the upper platen was rotated slightly towards the front facesheet, and vice versa. Once the initial aligning was finished, the lower platen was moved back down such that there was approximately a 45 N force applied to the specimen.

All tests were performed in displacement control. Compressive loads were first applied at a stroke rate of 0.254 mm/min to approximately 80% of a specimen's ultimate failure load, and then slowed to 0.0254-0.0127 mm/min in order to create a loading condition that would favor stable damage growth. The purpose of the first test was to initiate a linear damage zone. Preliminary tests showed that LDZs initiated instantaneously at the edge of the notch, at locations near to the horizontal diameter of the hole. However, the length of the initial LDZ was finite, and stable propagation was obtained only with

further end shortening. In most cases, the dominant LDZ (the LDZ that propagated across the net section first) was the one that appeared first. Therefore, the initial compression test established the location of the LDZ, and the positioning of the local strain gages.

Table 3.3 summarizes the test matrix.

3.4.3 Alignment

The alignment of the specimen was checked by comparing the strain readings from the two far field back-to-back strain gages. Equation (3.1) was used to obtain a value for the relative difference between the measured strains:

$$\left(\frac{front - back}{front + back}\right) * 100 \; = \; \% \; difference \tag{3.1}$$

where *front* and *back* are the strain readings from the far field strain gages on the front and back facesheets, respectively. The standard edgewise sandwich panel compression test method [16] defines the allowable relative strain difference to be 5% in the early part of the test. Eqn. (3.1) is not a direct measure of the difference in strains, but it gives an indication of the difference in strains relative to the total amount of strain.

3.5   Damage Characterization

This section describes the techniques used to characterize damage. The primary macroscopic characterization technique used was visual inspection. The primary microscopic characterization technique used was cross-sectioning.

3.5.1 Visual Inspection

The primary method for detecting damage was visual inspection. Macroscopically, LDZs were characterized by an off-white color easily

Table 3.3   Test Matrix

Test Matrix		
Panel Size	M4	M5
Small	4	4
Medium	4	3
Large	2	2

distinguished from the normal facesheet color. Characterizing the length of damage was accomplished by marking the facesheet with a permanent fine tip marker at the tip of an LDZ. Since the line created by the marker had a finite thickness, the line was drawn such that the edge of the mark furthest from the hole edge was aligned with the tip. Measurements of LDZ length were done with calipers accurate to 0.0127 mm. During the compression test when any extension of the LDZ occurred, the new tip was marked. Each time that the LDZ advanced and was marked, the data acquisition program was marked as well. The output of the data acquisition program was in spreadsheet form; one row corresponded to the load and strains measured at that moment. Successive rows recorded similar values at later times. A column of data, reserved for marking, was normally filled with zeros. This data column was "marked" by clicking the mouse button, which resulted in recording a one instead of a zero. Therefore, the applied load and strains corresponding to the precise moment at which an LDZ advanced could be determined.

3.5.2 X-Radiography

All of the damage occuring in the facesheet was confined to LDZs, as described in detail in chapter 5. An X-radiograph taken of an LDZ after dye penetrant was applied confirmed this, as shown in figure 3.9. The dye penetrant was applied with a syringe to the LDZ and allowed to absorb for ten minutes (the same picture was obtained for a twenty minute soak time, with no difference). Although the LDZ cannot be seen directly in figure 3.9, the line of dye visible in the facesheet indicates that an LDZ was present. The dye was also absorbed by the core material still bonded to the facesheet. However, no damage was present outside the LDZ.

Before Dye Penetrant

After Dye Penetrant
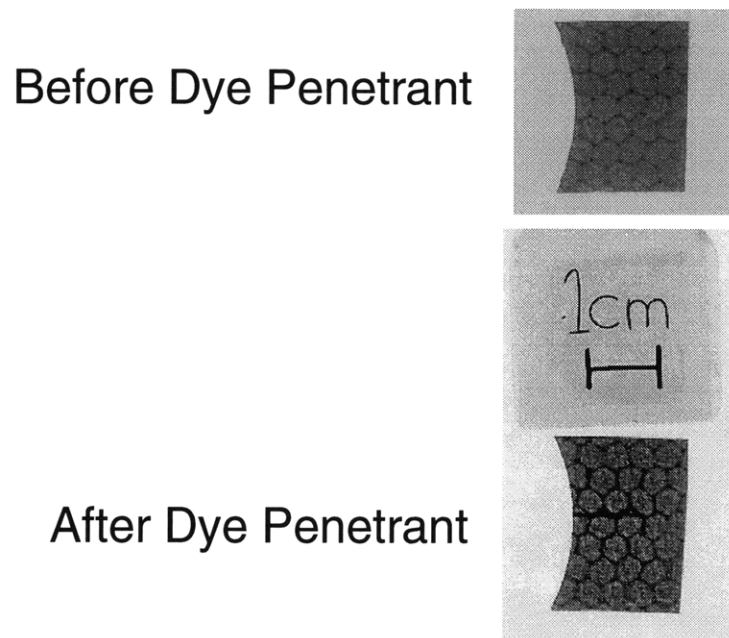
Figure 3.9   X-radiograph of dye penetrant enhanced LDZ. The dye penetrant was absorbed by the LDZ and the honeycomb core material. No damage outside of the LDZ is noted.

3.5.3 Cross-Sectioning

Cross-sectioning studies were carried out in order to determine the damage mechanisms present in the LDZs, as well as the sequence of damage mechanism development. This procedure involved bonding a piece of shim stock to the facesheet, cutting out a portion or all of an LDZ, mounting the specimen in resin, grinding and polishing the mounted specimen, and then viewing the cross-section with an optical microscope. As depicted in figure 3.10, cross-sections were done on several planes, and each view was associated with a different letter. For example, AAA1FRL represents the root view of an LDZ emanating on the front facesheet from the right edge of the hole on the first AAA sandwich panel.

Cross-sectioning studies were performed in either a root-to-tip or a tip-to-root fashion. For example, an "RR" view was considered to be a tip-to-root study, since the grinding plane began at the tip of the LDZ. Successive grinding planes were greater distances away from the tip towards the root. "Right" and "left" views were chosen in order to determine, if possible, the sequence of damage mechanism development. It should be noted that for a given LDZ, either a right or left view scheme should yield the same results, as long as the grinding planes are at the same location along the LDZ. However, some cases were more appropriate for a tip or root view. For example, relatively lengthy LDZs (as compared to the length of the mounting cup) were better suited for tip views. A root view may result in an unwieldy grinding specimen since a large amount of material needed to be ground away before the tip was reached. Otherwise, no preference was extended to either view.

On some specimens which were cross-sectioned for root or tip views, a triangular piece of shim stock was bonded in a position adjacent to the LDZ

Hole and Two
LDZs Shown

x
y
z

XLU (y-z)   XRU (y-z)

Root
XRL (x-z)

Tip   Tip
XLL (x-z)   XRR (x-z)

XLF (x-y)   XLR (x-z)   XRF (x-y)
                 Root

XLD (y-z)   XRD (y-z)

Arrows Indicate Direction of Grinding
Parantheses Indicate Parallel Plane of View
X = F for Front Facesheet
X = B for Back Facesheet
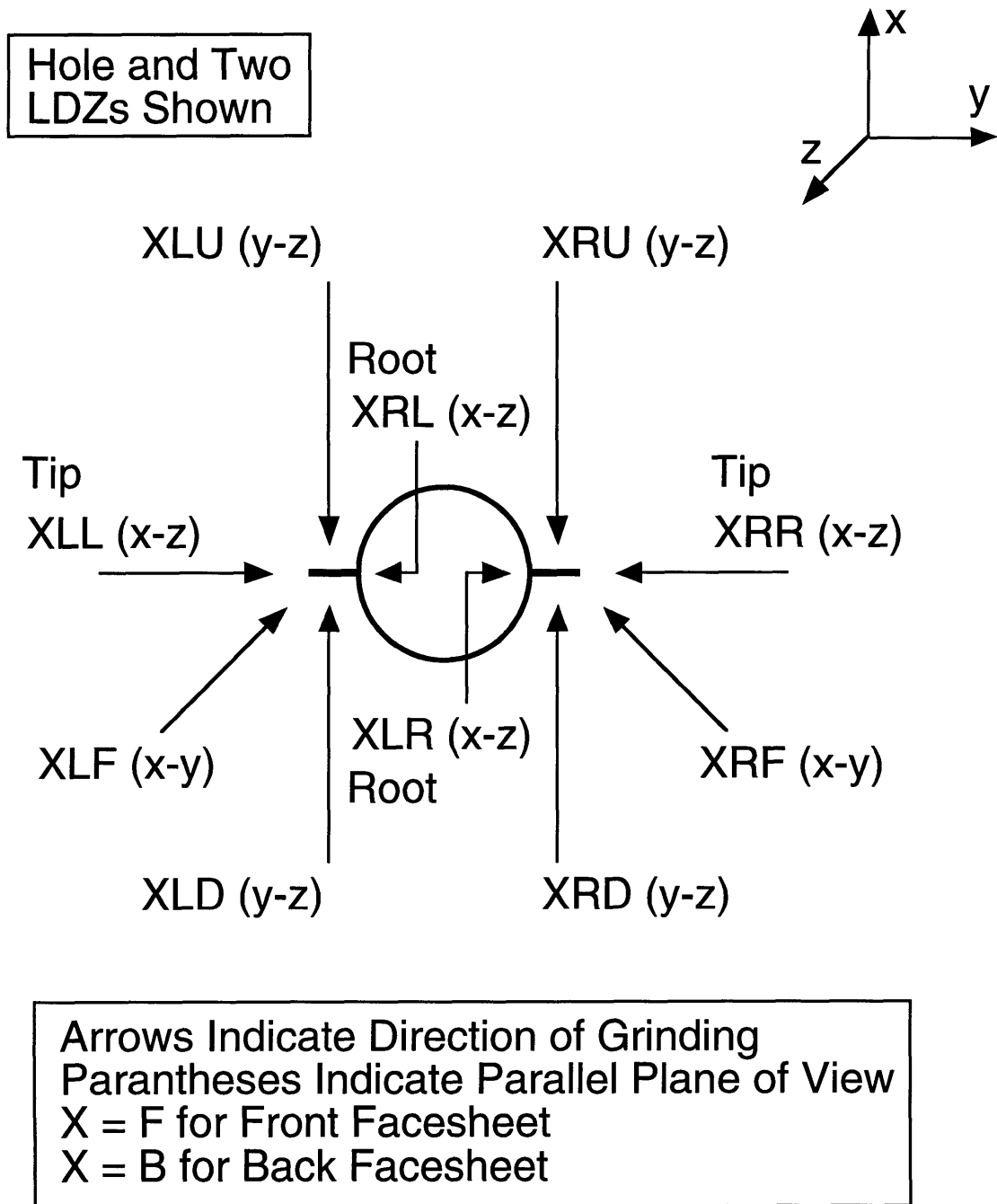
Figure 3.10   An illustration of the different possible cross-sectioning views.

using Duco® Cement. The metal was used as an indicator. As a result of the grinding and polishing process, the metal was easily distinguished under an optical microscope. The length of the metal observable at a given grinding plane gave an indication of how far the grinding had gone into the specimen. For this purpose, the metal shim was cut such that it had a 45° corner. The difference in metal length from a previous grinding step equalled the distance ground. Figure 3.11 illustrates the positioning of shim stock on a specimen.

Preliminary results indicated that the reliability of the metal shim technique was at best questionable with regard to measuring relative position along the LDZ. Two problems led to the decision to terminate distance measurements based on the amount of shim measured on a given cross-section. First, the actual measurement of the shim on the cross-section plane was limited by the precision and accuracy of the measurement. Parallax associated with the microscope resulted in poor measurements. The accuracy also suffered because of the extremely small measurements that needed to be taken, due to the small grinding distances. Second, grinding to the exact location of interest was extremely difficult. The minute difference between the point of interest (the very first appearance of fiber microbuckling, for example) and a location just beyond that point, coupled with the precision of the measuring technique, lessened the reliability of mechanism length measurements. Therefore, any measurements of this kind are not reported. As a result, cross-sectioning plane locations are reported as respective locations in chapter 5. For example, a cross-section plane may be either further along the LDZ towards the tip or root with respect to a previous cross-section plane.

After the shim stock was bonded to the facesheet in the appropriate location, the LDZ, along with a finite surrounding area (approximately 6.5 mm

Hole and
LDZ Shown

A

≈ 2.54mm

Root
View

Tip
View

B
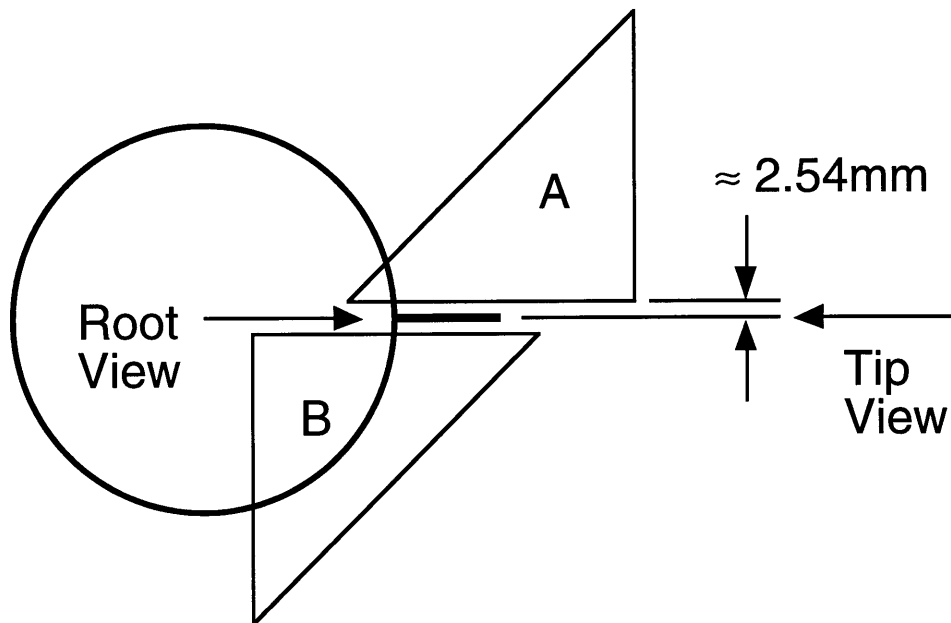
A: Positioning for Root View
B: Positioning for Tip View

Figure 3.11   Placement of metal shim stock on facesheet. Figure not drawn
to scale.

on any side of the LDZ), was cut out of the facesheet using a Dremel® Moto-Tool® with an emery cut-off wheel (attachment #409) and a razor blade. Prior to cutting, lines were drawn on the facesheet using a ruler and a marker in order to ensure that one cut was perpendicular or parallel to the LDZ, as shown in figure 3.12. The facesheet was cut through its thickness, along with about 6.5 mm of honeycomb core underneath it, with the cut-off wheel. A razor blade was then used to cut the core material in a direction parallel to the facesheet in order to sever the specimen from the sandwich panel. Once the section was removed from the facesheet, the core material was carefully removed from the facesheet using the razor blade. Although this step was not necessary, it made mounting the specimens much easier.

The specimens were mounted in Buehler® Sampl-Kup® 32 mm cylindrical plastic cups. The cups consisted of two parts, the lid and the shell. The damaged section was glued to the center of the lid with 5-Minute® Epoxy, such that the view of interest was facing the lid. For example, if the specimen was to be cross-sectioned using a root view, the specimen would be aligned such that the LDZ was perpendicular to the lid and the root of the LDZ would be oriented towards the lid (this face is referred to as the lid face), as shown in figure 3.13. The plane of grinding was parallel to the lid, and successive grinding removed material in a direction perpendicular to the plane of the lid. Although the epoxy took only five minutes to set, Buehler® Sampl-Klip® stainless steel specimen support springs or Buehler® Sampl-Klip® I plastic specimen support clips were used to hold the damaged section on the lid in order to ensure that the specimen remained aligned during filling of the mold. Once the specimen was securely in place, the shell was placed over the lid. Buehler® Epo-Kwick® Fast Cure Epoxy (15 g of resin and 3 g of hardener mixed together) were poured into the cup, and allowed to set overnight. The result

Hole and LDZ Shown
for Front Facesheet

X ≈ 6.35mm

X

B

X

A

C

D

Lines Drawn
to Guide Cut

Perpendicular to LDZ
 A: for FRL
 C: for FRR
Parallel to LDZ
 B: for FRU
 D: for FRD

Figure 3.12   An illustration showing that certain cuts must be made either
              perpendicular or parallel to the LDZ of interest, depending on the
              view desired. The relative positioning of the other lines, or the
              exact value of the dimension X are not important. Figure not
              drawn to scale.

Cup Assembly

Shell

Lid

Grinding/Polishing
Direction

**Specimen Positioning
for LDZ Root View**

LDZ Perpendicular
to Lid Face

Specimen

Specimen
Holder

Lid Face is Parallel
to Grinding Plane

Figure 3.13   Mounting of cross-sectioned specimens. Figure not drawn to
scale.

was a cylindrical specimen consisting of the LDZ embedded in the center of clear resin. This specimen was now ready for grinding.

A Struers® RotoPol-1® machine was used for grinding and polishing specimens. Several types of silicon-carbide wet grinding paper wheels were used. Struers® 1200 (14 μm), 2400 (7.5 μm), and 4000 (4.5 μm) grit wheels were used most often. Initially, grinding was accomplished by using the Struers® Pedemat® automatic press along with the RotoPol-1®. This device applied a specific force to the specimen. It should have resulted in parallel grinding, but using this apparatus resulted in crooked specimens; i.e. the cross-section planes were not parallel to the original plane created by the lid. Therefore, the specimens were ground using a manual method. Instead of using a machine to hold the specimen and apply the force, the specimen was held against the grinding/polishing wheel with two hands. It is impossible to give exact procedures governing the grinding process because no value of force could be measured.

The cross-sectioning process began by grinding the back face of the specimen (opposite of the lid, or front, face) so that it was parallel to the front face. Calipers were used to verify that both faces were parallel, and that successive cross-sections were parallel to each other. Once the front and back faces were parallel, the front face was ground with 1200 grit paper to a location near to the point of interest. The point of interest, usually the tip or root of an LDZ, could be seen through the clear resin. However, shim stock was useful in providing an indication of how far the point of interest was to the current grinding plane. Experience was the best guide in determining exactly how far to grind. 2400 grit paper was then used to grind nearer to the point of interest. At this point, it was necessary to constantly check the specimen under an optical microscope to ensure that the specimen was not ground down beyond

the point of interest.

Experience dictated when to change the silicon-carbide paper wheels and hence adjust the applied force. The grit would quickly become clogged with the material which was being ground away and become less efficient as a result. The most difficult part of the process was obtaining a polished surface at the point of interest, because in order to obtain a polished surface, a great deal of force was required. However, applying a large force resulted in a greater chance that the location of interest would be ground away. Because of the very short mechanism lengths (discussed in chapter 5) and the fact that even with fine grit paper material may be ground away when applying a large force, the only guide to accomplishing this process was experience. Nevertheless, when the point of interest was reached, as determined through the optical microscope, the surface was polished with as little force as possible using 4000 grit paper in order to obtain a surface that would yield a good picture. Pictures were then taken with a camera attached to an optical microscope using Polaroid® Type 55 or Type 52 instant film. If necessary, the length of metal shim was noted. The grinding/checking procedure was repeated until the LDZ was thoroughly examined. Table 3.4 summarizes the specimens cross-sectioned.

3.5.4 Scanning Electron Microscopy

The use of a scanning electron microscope (SEM) was not necessary for characterizing the damage found in the cross-sections, since the optical microscope was sufficient. However, an SEM provided outstanding images of LDZs.

The LDZ to be viewed under an SEM was cut out of a facesheet in a similar manner as described for the cross-sectioning procedure. The core was

Table 3.4   Cross-Sectioning List

Cross-Sectioning List	
Specimen	Cross-Section(s)
AAA2	FRU
AAA3	FRD, BLF, BRF
AAA4	FLR, FRF
ABB3	FLR
ABB4	FLR, FRR
ADC1	FLR, FRR
BAA3	BLR
BBB1	FRL, BLR
BBB3	FLR
BDC1	FLL, FRR

carefully removed from the specimen with a razor blade. Then, the specimen was attached to a circular mount (a metal disk) with carbon tabs. In order to facilitate views requiring extensive specimen rotation (i.e. viewing the top of the facesheet and then rotating the specimen 90° to view the edge of the hole), it is recommended that the specimen be attached to the disk such that the areas of interest are located away from the disk, although this step is not necessary. Carbon paint was brushed around the perimeter of the specimen located on the disk, such that it connected the facesheet material with the disk. Gold was then sputtered on the surface of the specimen. When a different SEM was used, a different type of mount was needed. In these cases, the disk that the specimen was already attached to was adhered to the new mount by using a liberal amount of carbon paint.

CHAPTER 4

ANALYSIS

This chapter presents the damage zone model (DZM) utilized to model the linear damage zone (LDZ) observed during experiments. First, an overview of the DZM is given. Secondly, specific applications of the DZM to compressively loaded composites is discussed. Thirdly, the construction of the DZM utilized in the present work is described. It should be noted that "DZM" refers to both damage zone modeling in general and specific damage zone models, as shown in chapter 2. Likewise, the model presented here is referred to as the DZM.

4.1   Damage Zone Modeling Overview

As discussed in chapter 2, attempts have been made to model damage zones (the damage zone observed in the present work is referred to as an LDZ) emanating from notch tips in compressively loaded composite laminates by applying DZMs. The concept of treating a damage zone as a bridged crack in tension comes in part from the Dugdale analysis [105]. Although compressive applications of the DZM differ from the Dugdale model, the key aspect of lumping damage mechanisms together and describing them with a traction law is analogous to the Dugdale model for a plastic zone.

The DZM framework allows for predictive capability in three areas. The LDZ growth, ultimate failure load, and strain distribution around the LDZ should all be predicted if the DZM is a self consistent physically-based model.

4.1.1 The Dugdale Approach

The Dugdale model (or strip yield model) was derived for an infinite metal plate with a through thickness crack subjected to a remote tensile stress. The model was originally derived to calculate the plastic zone size as a function of applied load and yield stress. It is assumed that the actual crack (the real crack) in the plate has plastic zones at each crack tip, as shown in figure 4.1. The plastic zone size, ρ, is unknown at the beginning of the analysis. An equivalent crack, with length equal to the actual crack length plus the length of the plastic zones, is used to model the damage in the metal plate. A constant closing traction acts along each flank of the equivalent crack for a distance ρ behind the crack tip, as shown in figure 4.1. The magnitude of the traction is equal to the material's yield stress, σ_{YS}.

An approach based on LEFM is used to determine crack stability. Two crack tip stress intensity factors (SIFs) are associated with the equivalent crack: K_s, the SIF due to the remote tensile load, and K_σ, the SIF due to the tractions. K_σ depends in part upon the length ρ on which the tractions are acting. The next step is key: the length ρ is chosen such that no stress singularity exists at the crack tip, and therefore equation (4.1) is satisfied:

$$K_s - K_\sigma = 0 \tag{4.1}$$

Equation (4.1) can be simplified by using the appropriate SIF solutions [5] :

$$\frac{a}{a+\rho} = \cos\left(\frac{\pi\sigma}{2\sigma_{YS}}\right) \tag{4.2}$$

Using equation (4.2), curves can be generated which relate the remote applied tensile stress, σ, to the crack length, a.
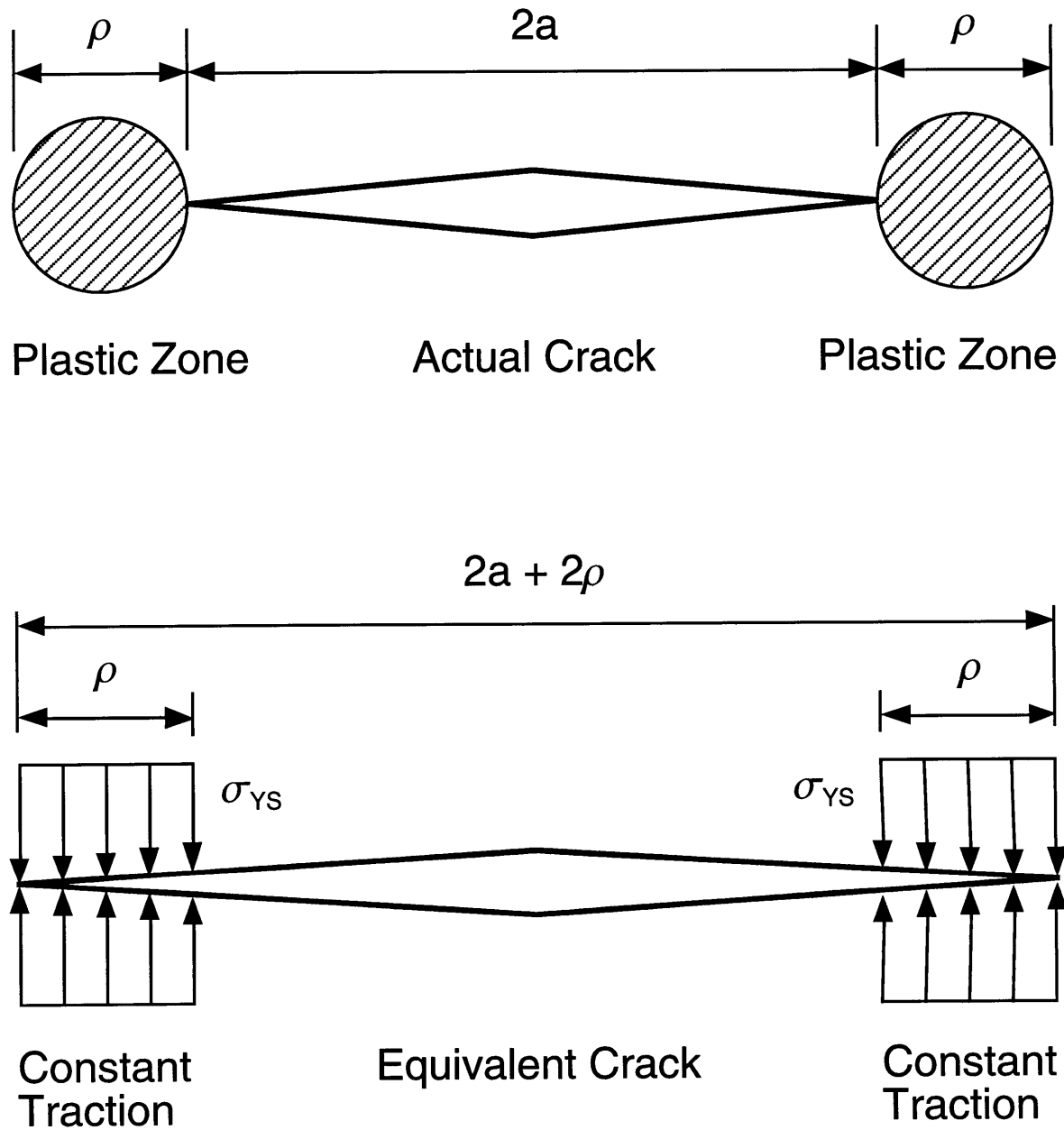
Figure 4.1   Dugdale modeling assumptions.

4.1.2 Application of Dugdale Approach to Compression

As described in chapter 2, damage zones consisting primarily of fiber microbuckling and kink bands have been found to emanate from notches in unidirectional [34-37] and multidirectional [38-42, 44] composite laminates under compressive loading. These damage zones behave like tensile cracks, propagating co-linearly and stably. The key assumption was treating the compressive damage zone as a crack. In some work [38, 39, 42, 44] the Dugdale model was used in a direct analogy to the tensile loading case; i.e. equation (4.1) was used directly. Solutions for the SIFs were obtained for two cracks emanating symmetrically from the edges of circular holes [116]. Different values for the constant traction acting on the equivalent crack faces have been used, including arbitrary values [38, 39], the unnotched laminate strength [42, 44], and the Euler buckling stress of a fiber [42, 44].

The approach can be modified in order to take into account K_0, the crack tip fracture toughness:

$$K_s - K_\sigma = K_0 \qquad\qquad (4.3)$$

When a constant traction is assumed, this approach is essentially identical to that used with equation (4.1). It has been used in a similar manner to predict the damage zone length as a function of applied load [35-37].

Experimental evidence suggests that damage zones do not behave in a manner consistent with the previously assumed constant stress traction law [40]. The damage zone exhibits a "softening" behavior, transferring less load at locations further behind the damage tip. This implies that compressive damage zones are better modeled by a strain softening traction law, as shown in figure 4.2. A strain softening traction law states that as the crack opening (or crack overlap in compression) displacement (v) increases, the stress (σ)
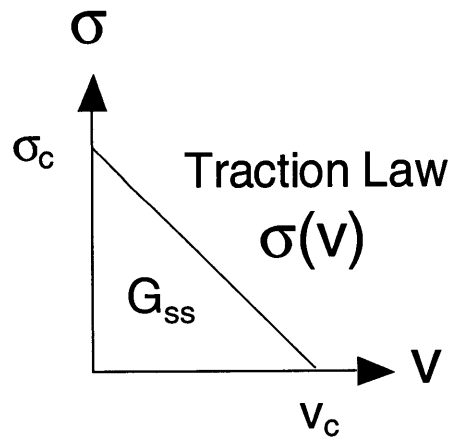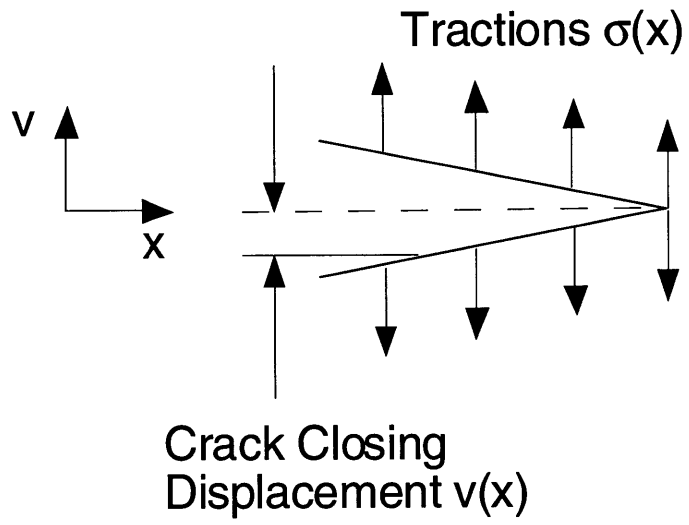
Figure 4.2   Two parameter linear strain softening traction law.

applied/transferred at that point along the crack decreases. As shown in figure 4.2, σ_c represents the maximum stress applied/transferred by the damage zone, corresponding to zero crack opening displacement (COD). Conversely, v_c represents the maximum COD beyond which no load transfer occurs. The area underneath the traction law curve, G_{ss}, represents the total energy per unit area dissipated by crack propagation in steady state. A strain softening traction law has been used together with the equilibrium condition in equation (4.1) [42, 44]. This analysis lacked crack profile convergence, which will be discussed later.

4.1.3 DZM Interrogation

Two models, the damage growth model and finite element model (FEM), are used to interrogate the DZM. The damage growth, ultimate failure load, and local strain distribution should all be predicted by the same DZM. The damage growth model is used to predict the damage growth and ultimate failure load. The FEM is used to predict the local strain distribution. The traction law must remain consistent throughout the DZM analysis; the traction law used in the damage growth model should be equivalent to the spring law used in the FEM.

The first step is to apply the damage growth model. The LDZ growth data is used to calibrate the crack growth resistance curves (R-curves) . The R-curve calibration establishes the material traction law. In the present investigation, the traction law is assumed to be a two parameter linear strain softening law. The ultimate failure stress (or load) is predicted from the R-curve by superimposing curves of constant stress. The traction law is converted to an equivalent spring law. Then, the FEM is used to compare the strain distribution measured during experiment.

The methodology described above can be reversed. An alternate sequence of calibration begins with the experimentally measured strain distribution. The FEM is used to calibrate the traction law based on the strain distribution. Once the traction law is calibrated, it can be used to generate resistance curves and predict strengths. If the traction law is a material property, then the sequence of calibration should not matter; i.e. an equivalent traction law will result from either calibration procedure.

4.2   Damage Growth Model

The damage growth model is used to predict the LDZ growth behavior and the ultimate failure load. The code was written in Mathematica® version 3.0. A printout of the code can be found in Appendix B. It should be noted that "crack" refers to the equivalent crack used to model the LDZ. Also, in order to remain consistent with reference [116], tensile loading was used for the analysis. Therefore, tensile related phenomena model the actual compressive phenomena; i.e. "crack opening" represents the LDZ closing behavior.

4.2.1 Assumptions

The following assumptions were made in order to apply the damage growth model:

- The facesheets act independently.

- An LDZ is treated as an equivalent crack of the same length.

- Stress intensity factor (SIF) and crack opening displacement (COD) equations derived for two symmetric cracks emanating from a hole in an infinite isotropic plate under tensile load can be used directly with woven composite facesheets under compressive load, along with applicable correction factors for the hole, finite width, and material orthotropy.

These solutions can be found in reference [116].

- The traction acts in the direction opposite to the uniform remote applied stress. This is accounted for by using the negative of the SIF and COD values due to the traction distribution.

- LDZs emanating from one side of the hole are treated as if two symmetric LDZs were emanating from the same hole.

- M4 and M5 materials possess fracture toughnesses K_0.

- An assumed inherent flaw (LDZ) of length 0.0254 mm along with the experimentally measured LDZ initiation stress, is used to calculate K_0.

- The traction law is a material property.

- Crack growth resistance curves (R-curves) used with constant stress curves (load control) are valid for failure prediction.

4.2.2 Framework

The damage growth analysis considers the superposition of two cases. Each has an associated SIF and crack opening displacement. The two geometries are illustrated in figures 4.3 and 4.4. Figure 4.3 shows a symmetric crack of length $d - r$ emanating from a hole in a finite width plate subjected to a remote uniform stress S. Figure 4.4 shows a similar crack subjected to a constant traction σ acting on the crack faces. The SIF due to a uniform remote stress is:

$$K_s = K_\infty^s \, F_h^s \, F_w^s \, F_o^s \tag{4.4}$$

where:

$$K_\infty^s = S \, \sqrt{\pi d} \tag{4.5}$$

The correction factors [116] for the hole (K_h^s), finite width,(K_w^s), and orthotropy (K_o^s) are, respectively:
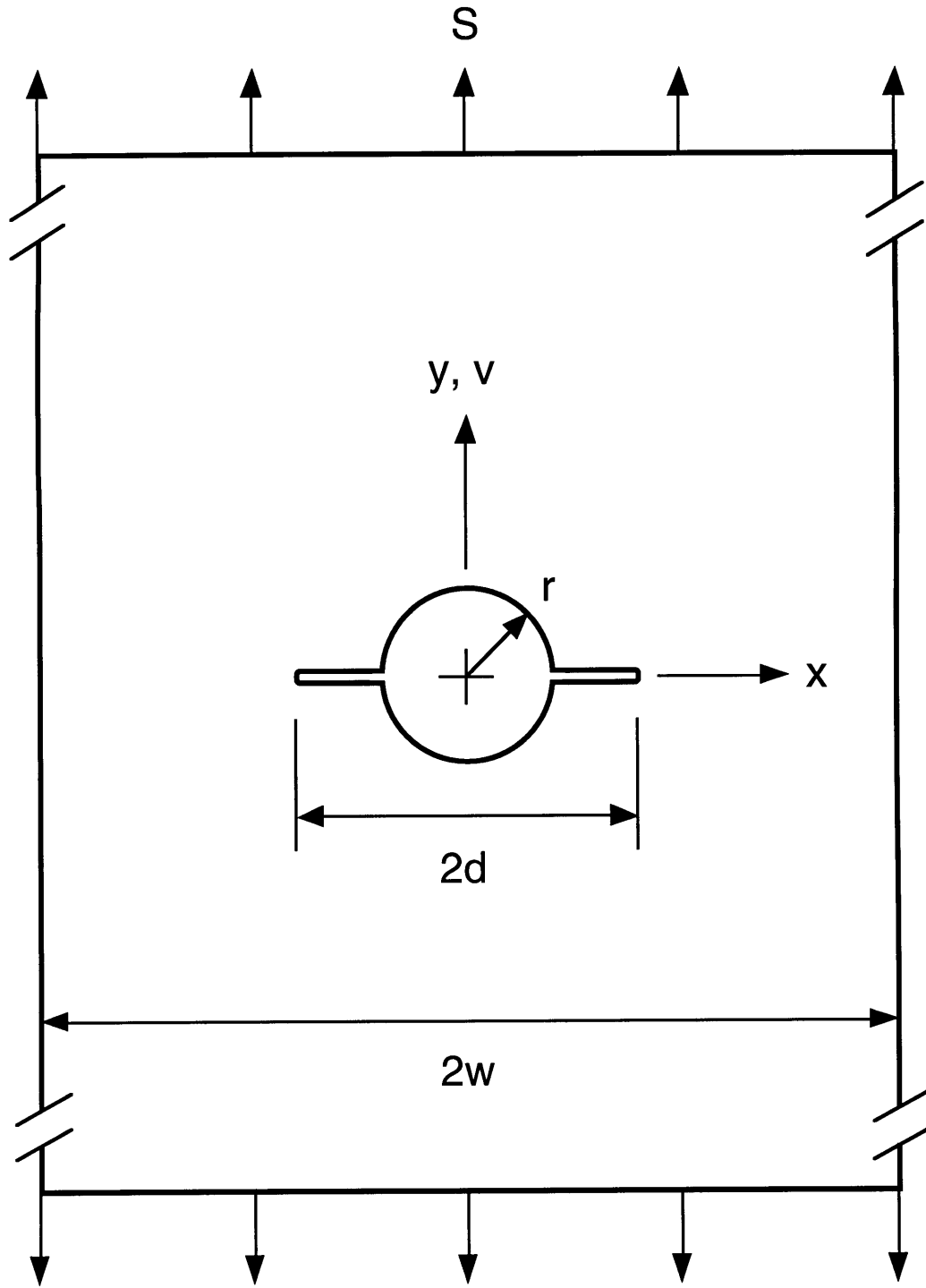
Figure 4.3   Geometry 1, consiting of a remote applied stress acting on a finite width plate containing two symmetric cracks emanating from a circular hole.
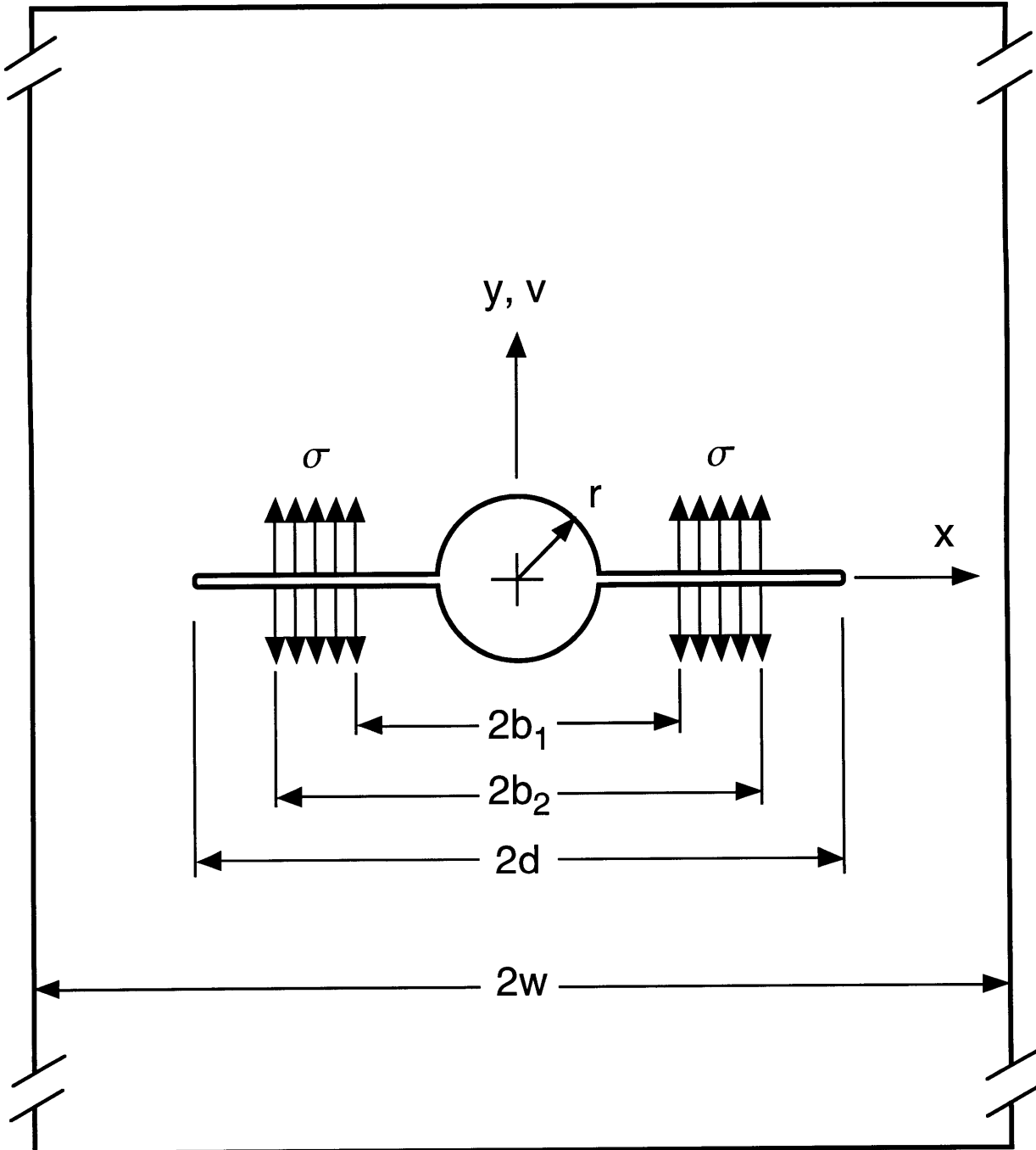
Figure 4.4   Geometry 2, consiting of a constant traction acting on a portion of two symmetric cracks emanating from a circular hole in a finite width plate.

$$F_h^s = \sqrt{1 - \frac{r}{d}} \, f_n \tag{4.6}$$

$$F_w^s = \sqrt{\sec\left(\frac{\pi r}{2w}\right) \sec\left(\frac{\pi d}{2w}\right)} \tag{4.7}$$

$$F_o^s = 1.35 \tag{4.8}$$

where:

$$f_n = 1 + 0.358\lambda + 1.425\lambda^2 - 1.578\lambda^3 + 2.156\lambda^4 \tag{4.9}$$

$$\lambda = \frac{r}{d} \tag{4.10}$$

Equation (4.4) is valid in the range $0 \le \lambda < 1$, $r/w \le 0.5$, and $d/w \le 0.7$. The orthotropic correction factor is obtained from the finite element analysis and is specific to the particular materials used in the present study.

The crack opening displacement profile due to a uniform remote stress is:

$$V_s(x) = \frac{2(1 - \eta^2)S}{E} \sqrt{d^2 - x^2} \, F_h^s F_w^s F_o^s \tag{4.11}$$

where $|x| \le d$, and $\eta = 0$ for plane stress.

The SIF due to a constant traction acting on the crack from b_1 to b_2 is:

$$K_\sigma = K_\infty^\sigma \left[\sin^{-1}\left(\frac{b_2}{d}\right) \sin^{-1}\left(\frac{b_1}{d}\right) \right] F_h^\sigma \, F_w^\sigma \, F_o^\sigma \tag{4.12}$$

where:

$$K_\infty^\sigma = \frac{2\sigma}{\pi} \sqrt{\pi d} \tag{4.13}$$

The correction factors [116] for the hole (K_h^σ), finite width (K_h^σ), and orthotropy (K_h^σ) are, respectively:

$$F_h^\sigma = \frac{G(\gamma,\lambda)}{\sin^{-1}\left(\dfrac{b_2}{d}\right) - \sin^{-1}\left(\dfrac{b_1}{d}\right)} \tag{4.14}$$

$$F_w^\sigma = \left[\frac{\sin^{-1} B_2 - \sin^{-1} B_1}{\sin^{-1}\left(\dfrac{b_2}{d}\right) - \sin^{-1}\left(\dfrac{b_1}{d}\right)}\right]\sqrt{\sec\left(\frac{\pi d}{2w}\right)} \tag{4.15}$$

$$F_o^\sigma = 1.35 \tag{4.16}$$

where:

$$G(\gamma,\lambda) = \left\{\left[1 + \frac{A_1}{1-\lambda} + \frac{3A_2}{2(1-\lambda)^2}\right]\sin^{-1}\gamma + \left[\frac{A_1}{1-\lambda} + \frac{(4-\gamma)A_2}{2(1-\lambda)^2}\right]\sqrt{1-\gamma^2}\right\}\Bigg|_{\gamma=\frac{b_1}{d}}^{\gamma=\frac{b_2}{d}} \tag{4.17}$$

$$A_2 = 0.221\lambda^2 + 0.046\lambda^4 \tag{4.18}$$

$$A_1 = -0.02\lambda^2 + 0.558\lambda^4 \tag{4.19}$$

$$B_k = \frac{\sin\left(\dfrac{\pi b_k}{2w}\right)}{\sin\left(\dfrac{\pi d}{2w}\right)} \tag{4.20}$$

Equation (4.12) is valid in the range $0 \le \lambda < 1$, $r/w \le 0.25$, and $d/w \le 0.7$.

The crack opening displacement profile due to a constant traction is:

$$V_\sigma(x) = \left[V_\infty^\sigma(x) + V_\infty^\sigma(-x)\right]F_h^\sigma F_w^\sigma F_o^\sigma \tag{4.21}$$

where:

$$V_\infty^\sigma = \frac{2(1-\eta^2)\sigma}{\pi E}\left[(b-x)\cosh^{-1}\left(\frac{d^2-bx}{d\,|\,b-x\,|}\right) + \sqrt{d^2-x^2}\sin^{-1}\left(\frac{b}{d}\right)\right]\Bigg|_{b=b_1}^{b=b_2} \tag{4.22}$$

for $|x| \le d$.

Equation (4.12) is valid for a constant traction acting on the crack over a finite length; i.e. from b_1 to b_2 as shown in figure 4.4. If the traction varies with the

crack opening displacement, equation (4.12) cannot be used directly to obtain the SIF. The crack must be discretized in order to determine an approximate SIF. Figure 4.5 illustrates the discretization of a crack into n segments. The crack is discretized such that:

$$f_i = d - \left(\frac{i}{n}\right)(d - r)$$

(4.23)

$$g_i = d - \left(\frac{i-1}{n}\right)(d - r)$$

(4.24)

$$x_i = d - \left(\frac{i - \frac{1}{2}}{n}\right)(d - r)$$

(4.25)

where i is incremented from 1 to n. Each segment of the crack is associated with a SIF and contributes to the crack opening profile. For example, a constant traction is assumed to act on segment i, defined to exist between f_i and g_i, as shown in figure 4.5. The constant traction is calculated from the traction law using the stress associated with x_i, the point between f_i and g_i. An approximation for the SIF due to the entire traction effect on the crack is obtained via the superposition of the SIFs associated with the n segments:

$$K_\sigma = \sum_{i=1}^{n} K_{\sigma_i}$$

(4.26)

The same approach can be used to obtain the crack opening profile due to the traction:

$$V_\sigma(x) = \sum_{i=1}^{n} V_{\sigma_i}(x)$$

(4.27)

A strain softening traction law is assumed, as shown in figure 4.2. The traction law can be represented as:
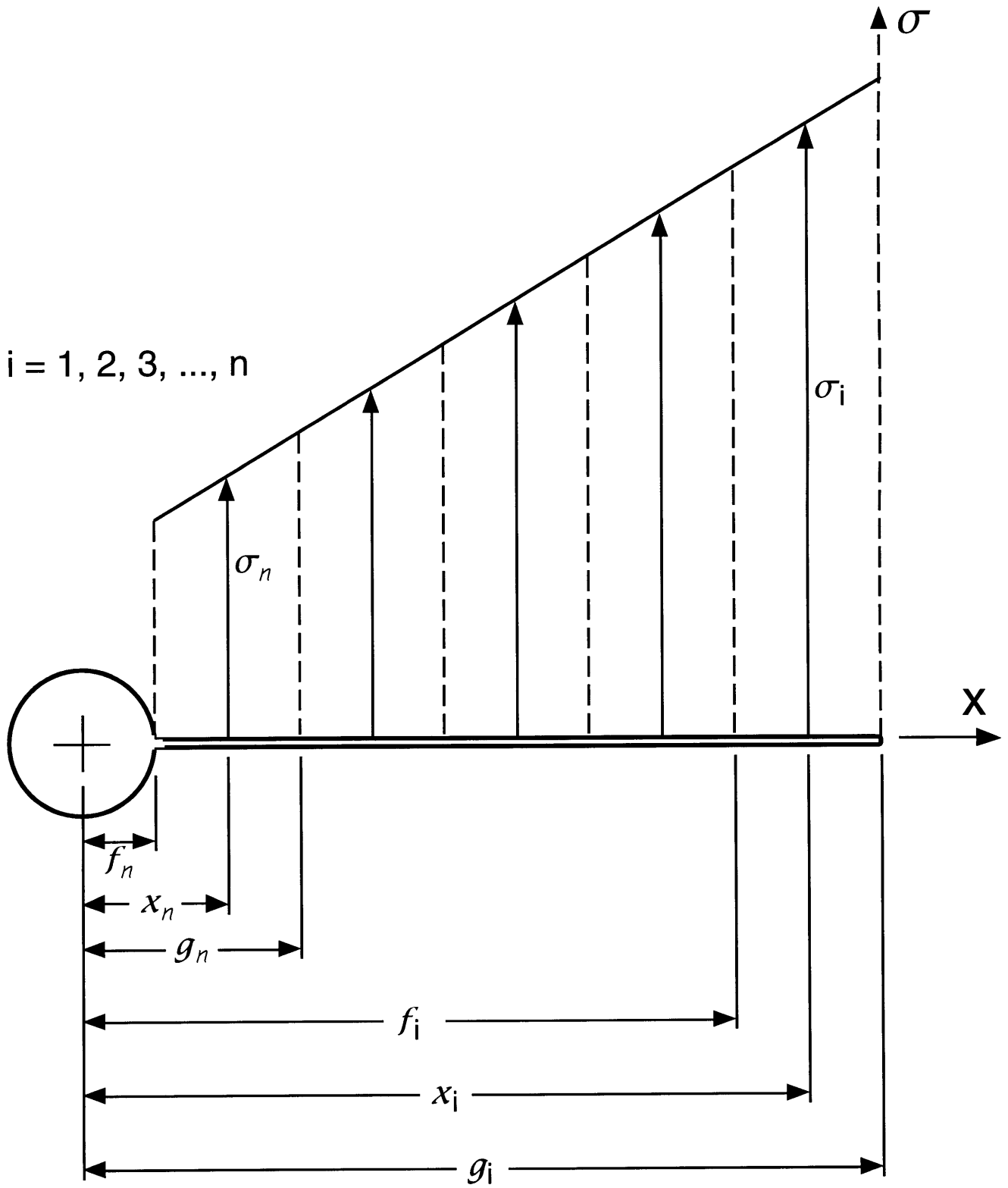
Figure 4.5   Crack discretization.

$$\sigma(v) = \sigma_c \left(1 - \frac{v(x)}{v_c} \right)$$

(4.28)

The traction law relates the stress to the crack opening displacement. For any crack profile, $V(x)$, the stress can be found at any distance x along the crack face.

The correction factor for material orthotropy was obtained by comparing the crack opening profiles (discrete CODs) from the damage growth model and the FEM (the FEM is discussed below). The two loading cases correspond to the crack opening profile due to a remote applied stress and the crack opening profile due to a point load on the crack face. Figures 4.6 and 4.7 show an example of the COD comparisons for the remote stress and point load, respectively. Generally, the isotropic profile from the FEM matched within 5% of the profile from the damage growth model, which are also for an isotropic material. This error applied to both loading cases. However, the CODs from the FEM considering an orthotropic material consistently varied from the COD solutions (equations 4.11 and 4.21) by approximately 35%. Therefore, an orthotropic correction factor of *1.35* was applied to the COD solutions, and equivalently, to the SIF solutions.

4.2.3 Procedure

The flowchart shown in figure 4.8 illustrates the analytical procedure. The analysis begins with an assumed initial crack length, taken to be 0.0254 mm for numerical purposes. Varying the assumed crack length will not significantly affect the analysis, as discussed below. The material fracture toughness, K_0, is calculated for each specimen using the initial LDZ length and the stress at which the LDZ initiated during experiment. The lowest value of K_0 is used for each material. The first point on the R-curve corresponds to the
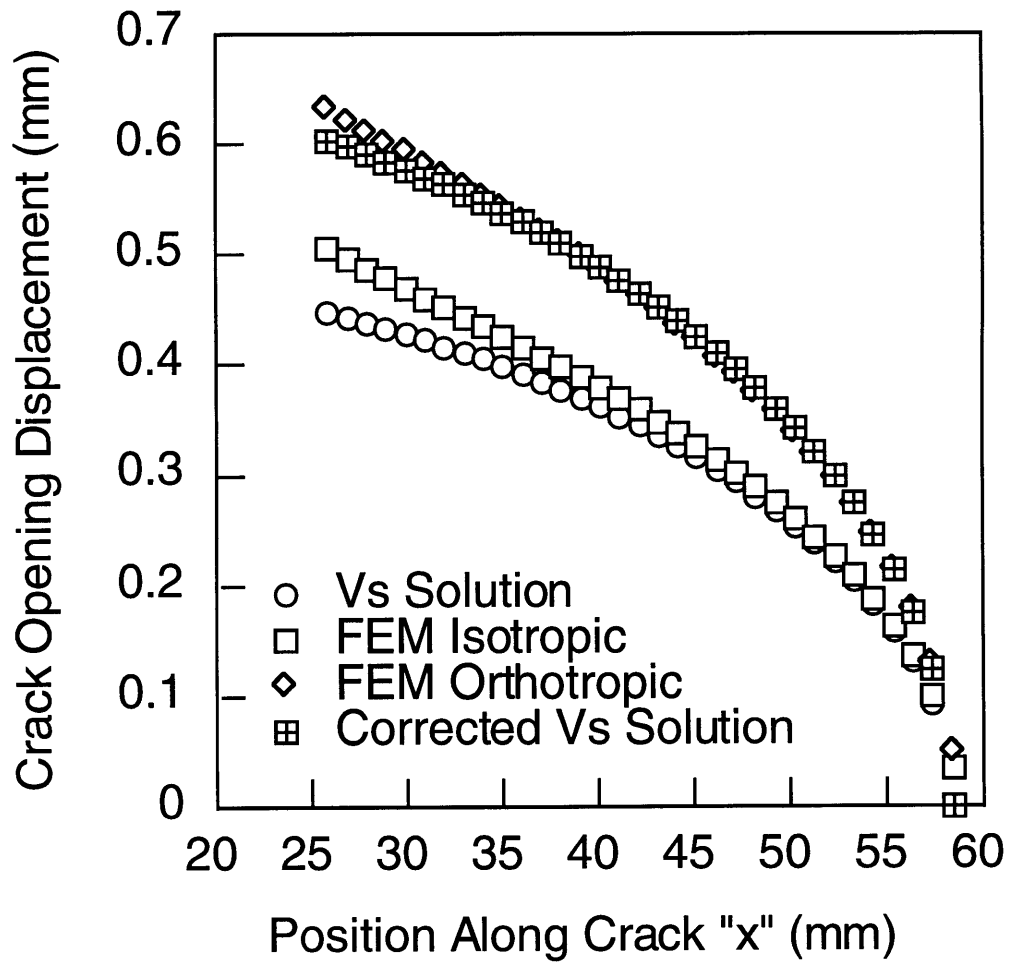
Figure 4.6   COD comparison of numerical solution (reference [116]) and FEM neglecting tractions for remote stress case.
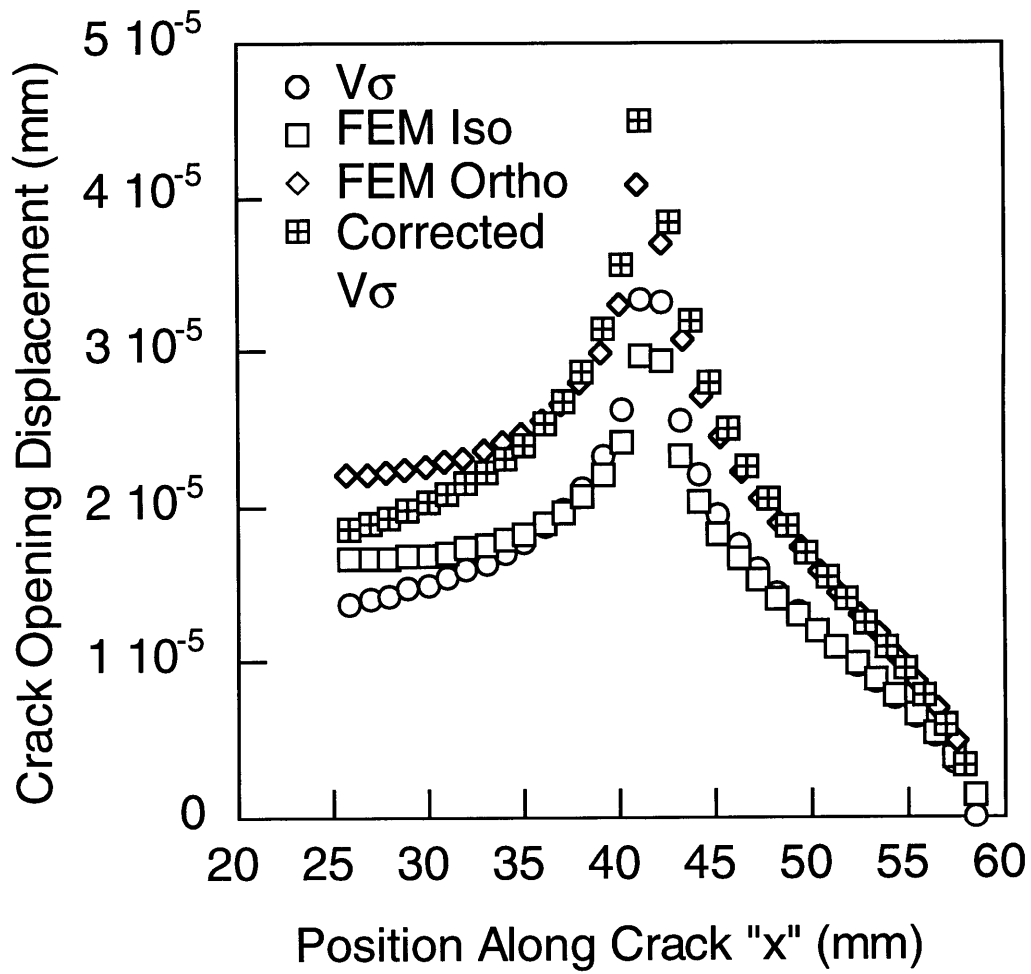
Figure 4.7   COD comparison of numerical solution (reference [116]) and
              FEM neglecting tractions for point load on crack face.
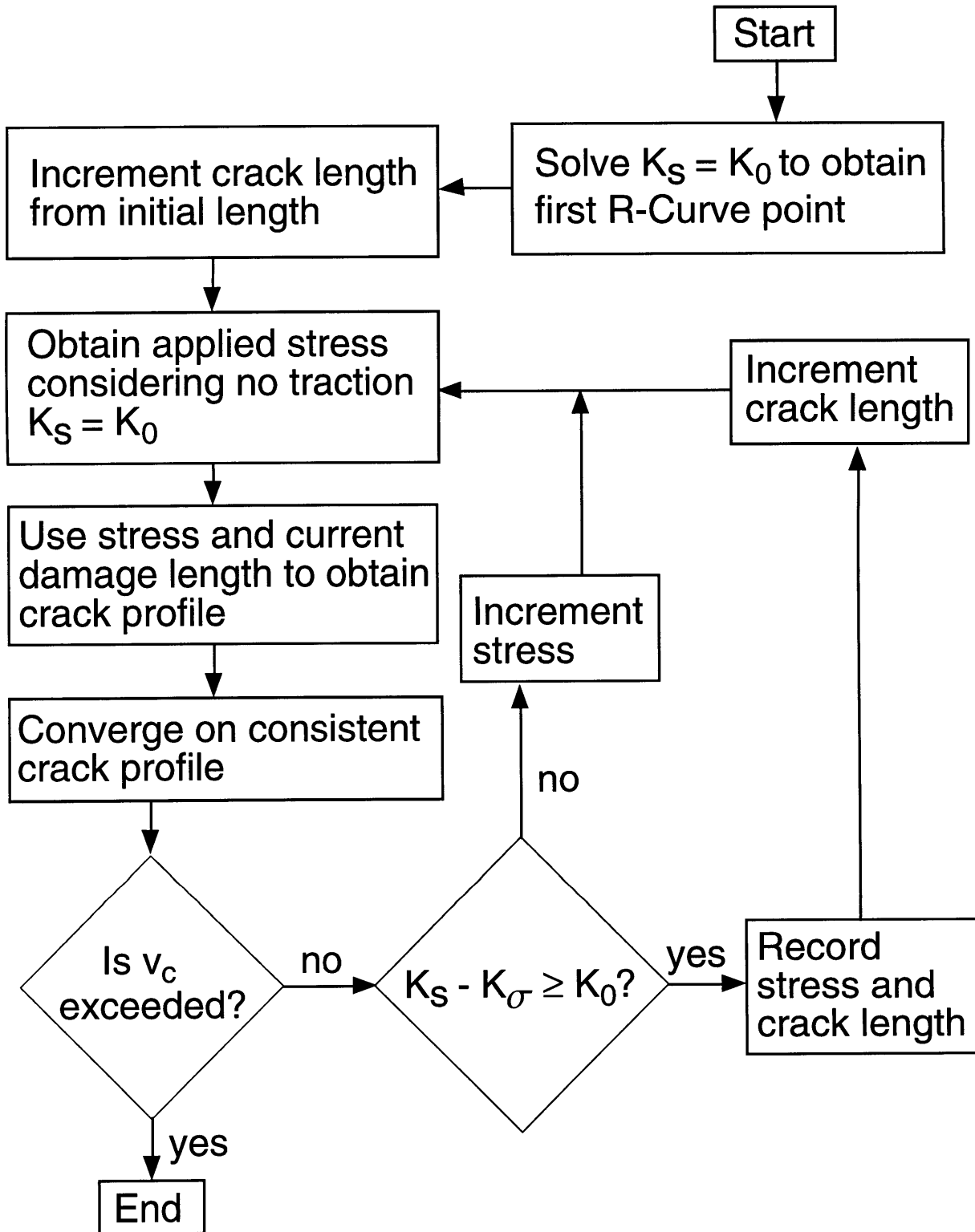
Figure 4.8   Flowchart describing damage growth model procedure.

case with no traction influence:

$$K_s = K_0 \qquad (4.29)$$

The crack length is incremented. The crack opening profile is chosen such that it converges to the appropriate crack opening profile, as described below.

The tractions are neglected to obtain an initial crack opening profile $V_i(x)$. Equation (4.29) is solved for the applied stress, S, using the current crack length, d. It should be noted that d represents the crack length plus the hole radius; i.e. the crack length is "$d - r$". S and d are used to calculate the crack opening profile $V_s(x)$ using equation (4.11). The crack opening profile $V_i(x)$ is set equal to $V_s(x)$.

The crack opening profile $V_i(x)$ is used to obtain the crack opening profile due to the traction, $V_{\sigma(i)}(x)$. $V_i(x)$ is substituted into the traction law, $\sigma(v)$ to obtain the traction distribution $\sigma(x)$. The crack is discretized into n segments. Equation (4.21) is used along with the traction distribution and the discretized crack to determine $V_\sigma(x)$. The subsequent "guess" for the crack opening profile is:

$$V_{i+1}(x) = V_i(x) - V_{\sigma i}(x) = V_s(x) - V_{\sigma i}(x) \qquad (4.30)$$

In some instances, the profile may yield negative crack opening displacements. This occurs because at long crack lengths, $V_{\sigma(i)}(x)$ will be greater than $V_s(x)$. Therefore, equation (4.30) will yield negative values for CODs. In these cases, the applied stress is incremented, resulting in a greater crack opening profile. The crack profile convergence begins again from equation (4.29). It should be noted that the procedure is modified to allow for negative CODs, as discussed in chapter 6.

A maximum error, defined as:

$$error = V_{i+1}(x) - V_i(x) \qquad (4.31)$$

The maximum allowable error is chosen to be 0.04% of the critical crack opening displacement, v_c. Smaller values of maximum error yielded nearly identical results, as discussed below. The error is computed at n locations along the crack corresponding to the locations x_i, as shown in figure 4.5. If the error at each point is not below the maximum error, then $V_{i+1}(x)$ is used to determine the crack opening profile due to the traction $V_{\sigma(i+1)}(x)$, and the next iteration defines the crack opening profile as:

$$V_{i+2}(x) = V_s(x) - V_{\sigma(i+1)}(x) \qquad (4.32)$$

The process is repeated until convergence on a consistent crack opening profile is reached, defined to occur when the error at all n locations is below the maximum error.

The SIF due to the traction is then computed via superposition as described above. The criteria for crack growth,

$$K_s - K_\sigma \geq K_0 \qquad (4.33)$$

is checked using the current crack length and applied stress (d and S). Since the traction will offset the equilibrium in equation (4.29), equation (4.33) will not be satisfied. The remote applied stress S is incremented. The new crack profile and the SIF due to the traction are determined using the procedures described above. The entire process is repeated until equation (4.33) is satisfied.

The stress and crack length at which equation (4.33) is satisfied corresponds to one point on the R-curve. Once equation (4.33) is satisfied, the crack length is incremented. The procedure is repeated until the critical crack opening displacement is exceeded, terminating the analysis.

4.2.4 Implementation

The damage growth model is used to predict two phenomena, the LDZ growth behavior and the ultimate failure load. The instrument used for the implementation of the damage growth model is the R-curve, traditionally used to model crack growth in metals and more recently applied to the growth of fiber-bridged cracks in metal and ceramic matrix composites [117].

The R-curve is a plot of applied strain energy release rate versus crack length. Equivalently, the applied SIF can be plotted versus the crack length. R-curves are one way of representing a material's resistance to crack growth, and the concept is applied analogously to LDZ growth in the present work. For illustrative purposes, figure 4.9 shows a model R-curve. The curve is offset due to the initial flaw size and material fracture toughness. The rising characteristic indicates that toughening mechanisms are operating in the crack wake.

If curves of constant stress are superimposed on the R-curve, as shown in figure 4.9, then an ultimate failure stress prediction can be made assuming that the test was performed in load control. In figure 4.9, an applied stress of σ_1 will result in the crack extending to a length of a_1. Crack extension will continue in a similar manner until an applied stress of σ_3 causes fracture. In the example shown in figure 4.9, the failure stress curve is tangent to the R-curve at the point where v_c is reached. This point also corresponds to the critical crack length, and satisfies:

$$\frac{\partial K}{\partial a} \geq \frac{\partial R}{\partial a} \qquad (4.34)$$

At this stress and crack length, the material's crack resistance is rising at a slower rate than the applied SIF with respect to the crack length.

Experimental R-curves are constructed by calculating applied stress
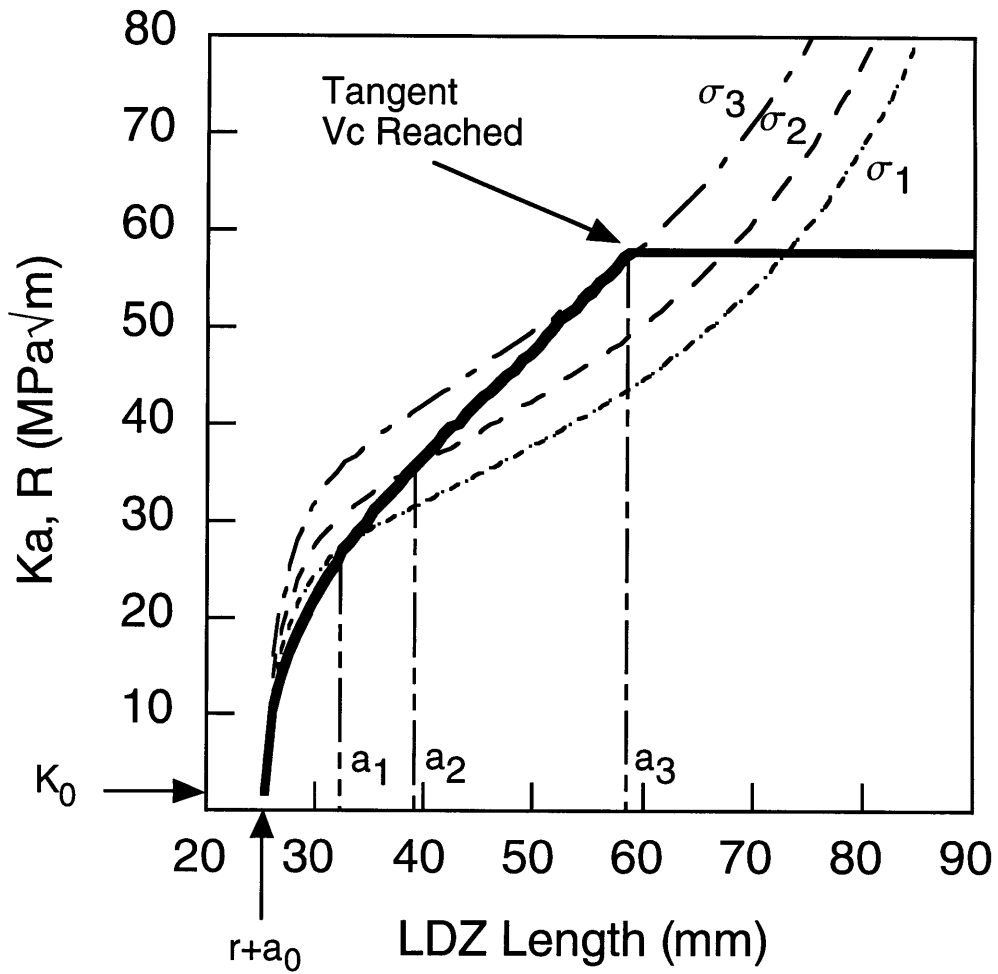
Figure 4.9   Typical R-curve, with lines of K_0 corresponding to constant stress superimposed.

intensity factors based on the stress that caused a change in LDZ length and the current LDZ length. For example, the first point on the R-curve corresponds to the initial assumed LDZ length. The stress associated with the first point on the R-curve is the stress that caused the LDZ to propagate from the initial length. The applied stress values are converted to applied SIFs using equation (4.4).

The ultimate failure stress was predicted using a method which strictly only applies for load control. Equation (4.4) is used to obtain curves of constant applied stress. The offset associated with the driving force curves, equal to the assumed initial LDZ length, is negligible when predicting the failure stress. The ultimate failure stress is associated with the driving force curve tangent to the predicted R-curve.

4.2.5 Calibration

The traction law is calibrated using the damage growth data for the large specimens. One set of data was chosen for a material system: ADC2BR and BDC1BR data are chosen because of their large number of data points. The R-curve is calibrated to this data by repeatedly applying different traction laws. Once the data is fit with a traction law, R-curves for the other specimens are constructed using the same traction law for the respective material system. No further iteration on the traction laws are necessary because the R-curve fits are acceptable for all geometries. The parameters defining the traction laws are tabulated in table 4.1.

4.2.6 Sensitivity

The predicted LDZ growth behavior depends primarily on the traction law. Other factors which influence the predicted behavior are material properties, particularly E_1, and other model parameters such as the number of

Table 4.1   Traction Law and Fracture Parameters from Damage Growth Calibration

Material	Traction Law / Fracture Parameters		
	LDZ Growth Data Calibration		
	σ_c (MPa)	v_c (mm)	K_0 (MPa$\sqrt{m}$)
M4	121	0.64	2.0
M5	121	0.64	1.6

crack segments used in crack discretization, the maximum allowable crack opening profile convergence error, and the number of points defining the R-curve.

A model R-curve and failure prediction value is used to illustrate the sensitivity of the damage growth model to the parameters listed above. The model uses the traction law and fracture parameters listed in table 4.1, and the standard damage growth model parameters, listed in table 4.2. Different R-curves and failure predictions are obtained by changing the traction law parameters. Specifically, σ_c, v_c, and G_{ss} (keeping σ_c and v_c proportional to their original values) are independently halved and doubled. Other variable parameters are varied as well, as listed in table 4.3. Table 4.3 lists the different traction law configurations and variable parameter values and relative error of the failure predictions compared to the standard prediction. Figures 4.10-4.12 show the R-curve variations corresponding to traction law variations.

4.2.7 Net-Section

The damage growth model is also used to obtain information about the net-section stress. For each damage length, the applied force, the force carried by the LDZ, and the net-section forces are calculated using the appropriate stresses, as shown in figure 4.13.

A stress-based approach to failure states that the facesheet will fail when the applied load is greater than or equal to the load carried by the LDZ plus the load carried by the undamaged ligament. The ligaments are assumed to fail when the average ligament stress equals the ultimate failure stress. The applied load on the facesheet, the load carried by the LDZ, and the load carried by the total net-section are, respectively:

Table 4.2   Standard Damage Growth Model Parameters

Standard Model Parameters	
Parameter	Value
Initial crack length (mm)	0.0254
Stress increment (kPa)	689.476
Maximum crack length (mm)	0.7*w
Crack length increment (mm)	Max/100
Crack discretizations	10
Allowable error	10^{-5}

Table 4.3   Damage Growth Model Sensitivity

Damage Growth Model Sensitivity		
Variation	Failure Stress (MPa)	% Difference
Standard	72.395	0.0
σ_c x 2	119.969	-66
$\sigma_c \div 2$	43.092	41
v_c x 2	84.806	-17
$v_c \div 2$	60.674	16
G_{ss} x 2	102.731	-42
$G_{ss} \div 2$	51.711	29
Crack increment $\div$ 10	71.016	1.9
Crack increment x 2	72.740	-0.5
All futher comparisons made with crack increment $\div$ 10		
Stress increment $\div$ 10	71.188	1.7
Stress increment x 10	71.705	1.0
max error $\div$ 100	71.016	1.9
E_1 x 2	83.082	-15
$E_1 \div 2$	58.605	19
K_0 x 2	72.740	-0.5
$K_0 \div 2$	71.016	1.9
n x 10	71.705	1.0
$n \div 2$	71.016	1.9
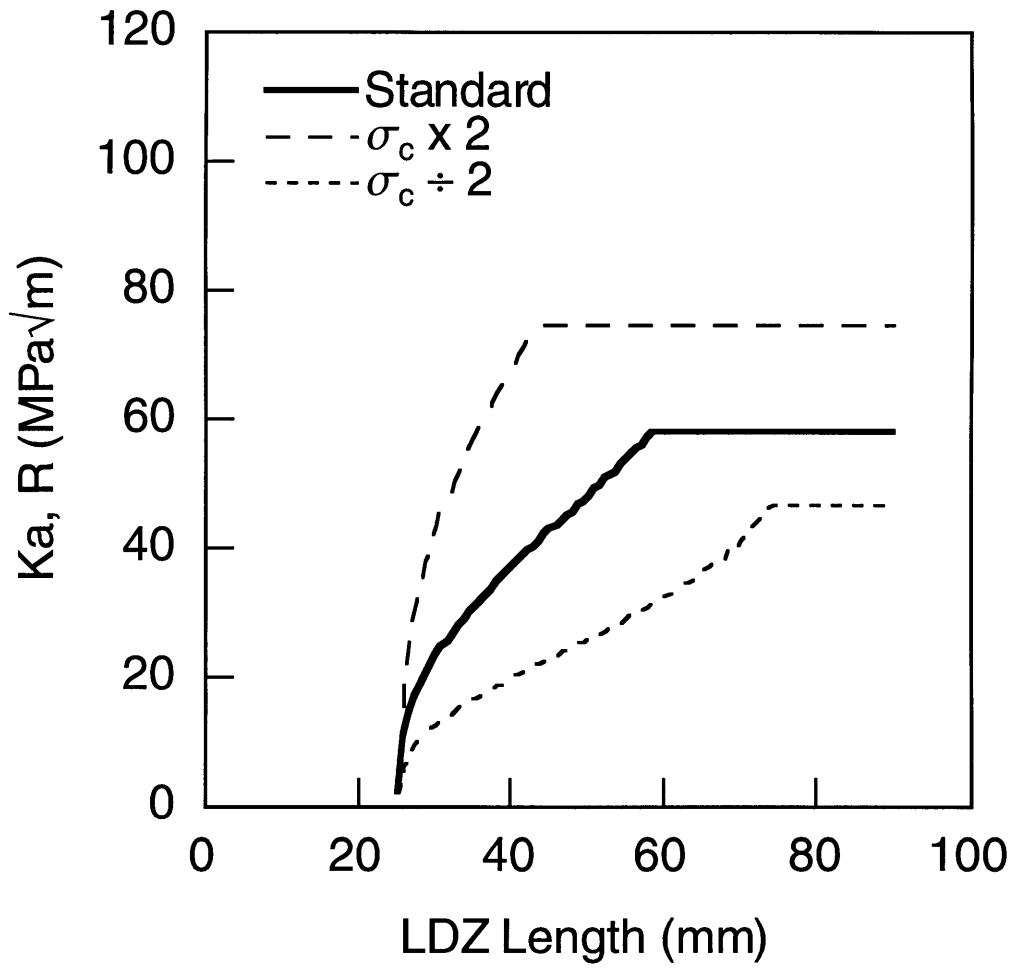
Figure 4.10 σ_c variation effect on model R-curve; v_c = constant.
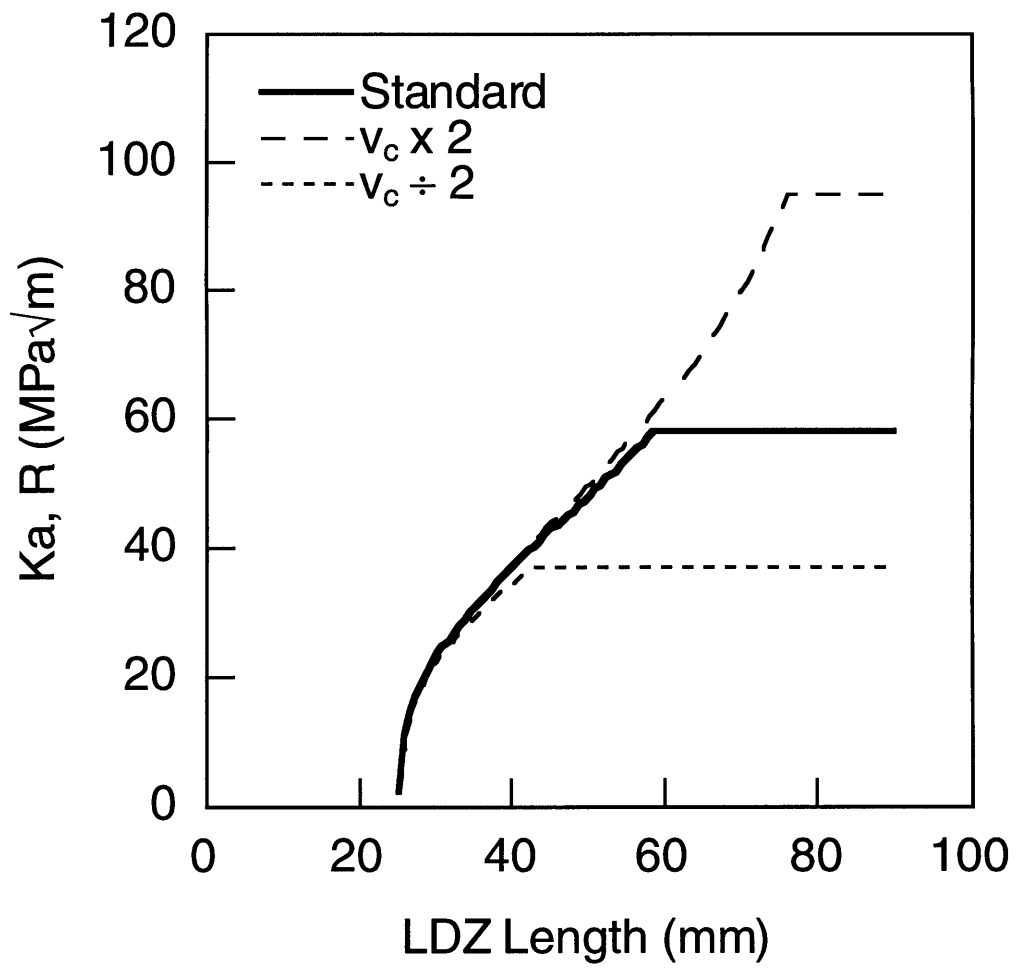
Figure 4.11 v_c variation effect on model R-curve; σ_c = constant.
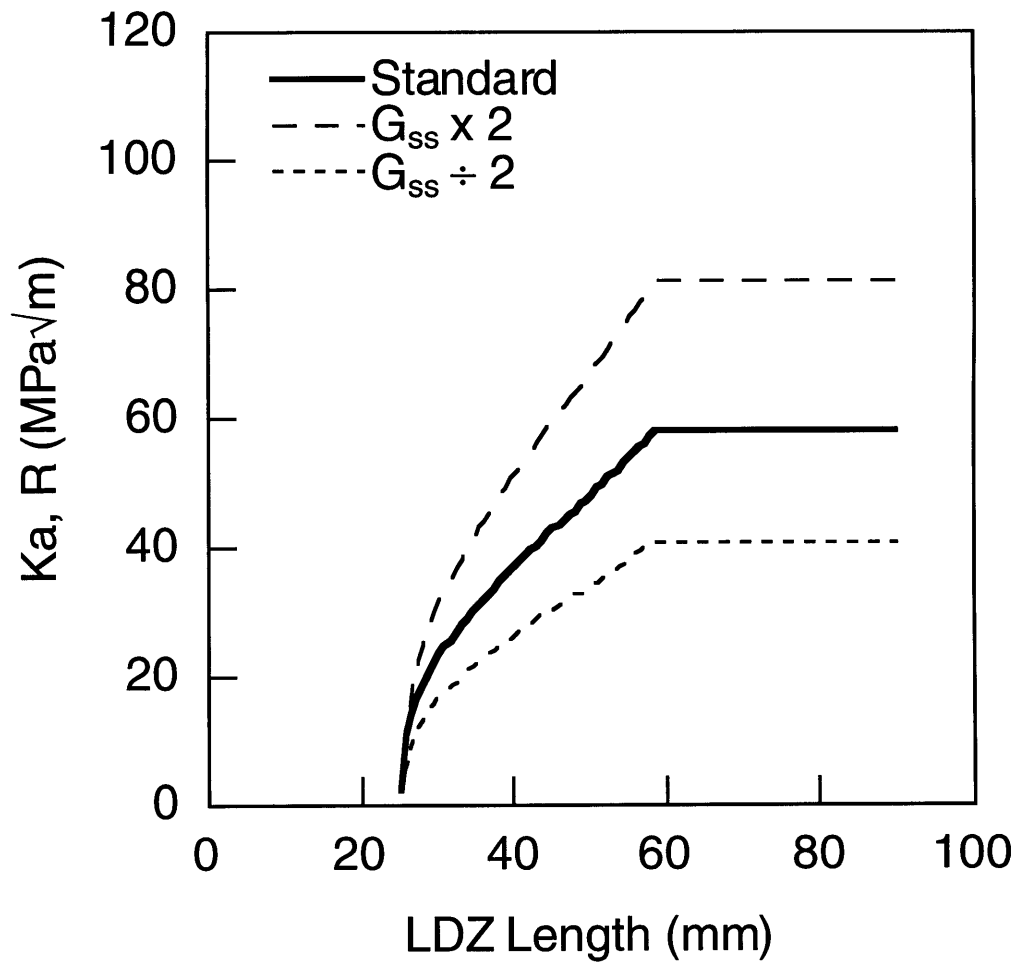
Figure 4.12 G_{ss} variation effect on R-curve; σ_c, v_c proportional.
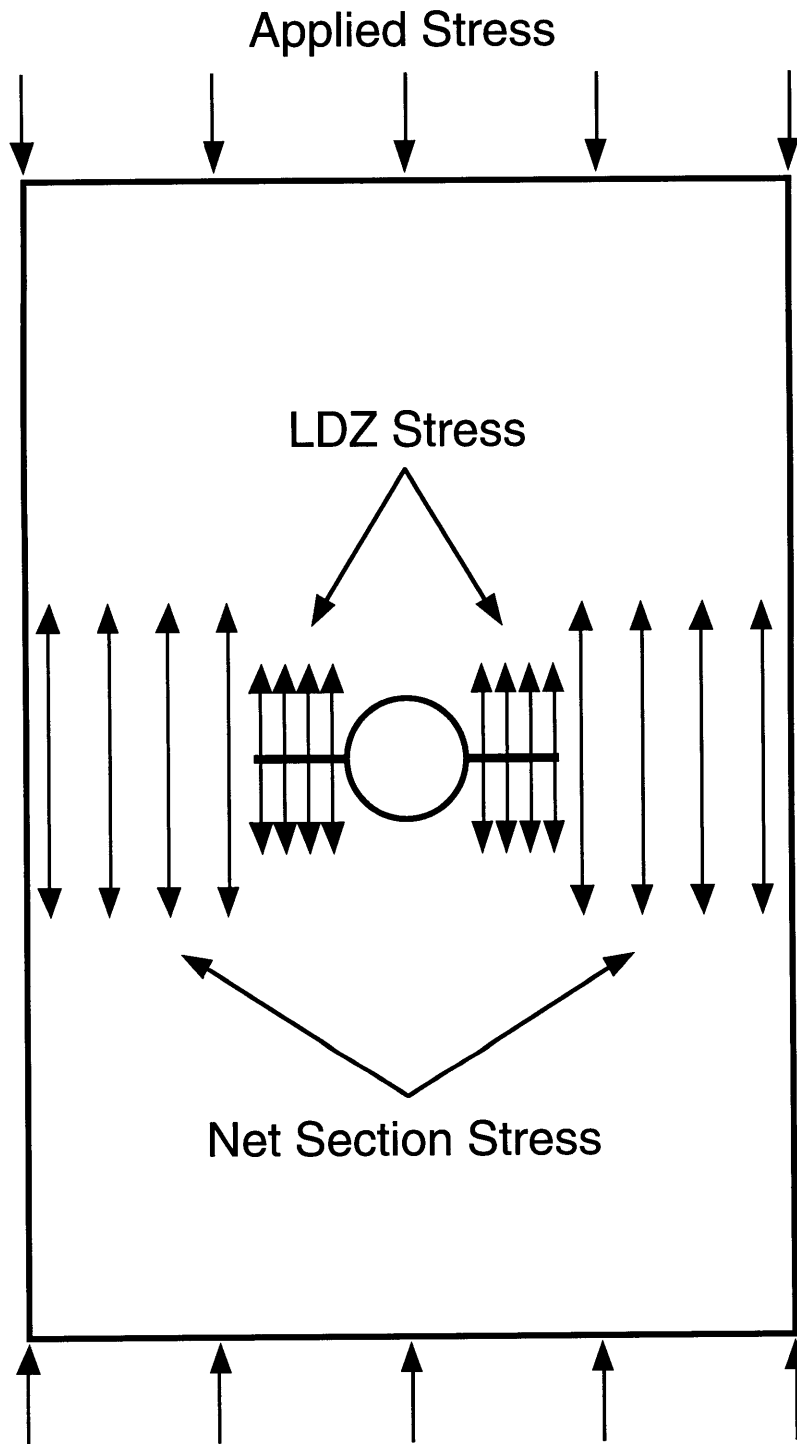
Figure 4.13   Net-section stress.

$$Applied\ Force\ =\ \frac{S}{2} * tk * w \tag{4.35}$$

$$LDZ\ Force\ =\ \sum_{i=1}^{n}\left(\sigma_i * tk * \frac{d_i - r}{n}\right) \tag{4.36}$$

$$Ligament\ Force\ =\ 2 * \sigma_{un} * tk * (w - d_i) \tag{4.37}$$

4.3 Finite Element Model

The FEM is constructed and implemented using I-DEAS Master Series™ 6 as the pre and post-processor. Abaqus™ version 5.8 is used as the processor. The purpose of the FEM is to obtain a predicted strain distribution around an LDZ.

4.3.1 Assumptions

The following assumptions apply to the FEM:

- The facesheets can be analyzed independently.

- The facesheet is represented with a quarter symmetric model.

- The composite laminate is equivalent to an orthotropic plate under plane stress conditions.

- The response under a tensile load is analogous to the response under a compressive load.

- The LDZ can be modeled with a series of discrete nonlinear springs.

- The traction law, defined by σ_c and v_c in the damage growth model, can be converted to an equivalent nonlinear spring law, defined by F_c and v_c.

4.3.2 Construction of the Model

A one-quarter symmetric mesh is used to model one facesheet. I-DEAS Master Series™ 6 is used to create a wire-frame boundary of the geometry, as

shown in figure 4.14. The dimensions of the boundary correspond to the dimensions of the facesheet being modeled. Lines are drawn in the boundary in order to provide areas for mesh refinement. Rectangular wireframes are also drawn in the boundary in locations corresponding to the positions of the strain gages.

Two-dimensional plane stress elements are used to model the facesheet. Eight node quadrilateral elements are used throughout the mesh. Six node triangular elements are used as transition elements. The elements are assigned a thickness which corresponded to the facesheet thickness.

Nonlinear node-to-ground springs are used to model the LDZ. Nodes on the x-symmetry line that correspond to the LDZ are released from the symmetry boundary condition and attached to springs, as shown in figure 4.15.

The nodes along the top edge corresponded to the locations of loading. These nodes are *tied* together to simulate the loading conditions (compression platens); all the top nodes displace the same amount in the loading direction.

4.3.3 Mesh Convergence

The basic mesh without springs is shown in figure 4.16. The "base element number" refers to the number of elements located on the first partition, as shown in figure 4.16. An LDZ that had propagated between strain gages L12 and L13 on specimen ADC2 was used to obtain mesh convergence. Figure 4.17 illustrates local strain gage data as a function of the base element number. Initial tests, including the convergence tests, were done in compression. However, strain values are reported as positive.

According to figure 4.17, mesh convergence is reached before two hundred base elements. However, the springs in the FEM are utilized to model a continuous phenomenon; i.e. the LDZ. Therefore, using more springs would
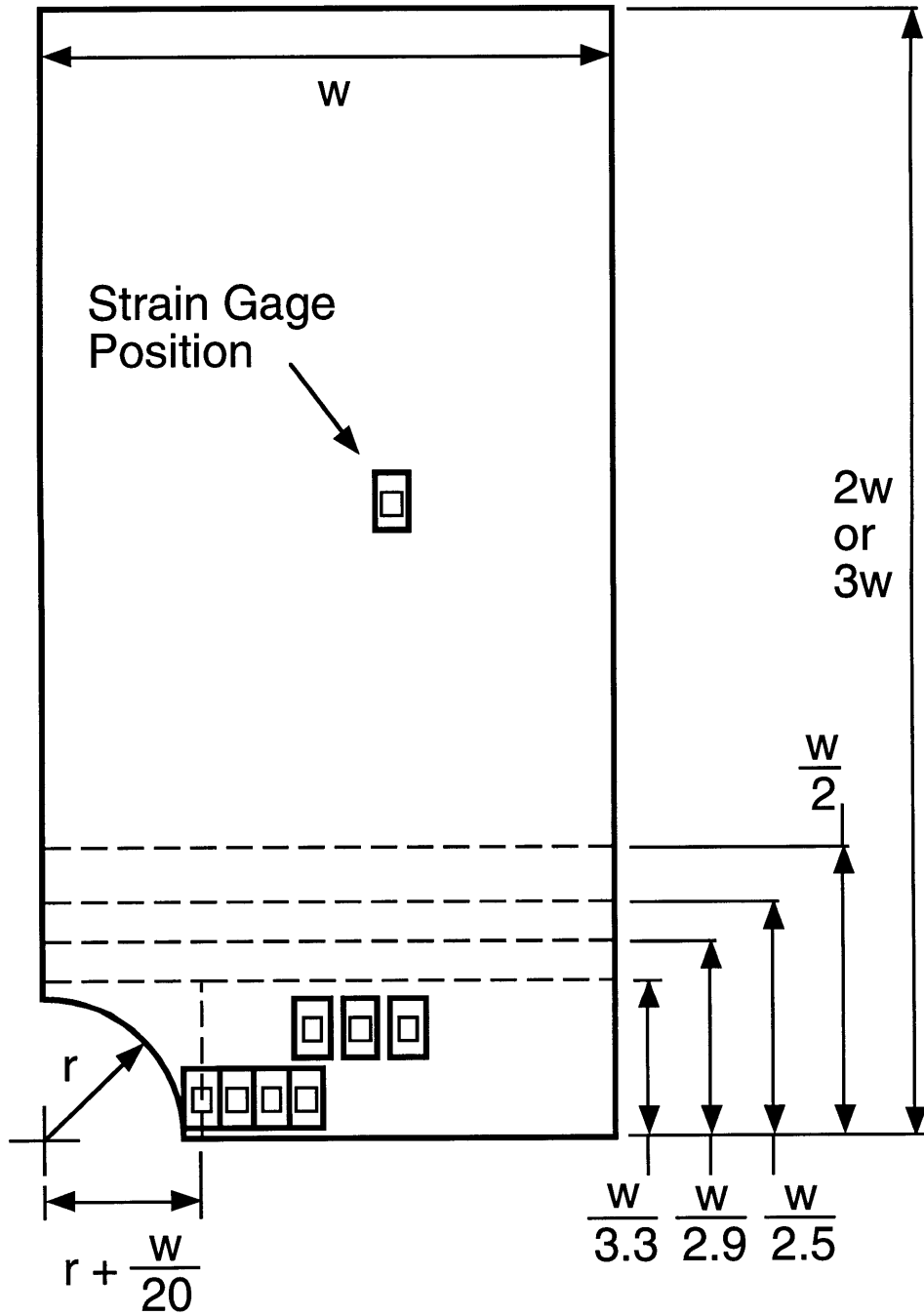
Figure 4.14   Finite element mesh boundary.

Applied Force

Top Nodes Tied

x

y

y-Symmetry

LDZ
Length

x-Symmetry

Node-to-Ground
Springs
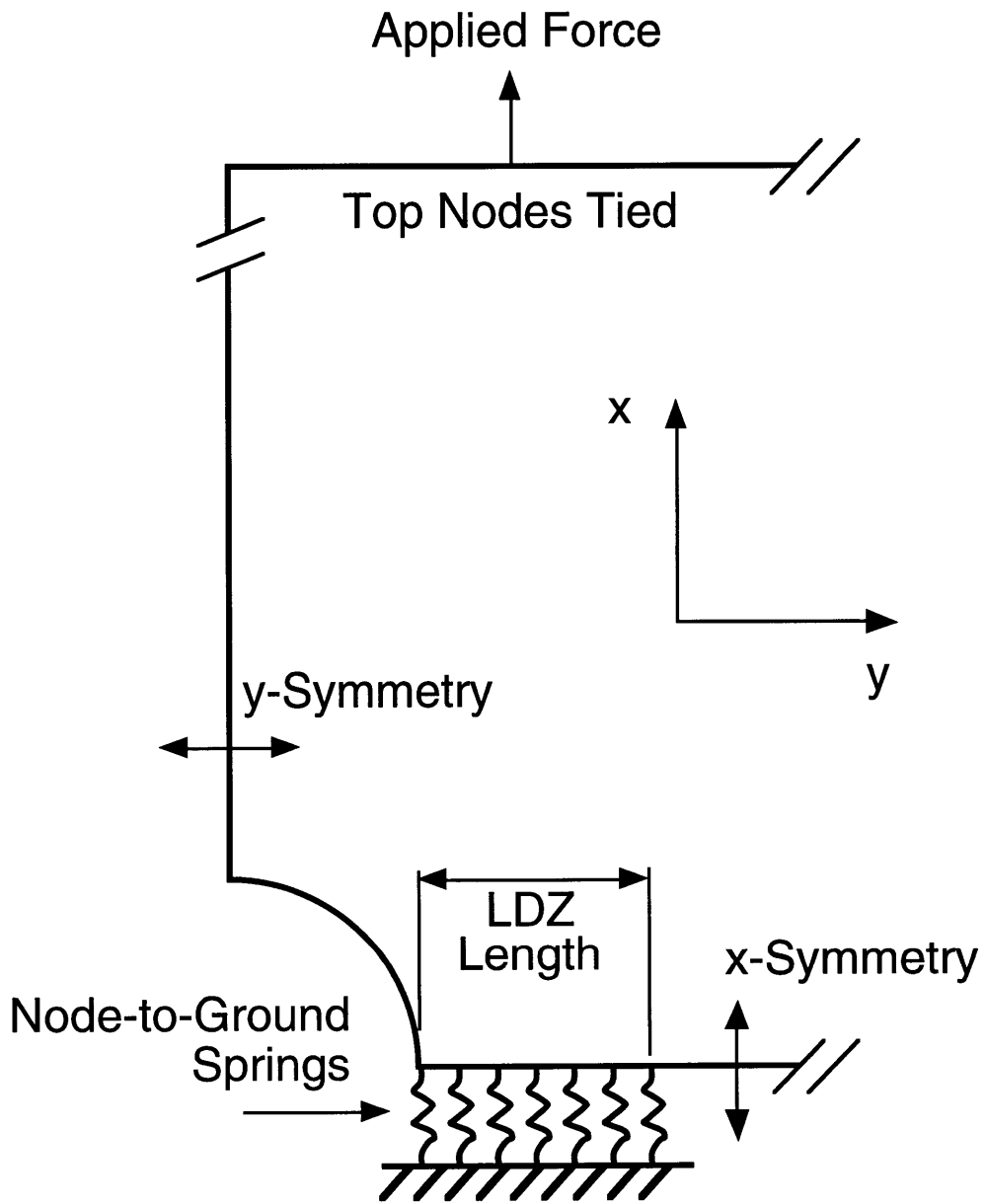
Figure 4.15   Illustration of use of discrete nonlinear node-to-ground springs to
model the LDZ.
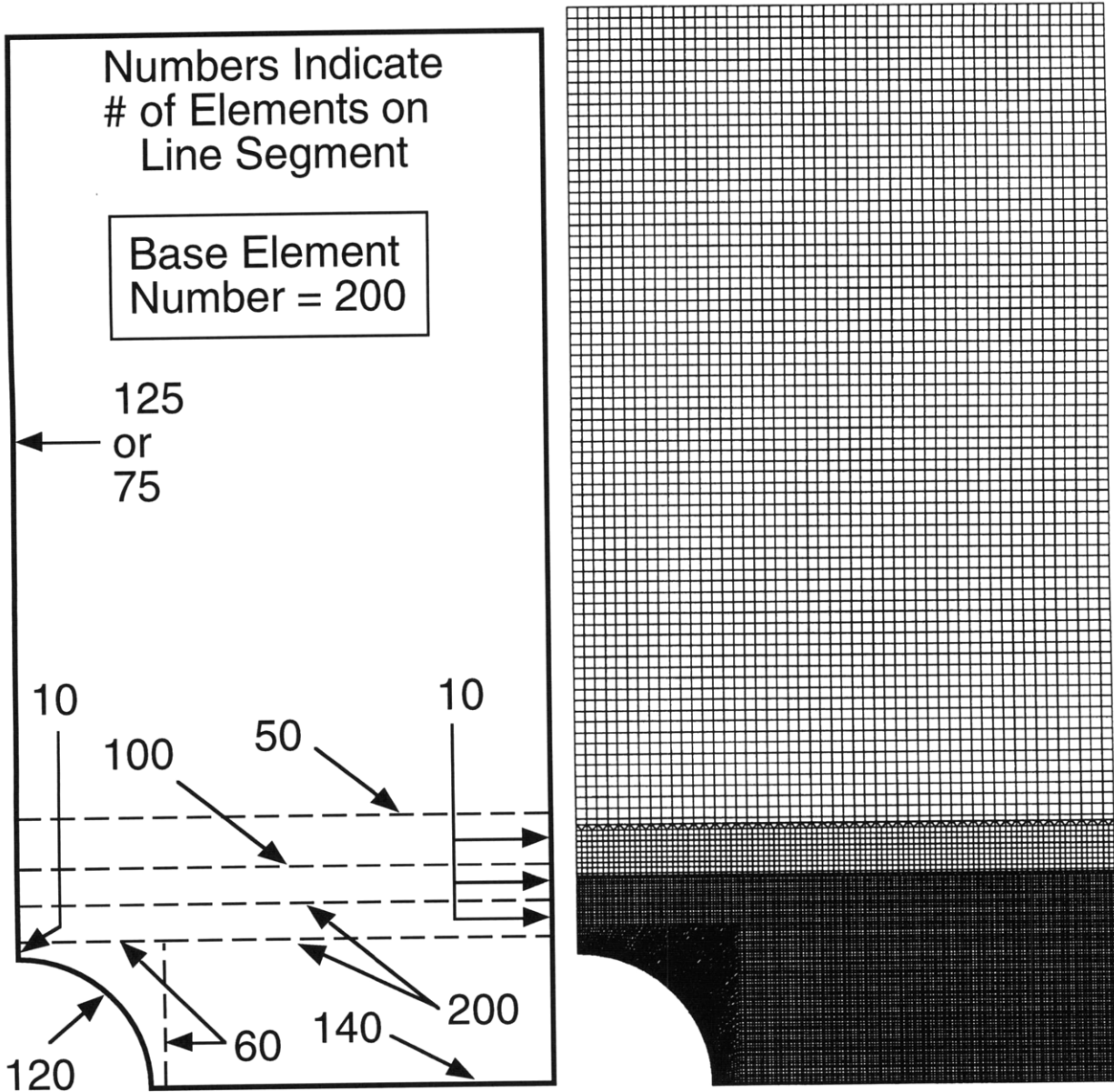
Figure 4.16   Finite element model standard mesh.
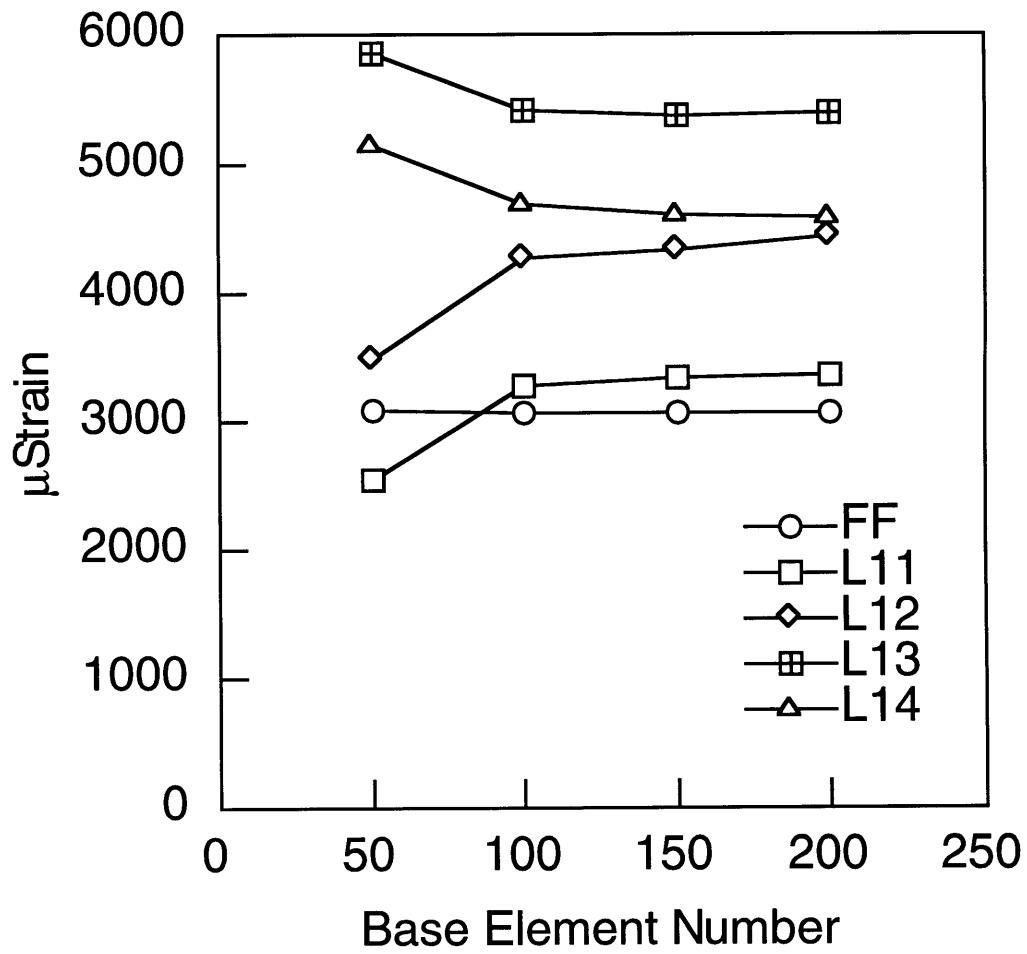
Figure 4.17   Finite element model convergence.

lead to a more accurate representation of a *continuous spring*. Disk space considerations limited the model to two hundred base elements for the mesh configuration used. This corresponds to one spring for every 0.508 mm of LDZ being modeled.

4.3.4 Spring Law

The nodes on the x-symmetry line corresponding to the LDZ are released from the symmetric boundary condition. Discrete nonlinear node-to-ground springs are attached to all of the released nodes. In order to model an equivalent continuous traction law as that used in the damage growth model, the discrete spring law is calibrated according to the specific FEM case. The force-displacement spring law is adjusted depending on the LDZ length, thickness of the laminate, and the number of springs on the LDZ to yield the required value of σ_c. The critical COD, v_c, remains constant between the traction law and the spring law. The critical stress, σ_c, is converted to a critical force F_c:

$$F_c = \sigma_c * \frac{(LDZ\ length)\ (tk)}{(\#\ of\ springs\ on\ LDZ)} \tag{4.38}$$

where *tk* is the laminate thickness.

For numerical purposes, the spring law that is used is not a solely softening constitutive relationship, as is the traction law (figure 4.2). Initial tests showed that the FEM processor had difficulties at non-zero force intercepts (a spring force at zero spring displacement). Therefore, the spring law has a modified shape as shown in figure 4.18. The linear region accounts for 95% of the constitutive behavior. The remaining 5% is used to obtain a smooth transition from an initially steep parabolic curve with positive slopes to the negative slope of the linear region. The model spring law is based on the
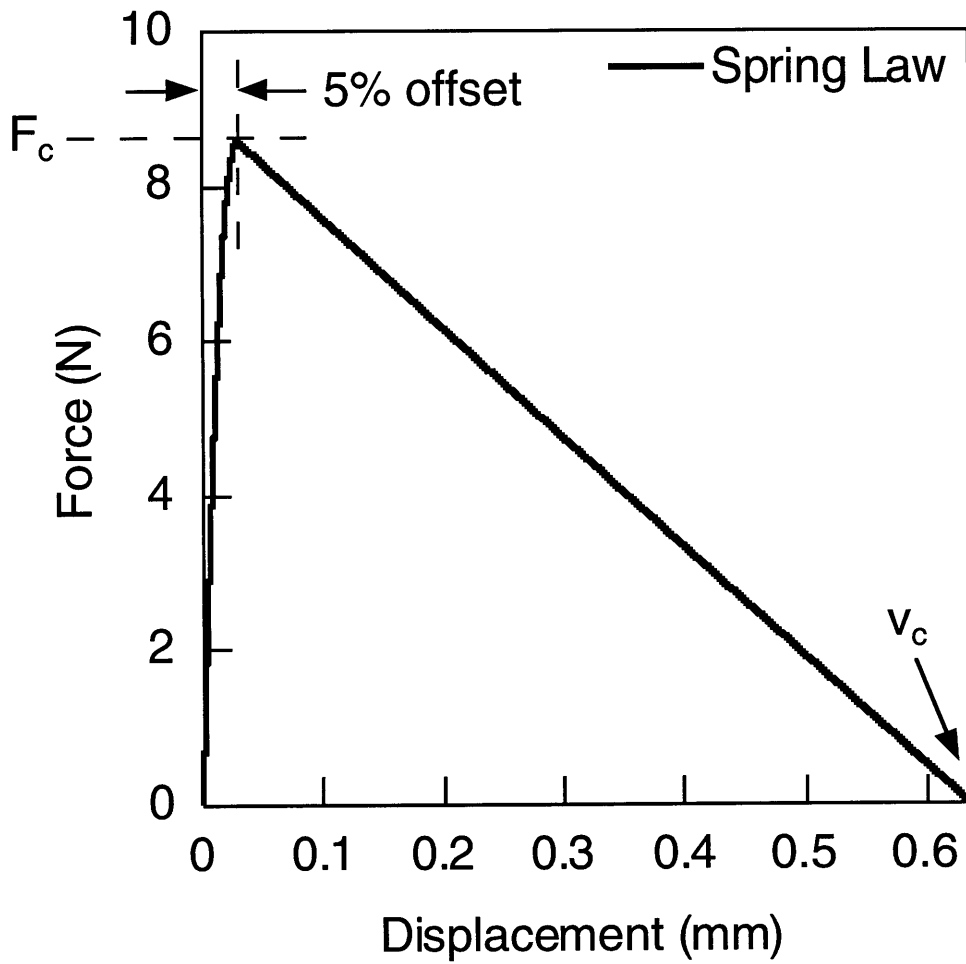
Figure 4.18   Finite element model spring law.

connection of two continuous smooth curves, as shown in figure 4.19. Each spring law used in the FEM is scaled from the model spring law using equation (4.38), while v_c is scaled to remain constant with the traction law. Microsoft® Excel 98 was used to generate 1000 force-relative displacement pairs along each of the four curve sections, as shown in figure 4.19.

4.3.5 Implementation

The finite element model is used to model one equilibrium state at a time. For example, during a mechanical test, an LDZ would propagate to a certain distance at a given load. The immediate recorded load change due to the propagating LDZ was negligible. An FEM is created for a specific LDZ length and load from experiment. The variable parameter in the FEM is the spring law. Every time the LDZ changes length, which results in the release of more nodes, the spring law must be updated. Once the FEM is processed, the average strain across each strain gage area is recorded.

4.3.6 Calibration

A mentioned above, the traction law can also be calibrated by the strain distribution from the FEM. Instead of obtaining the best correlation to the experimentally measured resistance curve, the best correlation to strain data is used to obtain the traction law.

Two representative experimental strain distributions are chosen for calibration purposes for each material system: ADC2BR and BDC1BR. In either case, the LDZ displays both high and low load carrying capability, depending on the location of the strain measurement with respect to the LDZ tip. Therefore, both a maximum and minimum strain are required to calibrate the traction law; i.e. the traction law must yield equivalent maximum and minimum strain values compared to the measured values. Unfortunately, this
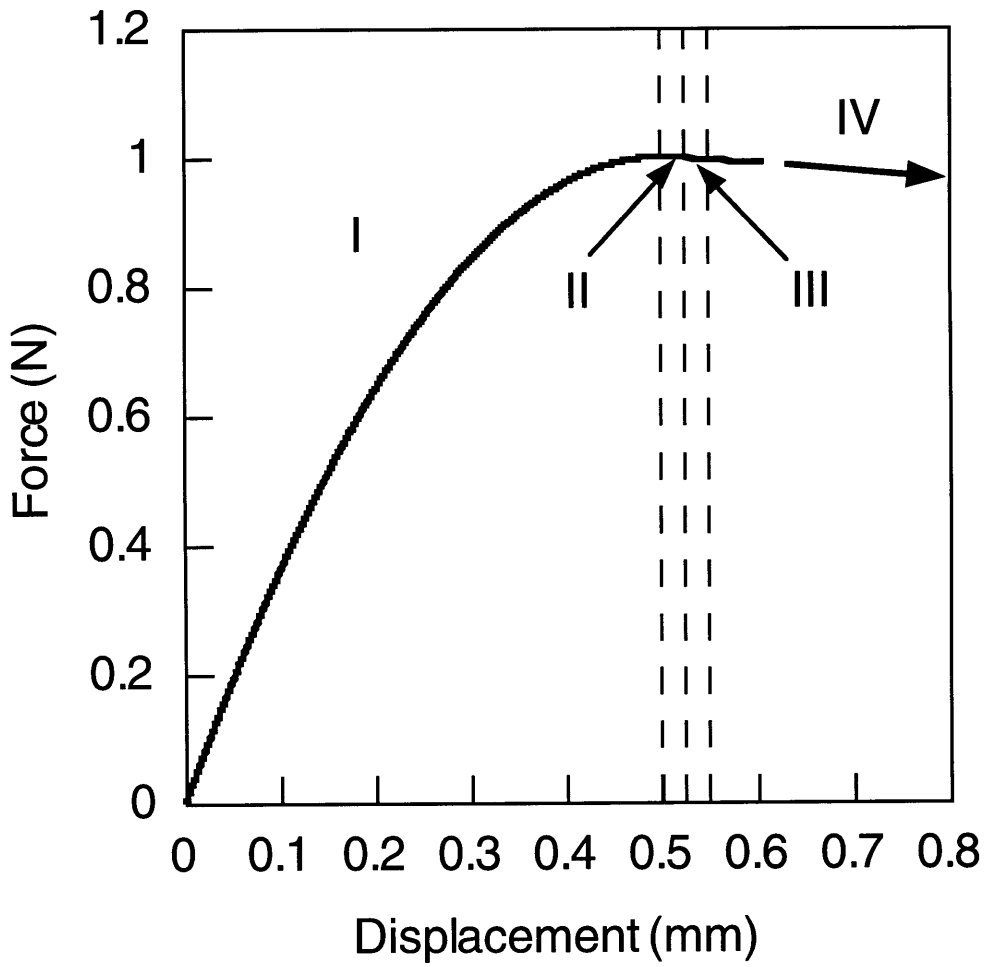
Segment	Displacement	Equation
I	$0 \le v \le 0.5$	$\left.\begin{array}{l}\end{array}\right\}$ $F = -4v^2 + 4v$
II	$0.5 \le v \le 0.5125$	
III	$0.5125 \le v \le 0.525$	$\left.\begin{array}{l}\end{array}\right\}$ $F = -v/10 + 1.050625$
IV	$0.525 \le v \le 10.50625$	

Figure 4.19   Model spring law definition.

is impossible with the current traction law. It is possible to match either the maximum or minimum strain value, but not both.

In order to calibrate the traction law, an LDZ length is chosen which experimentally records both a relatively high and low strain measurement. Typically, an LDZ of this length corresponds to one whose tip is somewhere between two local strain gages. For example, figure 4.20 shows this location for BDC1BR. Gage L13 recorded the highest strain and gage L11 recorded the lowest when the LDZ was at a length of 14.2 mm. The FEM can be used to match either local strain gage, but not both. Therefore, the traction law is considered calibrated when the error from the FEM strain correlation for both gages is approximately equal. Table 4.4 lists the traction law parameters obtained via the FEM strain calibration.

4.3.7 Sensitivity

The FEM results depend solely on the spring law, since all other parameters (such as material properties) remain constant for every run and are considered invariable. The sensitivity of the strain results is illustrated by comparing model results to results from a varying spring law. Recall that the spring law is directly related to, and therefore considered "equivalent" to, the traction law. Therefore, σ_c, v_c, and G_{ss} (keeping σ_c and v_c proportional to their original values) are independently halved and doubled. The BDC1 test case with an LDZ length of 14.2 mm is chosen as the model geometry. The M5 traction law calibrated with the FEM strains is chosen as the model traction law. Table 4.5 lists the different traction law configurations and relative error of the strain predictions compared to the model prediction.
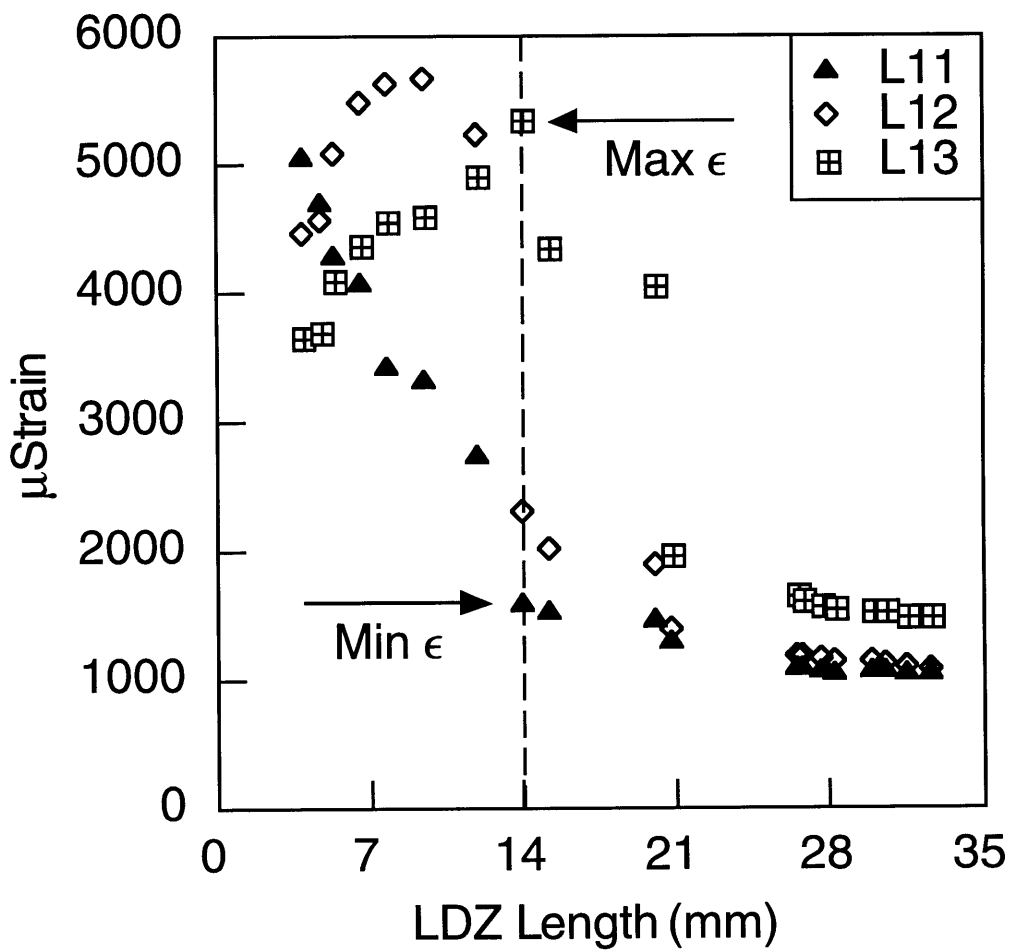
Figure 4.20   Use of local strain gage data for traction law calibration on experimentally observed strains.

Table 4.4   Traction Law and Fracture Parameters from Finite Element Model Strains Calibration

| | Traction Law / Fracture Parameters | | |
| | FEM Strain Data Calibration | | |
Material	σ_c (MPa)	v_c (mm)	K_0 (kPa$\sqrt{m}$)
M4	59	0.64	2.0
M5	48	0.64	1.6

Table 4.5   Finite Element Model Sensitivity

Finite Element Model Sensitivity										
	Strain / % Difference									
Variable	FF	%	L11	%	L12	%	L13	%	L21	%
Model	2963	0.0	1753	0.0	2519	0.0	5210	0.0	4434	0.0
σ_c x 2	2910	1.8	3607	-106	3965	-57	4667	10.4	3965	11
$\sigma_c \div 2$	2986	-0.8	1019	42	1909	24	5396	-3.6	4626	-4.3
v_c x 2	2957	0.2	2011	-15	2662	-5.7	5113	1.9	4378	1.3
$v_c \div 2$	2981	-0.6	1106	37	2146	15	5429	-4.2	4585	-3.4
G_{ss} x 2	2938	0.8	2636	-50	3181	-26	4952	5.0	4217	4.9
$G_{ss} \div 2$	2982	-0.6	1126	36	2046	19	5387	-3.4	4593	-3.6

4.4 Summary

The damage zone model has been applied previously to notched composite laminates under compression. These models achieved some success in predicting both experimentally observed damage zone growth and crack overlap displacement behavior. This chapter, however, presents a standard methodology for the interrogation of traction law-based damage zone models. The traction law is assumed to be a material parameter, and is consistent in the investigative approach. The damage growth model is capable of predicting the LDZ resistance behavior and the strength. The finite element model is capable of predicting the local strain distribution.

The traction law can be obtained primarily by either of two methods. First, the LDZ growth data can be used to calibrate the traction law. Second, the FEM can be used to calibrate the spring law, which in turn tells the traction law. Once the traction law is obtained through calibration by experimental observations, it can be used to predict the LDZ growth, strength, and strain distribution for notched laminates of the same material.

This methodology allows for a true assessment of the DZM. However, it should be noted that the DZM presented here is based on a two parameter strain softening traction law. The approach presented can also be used to investigate other traction law shapes.

CHAPTER 5

RESULTS

This chapter presents the results of the experiments and analysis. First, the sandwich panel compressive response is reported. Second, the damage mechanisms observed from experiment and cross-sectioning are reported. Finally, the results from the damage zone model investigation are reported.

5.1 Compressive Response

This section presents both the global and local sandwich panel compressive response as measured by the far field and local strain gages, respectively.

5.1.1 Global Behavior

The far field strain gages were used to give an indication of the relative bending that occurred in the sandwich panel during the test. Equation (3.1) was used to obtain a value for *alignment*. A typical alignment response is shown in figure 5.1. The alignment plots were generally characterized by three regions. The first region, or the initial loading period, began at zero load and extended until approximately 20% of the failure load was reached. It was characterized by alignment values of which the majority were more than 10%. The alignment in this region was scattered, since at low loads the variation in strain as measured by equation (3.1) could be great. Manual adjustment of the
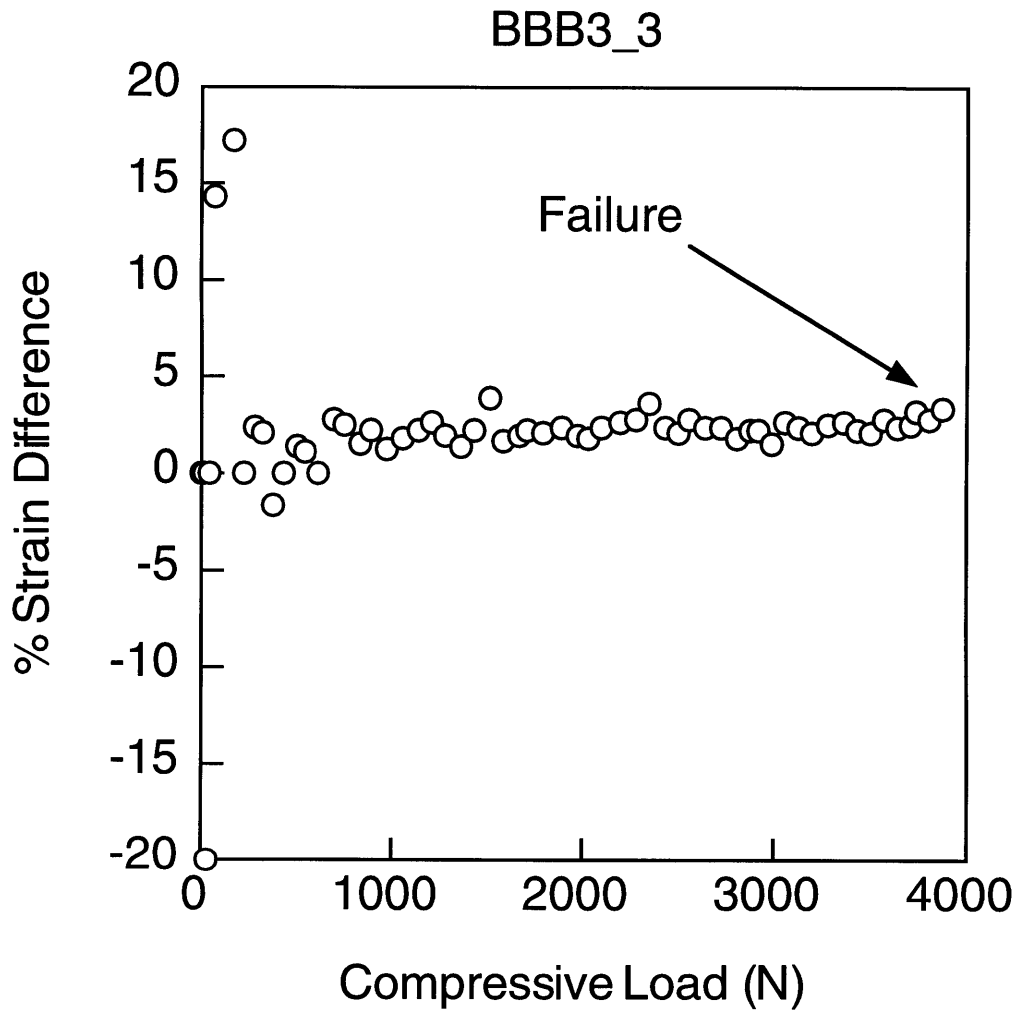
Figure 5.1 Typical data showing excellent alignment throughout the entire test.

self-aligning platen also contributed significantly to sudden alignment changes in the initial region.

After the initial loading period, the alignment was generally characterized by values below 5% up to failure. Some specimens had alignment worse than 5%, but in all cases better than 10%. This second region occasionally exhibited a discontinuity in alignment due to manual adjustment of the platen, as shown in figure 5.2. In these cases, the adjustment was made in order to improve the alignment.

The alignment response was also characterized by a third region in some cases. This part of the curve was associated with the final part of an experiment, after an LDZ had initiated. The load and alignment in this region changed significantly. Typically, the load decreased and the alignment changed, as shown in figure 5.3. However, the alignment generally remained better than 5% in the LDZ propagation regime.

A representative stress-strain plot for M4 and M5 materials is shown in figures 5.4 and 5.5, respectively. On each plot, the front and back facesheet response deviated slightly indicating the development of bending deformations. The average modulus for both materials was approximately 22.1 GPa.

The macroscopic LDZ behavior was characterized by three phenomena: initiation, stable propagation, and catastrophic propagation, as described below. *Failure* is defined as the load at which catastrophic LDZ propagation occurs. Table 5.1 lists both the LDZ initiation and failure loads along with the average values and coefficients of variation. In all but two tests, the failure load was greater than the initiation load. Figures 5.6 and 5.7 illustrate the effect of panel size on the failure stress for M4 and M5 materials, respectively. Figures 5.8 and 5.9 show the failure stress correlations with predicted values for M4 and M5 materials, respectively. The predictions are based on both

AAA4_2
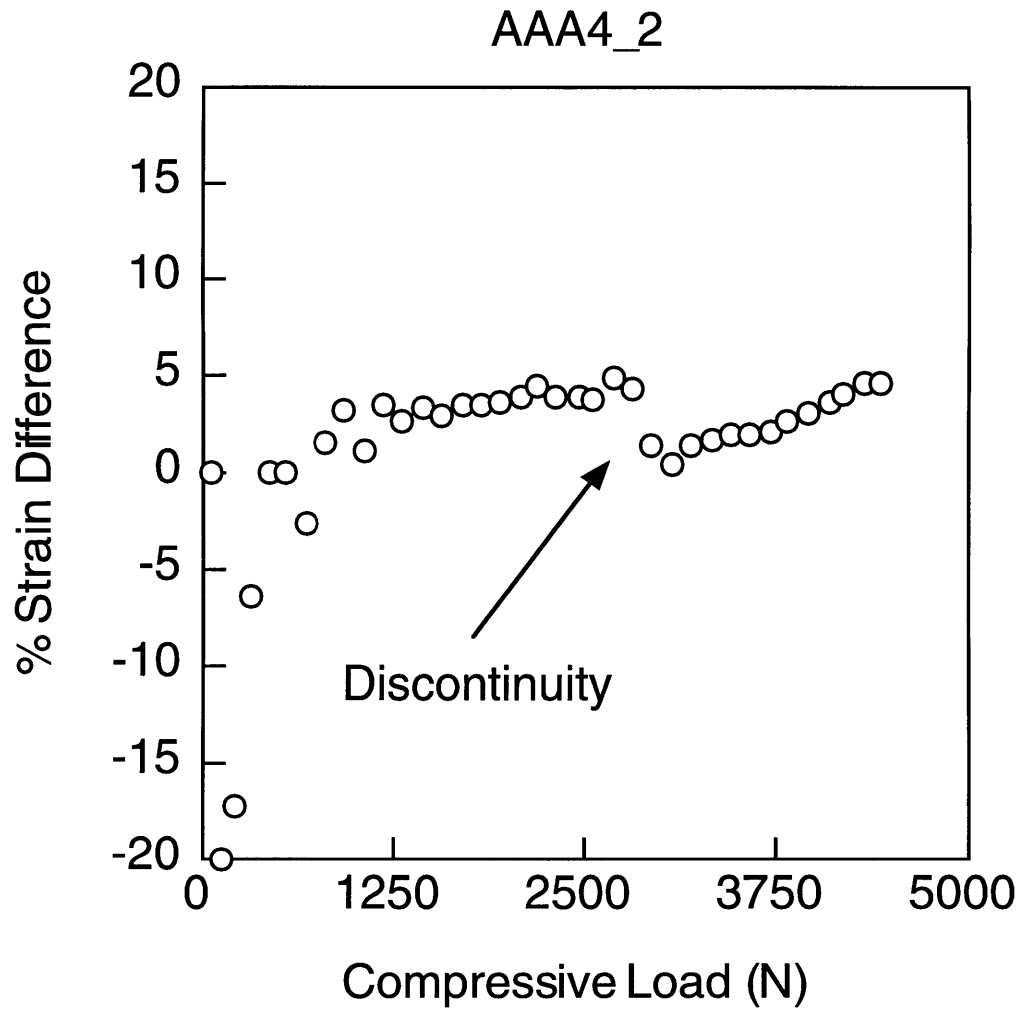
Figure 5.2   Alignment data showing sharp discontinuity resulting from manual adjustment of upper platen.
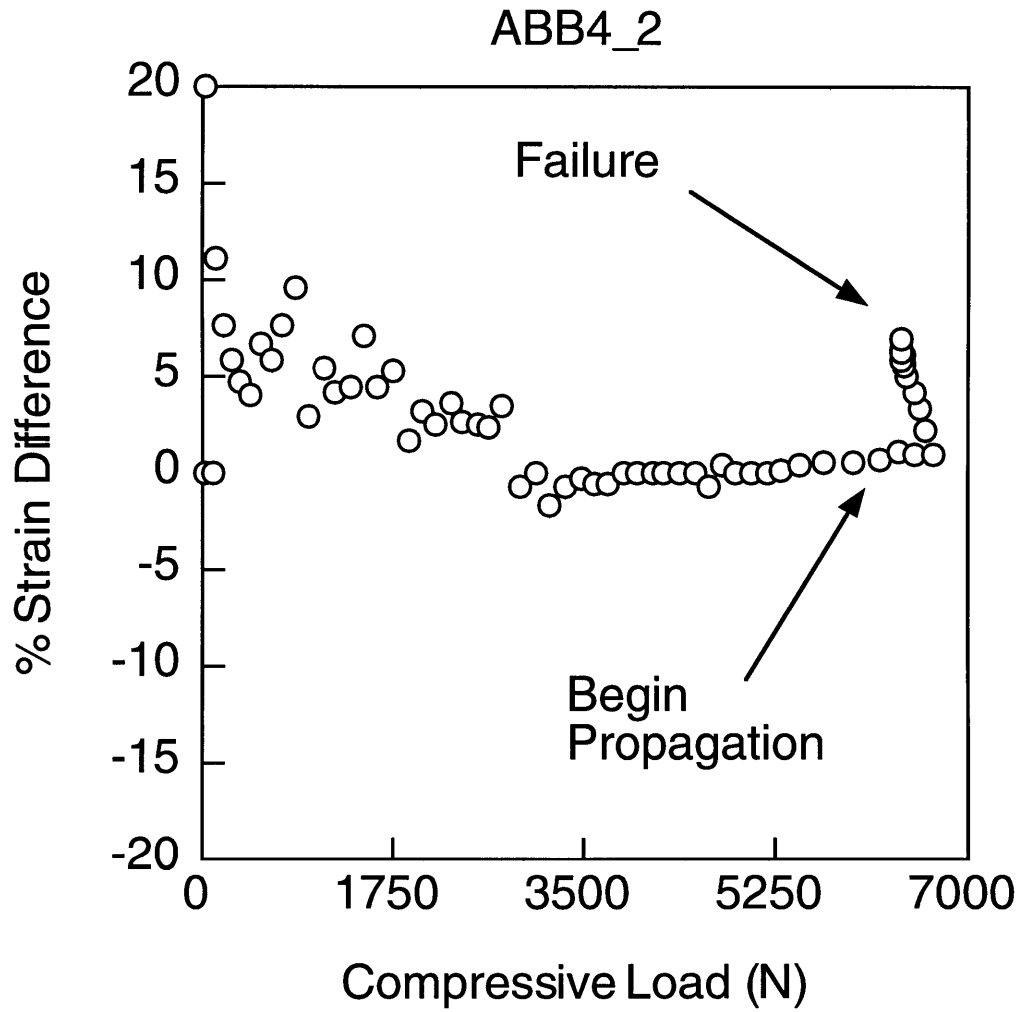
Figure 5.3   LDZ propagation effect on alignment found on some specimens.

——y = -1.1019 + 22330x R= 0.99979

- - - - -y = -0.010973 + 21545x R= 0.99957
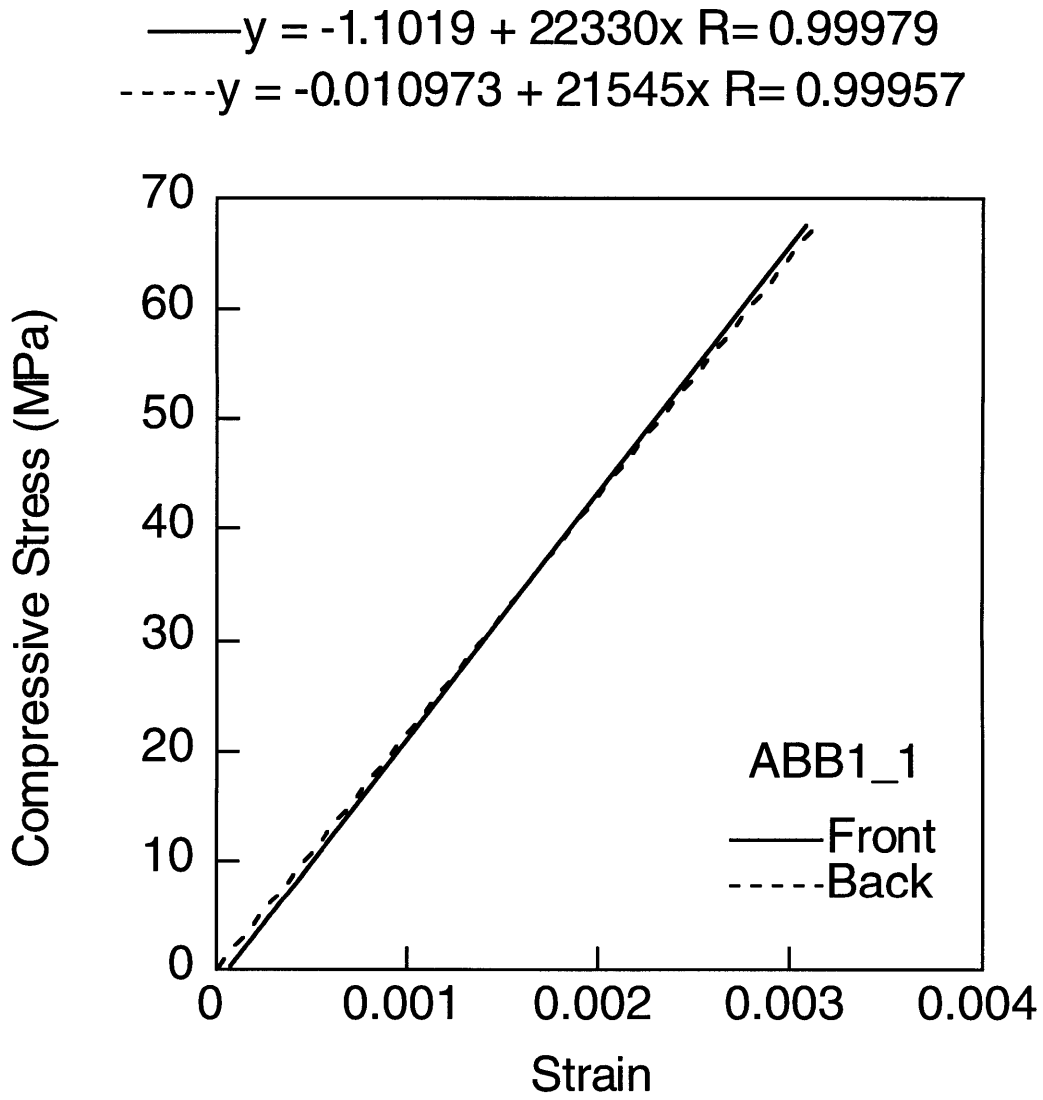
Figure 5.4   Typical stress-strain behavior for M4 specimens.

——y = 1.2009 + 22762x R= 0.99923
-----y = 0.56064 + 23067x R= 0.99981
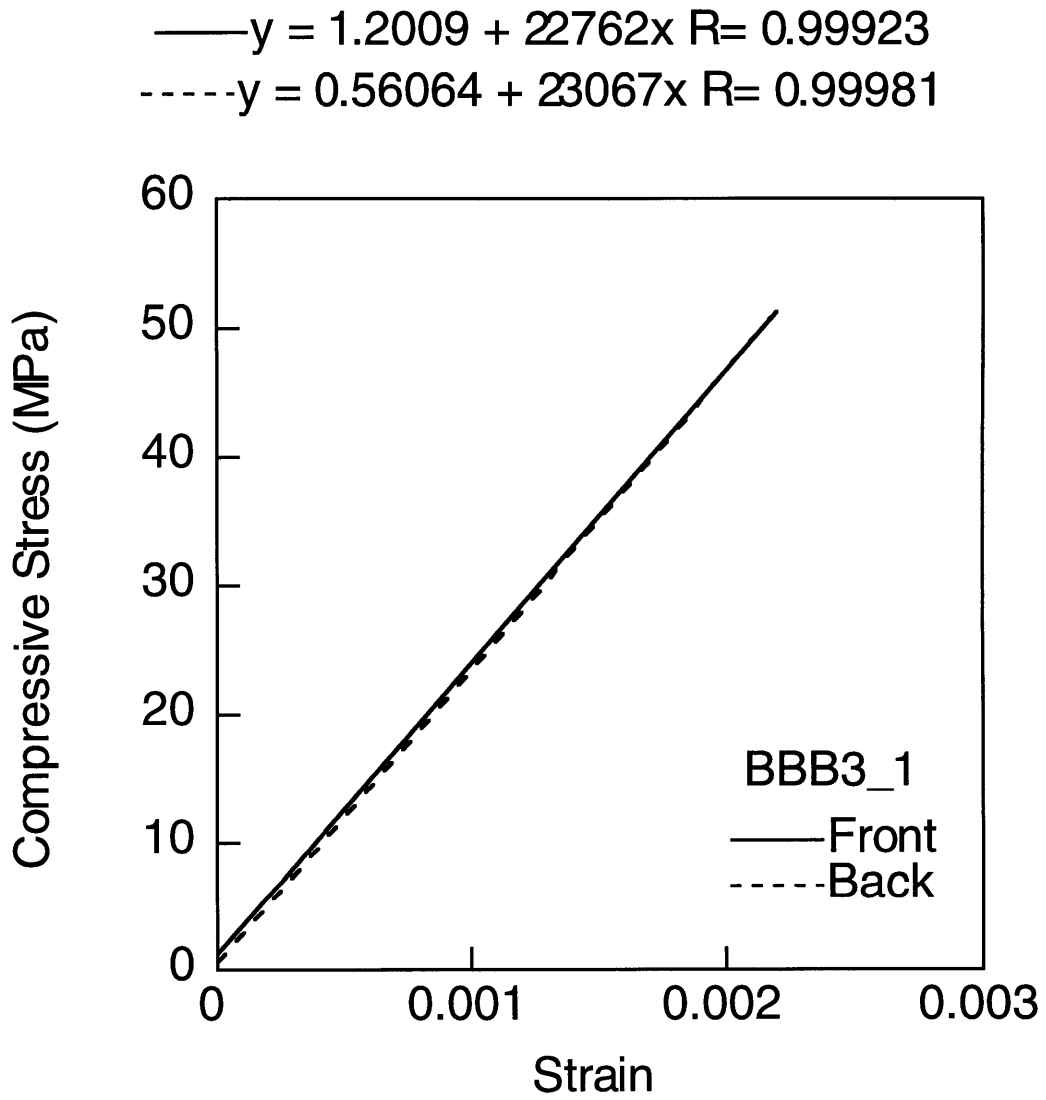
Figure 5.5   Typical stress-strain behavior for M5 specimens.

Table 5.1   Facesheet Initiation and Failure Loads

		Facesheet Loads (N)				
Panel	Initiation	Average	C. V.	Failure	Average	C. V.
AAA1	2038	2100	0.0637	2046	2135	0.0620
AAA2	2046			2055		
AAA3	2300			2329		
AAA4	2017			2108		
ABB1	3269	3279	0.0902	3332	3298	0.0316
ABB2	3696			3354		
ABB3	3023			3363		
ABB4	3127			3143		
ADC1	6781	6575	0.0444	6348	6642	0.0627
ADC2	6368			6937		
BAA1	856	926	0.0856	1359	1211	0.1074
BAA2	861			1158		
BAA3	1012			†		
BAA4	974			1115		
BBB1	1653	1578	0.0566	†	1962	0.0086
BBB3	1601			1951		
BBB4	1479			1974		
BDC1	2836	2889	0.0259	3118	3112	0.0030
BDC2	2942			3105		

†   Cross-sectioned after LDZ initiation
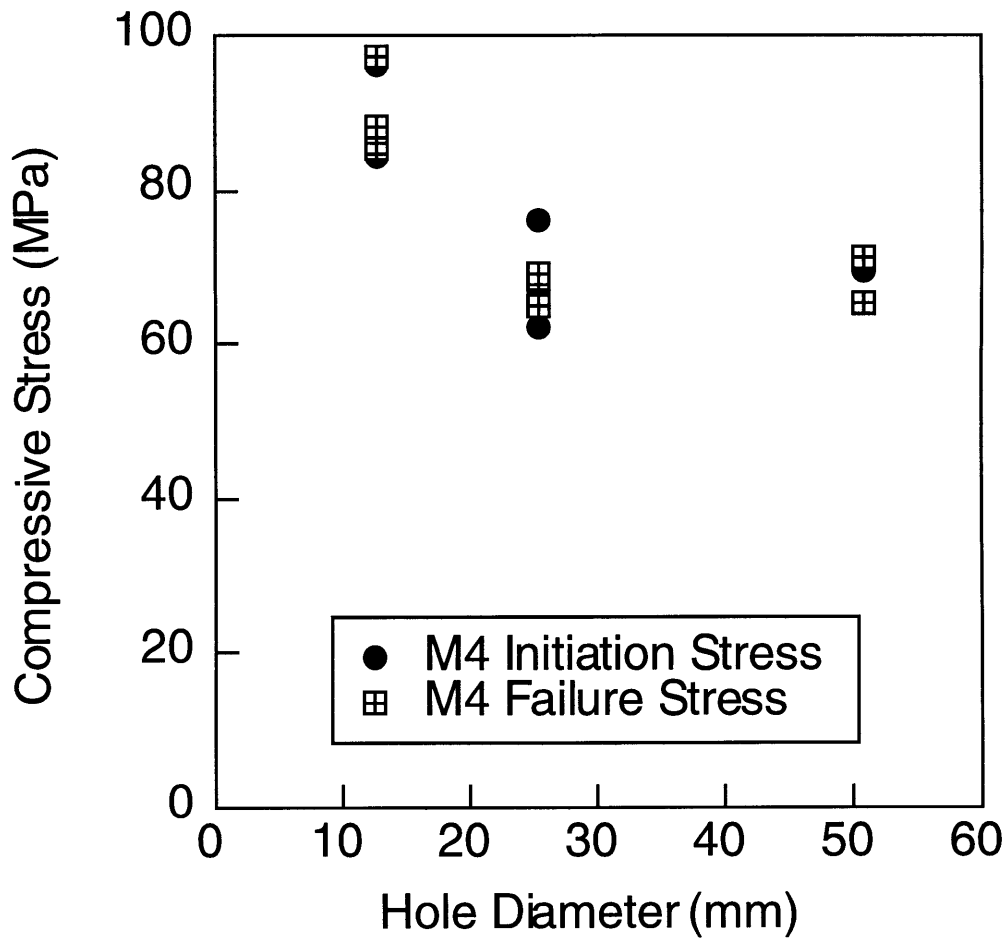
Figure 5.6   Failure stress versus notch size for M4 specimens.
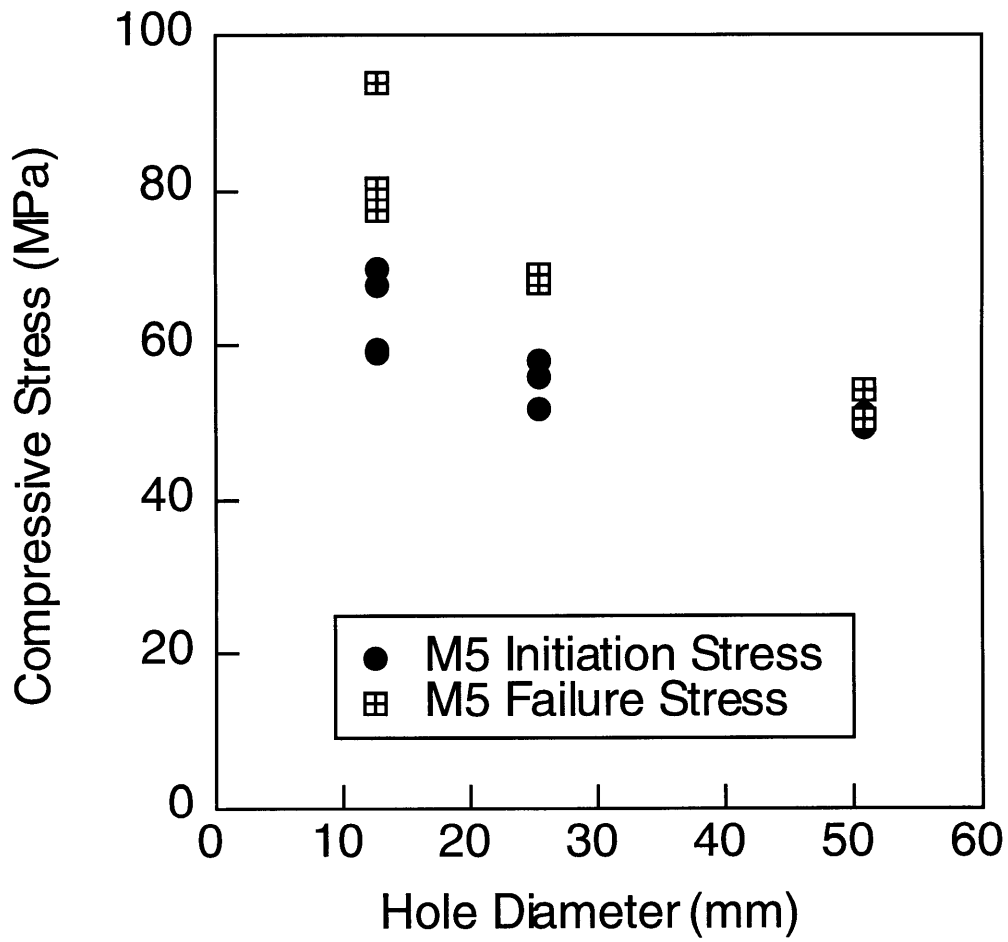
Figure 5.7   Failure stress versus notch size for M5 specimens.
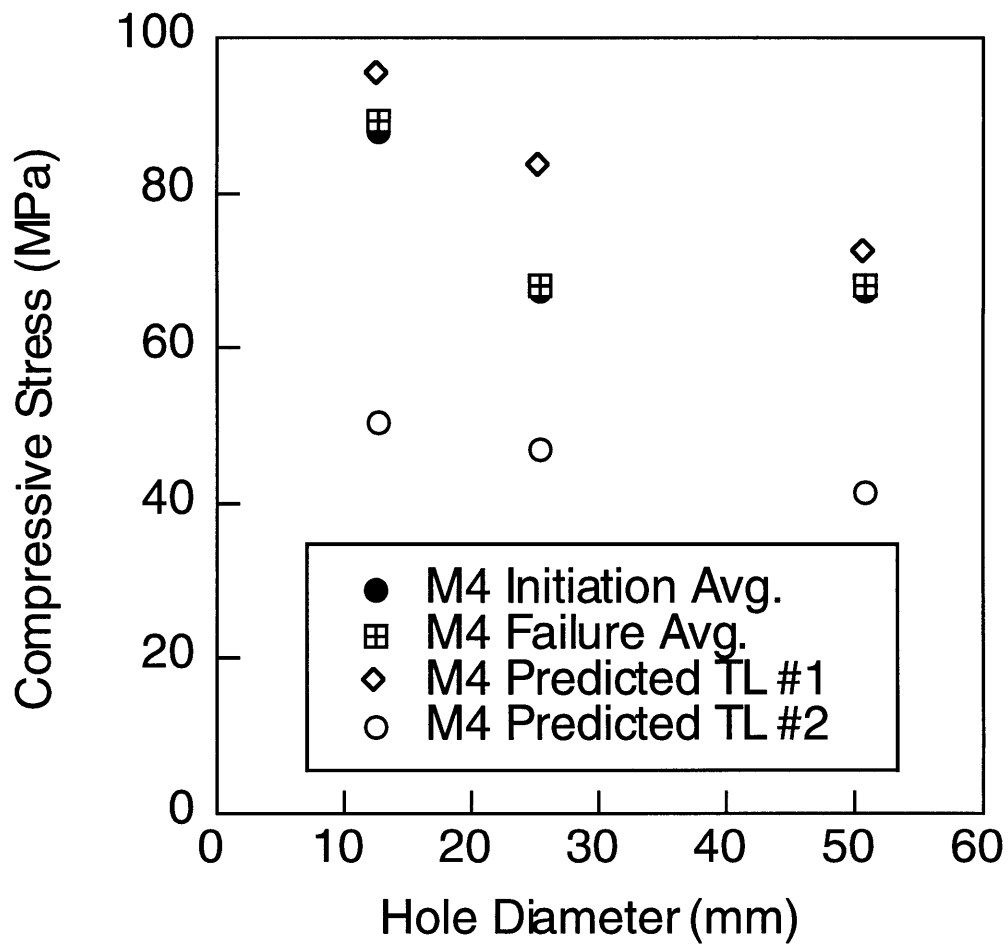
Figure 5.8   M4 average initiation and failure stresses and predicted failure
stresses versus notch size for both traction laws.
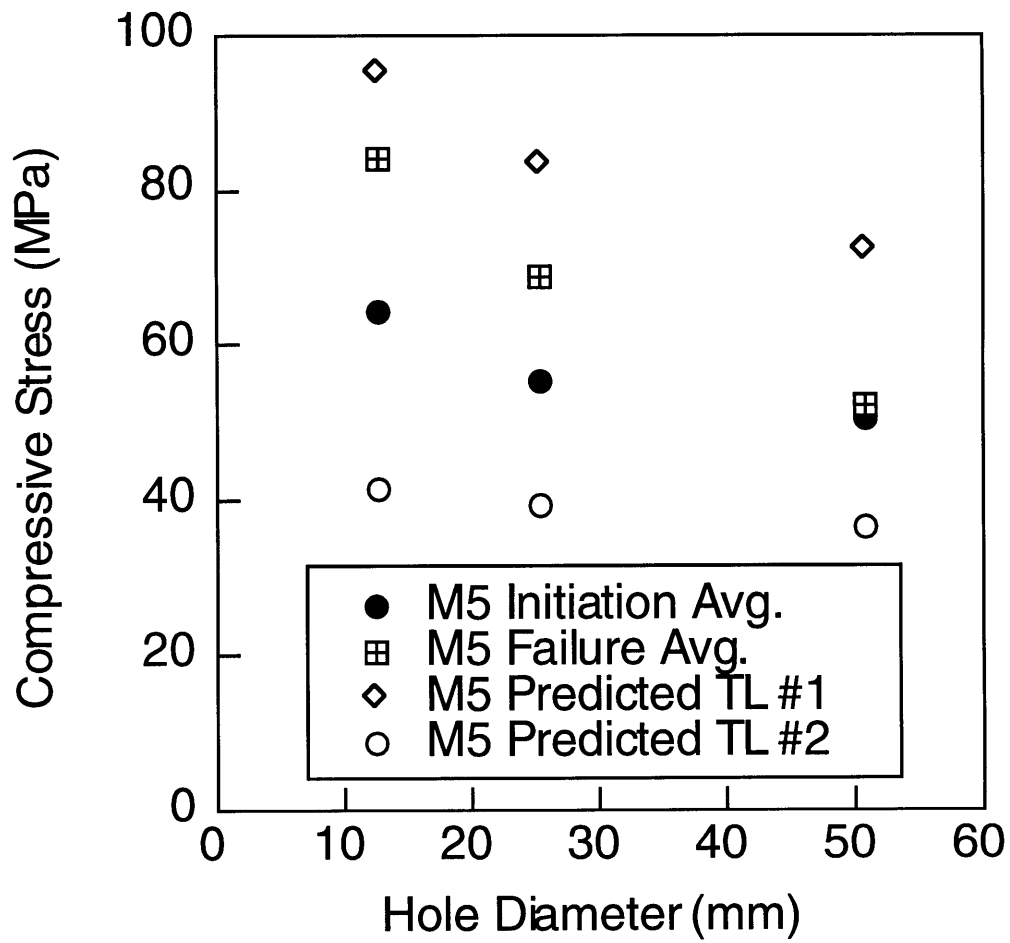
Figure 5.9   M5 average initiation and failure stresses and predicted failure stresses versus notch size for both traction laws.

traction laws. The experiments reflected the widely observed "hole size effect" [118]. Both the initiation and failure stresses decreased as the hole size increased.

5.1.2 Local Behavior

Local strain gages were used to measure the load carrying capability of the LDZ. In both M4 and M5 specimens, the local strain measurements indicated a behavior characteristic of a *softening* material. Figures 5.10-5.14 are representative plots of the variation in local strain behavior with LDZ growth for different specimen sizes from M4 and M5 materials. All specimens that exhibited LDZ growth past the "shadow" of a local gage were characterized by a similar trend. Those specimens which did not display significant LDZ growth prior to failure were characterized by rising local strain behavior only.

As the tip of the LDZ approached the shadow of a local gage, indicated by dashed lines in figures 5.10-5.14, the strain measured by that gage increased. A maximum strain was measured when the LDZ tip was in a location approximately under the gage (directly in the shadow). As the LDZ propagated further towards the edge of the facesheet, the LDZ tip moved away from the shadow of the gage. In all tests where the LDZ propagated past the shadow of a gage, the measured strain decreased with further LDZ extension. Once the tip had propagated away from the shadow of a strain gage, the measured strain reflected the load carrying characteristics of the LDZ *wake*. The data, especially that for the large specimens which exhibited longer LDZs, show that the LDZ wake was able to retain significant load carrying capability until failure.

Figure 5.10   Strain softening local behavior in ABB4.
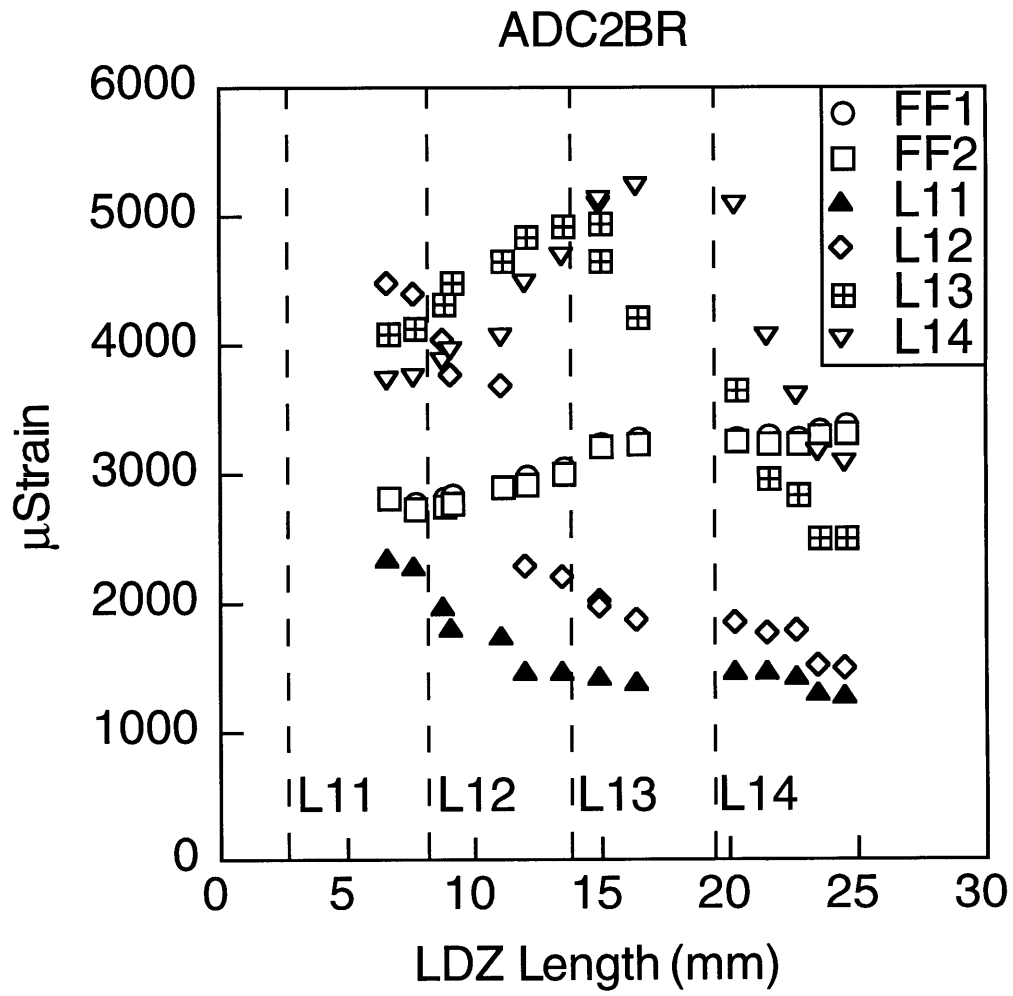
Figure 5.11   Strain softening local behavior in ADC2.
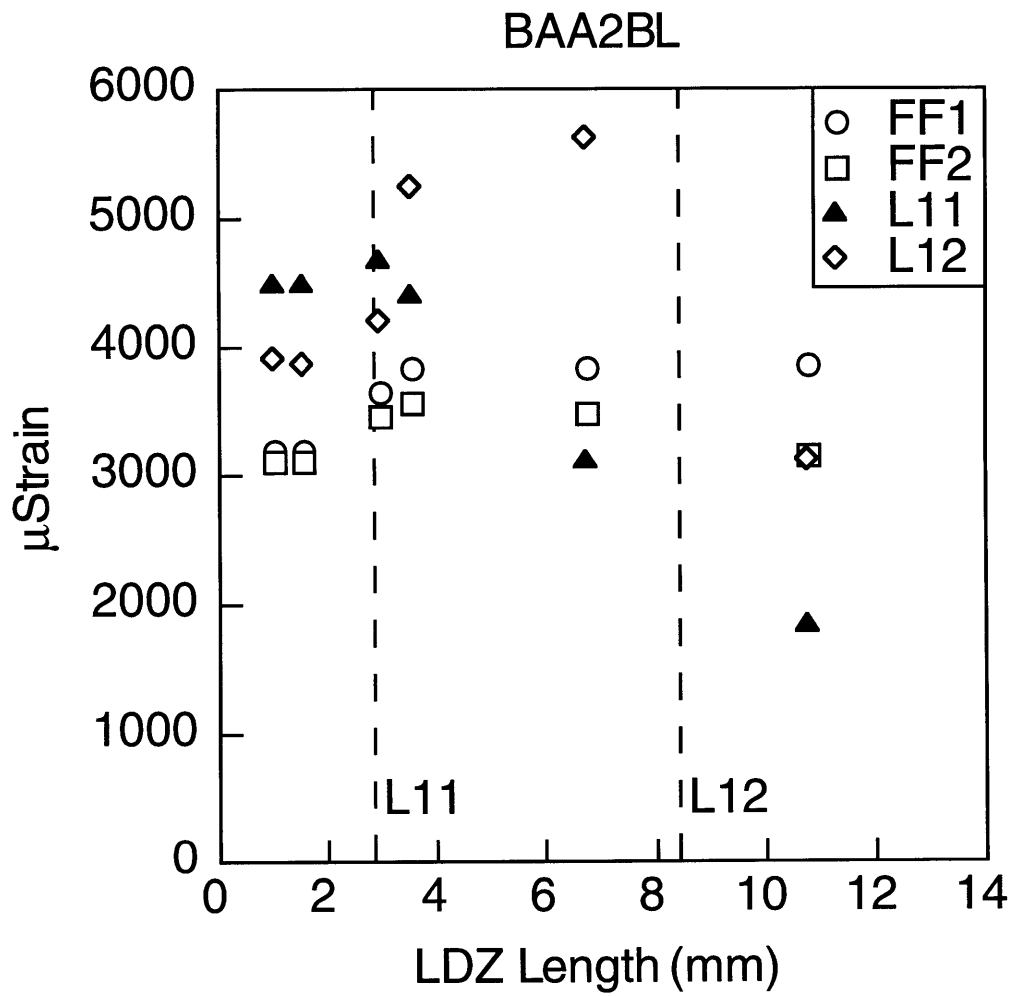
Figure 5.12   Strain softening local behavior in BAA2.
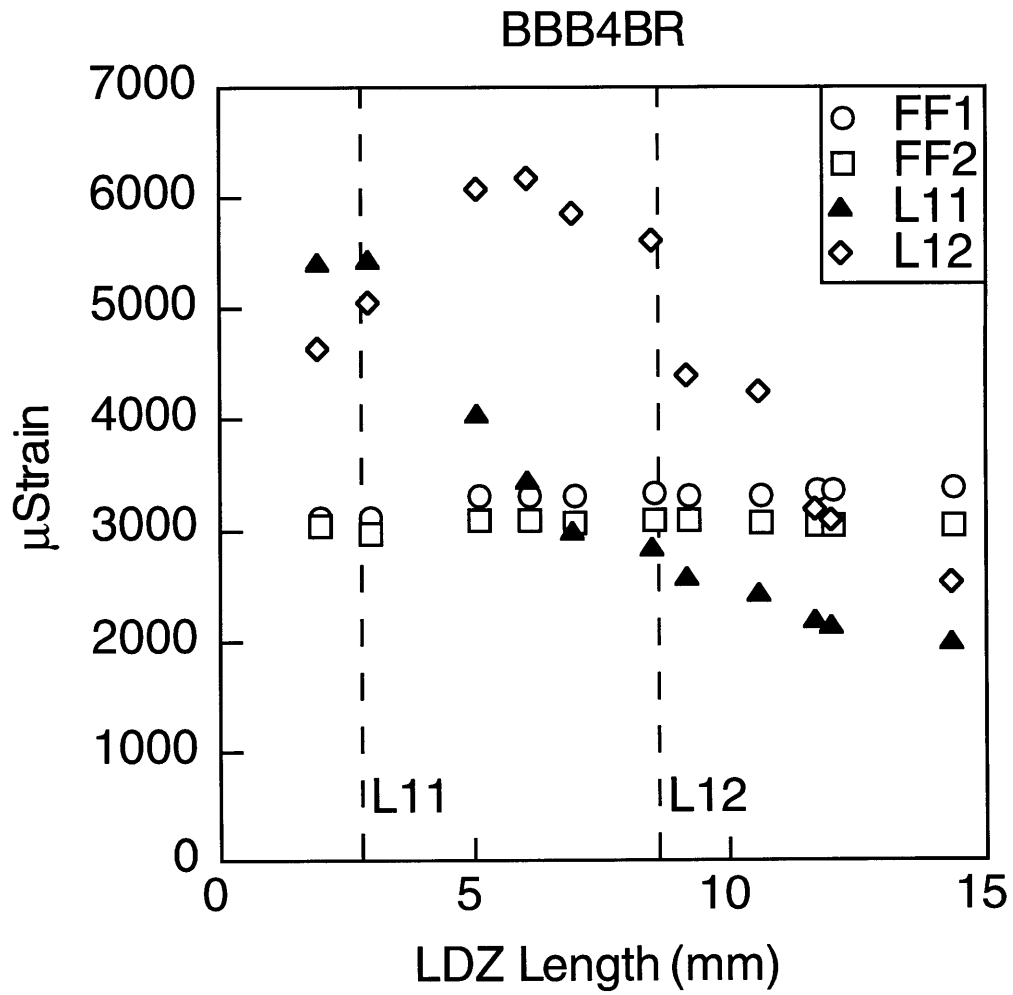
Figure 5.13   Strain softening local behavior in BBB4.
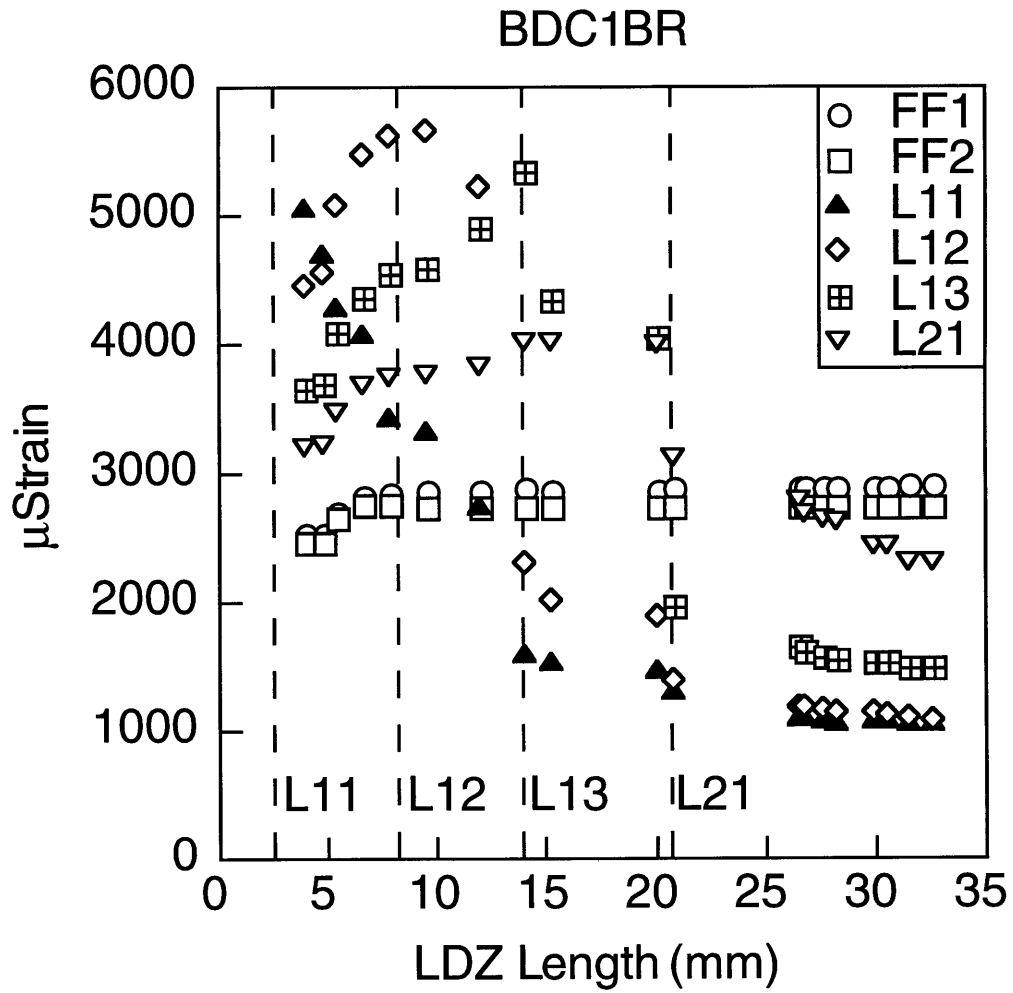
Figure 5.14   Strain softening local behavior in BDC1.

5.2   Damage Characterization

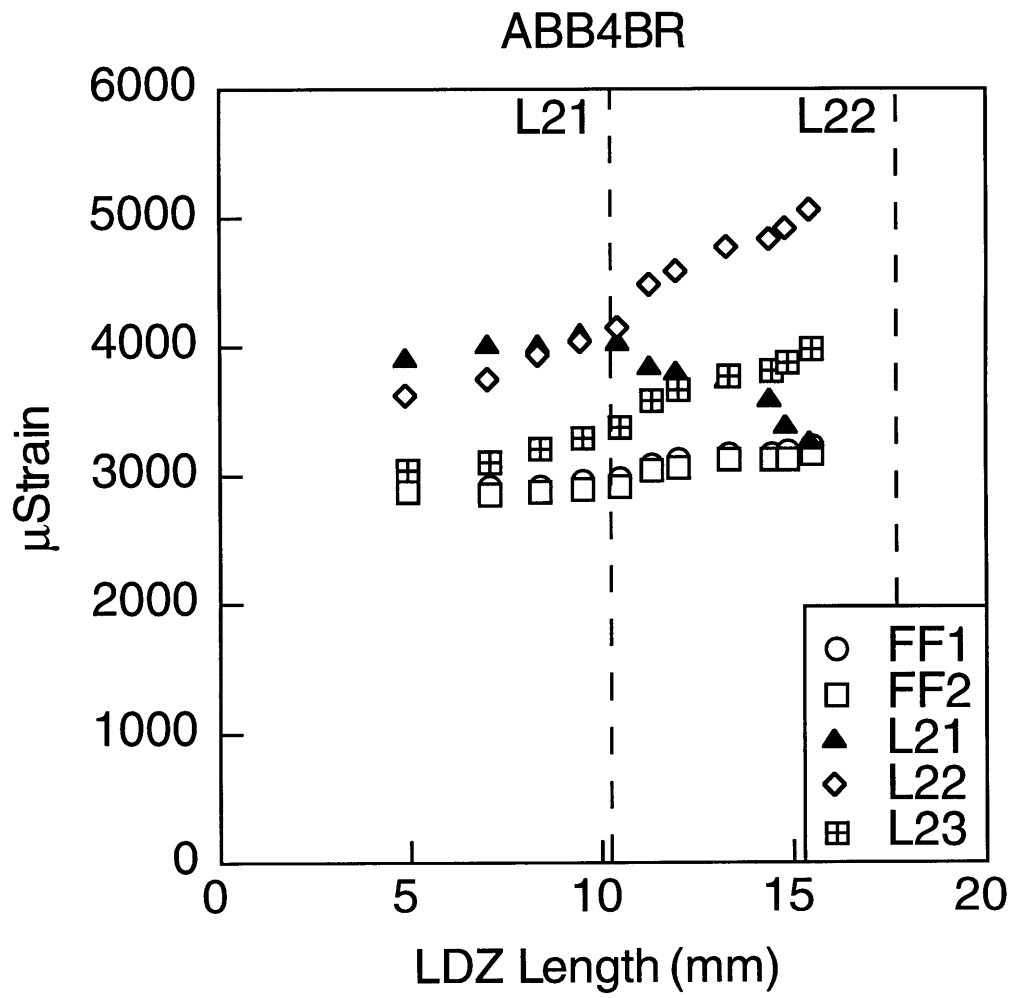This section presents observed LDZ characteristics.   First, the macroscopic behavior is reported.   Second, the microscopic behavior observed from the cross-sectioning study is presented.

5.2.1 Macroscopic Behavior

Linear damage zones were the only damage mechanisms visible to the naked eye.   LDZs initiated in the facesheets at the horizontal edges of the holes.   Up to four LDZs initiated and propagated on one specimen.   No bias was observed regarding which facesheet (smooth or rough) tended to fail by LDZ propagation.   Only one facesheet failed catastrophically.   Typically, LDZs initiated in one facesheet, but in limited cases both facesheets became damaged.   Regardless of how many LDZs initated, only one facesheet failed.

Failure was always characterized by LDZs instantaneously traversing the net-section of one facesheet.   In these cases, stable propagation was not observed, since the propagation occurred very fast.   If the front facesheet was the side that failed, the state of the back facesheet after failure was dependent on any pre-failure damage that had accumulated in the back facesheet.   Two possibilities existed.   If the back facesheet was undamaged up to failure, then it remained undamaged after the front facesheet failed.   If LDZs initiated on the back facesheet prior to failure, then the back facesheet was characterized by LDZs of finite width after failure.   Observations never confirmed that LDZs initiated as a result of post-failure end-shortening.

LDZs appeared as linear regions on the facesheet characterized by an off-white color.   Figure 5.15 shows a typical low magnification view of an LDZ.   This photograph was taken during preliminary testing of a panel with a slit
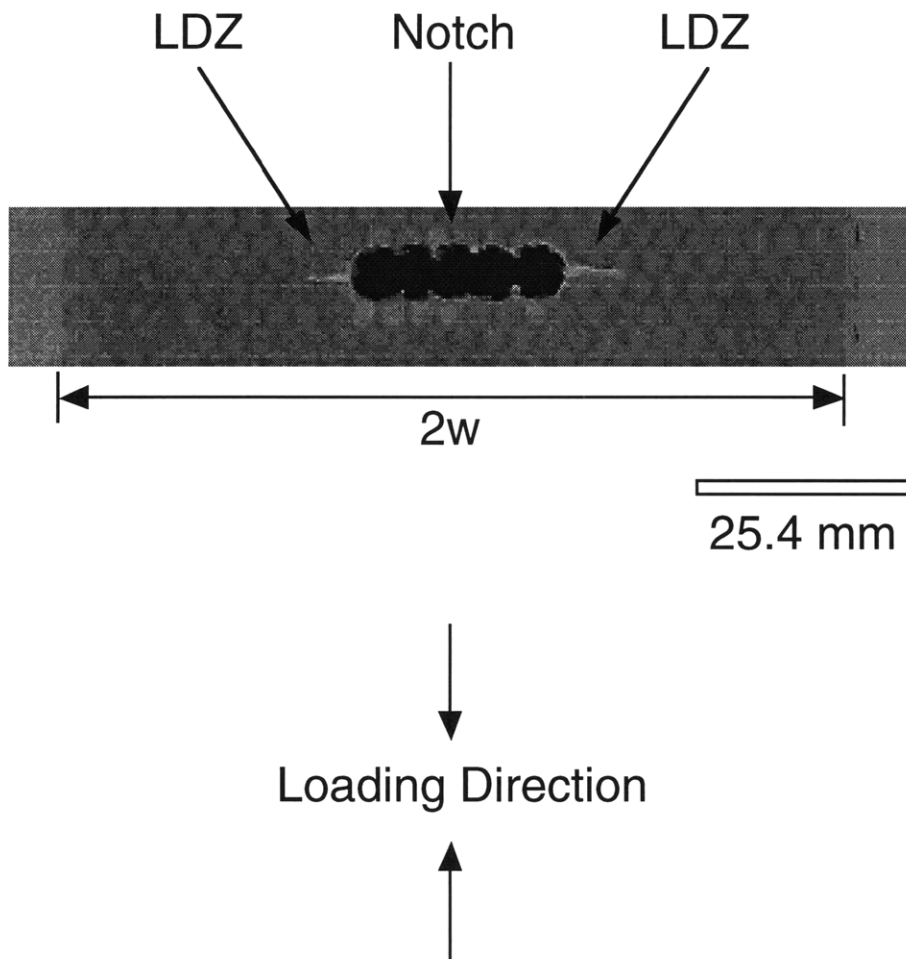
Figure 5.15   LDZs that initiated at notch tips propagating in a direction perpendicular to the applied load.

instead of a circular hole. With further end-shortening, the LDZ propagated in a series of stable increments. Figures 5.16 and 5.17 show photographs taken at different times during LDZ propagation on BDC1BR. The pen marks on the facesheet allude to the *semi-stable* incremental propagation behavior of the LDZ.

Usually, the speed at which the LDZ propagated to a new length was nearly instantaneous. Some increments of growth, however, occurred in a *steady state* manner; i.e. the propagation to a new length occurred via a continuous, stable propagation, at a slow speed compared to the usual very rapid increments. The amount of continuous propagation was very limited, and did not occur in all specimens. No measurements were taken of propagation velocity for either the semi-stable or stable propagation.

LDZ propagation in a facesheet generally occurred at near constant loads. However, some load variation was observed. Initiation loads were found to be both lower and higher than propagation loads. Usually, initiation loads were less than propagation loads. For example, figure 5.18 shows that the LDZ initiated at the lowest load. Higher loads were needed for propagation, but propagation occurred at approximately the same load. In a few cases, LDZ growth behavior initiated at a relatively high load, as shown in figure 5.19. Further propagation occurred at loads less than the initiation load. As in figure 5.18, propagation seemed to occur at approximately constant load.

5.2.2 Micromechanisms

The only damage which occurred as a result of compressive loading was contained within the linear damage zones. This was verified with the use of dye-penetrant enhanced X-radiography (refer to figure 3.9). The cross-sectioning technique was used to determine the microscopic damage

1. 5.76 kN

2. 6.15 kN

5.6 mm

3. 6.17 kN

4. 6.81 kN

Loading Direction
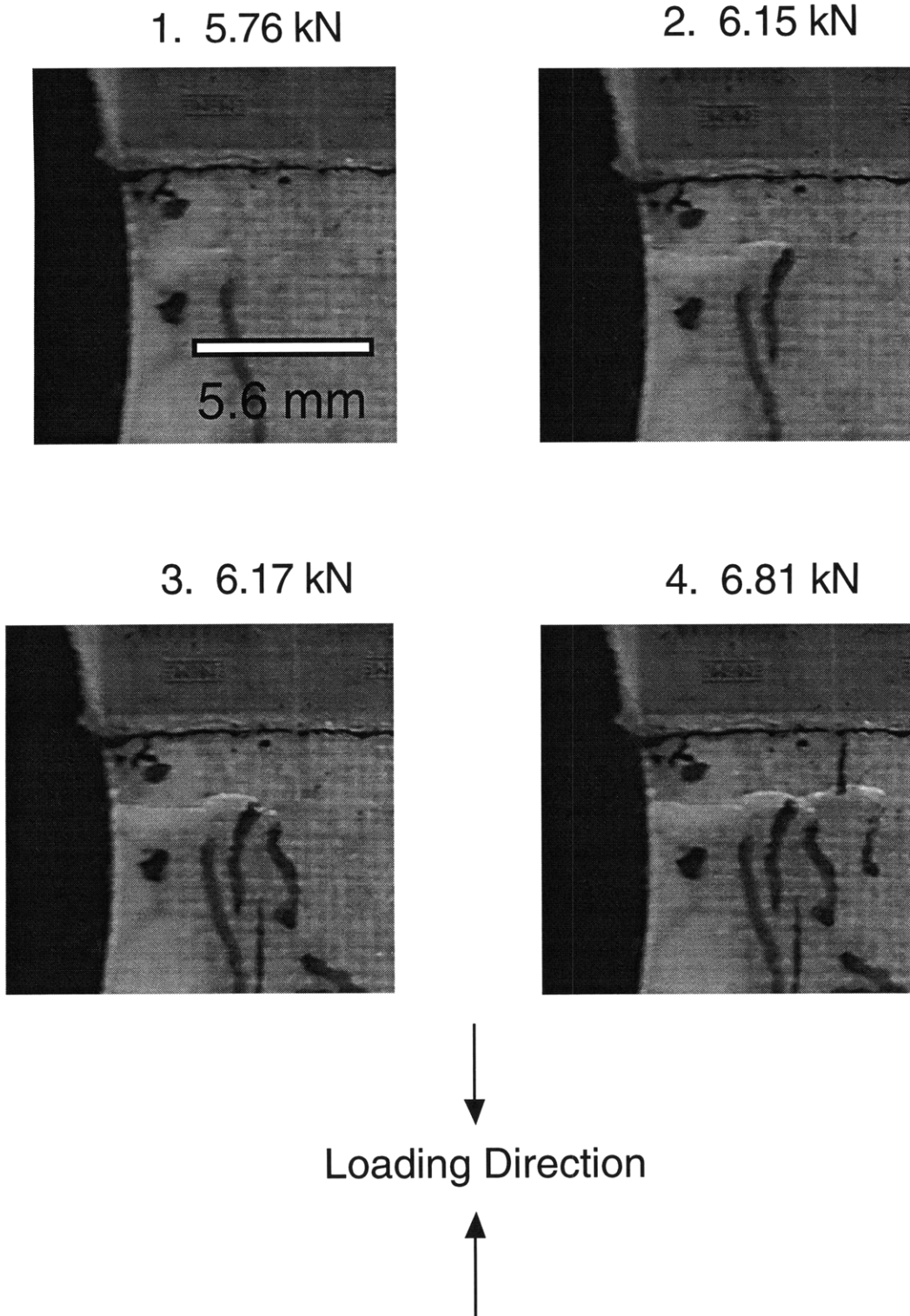
Figure 5.16   LDZ progression (1 of 2).
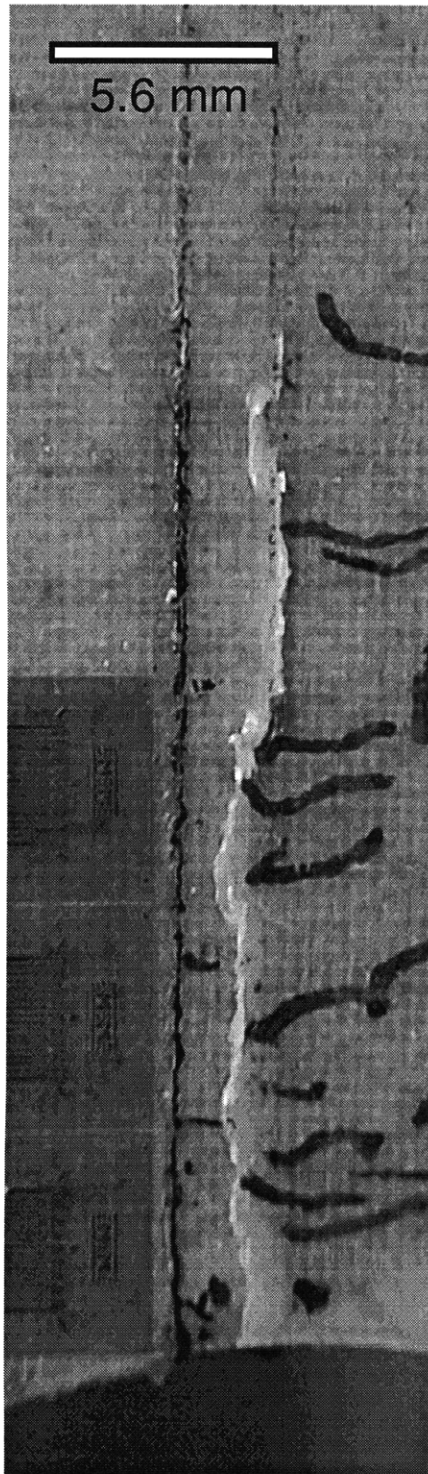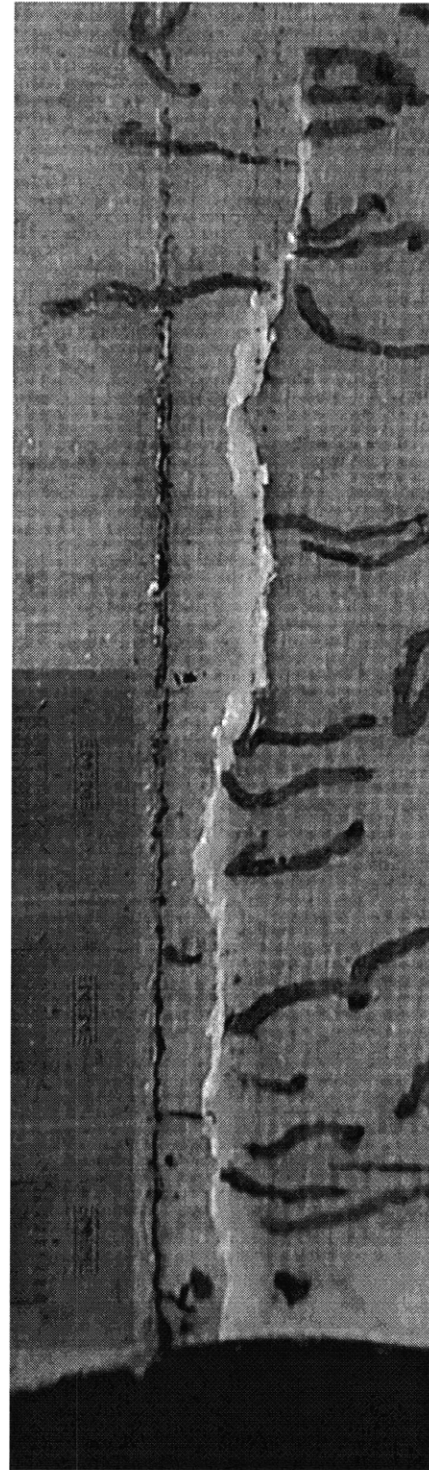
5. 6.73 kN   6. 6.71 kN

Figure 5.17   LDZ progression (2 of 2).
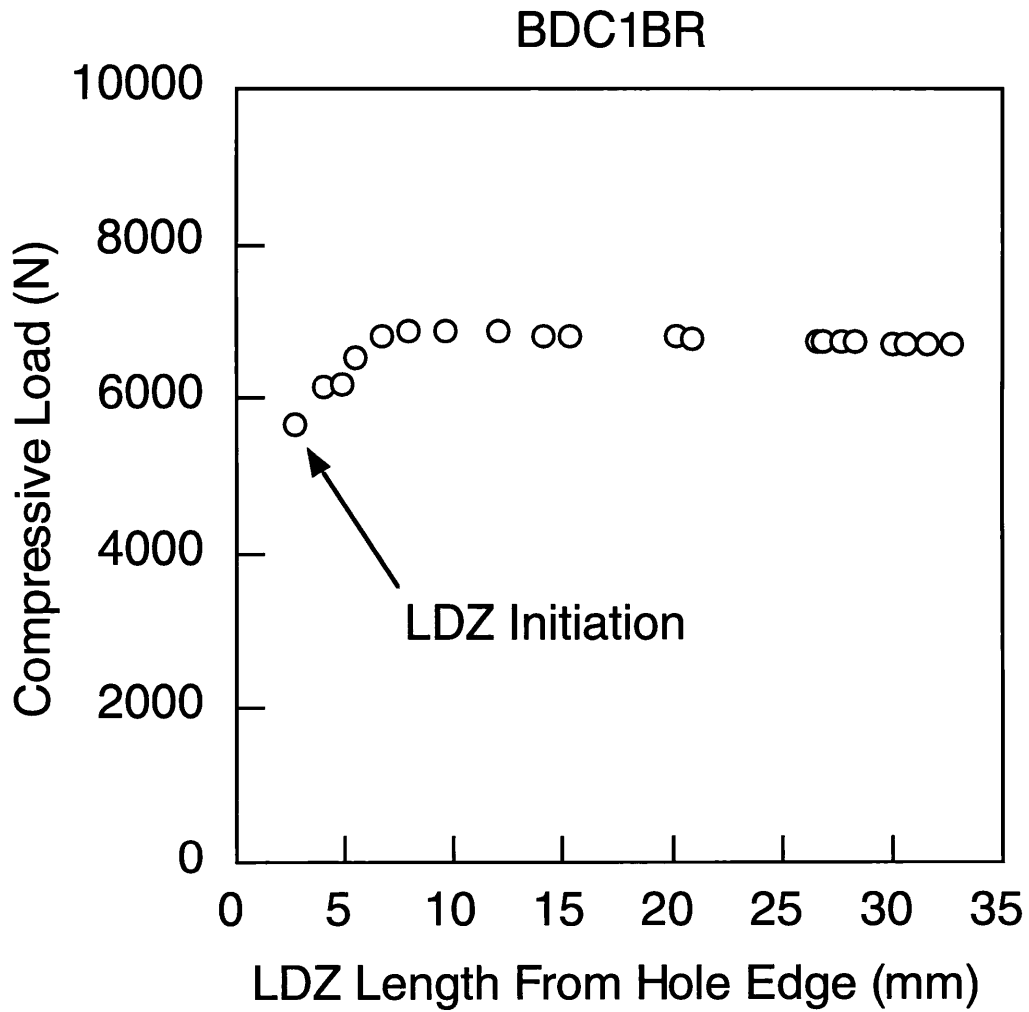
Figure 5.18   LDZ propagation data indicating an initial regime characterized by toughening, after which propagation occurred at a slightly decreasing load.

ADC2BR

LDZ Initiation

Compressive Load (N)

LDZ Length From Hole Edge (mm)
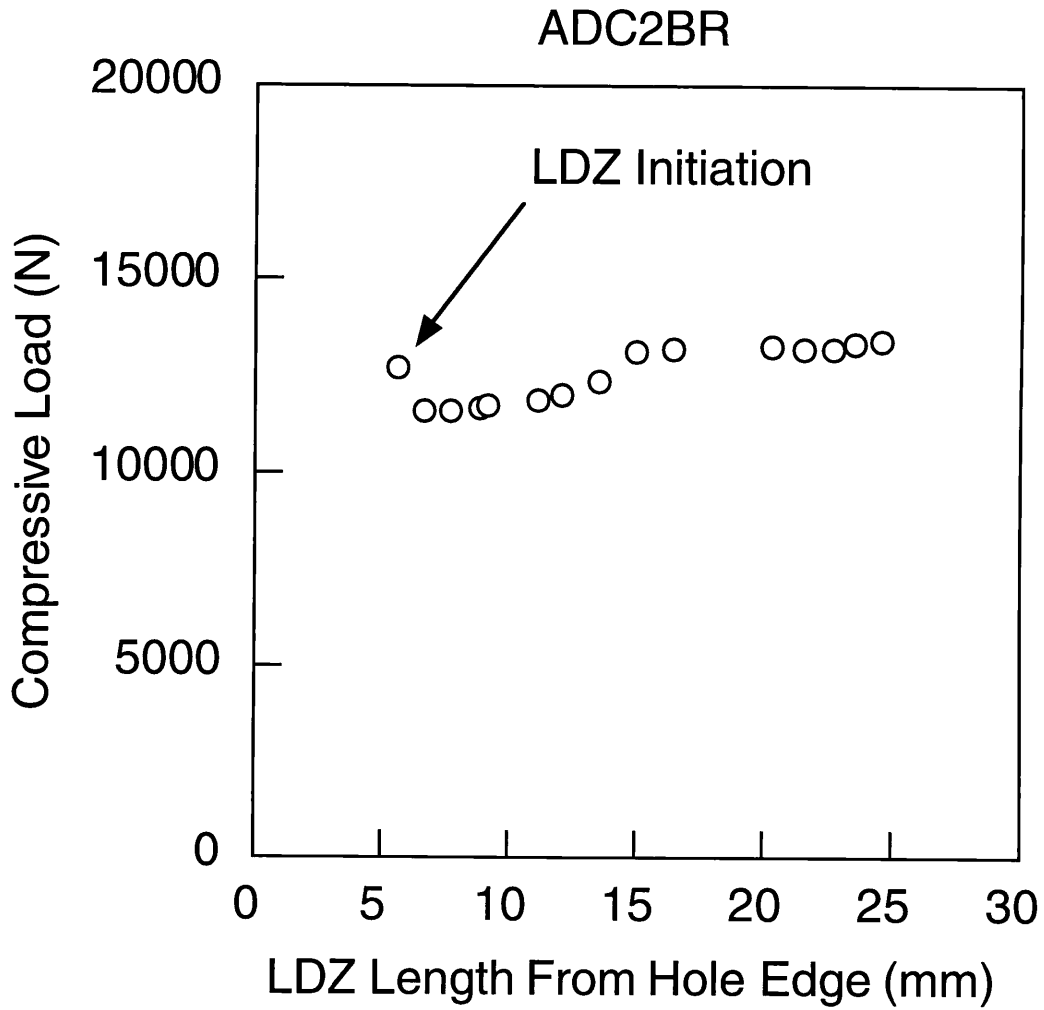
Figure 5.19 LDZ propagation data indicating a relatively high initiation load. The subsequent propagation regime is characterized by an increasing load.

mechanisms operating within the LDZ. LDZs which had not propagated across the full ligament were cut out of the facesheet and examined with the cross-sectioning technique.

It was found that only certain cross-sectioning views resulted in useful images of the micromechanisms. Therefore, after preliminary cross-sections, only the right and left views were used (front and back LL, LR, RR, RL, as shown in figure 3.10).

The key compressive micromechanisms were found to be warp fiber and warp tow microbuckling and weft tow splitting in both M4 and M5 materials (refer to figure 2.1 for schematics of microbuckling behaviors and angle definitions). Figure 5.20 shows damage near the tip of an LDZ in an M5 facesheet. Individual warp tow fiber microbuckling (as opposed to microbuckling of all warp tow fibers) in the out-of-plane direction was the only damage present at the tip of the damage zone. Only one of the three warp tows were affected. Two of the three are shown because the third tow has not yet appeared. Fiber microbuckling was only observed at the tips of LDZs in M5 materials.

Warp tow fiber microbuckling led to out-of-plane warp tow kinking of the same tow and kinking of other warp tows. Figure 5.21 shows a cross-section behind the LDZ tip in an M5 facesheet. Kinking of the initially microbuckled tow, along with out-of-plane warp tow microbuckling of a second tow are evident. No damage is evident in the third ply. Figure 5.22 shows the same type of phenomena in an M4 facesheet. The subsurface ply was damaged by warp tow kinking, while the surface ply was undamaged at this location. Figure 5.23 is another example of warp tow kinking in an M5 facesheet. In this case the surface ply was damaged while the subsurface ply remained undamaged. However, the cross-section shows that two of the three warp

BDC1 FRR

Buckle

0.284 mm

Figure 5.20   Cross-section showing individual warp tow fiber microbuckling
in subsurface warp tow near LDZ tip.
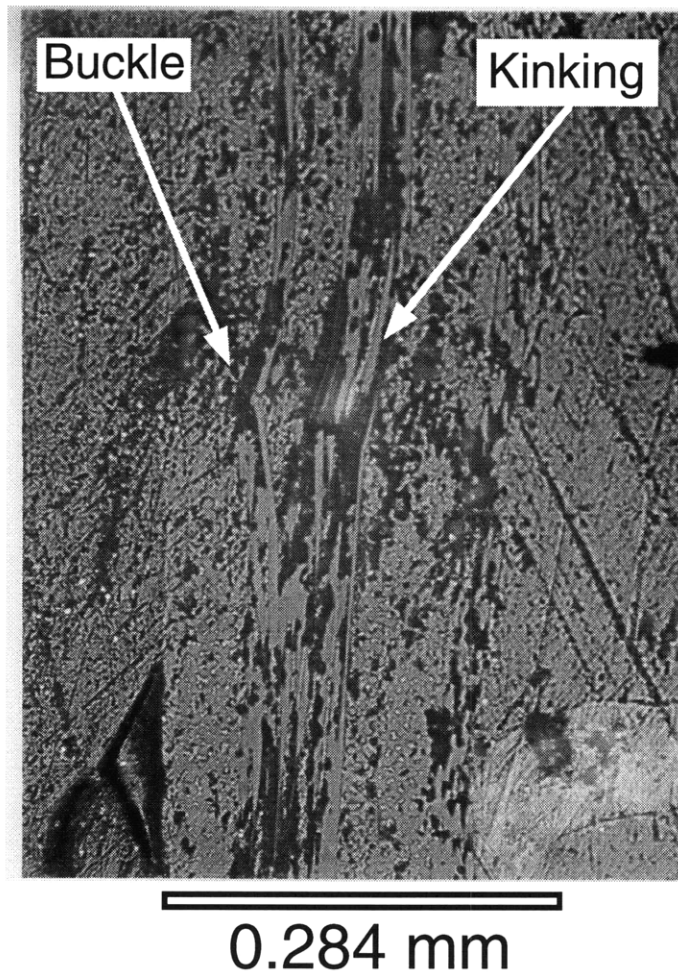
Figure 5.21   Cross-section showing warp tow microbuckling and kinking.

Figure 5.22   Cross-section showing warp tow kinking in subsurface ply.

BAA3 BLR

Kinking

0.284 mm
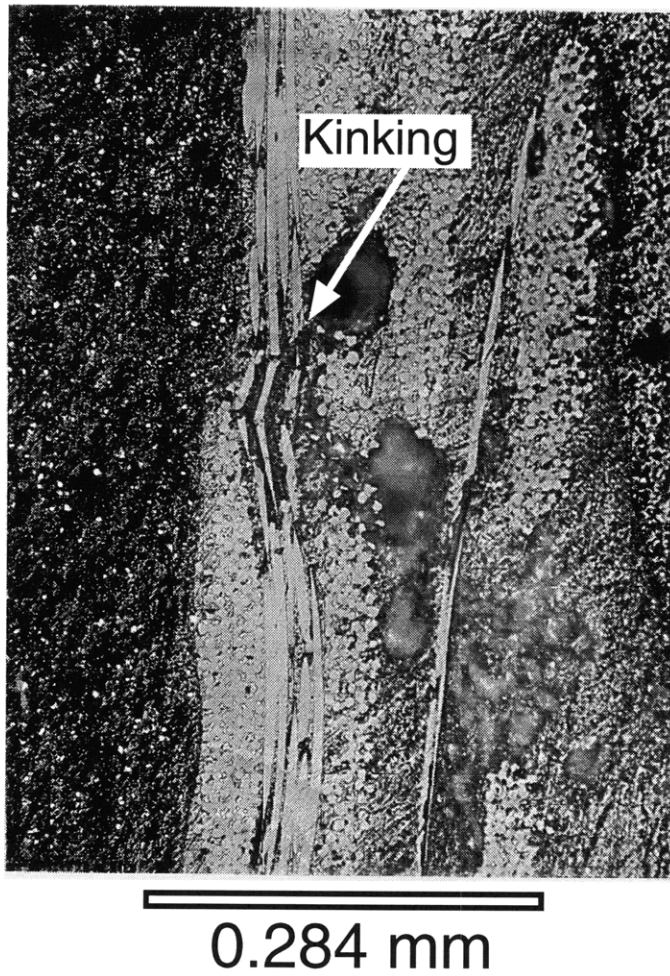
Figure 5.23   Cross-section showing shear crippling of surface ply.

tows are apparently missing, an important feature regarding cross-sectioning of woven laminates. Although neighboring tows (in this case warp tows) are generally side-by-side, distinct gaps between neighboring tows are quite common. Therefore, it was often very difficult in determining if specific micromechanisms terminated at the end of one tow or in the middle of two adjacent tows. Furthermore, figure 5.23 illustrates the possible ambiguity arising from the voids created by the grinding process. Voids were impossible to avoid, and may have hidden damage mechanisms.

Once shear crippling of one warp tow had occurred, out-of-plane kinking of the remaining warp tows followed. Figure 5.24 shows kinking in all three warp tows in an M5 facesheet. This cross-section was from a location further behind the LDZ tip. No other damage mechanisms were found behind the LDZ tip other than warp tow kinking in M5 materials (via the cross-sectioning technique).

The cross-sections also revealed weft tow splitting in M4 facesheets. This damage mechanism was found behind the LDZ tip, and was generally present when both warp tows had kinked. Figure 5.25 shows kinking in both warp tows, along with weft tow splitting. The *split line* was not straight in this case. Typically, splitting occurred on a line connecting the kink bands.

More severe kinking occurred as LDZs propagated to longer lengths, as shown for an M4 facesheet in figure 5.26. This picture of the LDZ root was taken prior to mounting the specimen in epoxy. Since greater loads and higher end displacements led to higher degrees of fiber rotation, characteristic kink band rotation angles varied. In fact, in some cases these angles varied for kink bands in different warp tows at the same location along the LDZ. Furthermore, significant relaxation was observed during the experiments upon release of load. This indicated the possibility of greater kink band fiber rotation

BAA3 BLR

Kinking

0.284 mm
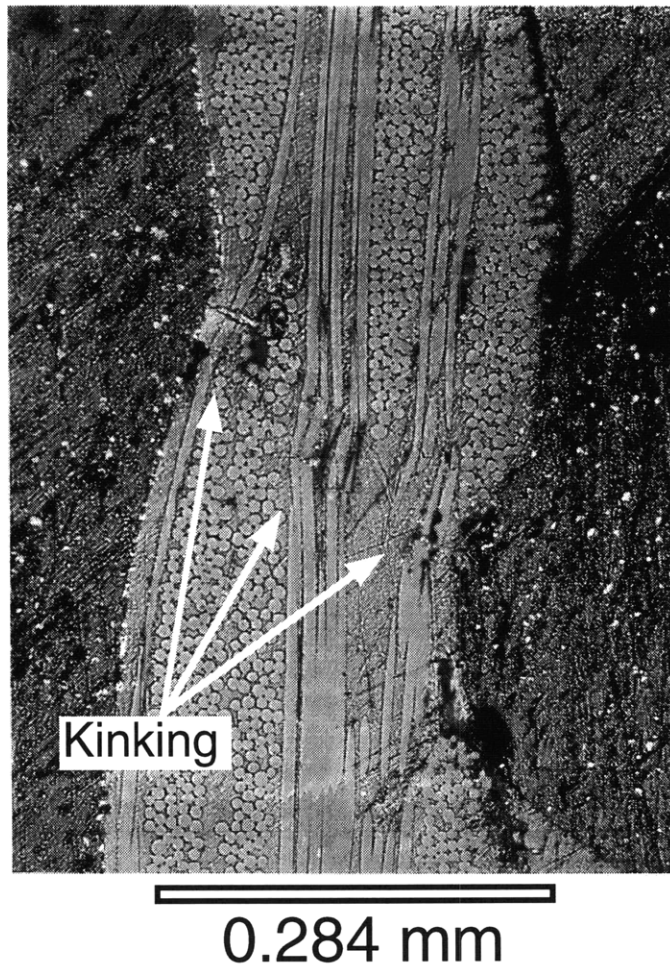
Figure 5.24   Cross-section showing warp tow kinking in all plies.

ADC1 FLR

Splitting

Kinking

0.483 mm
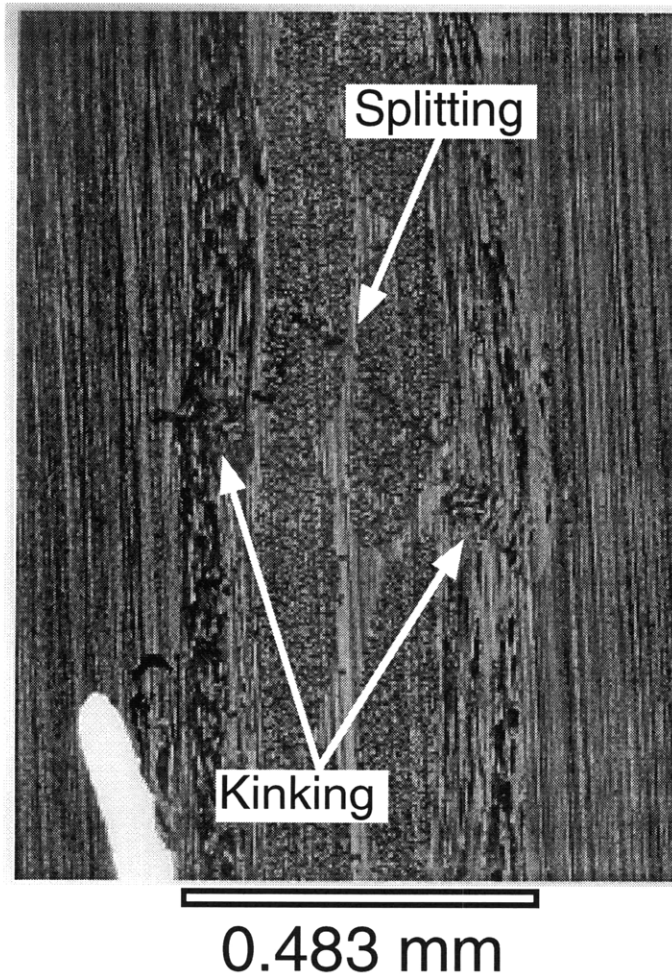
Figure 5.25   Cross-section showing kinking in warp tows and splitting in weft tows.

ABB4 FL(R)

Kinked Tows

0.483 mm
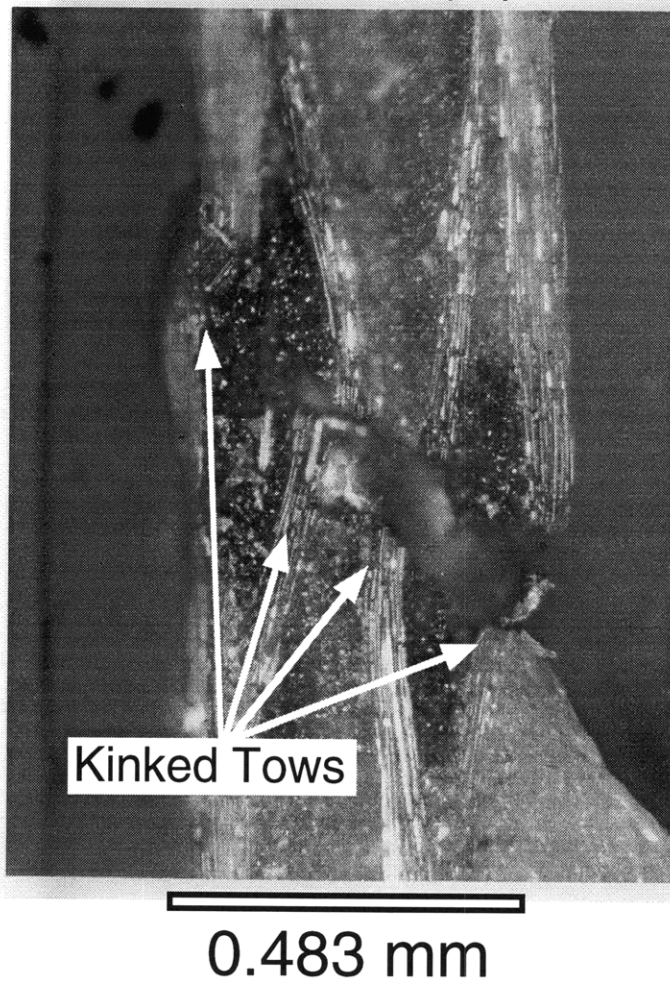
Figure 5.26   Photograph of LDZ root showing shear crippling of facesheet.

angles during experiment than those observed from photographs taken of cross-sections. For the limited cross-sections taken, the observed kink band fiber rotation angles for both materials were in the range of 10°-20°. Kink band inclination angles varied from approximately 20°-25°. Kink band widths were observed to be about 6-8 fiber diameters, or approximately 60μm and 50μm for M4 and M5 materials, respectively. Refer to figure 2.1 for angle definitions.

Photographs taken with a scanning electron microscope (SEM) gave an indication of the notch tip damage mechanisms. Figure 5.27 shows the root of an LDZ in an M5 facesheet. Tow fiber kinking in the warp tows is evident. Weft tow fiber splitting, a micromechanism which was not observed during cross-sectioning in M5 material, is also present. The split line runs from one kink band to the other. The two fracture lines observed on the surface of the facesheet give an indication of the kink band width. Figure 5.28 shows similar micromechanisms in an M4 facesheet. Again, the weft tow split line runs linearly between the kink bands. The shear crippled zone is clearly seen on the surface of the facesheet. The kink bands are clearly defined at the hole edge, as shown in figure 5.29. The out-of-plane characteristic of the kink band is evident; in-plane kinking was never observed.

5.3   Damage Growth Model

The damage growth model was used to determine the ability of the DZM to predict two phenomena: the LDZ growth behavior and ultimate failure load. Two traction laws were used for each material system as discussed in chapter 4. The first traction law (*traction law 1*) was obtained by calibrating the damage growth model based on the experimentally observed LDZ growth behavior. The second traction law (*traction law 2*) was obtained by calibrating the FEM based on the experimentally observed local strains. Figures 5.30-
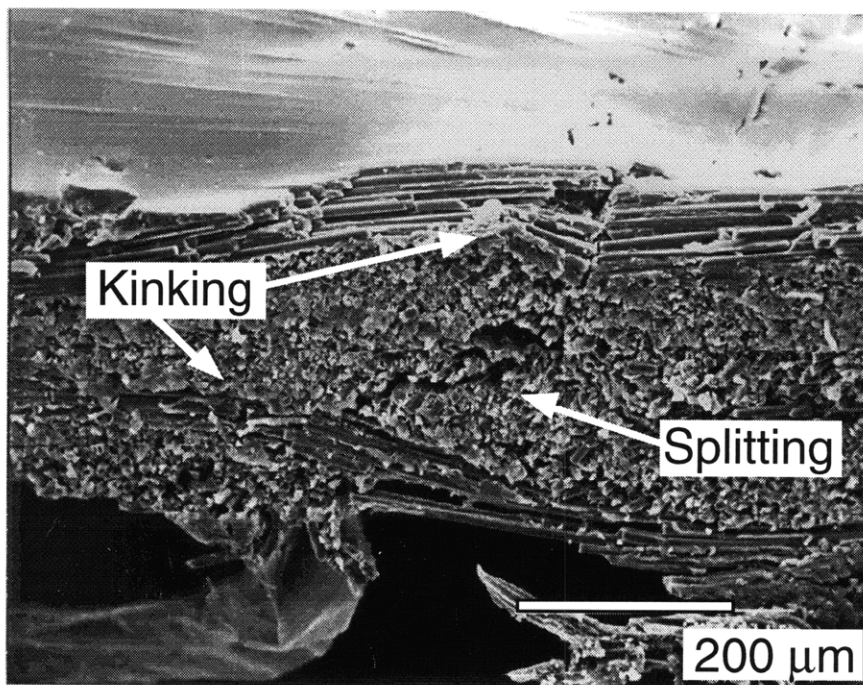
Figure 5.27   Scanning electron micrograph of LDZ root at hole edge in M5 facesheet. The SEM revealed weft tow splitting, a damage mechanism unobserved in M5 cross-sections.
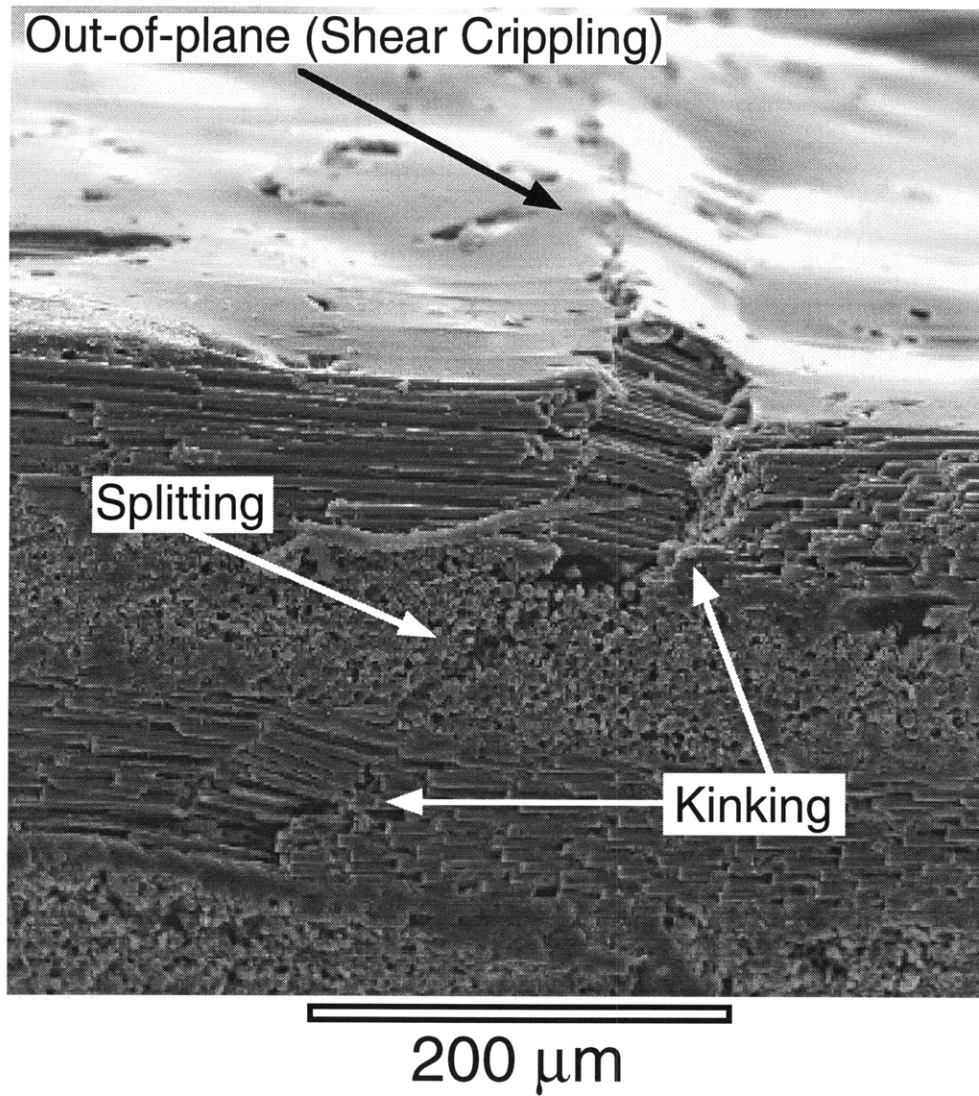
Figure 5.28   Scanning electron micrograph of LDZ root at hole edge in M4 facesheet.
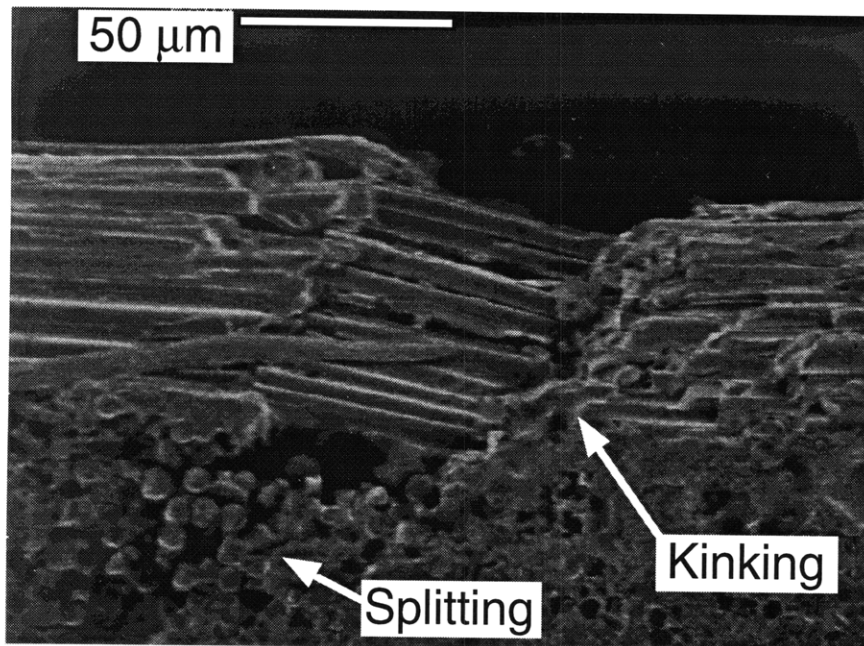
Figure 5.29   Scanning electron micrograph showing detail of kinked tow in M4 facesheet.

5.35 show R-curve predictions for different panel sizes for both materials. Clearly, the degree of correlation achieved using traction law 1 was much better than when using traction law 2, simply because traction law 1 was calibrated with the growth data. It should be noted that, although traction law 1 was obtained through calibration with the growth data, a remarkably good correlation was achieved for all specimen sizes with one traction law. All of the growth predictions using traction law 2 under-predicted the experimentally observed data.

Table 5.2 lists the ultimate failure load predictions for both materials. As with the LDZ growth correlations, the ultimate failure load correlations were obtained for both traction laws. The failure load is consistently over-predicted with traction law 1. When using traction law 2, the failure load was consistently under-predicted.

Table 5.3 lists the ultimate LDZ length correlations. As seen in the tabulated results, the correlations with failure loads and LDZ lengths for both traction laws were significantly inferior to the LDZ growth correlations with traction law 1. Both traction laws generally resulted in an over-prediction of critical LDZ length.

As mentioned in chapter 4, the damage growth model was also used to determine the net-section forces as the LDZ propagated. Tests indicated that the unnotched strength was approximately 162 MPa and 126 MPa for M4 and M5 materials, respectively. Table 5.4 lists the applicable forces for all materials, sizes, and traction laws. In all cases, the damage growth model indicates that failure will occur via LDZ propagation (v_c reached) before the ligament fails due to a load imbalance.
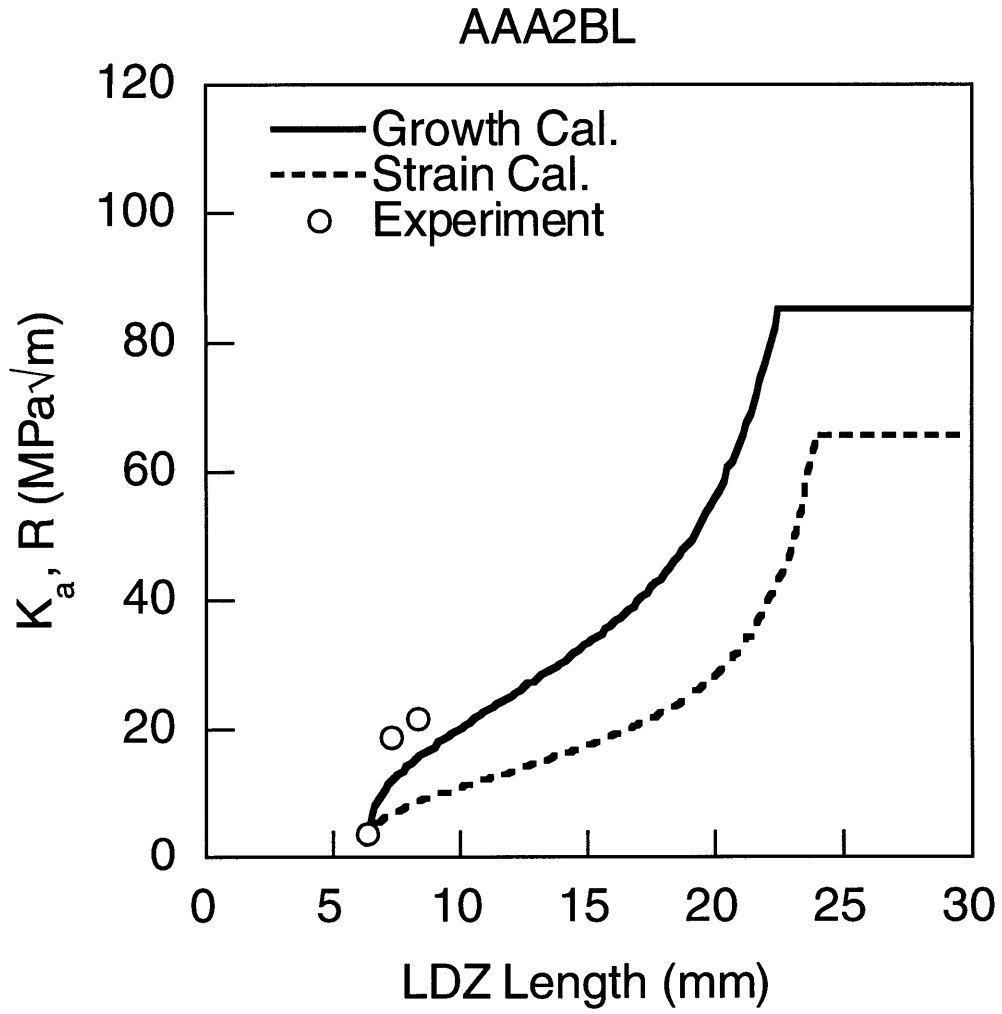
Figure 5.30   R-curves for AAA specimens.
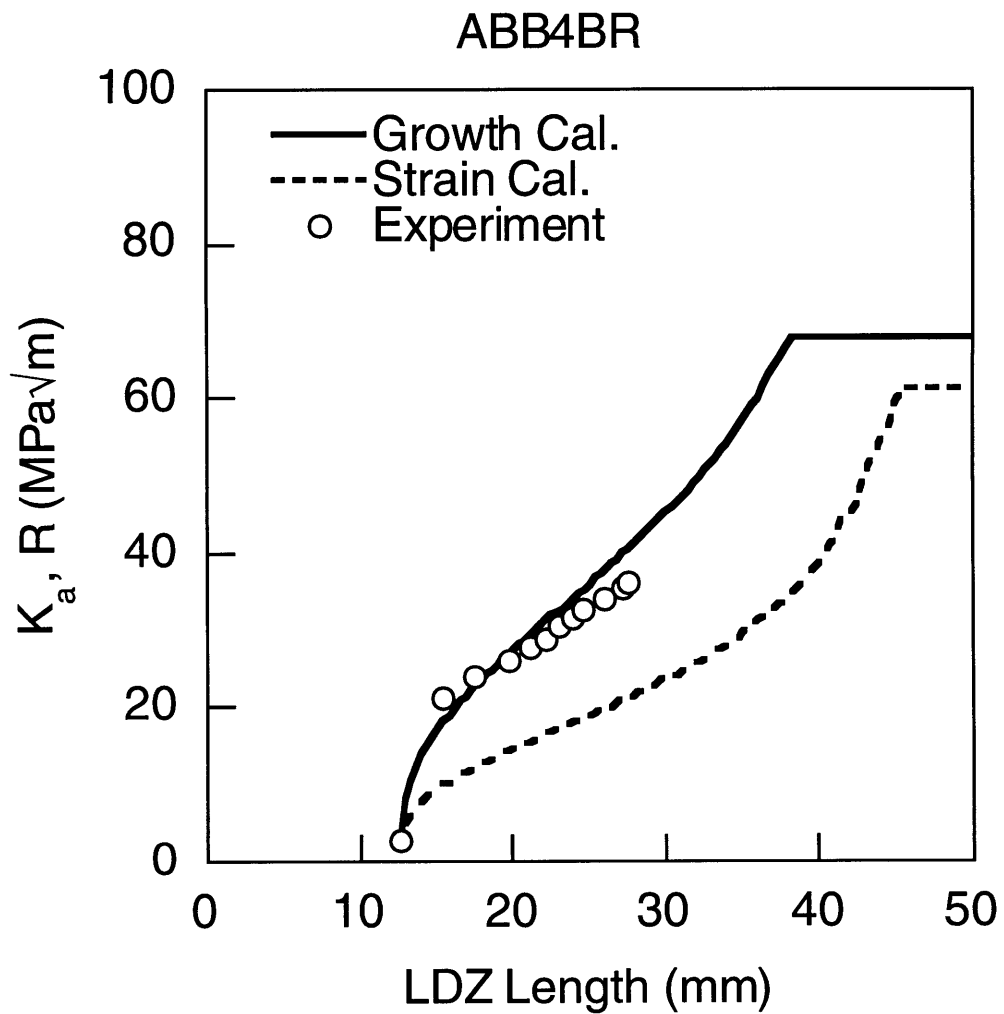
Figure 5.31   R-curves for ABB specimens.
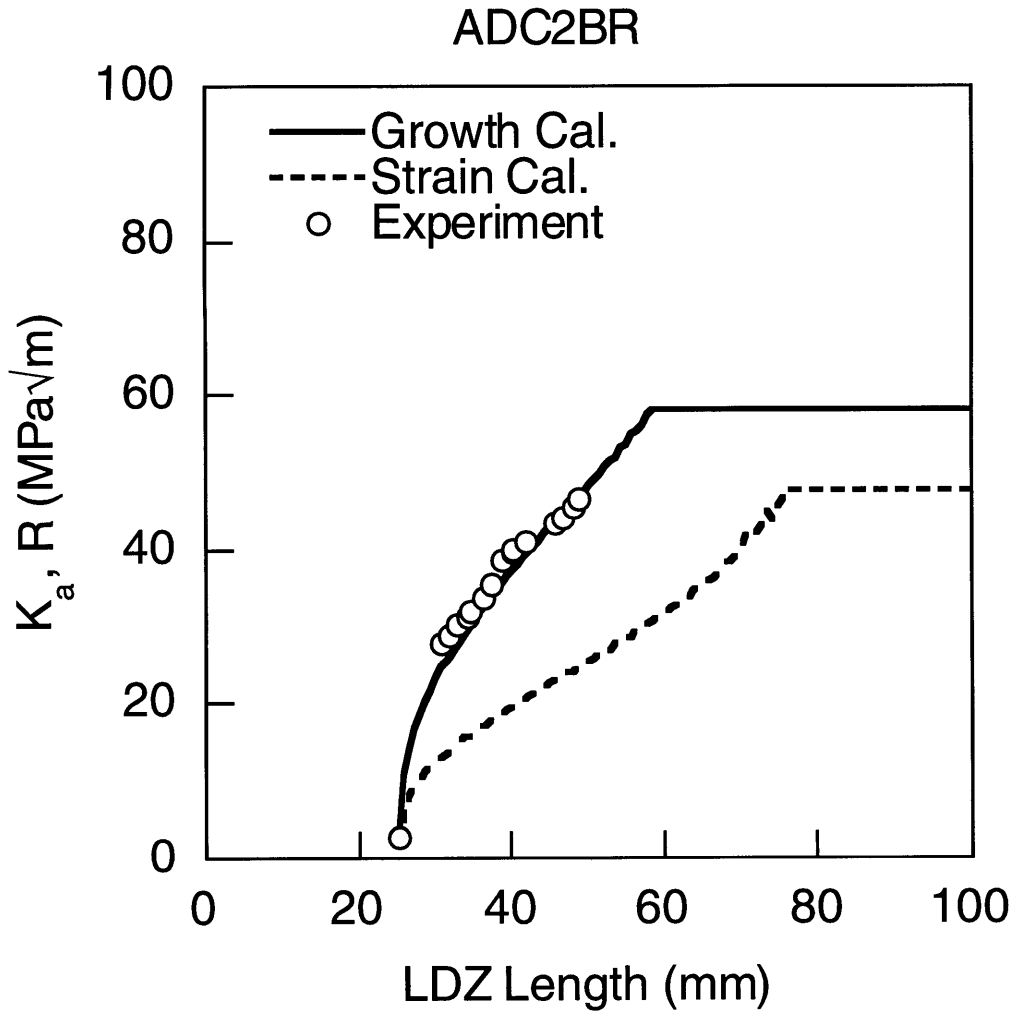
Figure 5.32   R-curves for ADC specimens.
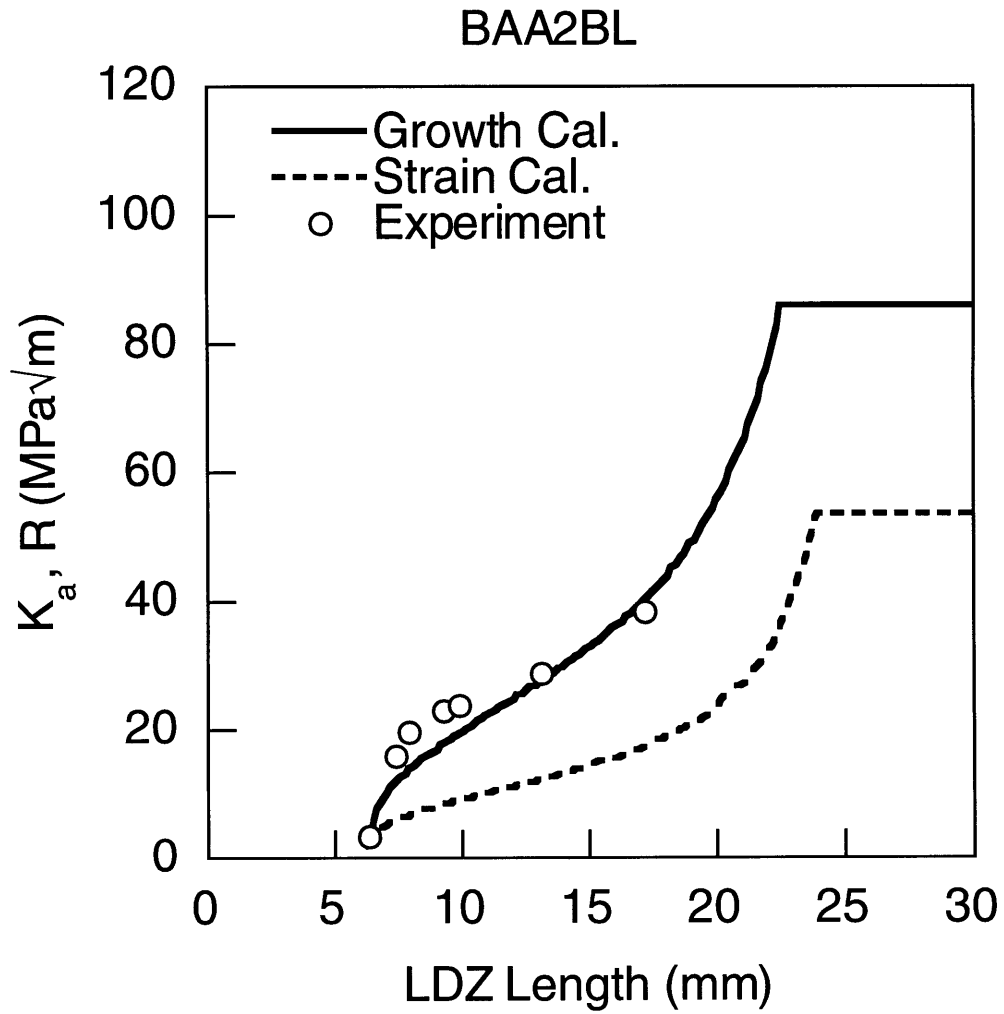
Figure 5.33   R-curves for BAA specimens.
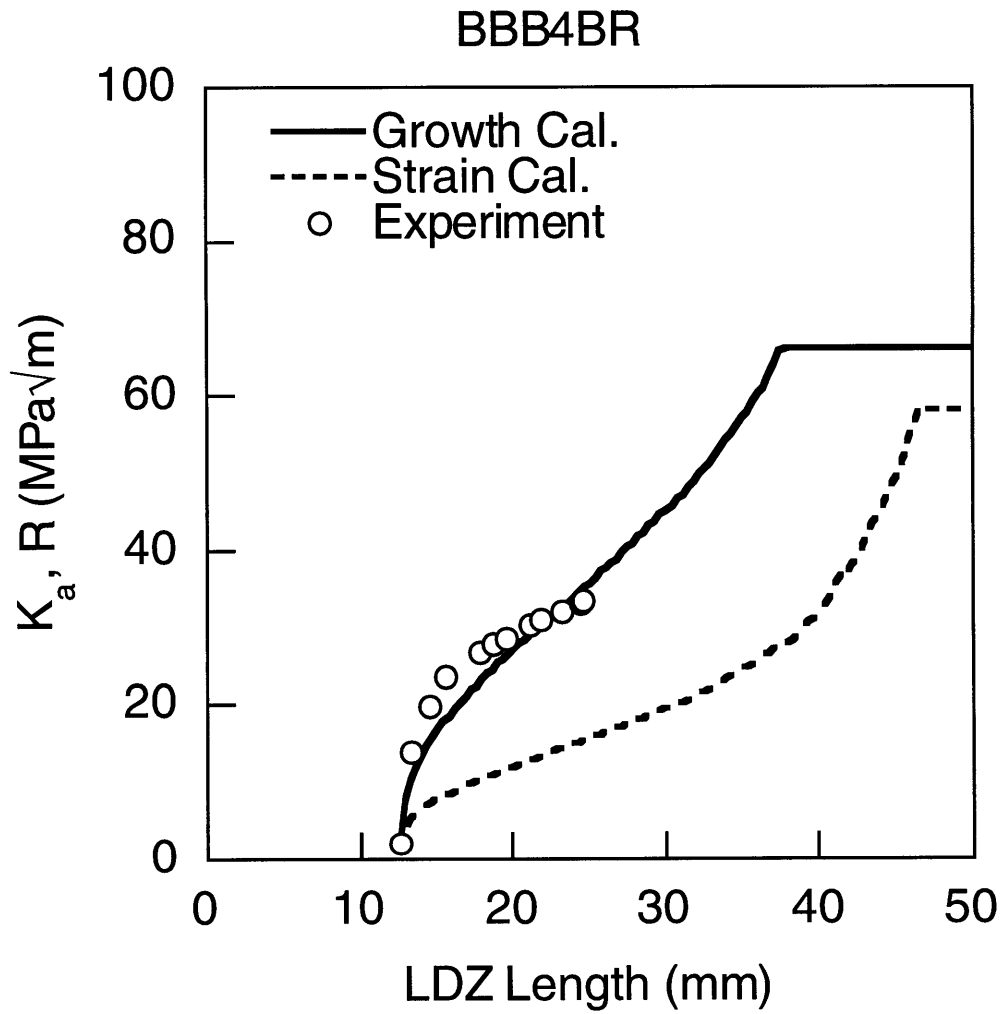
Figure 5.34   R-curves for BBB specimens.
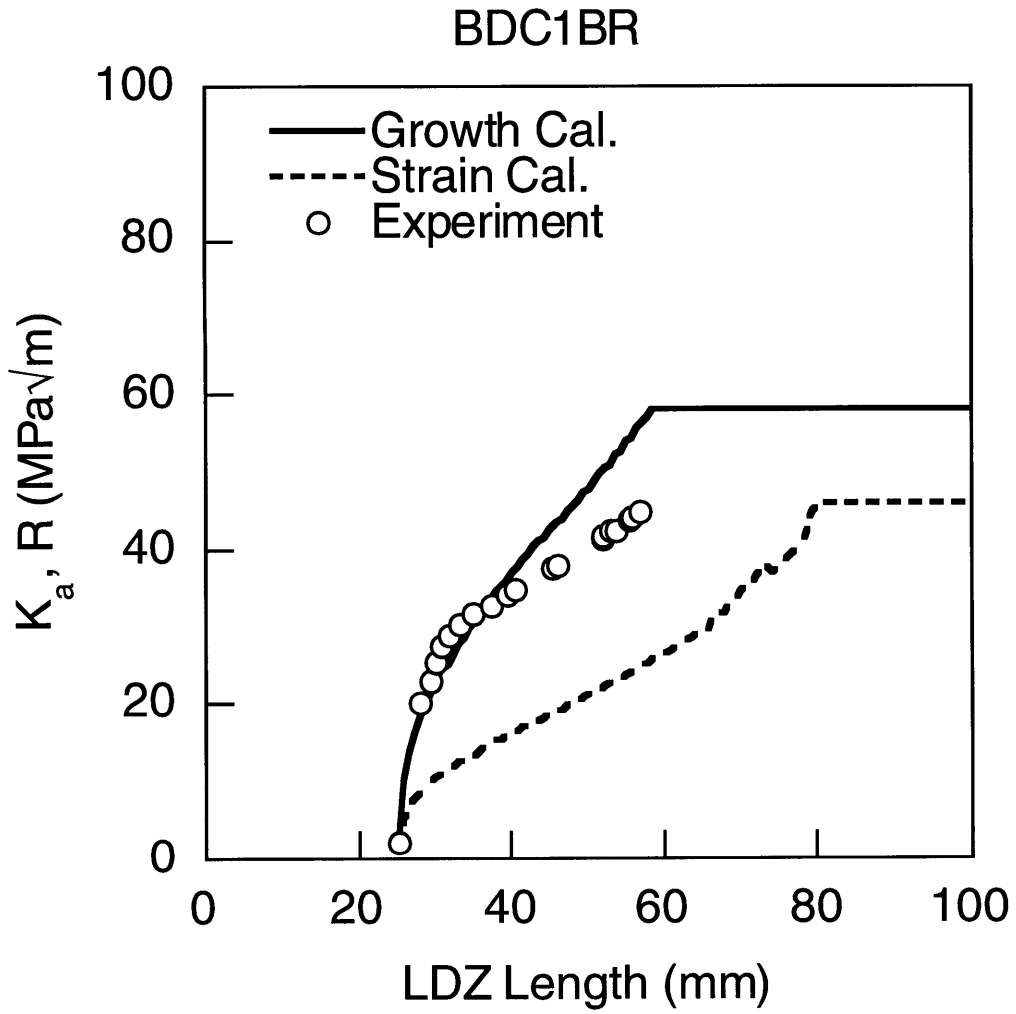
Figure 5.35   R-curves for BDC specimens.

Table 5.2   Failure Load Correlations

Failure Load Correlations (All loads in N)				
Material	Size	Experimental	Predicted	% Difference
Traction Law 1: LDZ Growth Data Calibration				
M4	Small	2135	2333	-9.3
	Medium	3298	4091	-24
	Large	6642	7099	-6.9
M5	Small	1211	1375	-13.5
	Medium	1962	2411	-22.9
	Large	3112	4185	-34.5
Traction Law 2: Local Strain Data Calibration				
M4	Small	2135	1234	42.2
	Medium	3298	2299	30.3
	Large	6642	4057	38.9
M5	Small	1211	598	50.6
	Medium	1962	1136	42.1
	Large	3112	2112	32.1

Table 5.3   Critical LDZ Length Correlations

Critical LDZ Length Correlations (All lengths in mm)				
Material	Size	Experimental	Predicted	% Difference
Traction Law 1: LDZ Growth Data Calibration				
M4	Small	13.7	16.2	-18.4
	Medium	21.3	25.6	-20.1
	Large	36.6	33.4	8.5
M5	Small	10.6	16.2	-52.2
	Medium	11.5	25.6	-122.8
	Large	34.4	33.4	2.8
Traction Law 2: Local Strain Data Calibration				
M4	Small	13.7	N/A	N/A
	Medium	21.3	32.7	-53.4
	Large	36.6	51.2	-40.1
M5	Small	10.6	17.6	-65.6
	Medium	11.5	33.8	-193.9
	Large	34.4	54.8	-59.3

Table 5.4   Stress-Based Failure Force Balance

Net-Section Failure Criteria (All forces in N)			
Forces listed correspond to the instant that v_c is reached			
Material	Size	Applied Force	Force on LDZ + Ligament
Traction Law 1: LDZ Growth Data Calibration			
M4	Small	1160	1348
	Medium	2056	3370
	Large	3572	8371
M5	Small	1170	1210
	Medium	1201	1746
	Large	2111	4039
Traction Law 2: Local Strain Data Calibration			
M4	Small	619	687
	Medium	1136	1715
	Large	2046	5173
M5	Small	505	570
	Medium	564	750
	Large	1053	2143

5.4   Finite Element Model

The finite element model was used to assess the DZMs ability to consistently predict the local strain behavior. Preliminary FEM tests indicated that all three panel sizes yielded the same strain behavior for a given traction law. For example, regardless of specimen size, a consistent spring law produced similar trends in local strain behavior. Furthermore, local strain correlations for L2X gages were much better than for L1X gages, because L2X gages were located further away from the LDZ.

One specimen from each material system was chosen as a representative test case for the strain correlations. ADC2 and BDC1 were chosen for M4 and M5, respectively. Since both of these specimens exhibited significant LDZ propagation prior to failure, the load carrying capability of the LDZ wake could be more readily modeled and compared with experimental data.

Both traction laws were used in the FEM with both test cases. Figures 5.36-5.41 show strain correlations for both test cases using *spring law 1*, the equivalent of traction law 1. Both M4 and M5 specimens show a good correlation with far field strain gage data. However, in both test cases, the local strain behavior observed during experiment did not correlate well. All figures indicate that spring law 1 does not properly model the load carrying characteristics of the LDZ wake. The experimental data showed a decrease in local strain as the LDZ tip passed through the shadow of a local strain gage. The FEM indicated that the strain remains relatively constant along the LDZ wake, with little or no strain reduction along the wake.

The alternate traction law calibration, as discussed in chapter 4, was used to obtain new traction laws for each material. Figures 5.42-5.47 show the
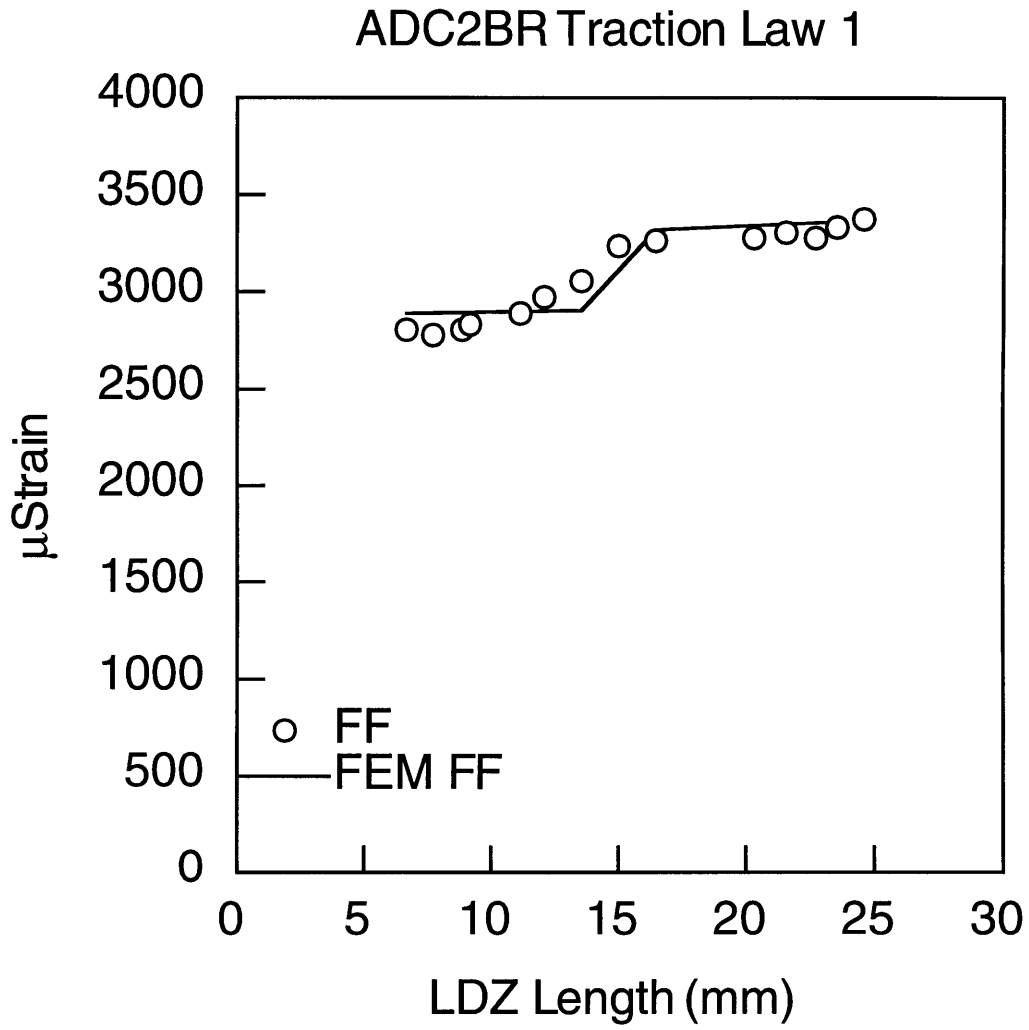
Figure 5.36   Far field strain correlation of M4 specimen from FEM using traction law 1.
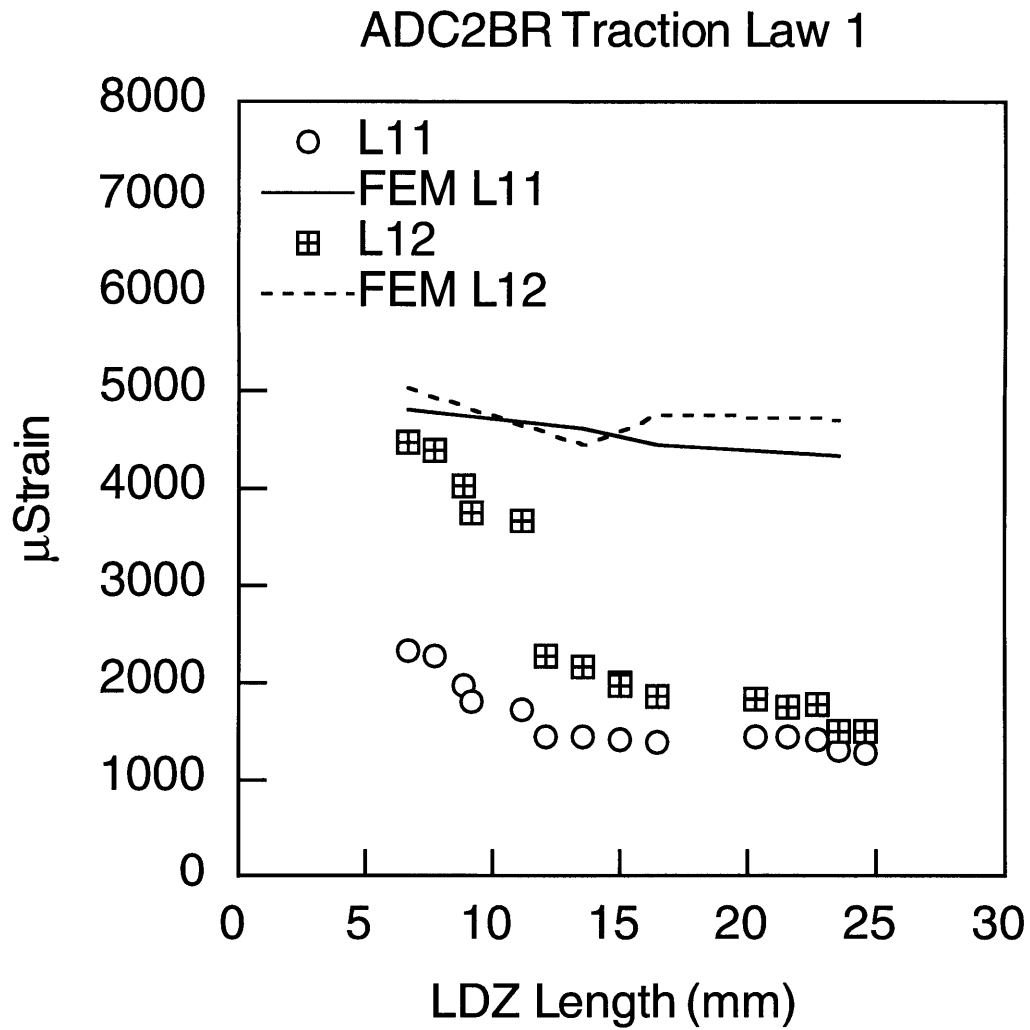
Figure 5.37   Local strain correlations (1 of 2) of M4 specimen from FEM
using traction law 1.
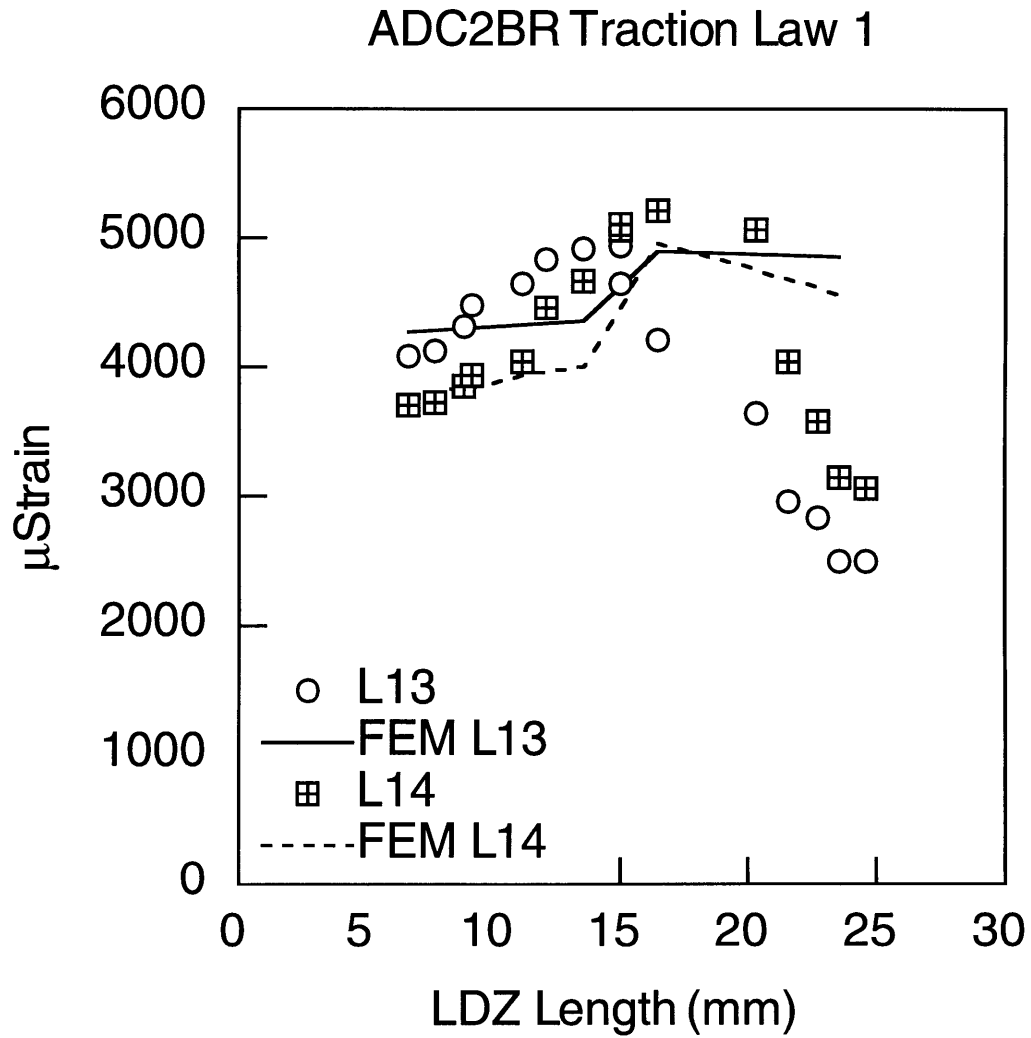
Figure 5.38   Local strain correlations (2 of 2) of M4 specimen from FEM
using traction law 1.
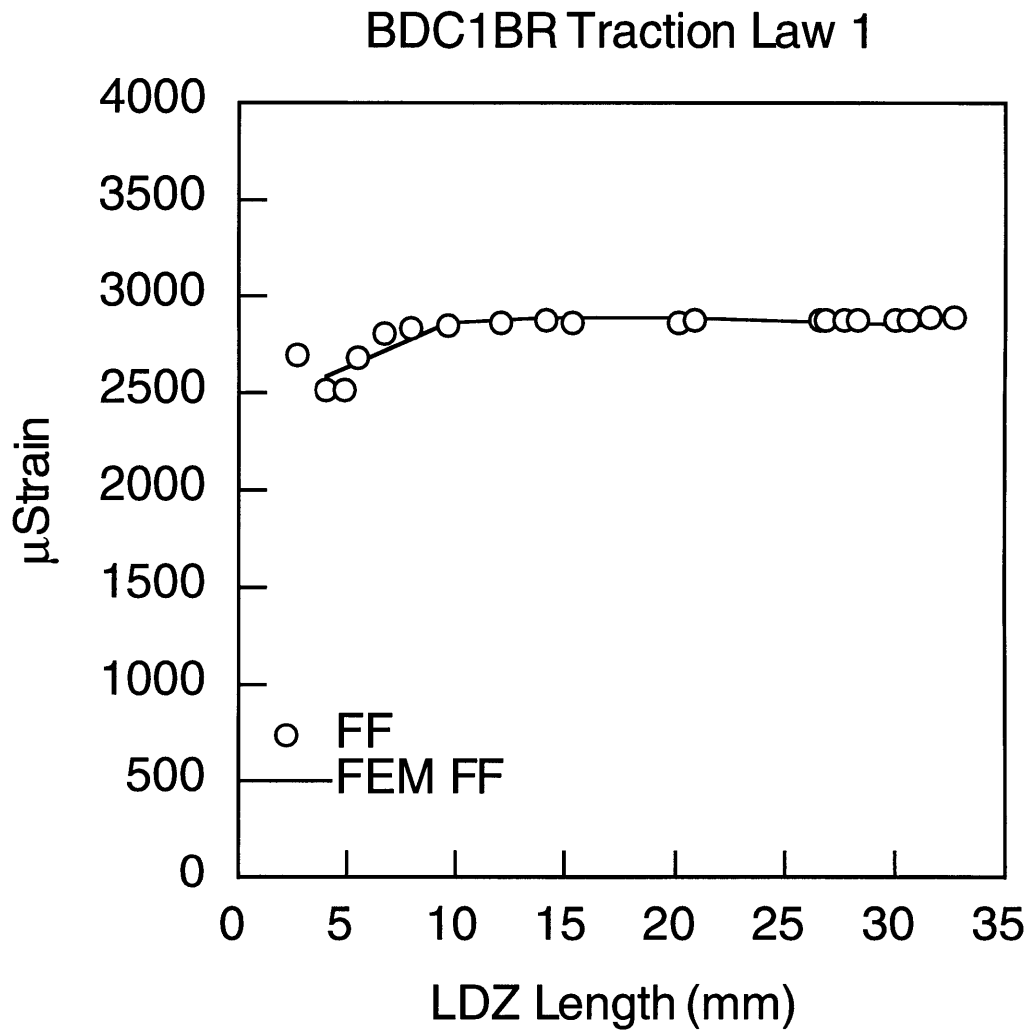
Figure 5.39   Far field strain correlation of M5 specimen from FEM using traction law 1.
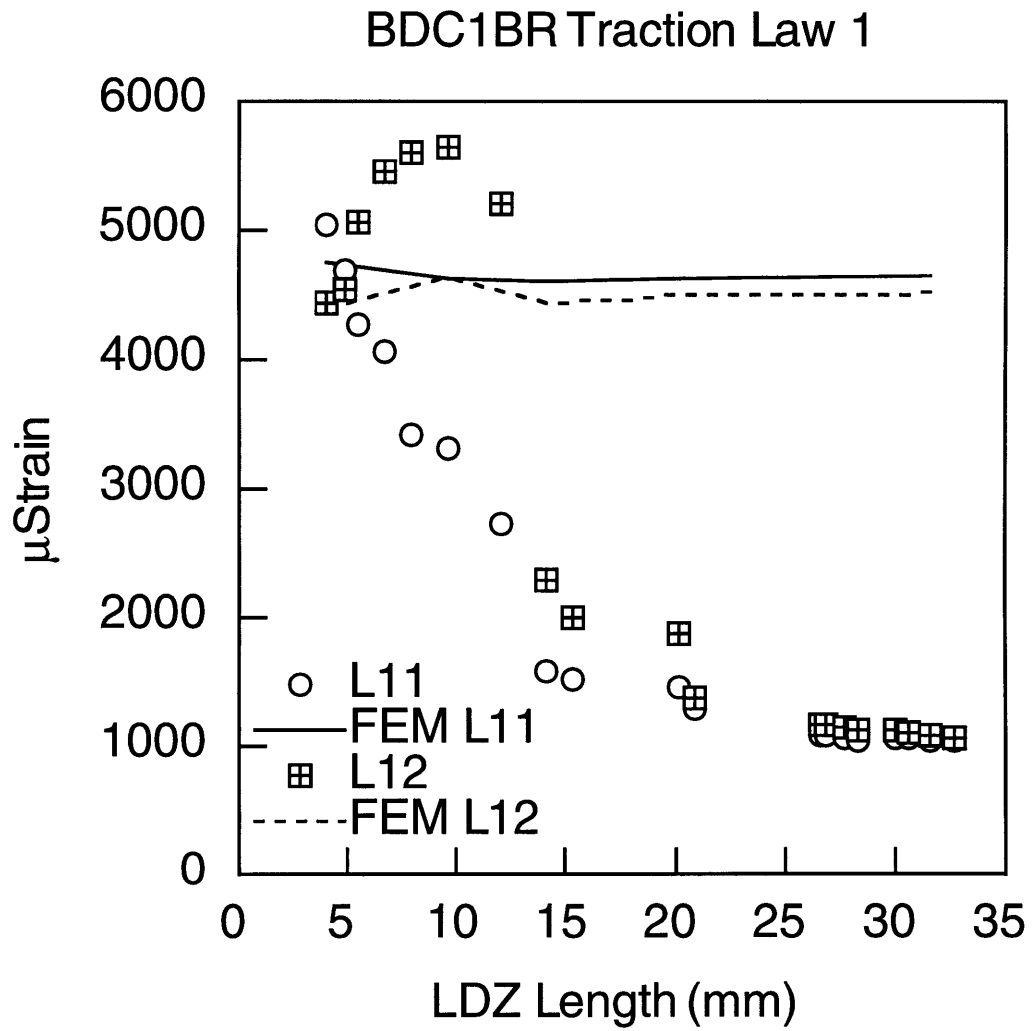
Figure 5.40   Local strain correlations (1 of 2) of M5 specimen from FEM
using traction law 1.
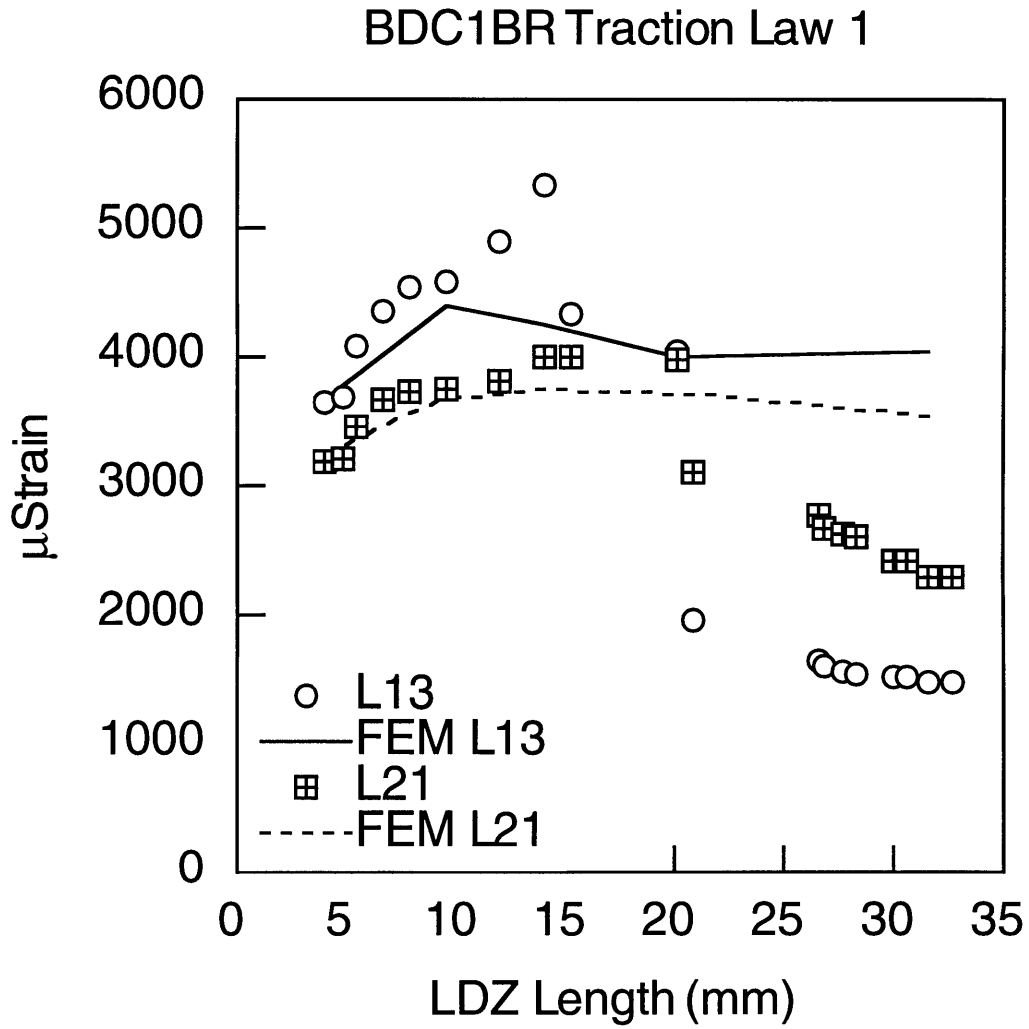
Figure 5.41   Local strain correlations (2 of 2) of M5 specimen from FEM
using traction law 1.
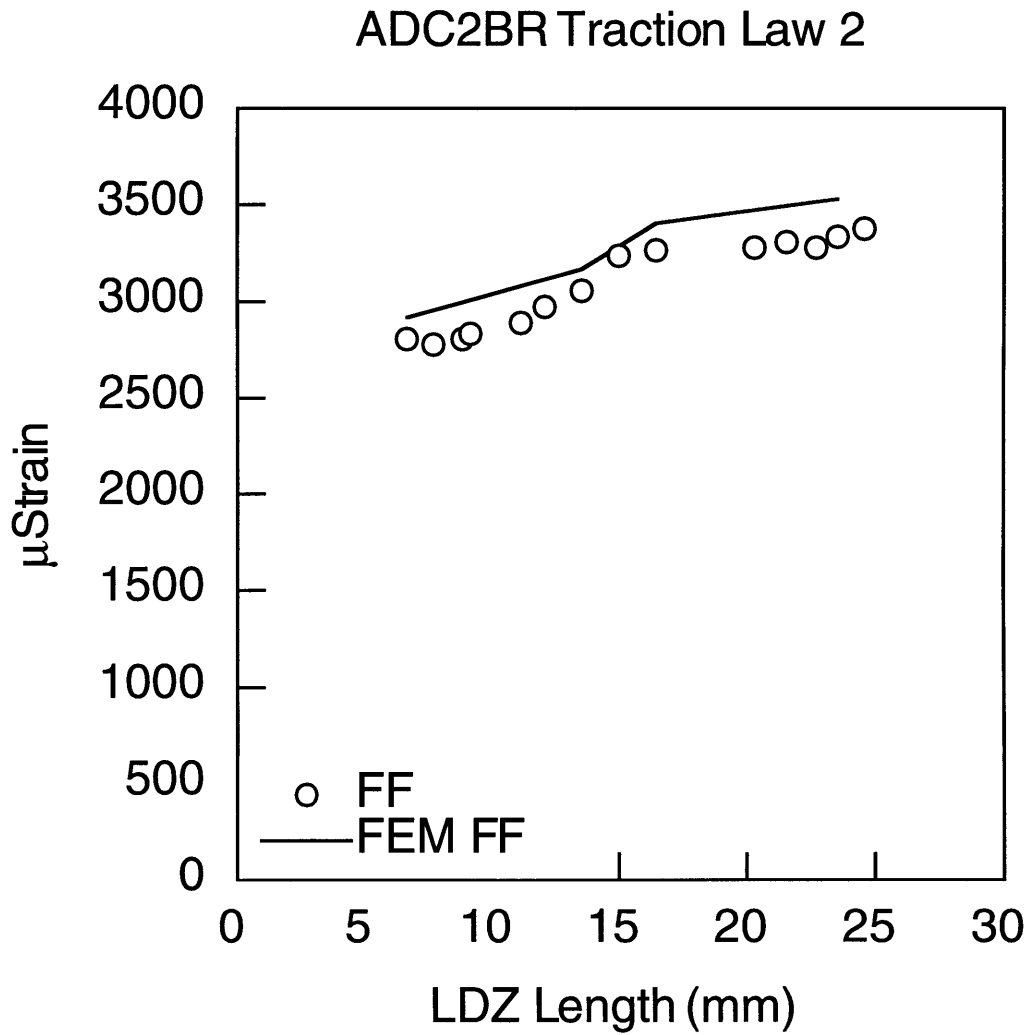
Figure 5.42   Far field strain correlation of M4 specimen from FEM using
traction law 2.
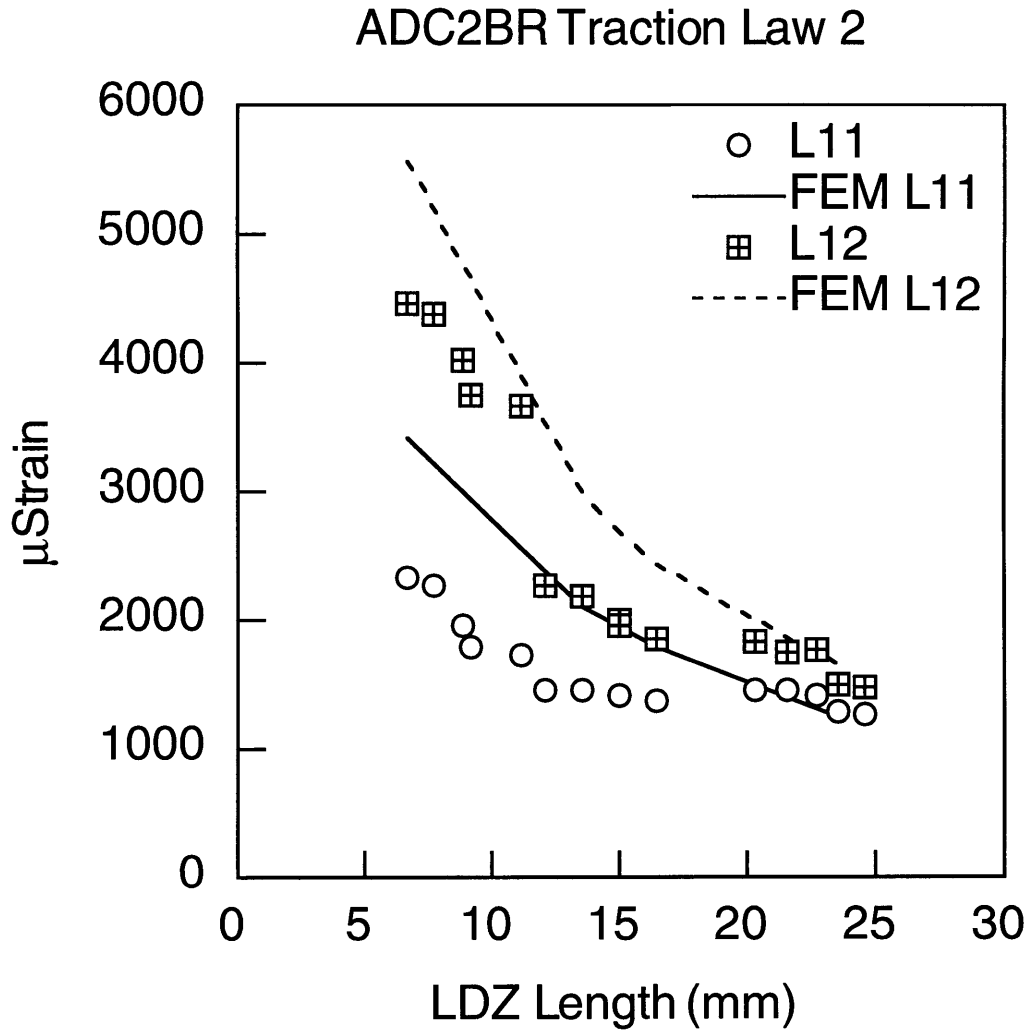
Figure 5.43   Local strain correlations (1 of 2) of M4 specimen from FEM
using traction law 2.
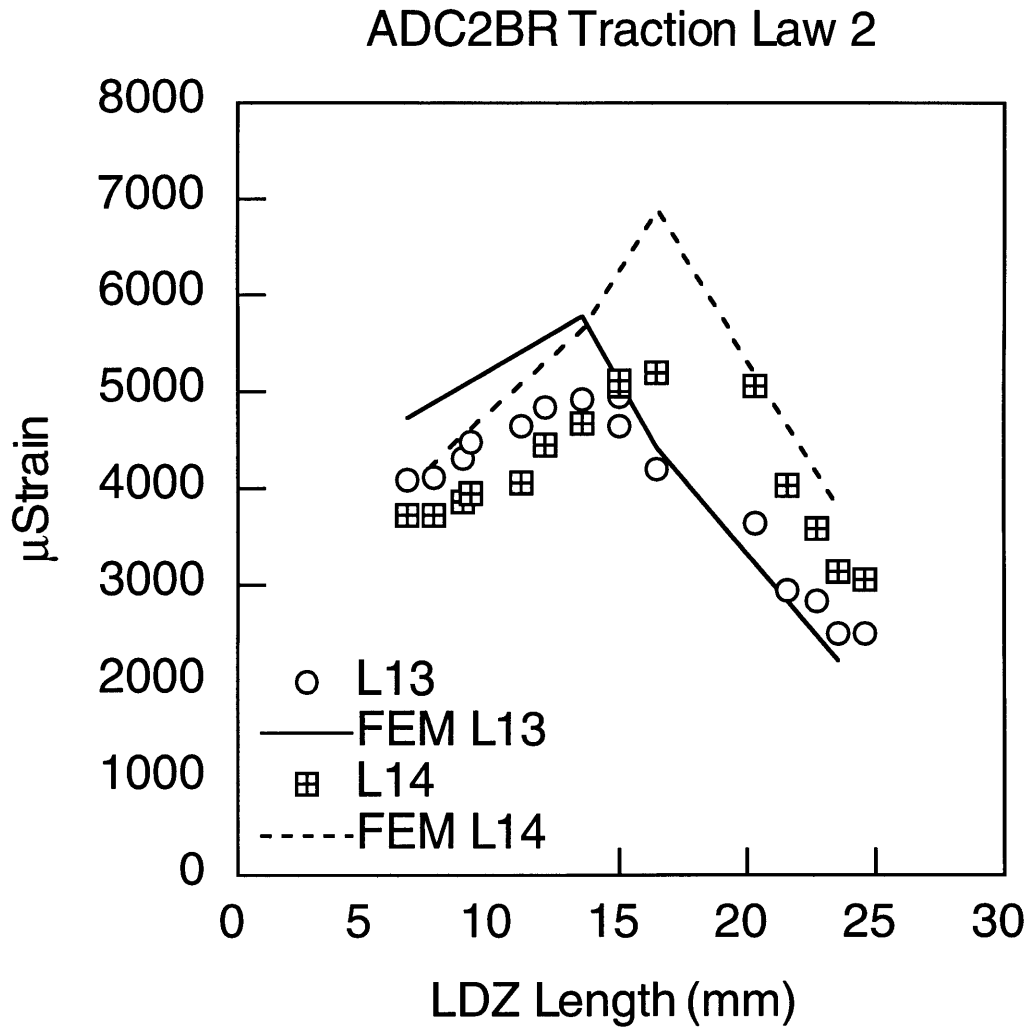
Figure 5.44   Local strain correlations (2 of 2) of M4 specimen from FEM
using traction law 2.
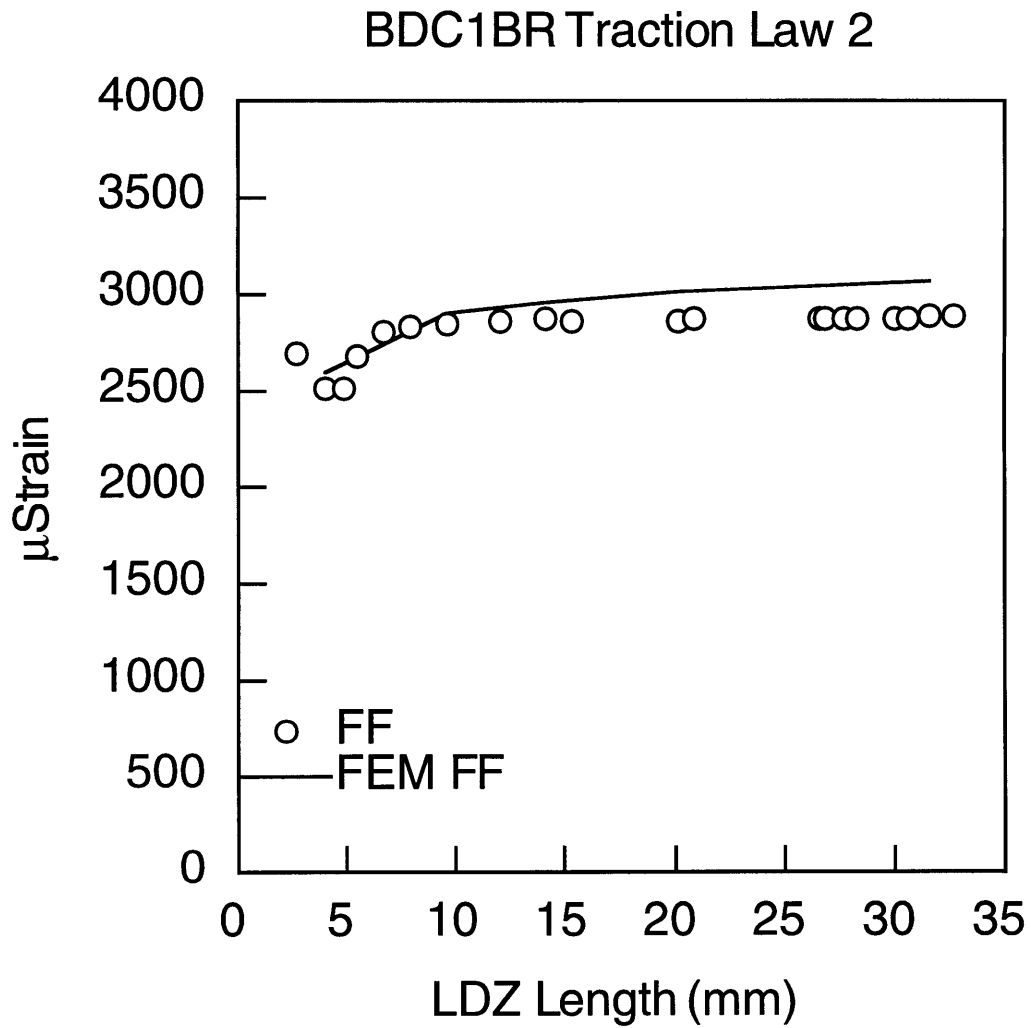
Figure 5.45   Far field strain correlation of M5 specimen from FEM using traction law 2.
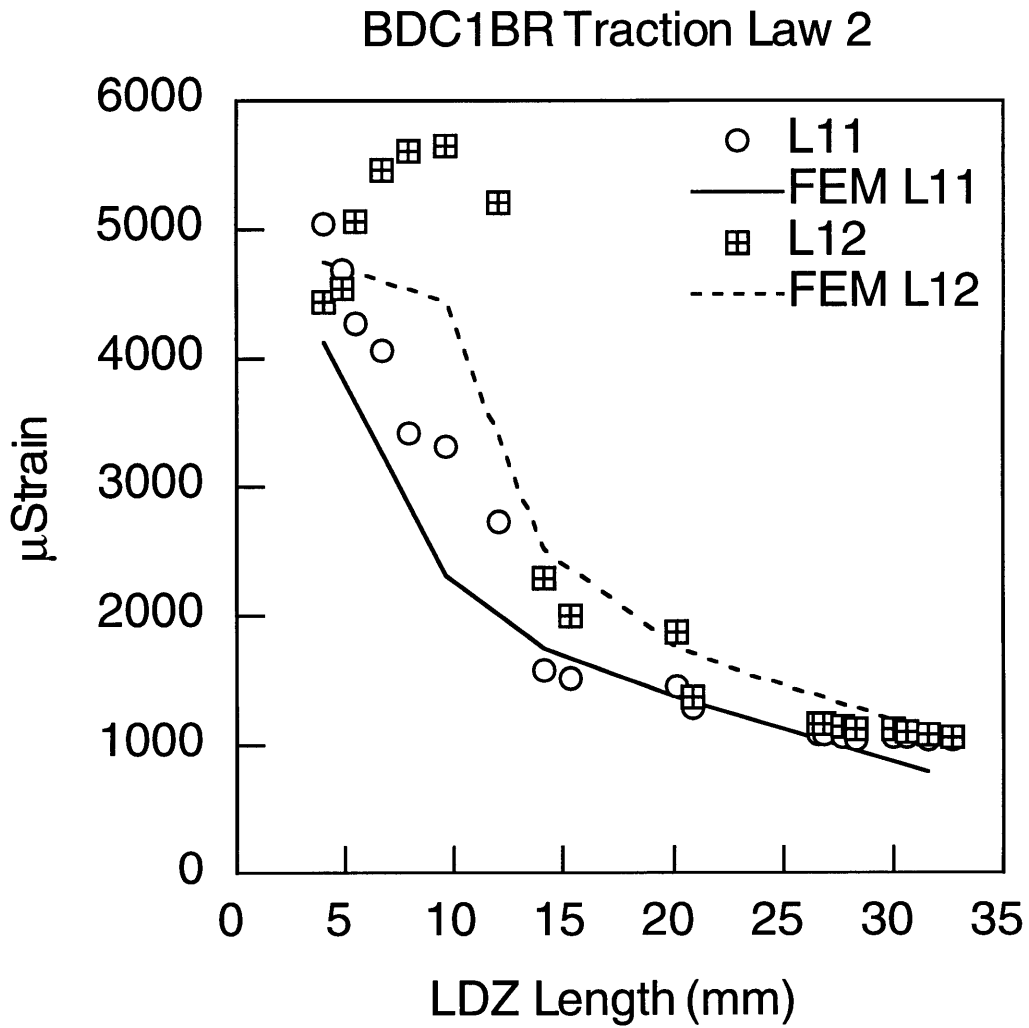
Figure 5.46   Local strain correlations (1 of 2) of M5 specimen from FEM
using traction law 2.
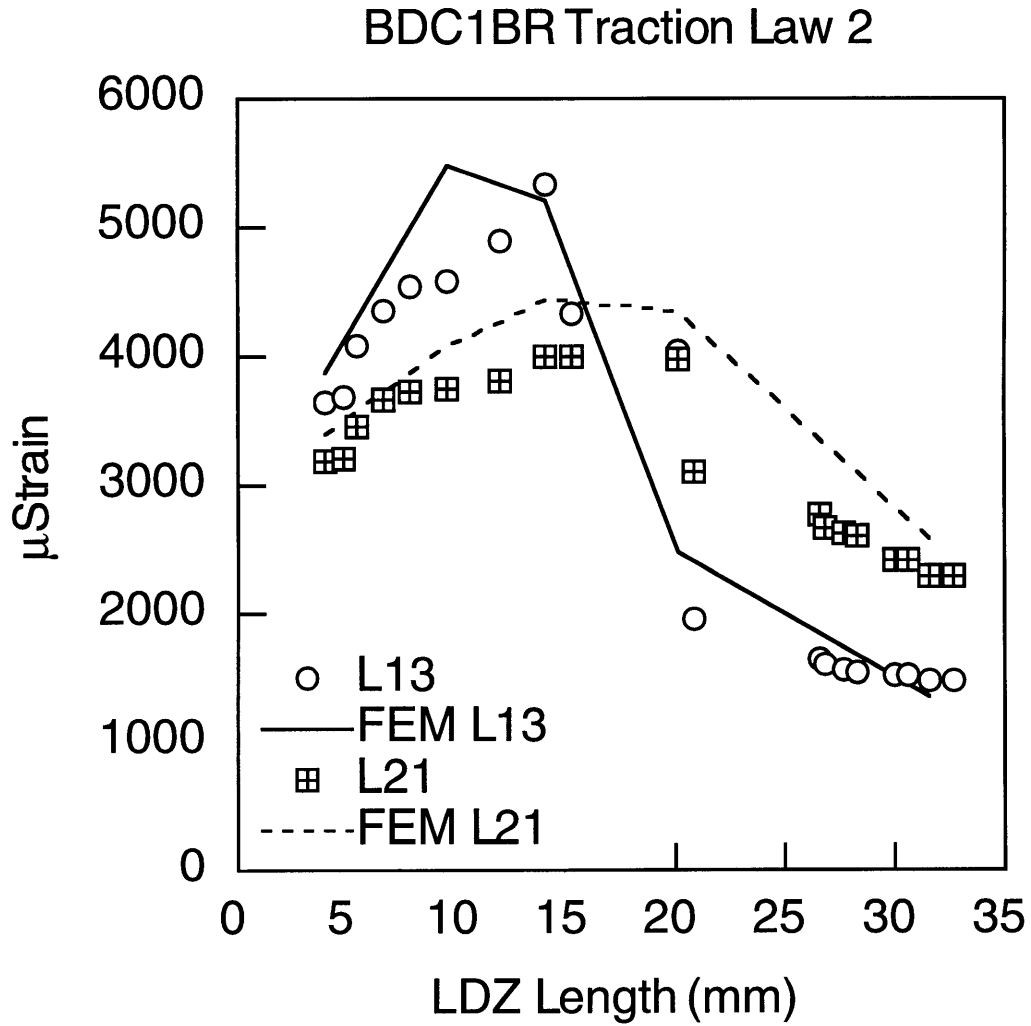
Figure 5.47   Local strain correlations (2 of 2) of M5 specimen from FEM
using traction law 2.

strain correlations for both test cases using *spring law 2*, the equivalent of traction law 2. The previous section presented results on the damage growth model's inability to accurately predict the LDZ growth behavior and failure load with traction law 2. However, the figures clearly indicate that traction law 2 results in superior strain correlations when compared to traction law 1. The springs correctly model the LDZ wake in allowing a reduction in strain to occur.

In order to assess the degree of accuracy between the damage growth model and the FEM, the crack opening profiles of similar cases were checked for consistency. Two LDZ lengths in a BDC specimen were chosen as representative cases for the crack opening profile comparisons. LDZs of lengths 9.652 mm and 20.32 mm were chosen in order to determine any length effect that the LDZ had on the modeling; i.e. a relatively short and long LDZ were chosen. Both traction laws were used in the comparison. Figures 5.48 and 5.49 show the COD comparisons between the growth model and the FEM for both LDZ lengths using traction law 1. The correlation for the short LDZ was very good. However, the correlation for the longer LDZ was poor. The COD result from the FEM indicated that there were problems with the spring law during the analysis, as will be discussed in chapter 6. Figures 5.50 and 5.51 show the COD comparisons for both LDZ lengths using traction law 2. The correlation for both LDZ lengths were excellent.
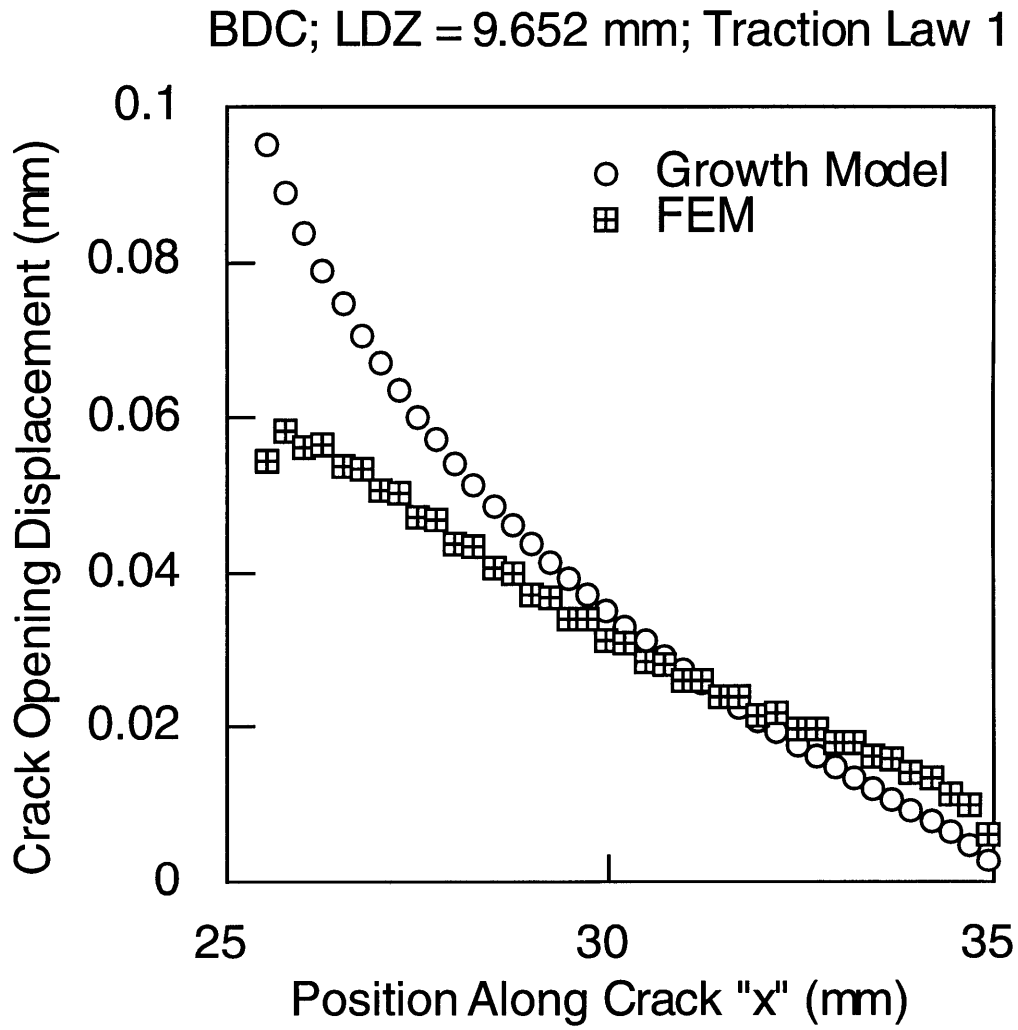
Figure 5.48   COD comparison for short LDZ using traction law 1.
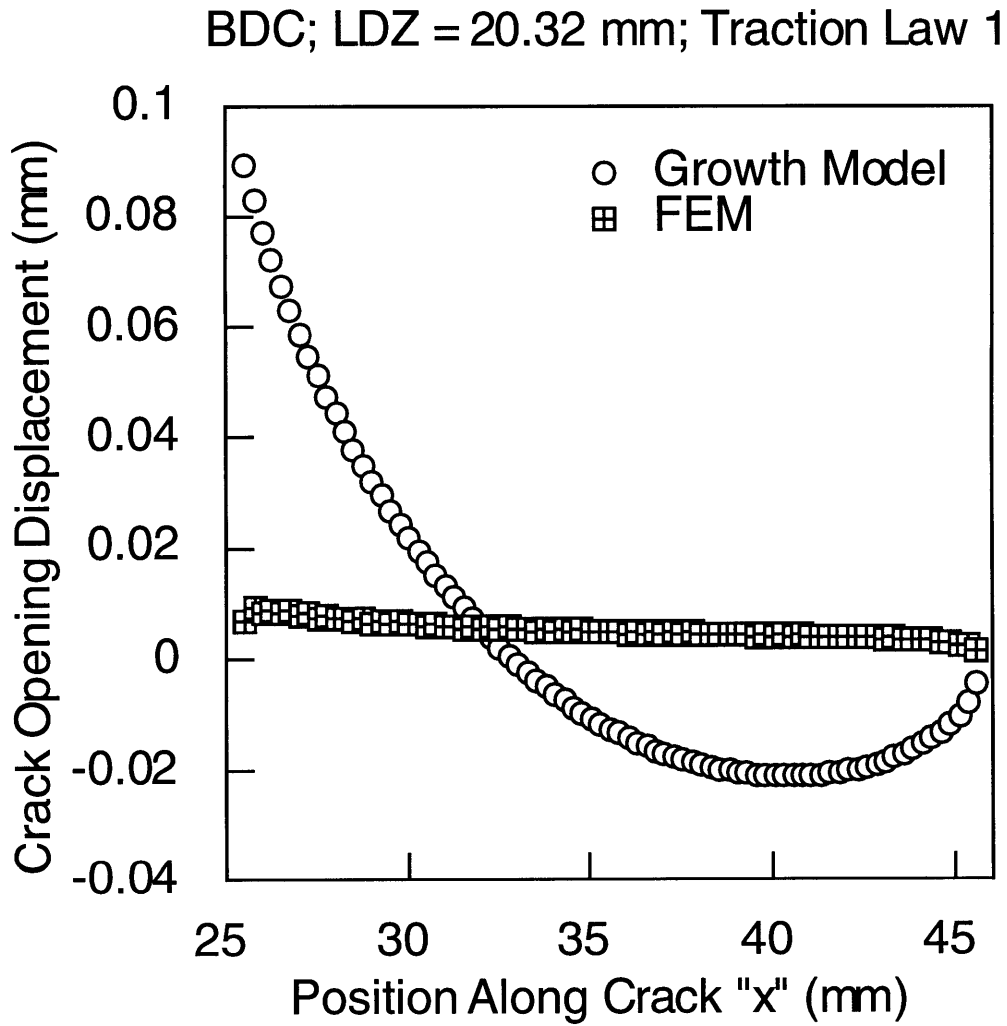
Figure 5.49   COD comparison for long LDZ using traction law 1.
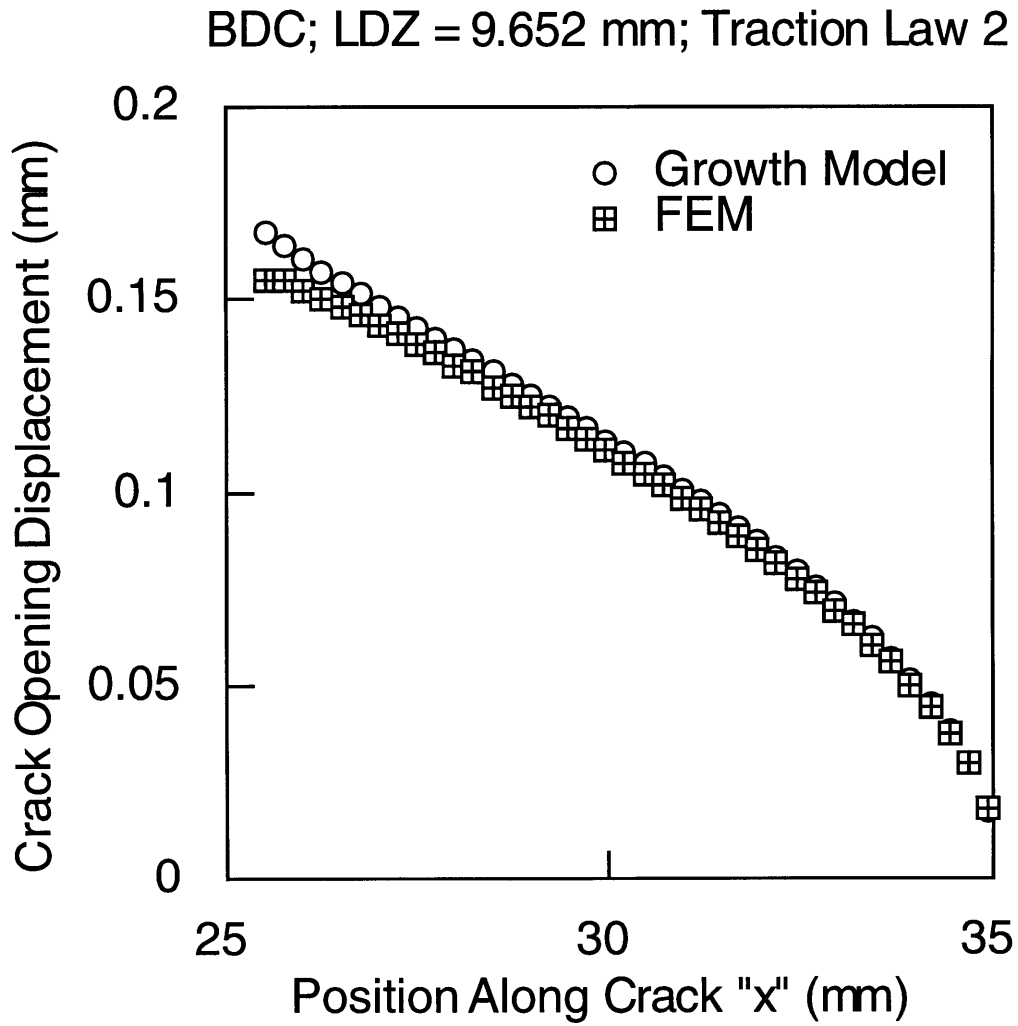
Figure 5.50   COD comparison for short LDZ using traction law 2.
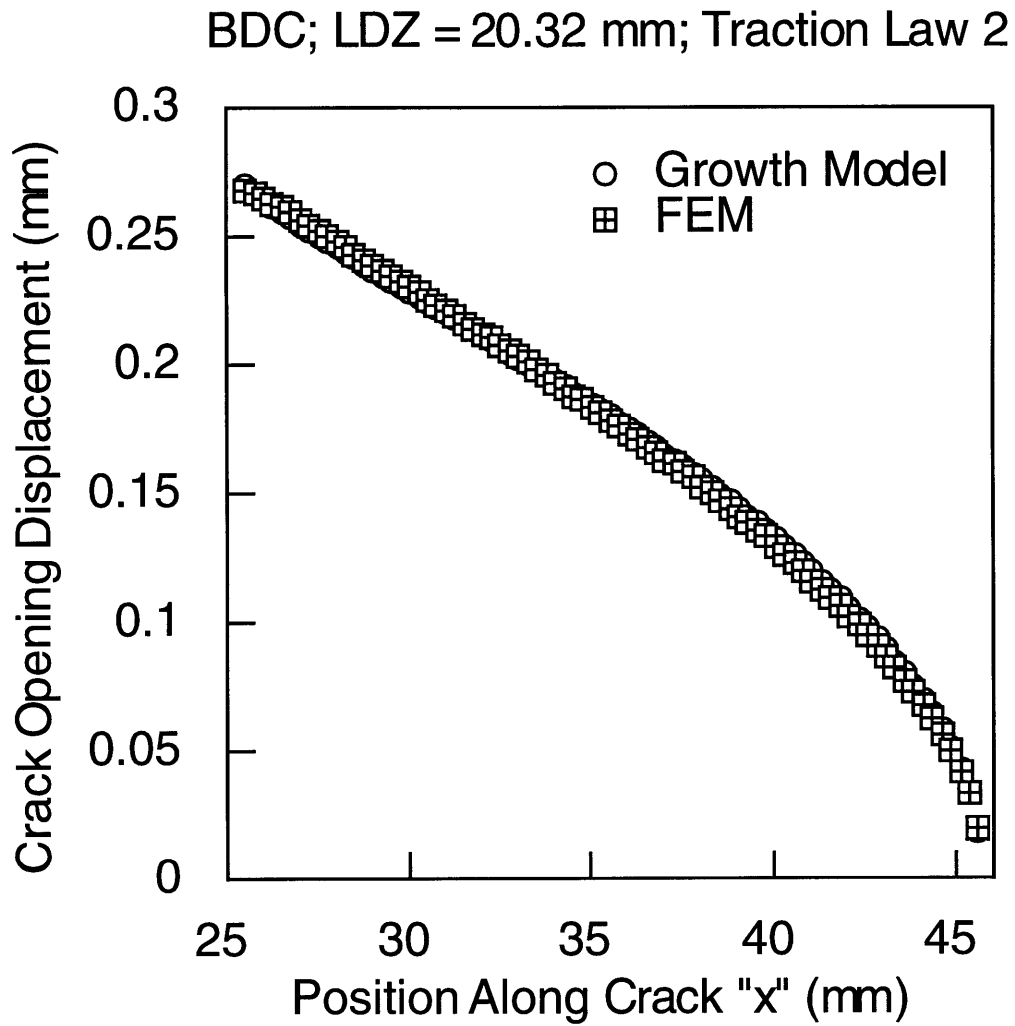
Figure 5.51   COD comparison for long LDZ using traction law 2.

5.5 Summary

The linear damage zone (LDZ) was identified as the critical damage mechanism in both materials and all specimen sizes under compression loading. LDZs initiated at the notch tips and exhibited semi-stable propagation in a direction perpendicular to the loading direction with further end-shortening. The damage zone consisted primarily of kinked warp tows along with transverse tow splitting. Fiber microbuckling in the out-of-plane direction led to warp tow kinking in all warp tows, and a local shear crippled zone.

Local strain measurements indicated that the LDZ was characterized by a *softening* response. A two parameter strain-softening traction law was used as a first modeling approximation of the LDZ constitutive behavior. The damage zone model (DZM) was interrogated by applying two models: the damage growth model and the finite element model (FEM).

Two traction laws were used for each material system. The first traction law was obtained with the damage growth model by calibration on experimental LDZ growth data. The second traction law was obtained with the FEM by calibration of the spring law on experimental local strain data.

As expected, each traction law provided a good correlation to the data with which it was calibrated. However, both traction laws resulted in relatively weaker correlations when the DZM was extended to predict the two other phenomena (from the three basic phenomena: ultimate strength, local strain distribution, and damage growth behavior). Furthermore, as a corollary, the predictions of the critical LDZ length were also significantly weaker than the initial correlations for both traction laws.

CHAPTER 6

DISCUSSION

This chapter presents a discussion of the results presented in chapter 5 in the context of the modeling of chapter 4. First, issues related to the experimental investigation are discussed. Then, the process used to evaluate the damage zone model is discussed. Finally, the potential of the DZM as a design tool is discussed.

6.1   Experimental Investigation

This section discusses the experimental procedures in the context of achieving the desired data and observations. The test fixture and procedure, strain measurement technique, and damage evaluation technique are evaluated.

6.1.1   Test Fixture and Method

The present work utilized a simple compression test fixture. Without additional supporting fixtures such as anti-buckling guides, the compression platens required only occasional adjustment of the self-aligning platen.

The primary goal of the test fixture was to evenly apply a compressive load throughout the *entire* test. Had significant bending occurred during preliminary tests, an anti-buckling device would have been necessary. Initial tests indicated that the loading generally remained within 10% in both front and back facesheets, avoiding the need for an antibuckling guide. The

acceptable level of alignment is evidenced by data such as that presented in figures 5.1-5.3.

In every test, the LDZ was the only damage observed, and each time it initiated, propagated, and caused failure of a facesheet in virtually the same way at similar load levels. Initial tests were performed at low displacement rates with the intention of inducing failure in the facesheets and avoiding failure modes associated with bending. In these respects the test methods clearly provided an appropriate means of obtaining reproducible results and provides for *in situ* observations of damage growth.

6.1.2 Local Measurements

The local strain behavior was monitored to provide a relatively direct calibration of the traction law (as opposed to indirect calibration via damage growth or strength measurements). If the damage growth model is used to obtain the traction law by calibration with LDZ growth data, then the local strain measurements serve as a verification data set. Conversely, the local strains are needed to calibrate the traction law via the FEM. In both cases, a single traction law should describe the damage growth, strength, and local strain response.

A strain mapping technique could be used to replace the strain gages for this purpose, and would offer several advantages. First, the entire local strain distribution could be monitored, as opposed to measurements at specific locations. Second, the LDZ propagation behavior could be monitored. Third, the *in situ* LDZ closing profile could be monitored, providing an indirect measurement of the kink band fiber rotation angles. Fourth, the technique could accomplish the above without altering the local stiffness; i.e. strain mapping is a "passive" process. Finally, experimental interruptions would not

be necessary, as was the case in the present study.

The obvious benefit of a strain mapping technique would be the direct determination of the traction law; i.e. no calibration would be necessary. The FEM would only be needed as a verification step, while the damage growth model could be used directly without calibration. However, in the absence of a strain mapping technique, the present study provided sufficient data to interrogate the DZM. The number of specimens tested, along with the fact that the *development* of the investigative models was not dependent on experimental measurements, indicate that strain mapping equipment would have been an unnecessary cost. Future testing and implementation would warrant the acquisition of such a system.

6.1.3 Damage Characterization

The visual inspection method utilized to characterize macroscopic LDZ growth behavior worked very well. Microscopic verification of measurements made visually indicated that the accuracy was sufficient (as discussed in chapter 3). However, the reliance on post-mortem cross-sectioning studies introduces limitations on the ability to characterize damage processes.

Direct, *in situ* observation of the progressive kinking process as well as the development of other subcritical damage mechanisms would help to add more physical basis to the DZM. Specifically, the relationship between the local strain distribution, kinked warp tow fiber rotation angles, and LDZ closing displacement (which may be caused by fiber rotation *and* large-scale sliding), would provide a clearer picture of the physical bases of the traction law, and also would be an aid in developing traction laws that better describe the LDZ phenomenon.

The cross-sectioning method for determination of key compressive

failure micromechanisms worked very well. The process allowed successive layers to be removed with a precision on the order of half a fiber diameter. The result was a complete picture of the failure mechanisms within the LDZ, as presented in chapter 5.

Progressive cross-sections provided an indication of the sequence of micromechanism occurrence. However, such studies revealed the state of damage at one instance, since the cross-section specimen contained an LDZ of finite length. The conclusion that individual tow fiber microbuckling consistently led to warp tow kinking as the tip of the LDZ advanced involved some speculation; i.e. the grounds for this conclusion lie in the fact that fiber microbuckling was the primary mechanism at the tip of the LDZ, for different LDZ lengths. It would be ideal but very difficult to monitor the evolution of the failure mechanisms *in situ*; a destructive evaluation process is necessary.

The cross-sectioning technique had certain limitations. The most important assumption involved with such studies is that the pictures obtained are representative of a known plane of view. In reality, it is virtually impossible to consistently grind on a parallel plane. Even with automated grinding/polishing equipment, successive cross-sections were never parallel. Furthermore, the woven fiber architecture of the facesheet material resulted in regular fiber undulations; uniform fiber cross-sections were not an indication of parallel planes. When dealing with measurements of phenomena at the fiber lengthscale (the kink band inclination or fiber rotation angle for example), the orientation of the plane of view must be known in order to obtain an accurate measurement.

It may be argued that the relative degree of parallelism between successive cross-sections is unimportant, since the literature typically presents kink band measurements in ranges. If the conclusions drawn from

the present study are reasonable, then the opposite extreme holds: only one cross-sectioning study of one LDZ is necessary to determine the evolution and type of critical micromechanisms. If this is true, another limiting factor, the large amount of time necessary to obtain quality cross-section photography, may be circumvented.

The other limitation to the cross-sectioning technique was the occasional appearance of voids. The voids were a result of material being ground away in large fragments. Currently, no method is known that would prevent void creation. Although voids did not affect all specimens, the possibility exists that a void would "mask" key phenomena such as microbuckling at the LDZ tip. If a void occurred far in the wake of the LDZ, where the damage mechanisms remain fairly consistent with respect to transition into different mechanisms, it would not be considered as an obstacle to accomplishing the goal.

6.2   Interrogation of Damage Zone Model

This section discusses the interrogative process utilized to determine the validity of the DZM. Specifically, the damage growth model and FEM are analyzed in the context of how well they provided for a consistent analysis tool. The investigative process/methodology is also discussed. Its effectiveness, as well as its relative importance in the context of damage tolerant design is discussed.

6.2.1   Damage Growth Model

The damage growth model is implemented in order to determine the LDZ growth and ultimate failure load characteristics. It is robust, efficient, and simple to use. Figures 5.30-5.35 show that traction law 1 results in excellent

correlations with LDZ growth data for *all* panel sizes of *both* materials. If the traction law is truly a material property, this type of correlative, or indeed predictive, power is expected. The LDZ growth response predicted for traction law 2 does not correlate with experimental data as well, as shown in figures 5.30-5.35.

It was found that there were a variety of traction laws that provided a good correlation with the experimental data. The sensitivity to σ_c and v_c listed in table 4.3 indicates that small variations in either parameter would still result in adequate correlations. As discussed above, direct determination of the traction law would resolve this ambiguity.

Figures 5.30-5.35 and table 5.3 clearly indicate the inability of the damage growth model to predict the critical LDZ length as accurately as LDZ growth behavior. The critical LDZ length is always over-predicted. Unfortunately, the critical LDZ length may be as important as the ultimate failure stress in the context of damage tolerant design. In-service inspections would easily be able to detect LDZ lengths via visual inspection. The current traction law results in an unconservative prediction, a result that is undesirable.

The predictive power of the DZM using the current traction law weakens as it is used to predict other phenomena. An example of this is the ultimate failure load correlations, tabulated in table 5.2 for both traction laws. While traction law 2 results in more conservative failure load values, the accuracy is not as good compared to the predictions of LDZ growth. The lack of accuracy may be due to the failure prediction technique. The current method is used strictly for load control tests, and was implemented as a first approximation for the failure load. Theoretically, load control test results would be consistent with DZM predictions in that LDZ growth would occur to the predicted length,

and failure would occur at the predicted maximum load. However, such a proposition is speculative. Further experiments can determine the applicability of the DZM to load control schemes. In order to more accurately assess the DZM's ability to predict the failure load, another method must be investigated which is appropriate for pure displacement control tests [5]. In particular, the elastic strain energy stored in the specimen away from the hole plays an important role in determining the stability of damage propagation.

6.2.2 Finite Element Model

The purpose of the FEM is to obtain analytical results for the local strain distribution. It can be used for calibration of the traction law (via the spring law), or for validation of the DZM by correlation with local strain behavior observed during experiment. In order to accurately investigate the DZM, the LDZ must be modeled correctly. In the present case, the LDZ is modeled as a continuous spring acting over a distance equivalent to the LDZ length. Discrete nonlinear springs are used as an approximation to a continuous spring, as discussed in chapter 4.

A two parameter linear strain softening traction law is used in the damage growth model. Initial tests of the FEM resulted in processing errors when an equivalent two parameter linear softening spring law was used. Specifically, an equivalent spring law indicates that a force exists in the springs at zero spring displacement. This resulted in errors due to the introduction of negative eigenvalues into the system matrix.

Several modifications were made to the spring law in an attempt to circumvent the problems encountered during FEM analysis. It was found that the relative *smoothness* of the spring law mattered. For example, a parabolic spring law (see figure 6.1) always resulted in error-free runs, while spring laws
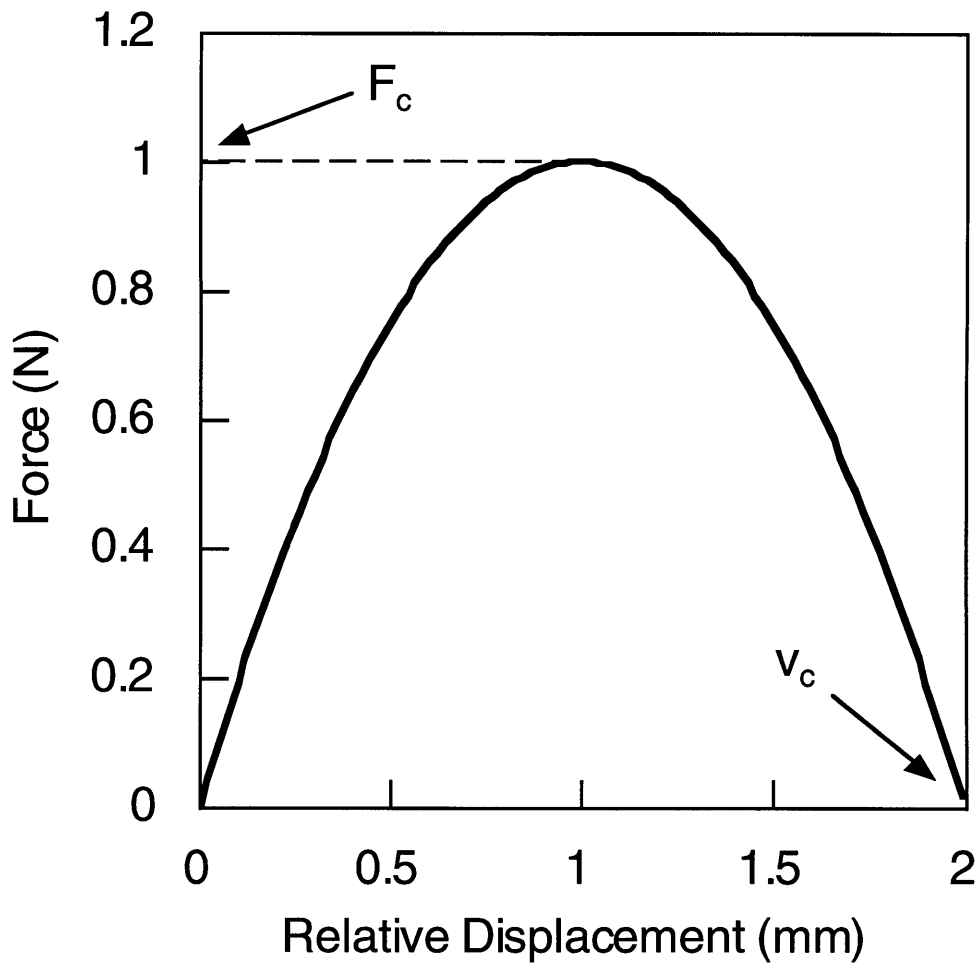
Figure 6.1   An example of a parabolic nonlinear spring law.

with discontinuous slopes typically resulted in errors. The smoothness of the spring law is also governed by the two parameters F_c and v_c. If either parameter was sufficiently large in comparison with the other, errors often occurred. However, a parabolic spring law never resulted in errors during this investigation, regardless of the ratio of the parameters. Rapid changes in slope, such as those associated with ramp functions transitioning from positive to negative slopes, also causes errors.

A spring law was chosen for the FEM equivalent to that shown in figure 4.18. The initial region begins with zero spring force at zero relative displacement. This point was chosen in order to avoid the problems associated with an initial force in the springs due to non-zero force at zero relative displacement. The first segment of the spring law is a parabola. A parabolic relationship was chosen in order to obtain a smooth transition from the initial point to the second linear "softening" segment; i.e. the parabola and the linear segment join at a point where the slope of both lines are equal. The linear softening portion of the spring law accounts for approximately 95% of the curve. A linear segment was chosen in order to match the traction law shape to that used in the damage growth model.

It should be noted that in general, the physical origin of the traction law/spring law is not discussed in the present work. The assumption of a two parameter linear strain softening law was chosen as an approximation to the softening behavior observed during experiments; i.e. the present traction law is an attempt to add a first-order physical basis to the DZM. Subsequent work is required to relate the two traction law parameter values and the *actual* physical parameters (e.g. fiber and matrix properties and microstructural parameters). Micromechanics models may be appropriate for establishing the connection between the different levels of material response. Notwithstanding

the desire to increase the physical basis, the current models may be applied in the absence of detailed supporting micromechanics models. When an increased modeling capability is achieved, it may be linked with the damage zone model.

FEM tests indicated that all of the spring law parameters investigated during local strain predictions and correlations, as well as those used to determine model sensitivity, were acceptable. However, although convergence was reached in all cases, traction law 1 caused severe problems as discussed below.

The COD comparisons, shown in figures 5.48-5.51, indicate inconsistencies between the models. This is evident particularly in the case of traction law 1 and a long crack, shown in figure 5.49. Figure 5.48 shows that for a shorter crack, significantly higher COD's are achieved. For the longer crack, almost zero COD results along the entire length. This result can be attributed to numerical issues associated with nonlinear spring laws, as discussed above.

6.2.3 Consistent Method

The problems associated with the current spring law, namely the shape inconsistency with the traction law and the numerical issues associated with the FEM, can be overcome. A consistent traction law exchange between the damage growth model and the FEM can be achieved if the tractions obtained from the growth model are directly applied to the crack in the FEM; i.e. no springs are used. For a given experimentally observed LDZ length and applied load, the convergence algorithm within the damage growth model can be used to obtain a discrete traction distribution. Specifically, the stress σ_i at n locations along the crack face (see figure 4.5) can be obtained. The algorithm is

modified such that n corresponds to the exact number of nodes along the crack in the FEM. The discrete stresses are converted into forces:

$$F_i = \sigma_i * \frac{(crack\ length)\ (tk)}{(\#\ of\ nodes\ on\ crack)}$$

(6.1)

The consistent traction law method (CTM) ensures that the same traction is applied to the crack in both models. The code utilized to obtain the discrete tractions can be found in Appendix C.

In order to implement the CTM, the damage growth model was modified to permit loading cases in which the crack faces overlap (i.e. a crack opening for an LDZ loaded in compression). For a given crack length and applied load, the crack may exhibit crack overlap behavior, depending on the magnitude of the closing tractions. Therefore, an assumption was made with regard to negative crack face displacements which specified assignment of σ_c at locations of negative COD. Figure 6.2 illustrates the traction law condition governing negative crack displacements. It should be noted (as shown in figure 6.2) that σ_c is assigned regardless of the magnitude of negative displacement. It should also be noted that discussion pertaining to the physical translation of the assumption is limited to the fact that the unbuckled fibers are exerting a greater force than those which have buckled.

Figures 6.3 and 6.4 show COD comparisons between the damage growth model and the FEM for both (short and long, respectively) crack lengths using traction law 1. Very good agreement is achieved. Figure 6.4 illustrates the crack closing phenomena found in the long crack, which also correlated very well. Comparatively, the nonlinear spring method results in a poor COD correlation, as shown in figure 5.49. Figures 6.5 and 6.6 show COD comparisons between the damage growth model and the FEM for both crack lengths using traction law 2. As when using discrete nonlinear springs, the
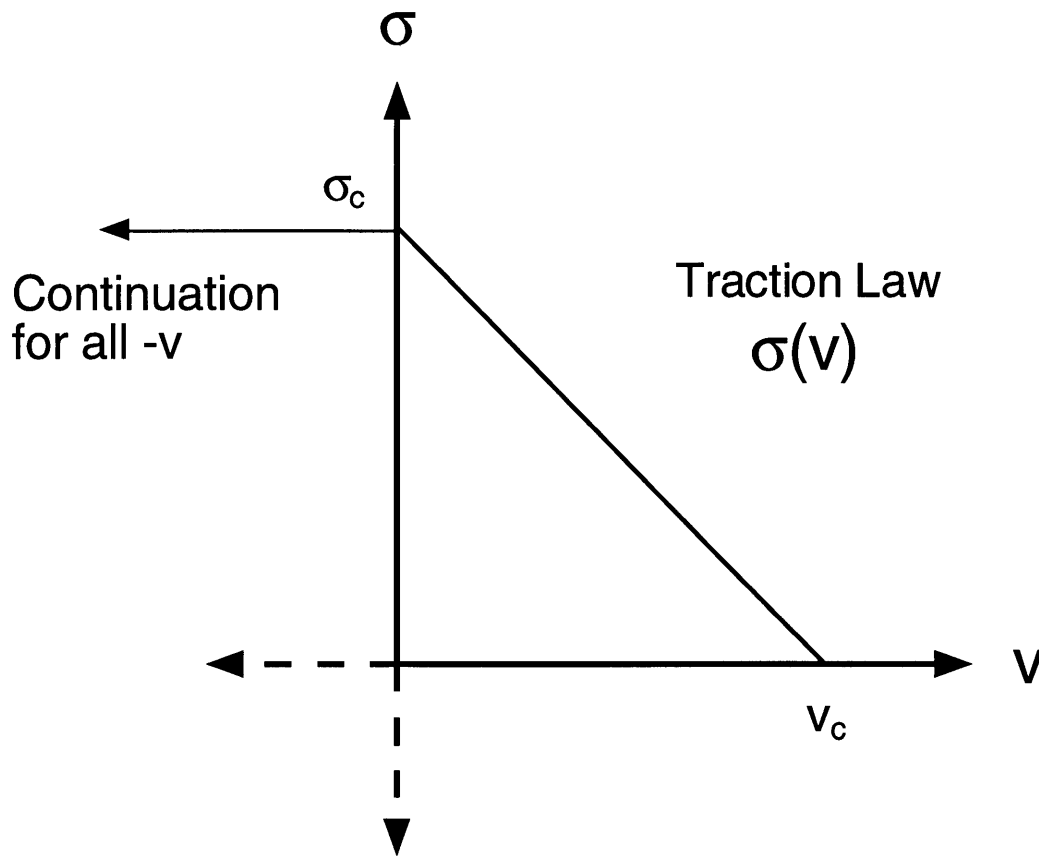
Figure 6.2   Two parameter strain softening traction law modified to allow
crack overlap displacements.
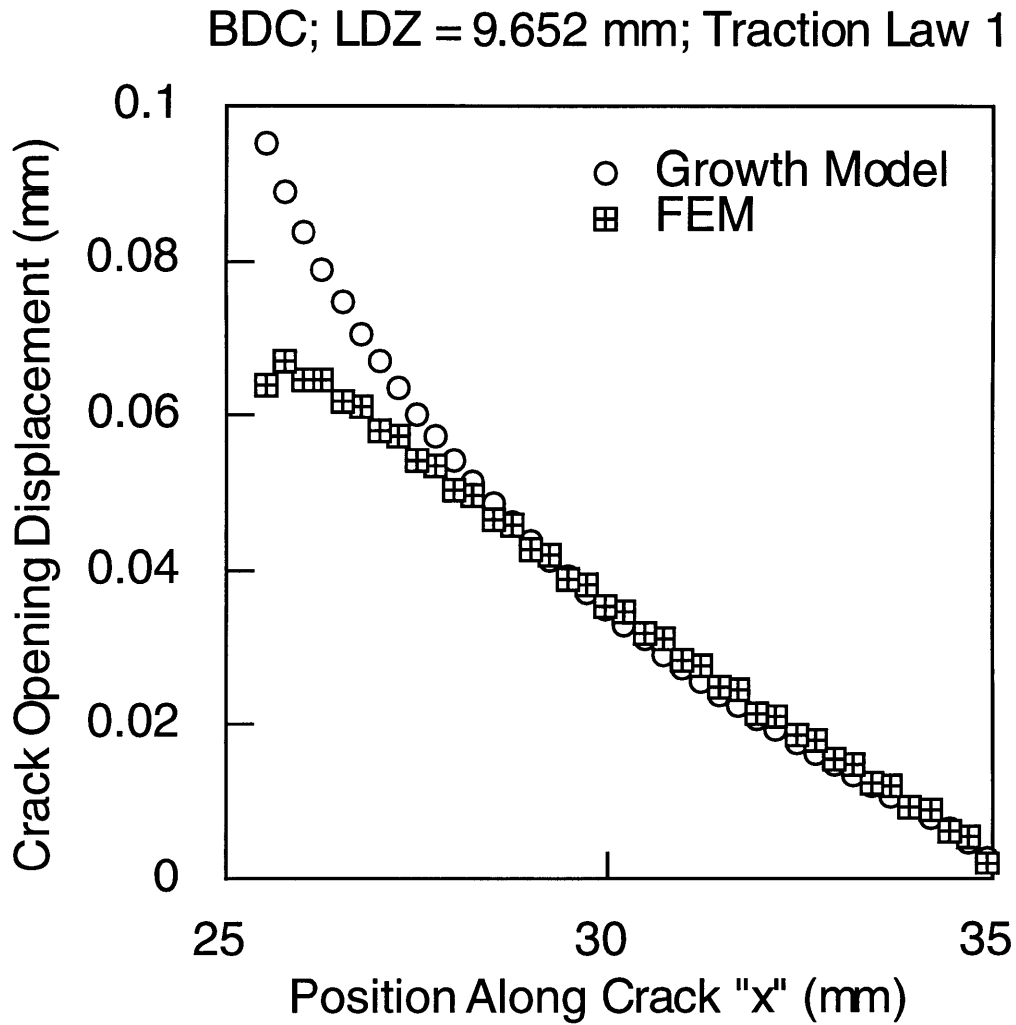
Figure 6.3   COD comparison for short LDZ using traction law 1 and the CTM.

BDC; LDZ = 20.32 mm; Traction Law 1
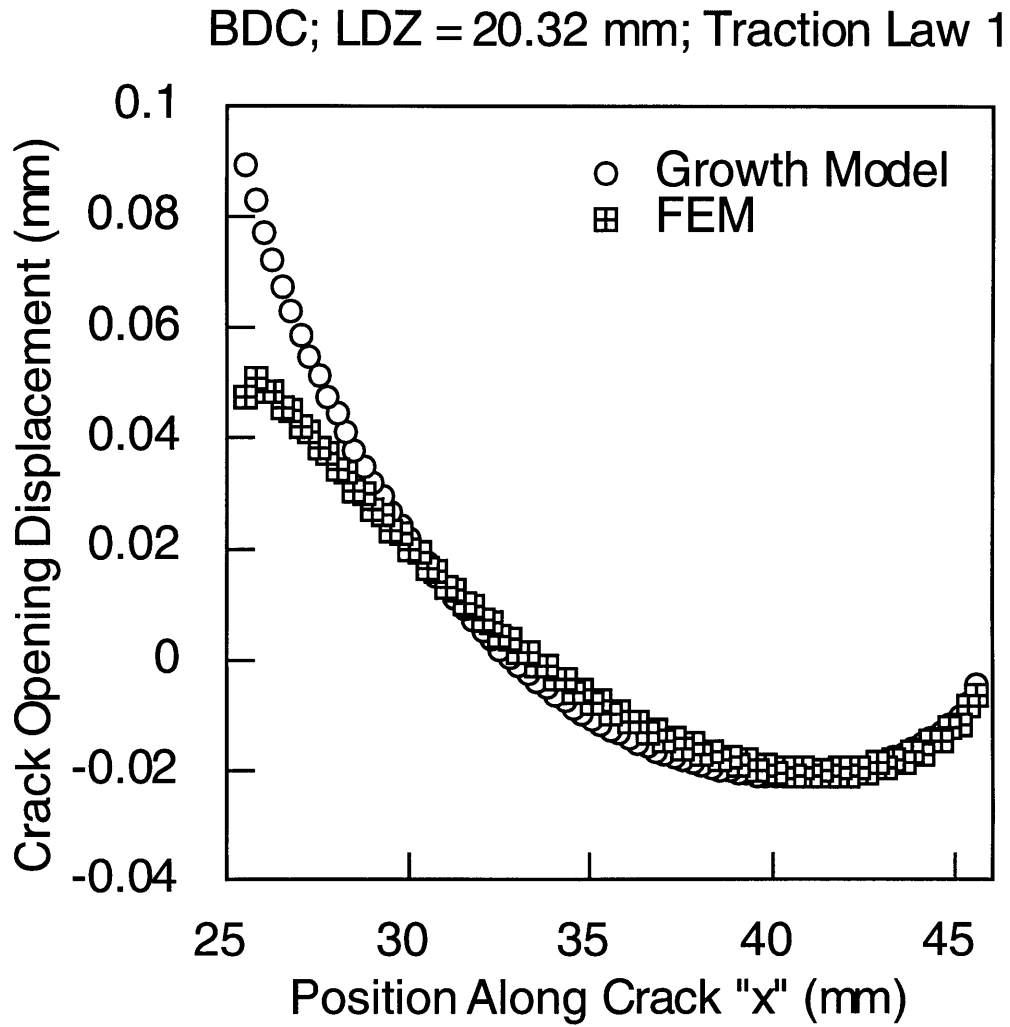
Figure 6.4   COD comparison for long LDZ using traction law 1 and the CTM.
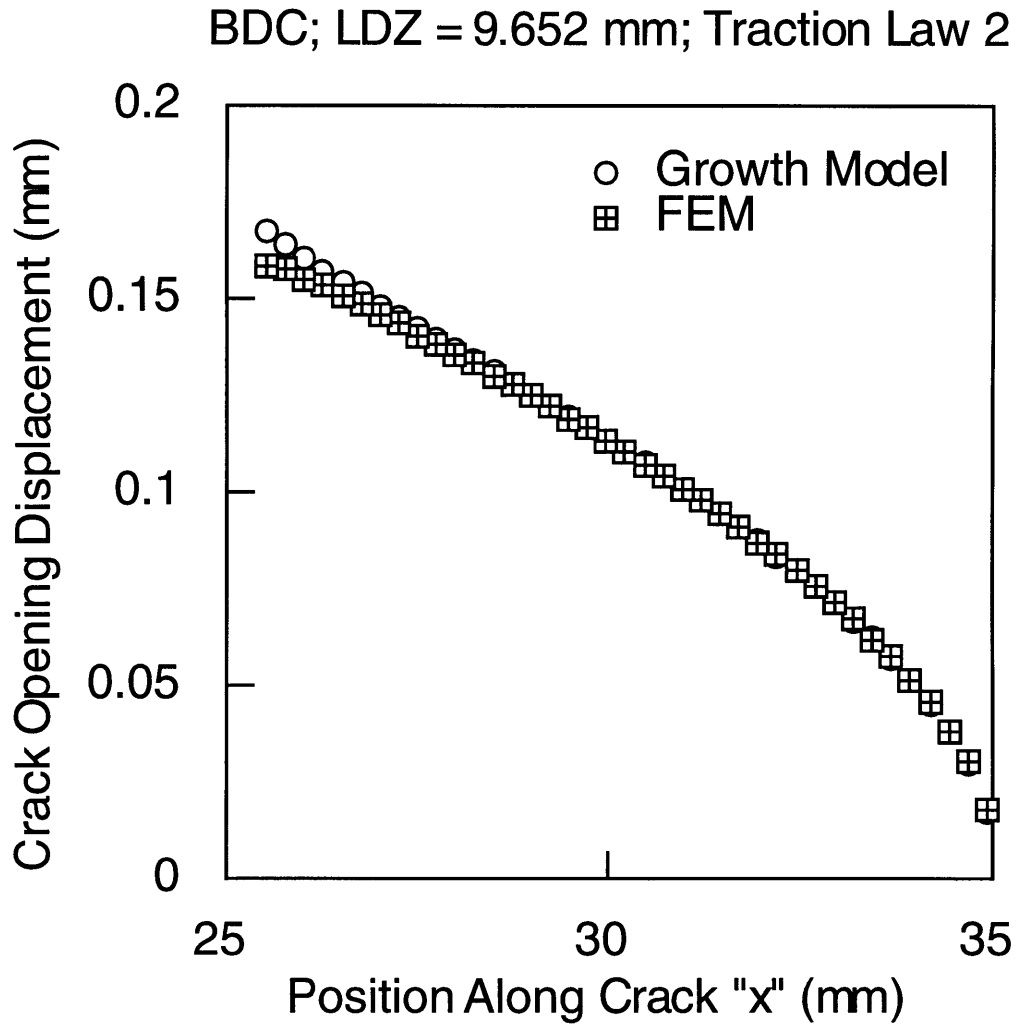
Figure 6.5   COD comparison for short LDZ using traction law 2 and the
CTM.

BDC; LDZ = 20.32 mm; Traction Law 2
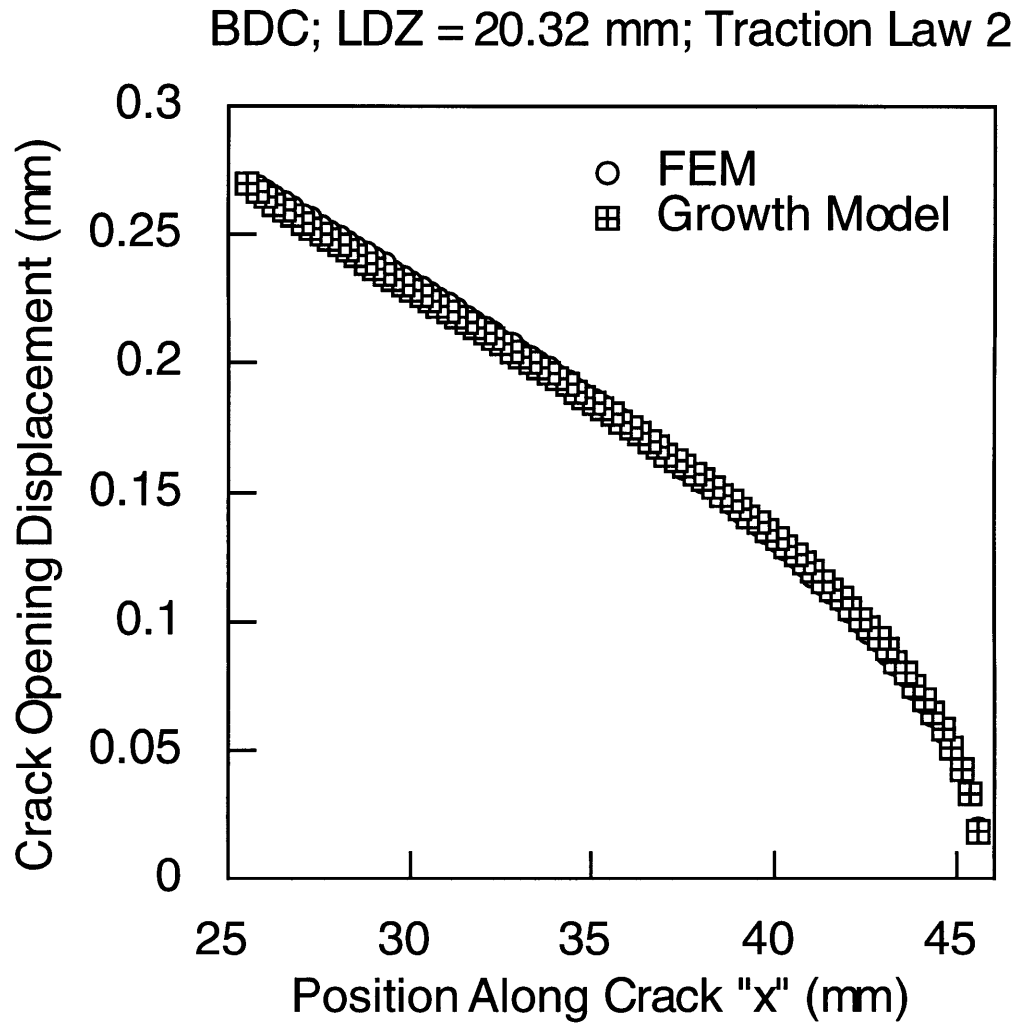
Figure 6.6   COD comparison for long LDZ using traction law 2 and the CTM.
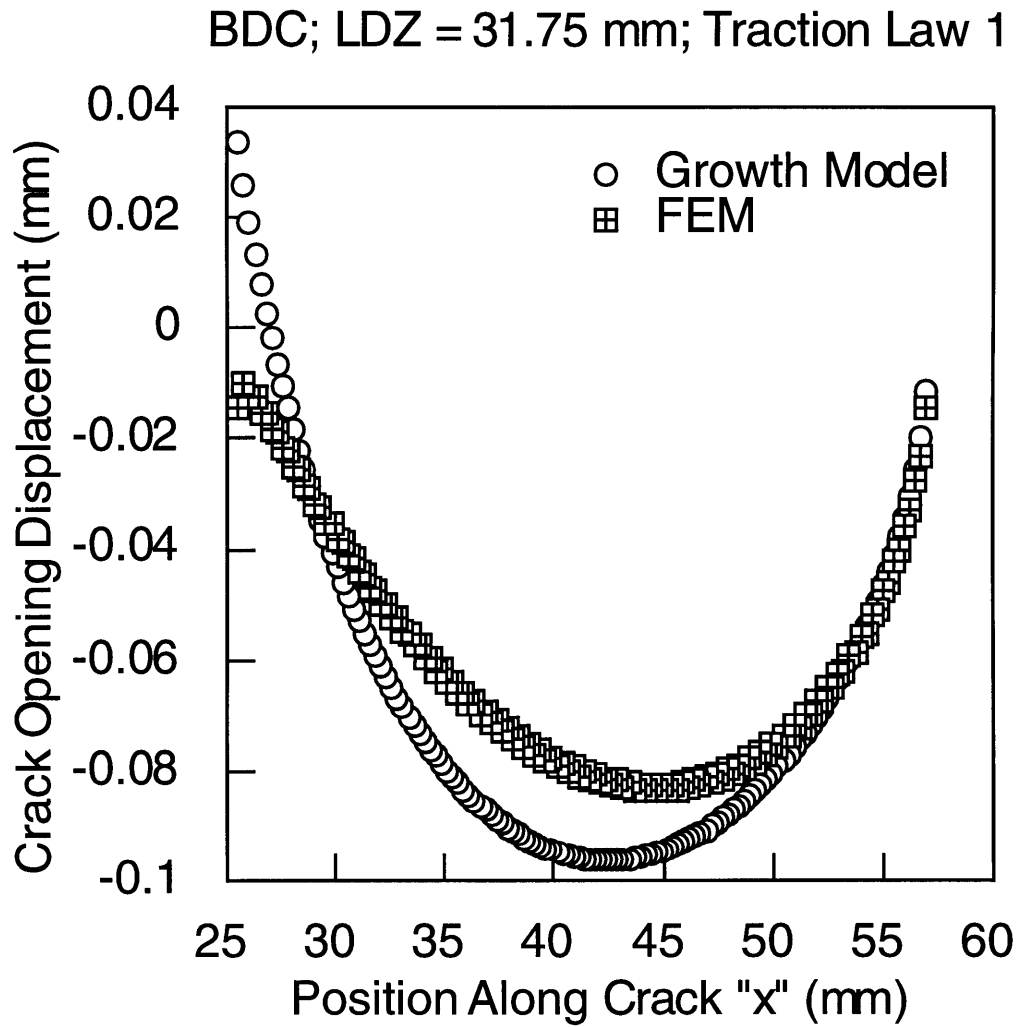
Figure 6.7   COD comparison illustrating complete crack overlap for a
relatively long LDZ using traction law 1 and the CTM.

correlation is excellent. Figure 6.7 shows the COD comparison for a much longer crack (31.75 mm) using traction law 1. Clearly, traction law 1 forces the entire crack to overlap, presumably due to the effect of a large σ_c value. Despite this, the correlation is relatively good. The CTM allows for a robust and consistent evaluation of the two parameter strain softening traction law in all cases. It should be noted, however, that in cases where the traction law needs to be obtained via strain measurements, discrete nonlinear springs are easier to use for calibration.

The CTM was also used to determine the inconsistencies in the predicted local strain behavior due to the differences between the spring law shape and the traction law used in the damage growth model. Figures 6.8-6.19 show local strain predictions for both materials and traction laws using the spring method and the CTM. Generally, the results from the two methods are the same, particularly when using traction law 2. Figure 6.13 shows some error associated with traction law 1 for the case of long cracks.

The results of the DZM investigation presented in chapter 5 indicate that a two parameter linear strain softening law does not adequately predict the three key experimentally observed phenomena (strength, strains, and LDZ growth). Despite this result, the DZM may be the appropriate choice for notched sandwich panel damage tolerant design. The promising correlations that were presented warrant further experiments and investigation of different traction laws. The most important result presented throughout this work is the establishment of a methodology with which mechanism-based models can be investigated/validated. The framework established is necessary in order to determine if the DZM can accurately predict experimentally observable phenomena and be used as a damage tolerant design tool.
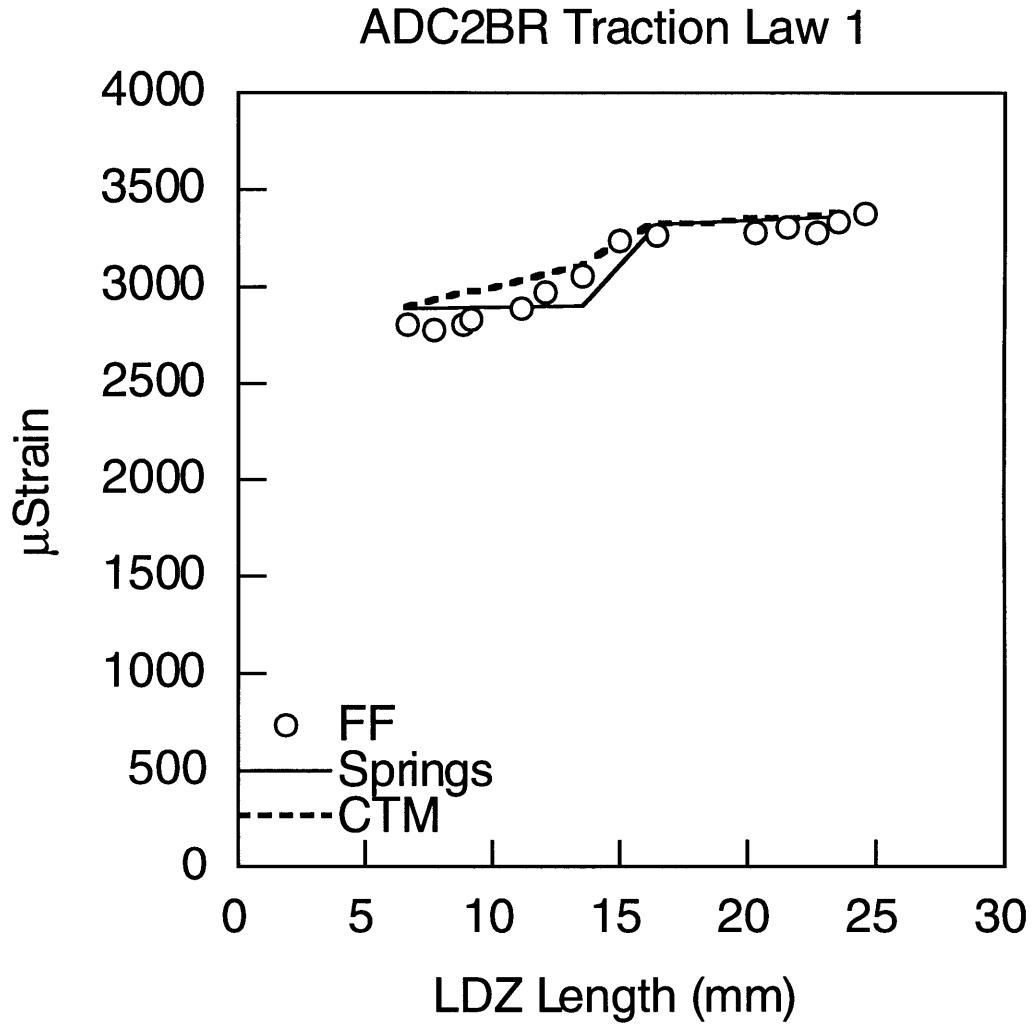
Figure 6.8   Far field strain correlation of M4 specimen using traction law 1 and the CTM.
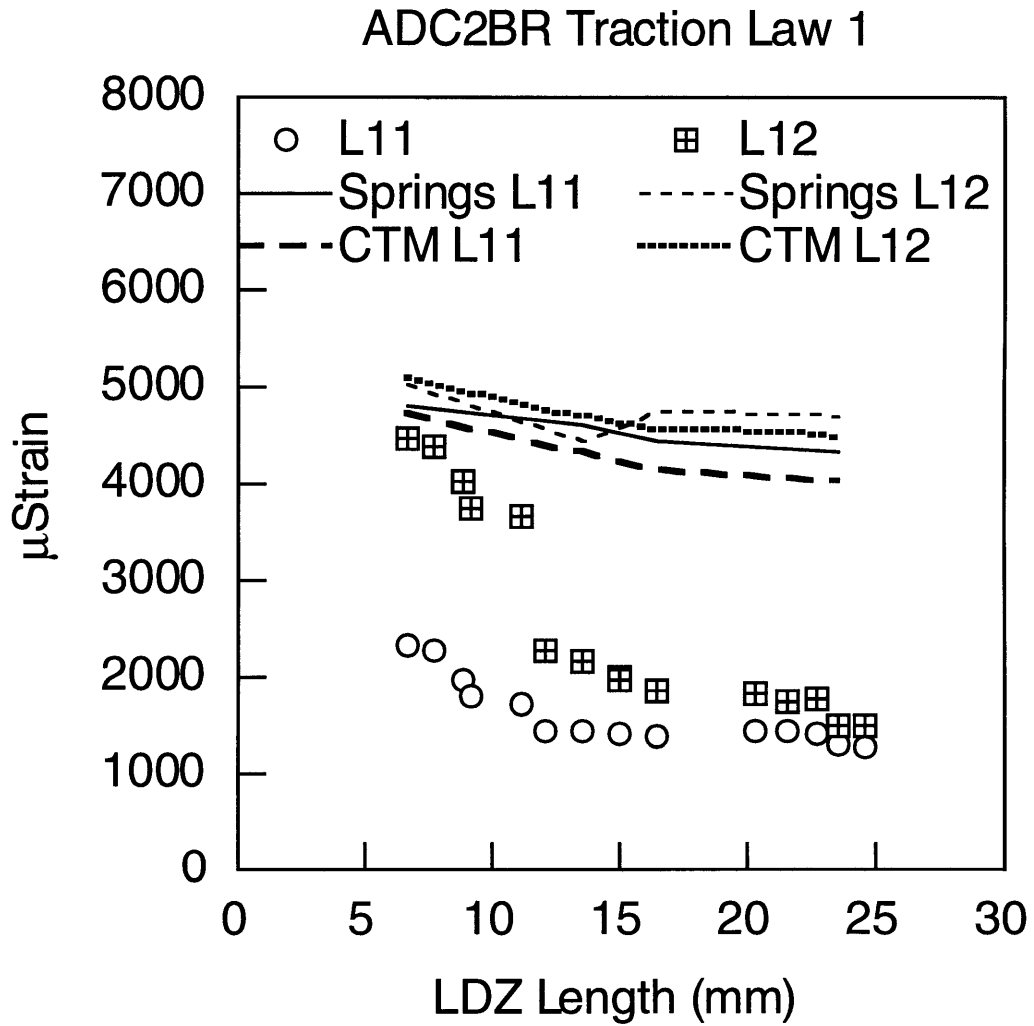
Figure 6.9   Local strain correlation (1 of 2) of M4 specimen using traction law 1 and the CTM.
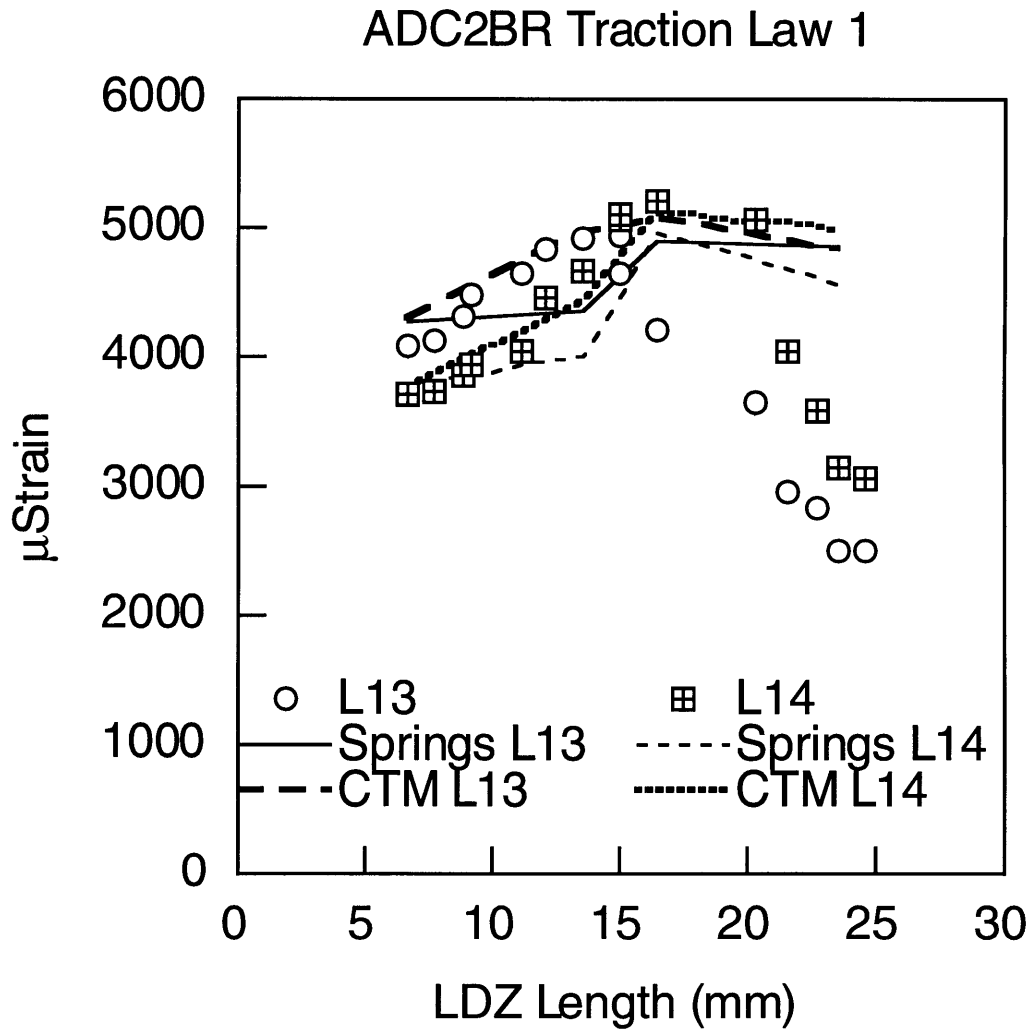
Figure 6.10   Local strain correlation (2 of 2) of M4 specimen using traction
law 1 and the CTM.
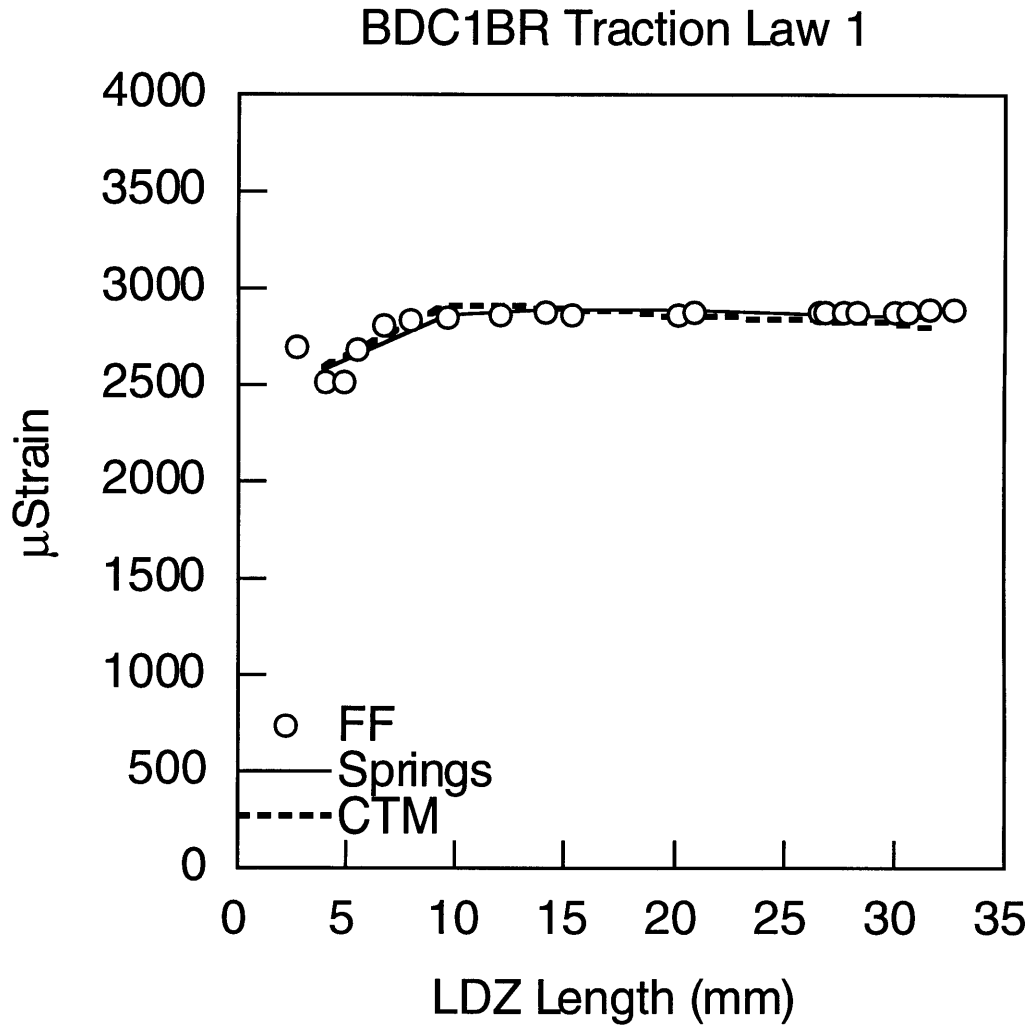
Figure 6.11   Far field strain correlation of M5 specimen using traction law 1
and the CTM.
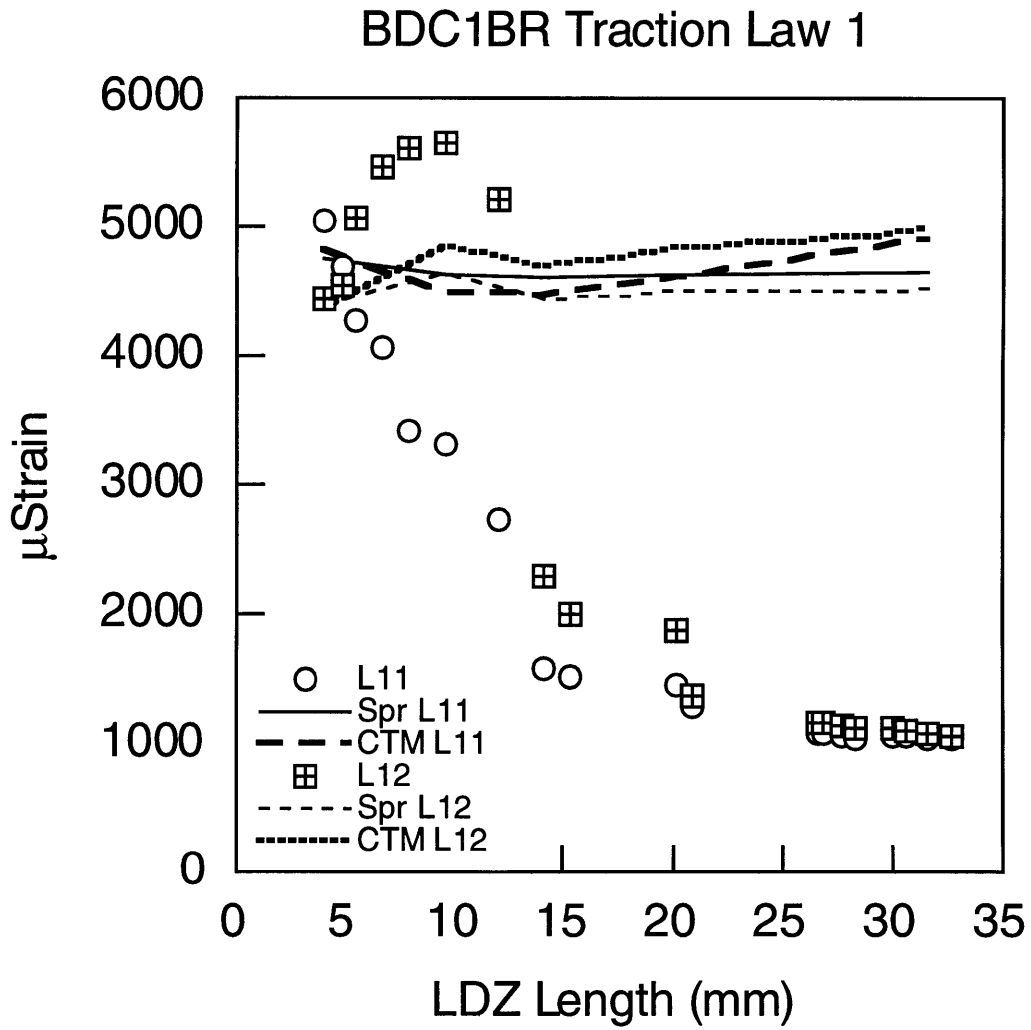
Figure 6.12   Local strain correlation (1 of 2) of M5 specimen using traction
               law 1 and the CTM.
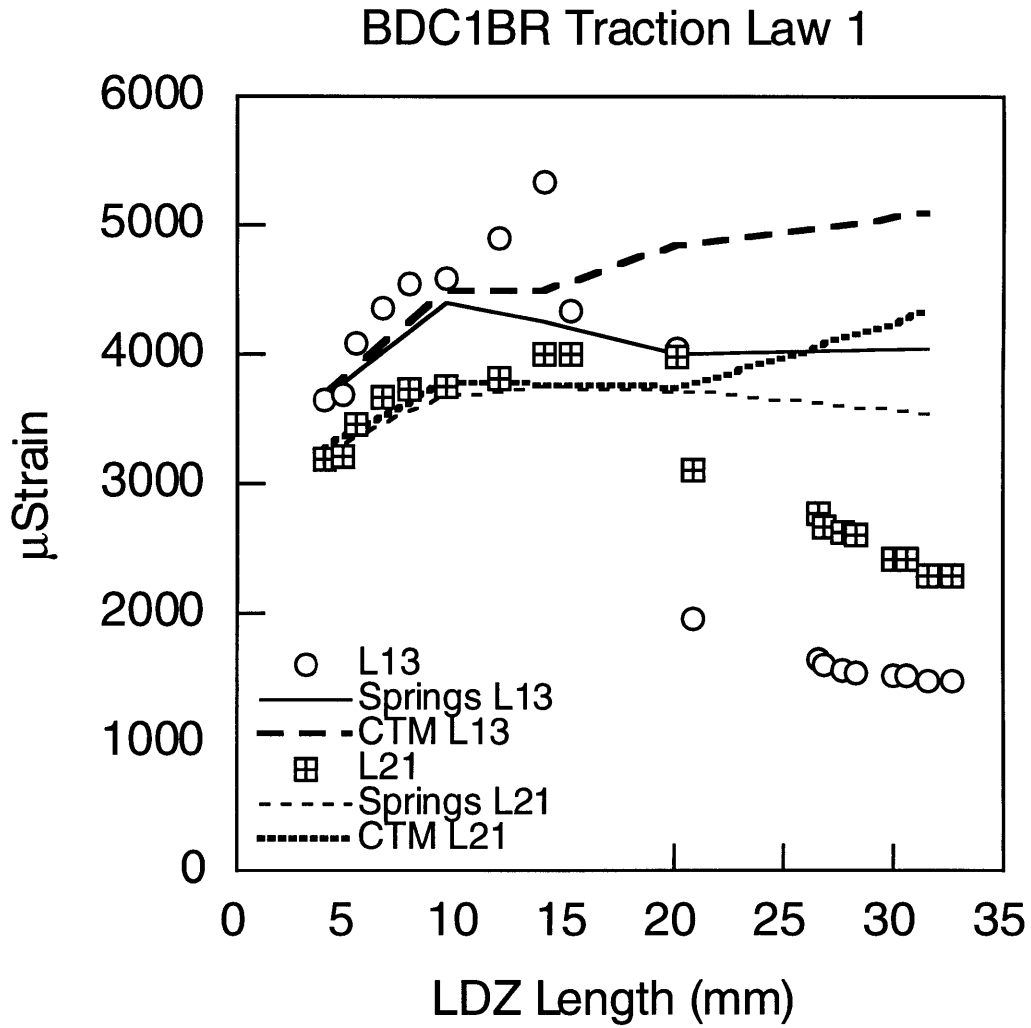
Figure 6.13   Local strain correlation (2 of 2) of M5 specimen using traction
law 1 and the CTM.

ADC2BR Traction Law 2
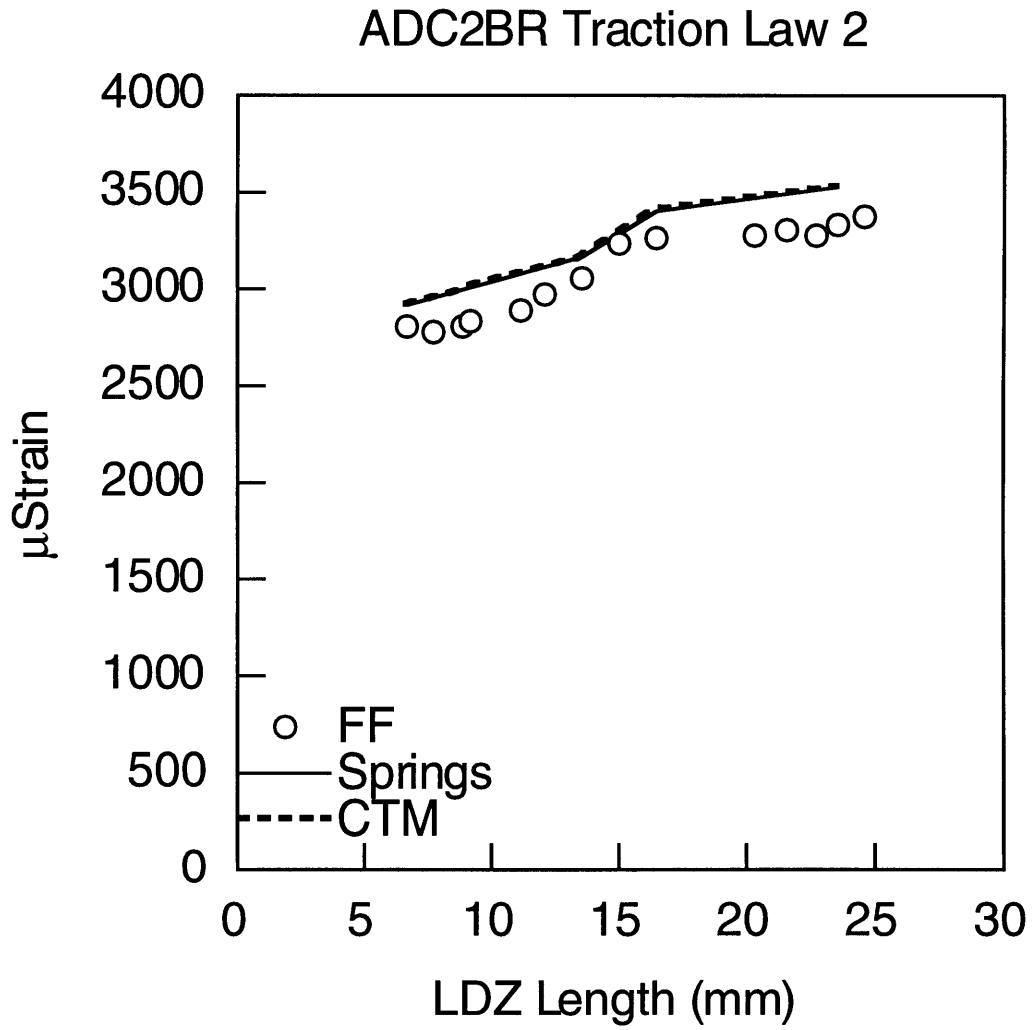
Figure 6.14   Far field strain correlation of M4 specimen using traction law 2 and the CTM.
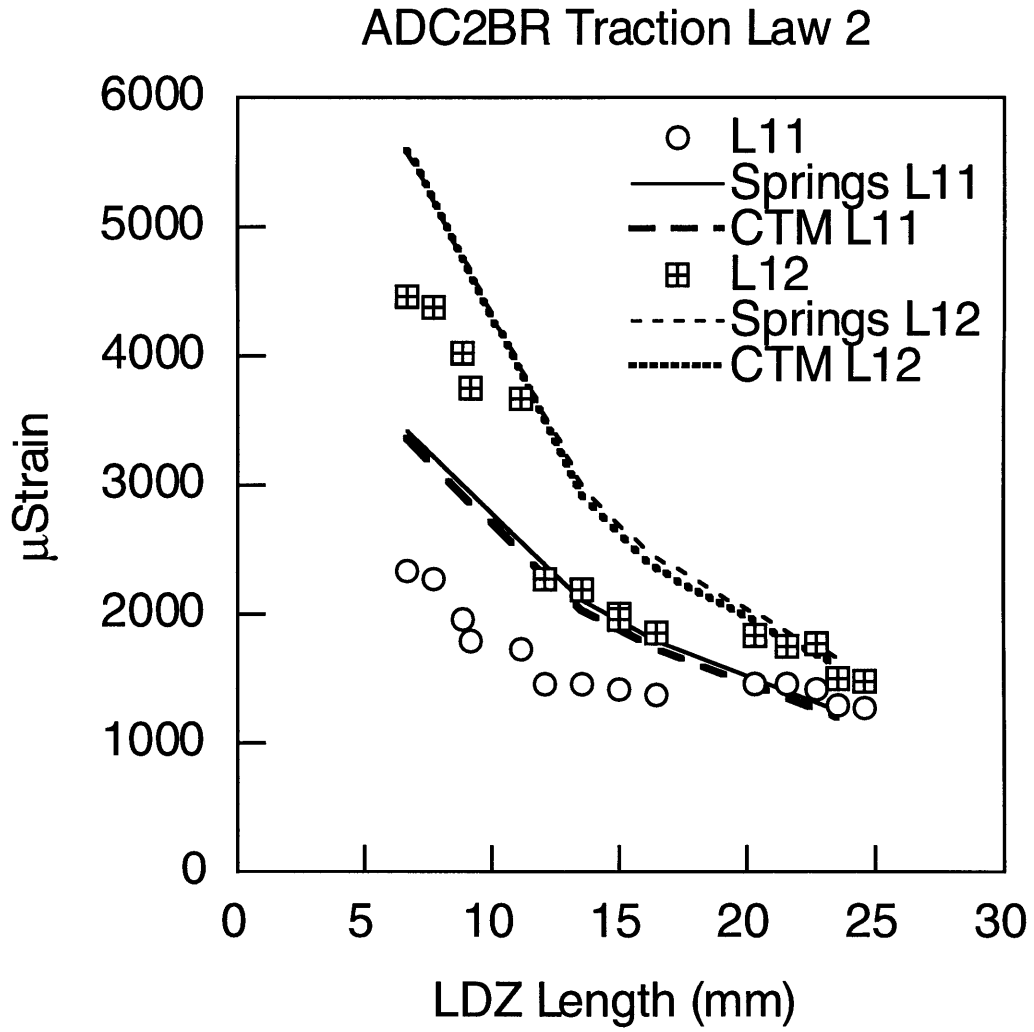
Figure 6.15   Local strain correlation (1 of 2) of M4 specimen using traction law 2 and the CTM.

ADC2BR Traction Law 2
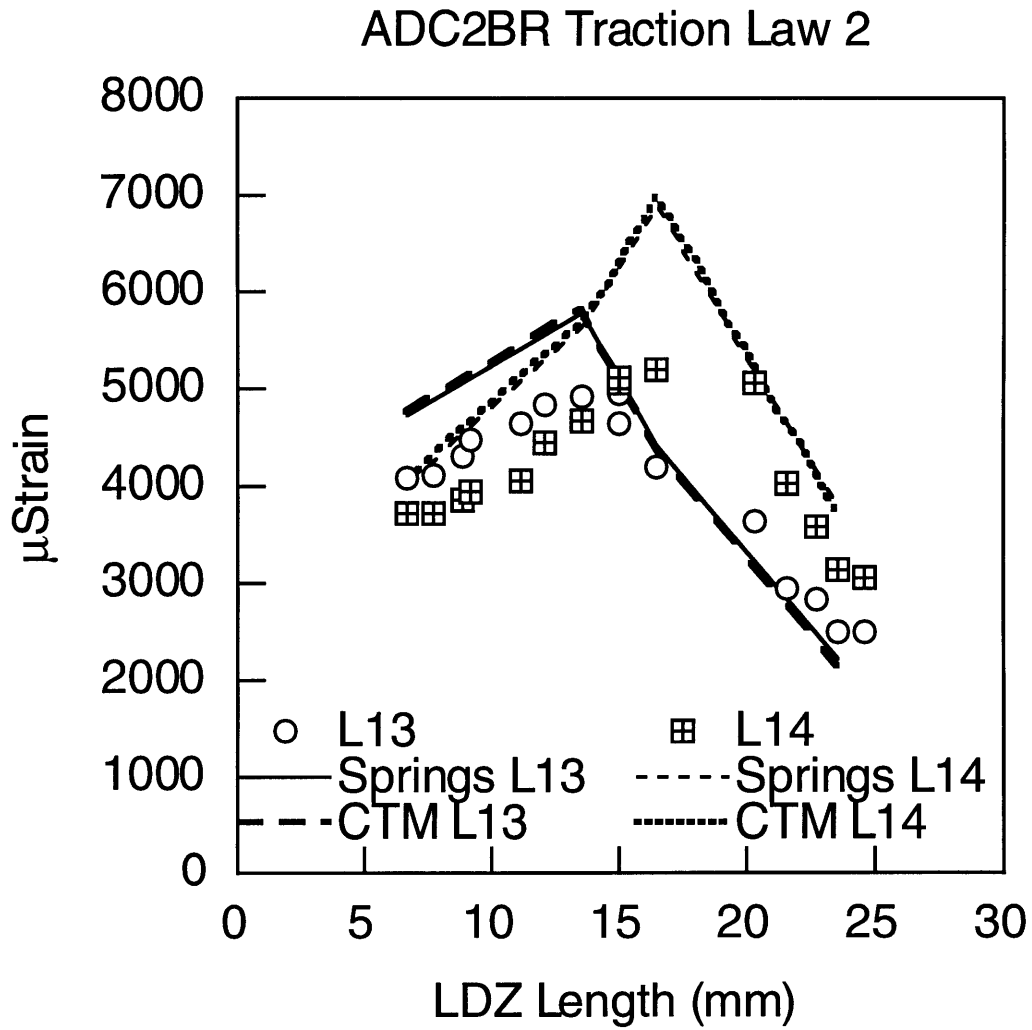
Figure 6.16   Local strain correlation (2 of 2) of M4 specimen using traction
law 2 and the CTM.
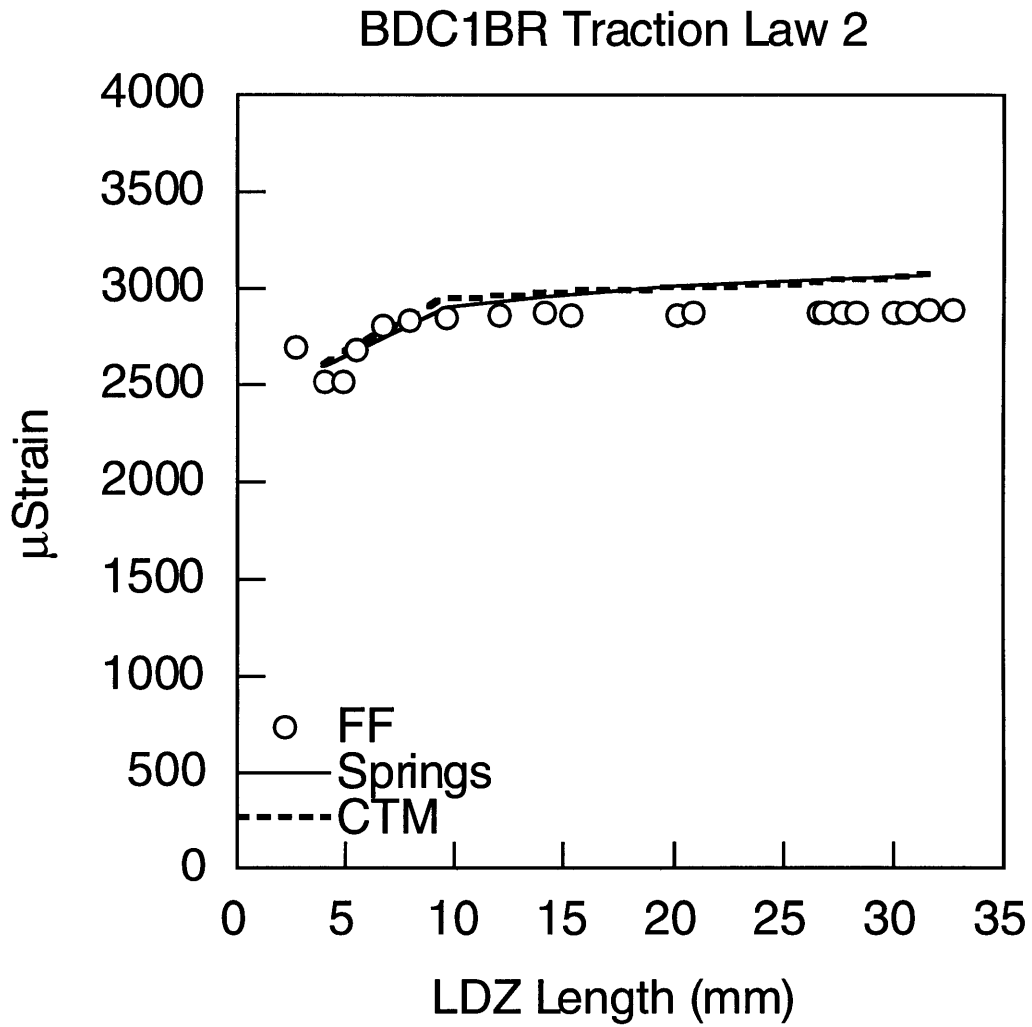
Figure 6.17   Far field strain correlation of M5 specimen using traction law 2
and the CTM.

BDC1BR Traction Law 2
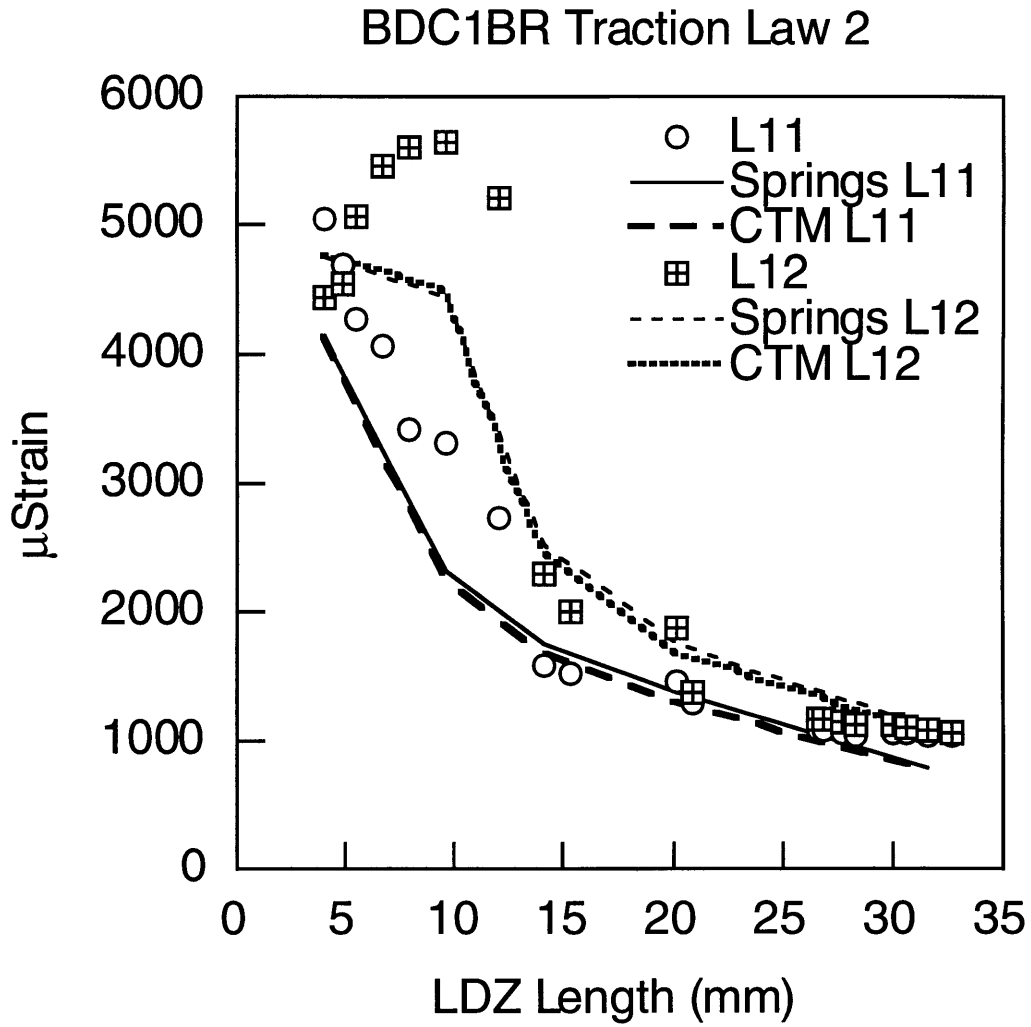
Figure 6.18   Local strain correlation (1 of 2) of M5 specimen using traction
law 2 and the CTM.
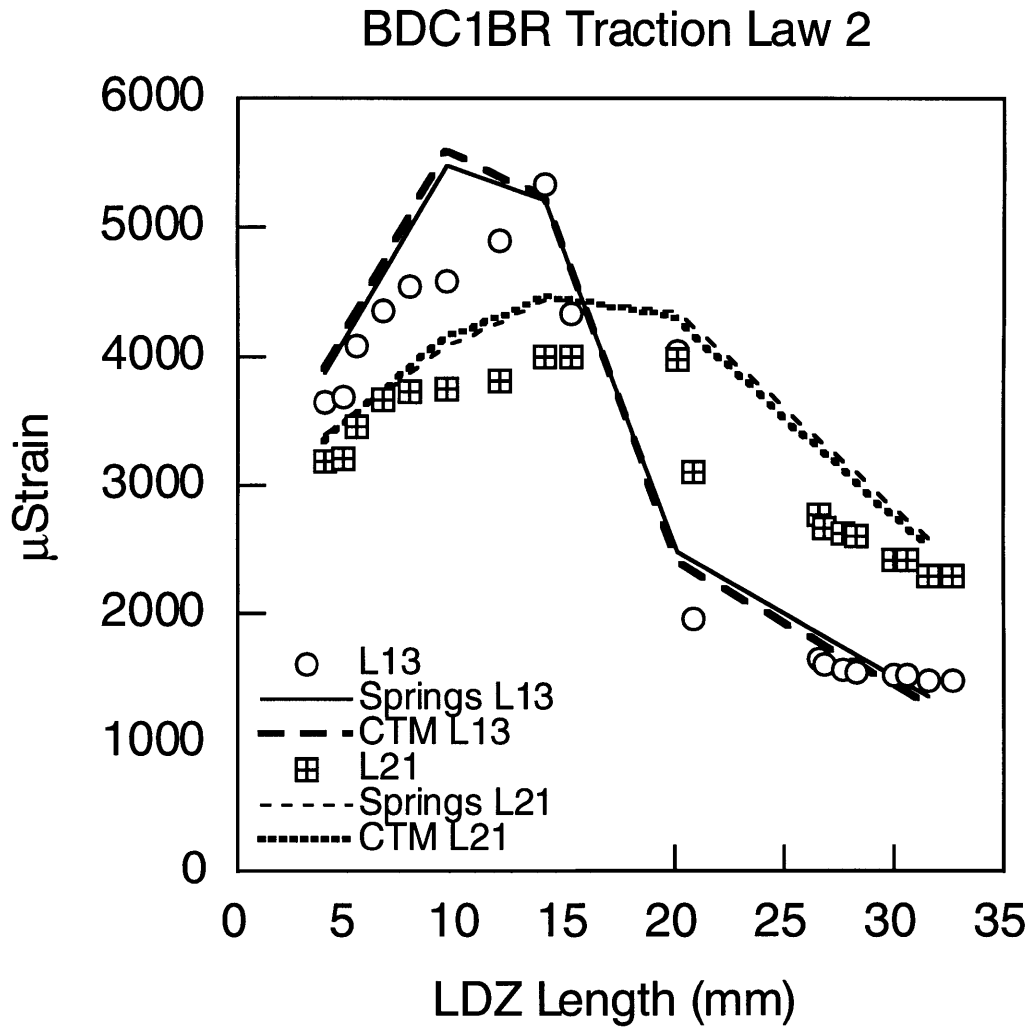
Figure 6.19   Local strain correlation (2 of 2) of M5 specimen using traction
law 2 and the CTM.

6.3   Implementation of Damage Zone Model

This section discusses the possible practical applications of the DZM.

6.3.1 Current Traction Law

The two parameter linear strain softening traction law does not accurately predict the three experimentally observed phenomena. It does result in good correlations with independently calibrated traction laws; i.e. a different traction law for LDZ growth and local strains.

6.3.2 Effectiveness of Damage Zone Model

At this point, a determination on the effectiveness of the DZM would be premature. The reason for this is that only one form of traction law was investigated. Arguably, the more important question lies in determining if the LDZ is indeed the key compressive damage mechanism in notched sandwich panels under various strain rates. As discussed in the first section of this chapter, further tests are necessary to determine strain rate dependence. In any case, the LDZ has been shown to be the key failure mechanism in low strain rate environments. Therefore, the DZM remains a simple model which has the promise of predicting key experimentally observed phenomena. Different traction laws must be investigated, and perhaps more importantly, different experimental techniques should be used to more quickly and accurately determine the traction law. As greater physical basis is added by such experiments, the DZM can be interrogated to determine its effectiveness.

6.3.3 Real-World Application

Assuming that the DZM is the correct model as determined by further experiments and analysis, its incorporation into damage tolerant design

processes would be very simple and efficient. The advantage of the DZM is that once a traction law is obtained for a given material, all of the information necessary to apply a damage tolerant design approach is available. Clearly, knowing a material's traction law *a priori* would benefit both the design and inspection processes of airframe applications of composite-honeycomb sandwich panels. The power of the DZM is evidenced by its ability to predict. True prediction is the ability to determine *a priori* any of the experimentally observable phenomena for *any and all* structural sizes. This can only be accomplished with a mechanism-based model.

6.3.4 Other Techniques

The only modeling framework presented in this work was the DZM framework, aside from the net-section stress calculations. Other techniques, such as the Mar-Lin correlation, were not investigated. Figures 5.6 and 5.7 illustrate the hole size effect commonly correlated with models such as the Mar-Lin correlation. However, the present investigation was only concerned with the validation of a mechanism-based model. Future investigations should continue to focus on such models. The use of strictly correlative/fitting approaches have severe limitations in the context of modeling, as discussed in chapter 2, and do not advance modeling predictive power.

6.4 Summary

The experimental investigation provided consistent results that established the LDZ as the key failure mechanism in notched composite-honeycomb sandwich panels. The test fixture and test method utilized resulted in reliable results, as evidenced by the repeatability of the results and the good alignment throughout the tests.

The DZM was chosen in part because of data from previous studies, which contained good correlations with compressive damage zone growth. A two parameter linear strain softening traction law was chosen as a representative LDZ constitutive behavior observed during experiments. Two models, the damage growth model and the finite element model, were used to investigate the ability of the DZM to predict three experimentally observed phenomena: the notched strength, local strain distribution, and LDZ growth behavior. The finite element model utilized a modified nonlinear spring law, which incorporated an initial steep parabolic region that transitioned into a linear softening region.

Results indicated that the current traction law was not able to predict all three phenomena. The logical conclusion is that the current traction law is not representative of the LDZ. Further experiments, analysis, and new techniques should be implemented in order to fully investigate the potential of the DZM, which has demonstrated limited predictive power in the present study. The established methodology provides a framework with which to investigate other, more physically-based traction laws.

CHAPTER 7

CONCLUSIONS AND RECOMMENDATIONS

This chapter discusses the conclusions of the present work. Following the conclusions, specific recommendations for future work are made.

7.1 Conclusions

7.1.1 Experimental Investigation

The experimental investigation established the linear damage zone (LDZ) as the critical compressive failure mechanism in notched (open hole) E-glass/epoxy-honeycomb sandwich panels. LDZs initiated at locations corresponding to the horizontal hole diameters, and appeared as distinct damaged areas. Further end-shortening resulted in semi-stable growth; the LDZs extended in an incremental manner in a direction perpendicular to the applied load. A significant amount of stable propagation was achieved prior to ultimate failure. Failure was characterized by the net-section failure of one facesheet, which occurred as a result of unstable LDZ propagation.

An investigation was conducted to determine the key microscopic damage mechanisms and consisted of cross-sectioning and surface inspection via scanning electron microscopy. It was found that out-of-plane microbuckling of individual warp tow fibers led to warp tow kinking immediately behind the LDZ tip. The LDZ wake was characterized by warp tow kinking of all warp tows, and transverse tow splitting.

Local strain gages revealed that the LDZ was characterized by a softening behavior. As the LDZ tip approached the "shadow" of a local strain gage, the strain measured by that gage steadily increased. A maximum strain was recorded by the gage when the LDZ tip was directly in its "shadow". As the LDZ tip propagated away from the "shadow", the strain measured by the gage decreased. The LDZ wake continued to retain a significant load carrying capability, as evidenced by nonzero strain readings far in its wake.

7.1.2 Analytical Investigation

The damage zone model (DZM) was chosen as the analysis framework to be applied to the current study. In contrast to many analytical/numerical models currently in use, the DZM possesses the ability to describe the key failure mechanism observed during experiment. Specifically, the DZM can model damage zone propagation.

In an attempt to add more physical basis to the DZM, a two parameter linear strain softening traction law, assumed to be a material property, was chosen to represent LDZ constitutive behavior observed during experiment. The DZM was investigated to determine if three experimentally observed phenomena could be predicted using the same traction law: the notched strength, local strain distribution, and LDZ growth behavior.

A framework and methodology was established in order to determine the validity of mechanism-based models. Specifically, two models were created and used to interrogate the DZM. The damage growth model was used to determine the DZM's ability to predict the LDZ growth behavior and notched strength. The finite element model (FEM) was used to determine the DZM's ability to predict the local strain distribution. Discrete nonlinear springs in the LDZ wake were used to model the LDZ as a continuous softening spring. A

modified spring law was used as an equivalent to the traction law used in the damage growth model.

It was found that the current traction law was not able to provide good agreement with all three phenomena. Although good correlations were achieved for the phenomenon which was used to calibrate the traction law, extension of the predictive capability to the other two phenomena resulted in weaker correlations. Despite the conclusion regarding the current traction law, the modeling framework and methodology established provide a robust tool for investigating the potential of adding physical bases to the DZM.

7.2 Recommendations for Future Work

Further experimental and numerical work is recommended in order to better assess the use of the DZM as a viable damage tolerance design tool.

7.2.1 Experimental Recommendations

- The strain rate dependence should be investigated; as noted in chapter 3 there was some evidence that faster loading rates resulted in less stable damage growth.

- The effect of specimen geometry should be investigated. Shorter, broader specimens should reduce the strain energy stored in the facesheet, and therefore affect the stability of LDZ growth.

- Since the open holes were used as an idealization of possible impact damage, other notches/damage should be investigated. Specifically, tests performed on sandwich panels with inclined slits or actual impact damage/penetration damage will give an indication on whether or not the LDZ is the driving failure mechanism in those cases as well.

- Further experiments should include a detailed strain mapping technique.

Currently, some techniques exist which may also measure the LDZ closing profile *in situ*.

- Any core effects should be investigated with tests done on otherwise identical specimens with different core materials.

- Information about the relative rate of strain increase/decrease compared to the applied strain rate and the LDZ propagation speed towards/away from the shadow of a local strain gage may be useful. Such information would lead to better traction law shape approximations.

7.2.2 Analytical Recommendations

- Pending results from further experiments, other traction laws should be investigated. Experimental results would yield the traction law directly.

- If necessary, and depending on the information obtained from experiments utilizing high definition zoom video to obtain information on the relationship between fiber rotation and LDZ length, a micromechanics analysis should be performed to add physical basis to the DZM.

- The FEM should be optimized. An adaptive meshing technique could be used to simplify the mesh and reduce run time.

- Dependent on the ability to obtain a traction law that provides an adequate prediction of damage growth, local strains, and ultimate strength, predictions of more realistic structural configurations should be made and tested.

References

1. Gibson, R. F., *Principles of Composite Material Mechanics*, McGraw-Hill Series in Aeronautical and Aerospace Engineering, ed. Anderson, J. D. McGraw-Hill, Inc., San Francisco, 1994.

2. Jones, R. M., *Mechanics of Composite Materials*, Hemisphere Publishing Corporation, 1975.

3. Schaffer, J. P., Saxena, A., Antolovich, S. D., Sanders, T. H., and Warner, S. B., *The Science and Design of Engineering Materials*, Irwin, Boston, 1995.

4. Tsang, P. H. W., "Impact Resistance and Damage Tolerance of Composite Sandwich Panels", Massachusetts Institute of Technology, TELAC Report 94-5, Ph. D. Thesis, 1994.

5. Anderson, T. L., *Fracture Mechanics Fundamentals and Applications*, 2nd ed. CRC Press, Ann Arbor, 1995.

6. Lagace, P. A., Spearing, S. M., and McManus, H. L., "A Proposed Design Methodology for the Failure and Durability of Composite Structures", TELAC Report 96-14, Massachusetts Institute of Technology, August, 1996.

7. Antolin, J. M. M., "Damage Characterization and Modeling of Notched Graphite/Epoxy Sandwich Panels in Compression", Massachusetts Institute of Technology, S. M. Thesis, 1999.

8. Fleck, N. A., "Compressive Failure of Fiber Composites", *Advances in Applied Mechanics*, Vol. 33, 1997, pp. 43-117.

9. "D 3410 / D 3410M Standard Test Method for Compressive Properties of Polymer Matrix Composite Materials with Unsupported Gage Section by Shear Loading", *Annual Book of ASTM Standards*, Vol. 15.03, 1998.

10. "D 695 Standard Test Method for Compressive Properties of Rigid Plastics", *Annual Book of ASTM Standards*, Vol. 08.01, 1998.

11. Adams, D. F. and Lewis, E. Q., "Influence of Specimen Gage Length and Loading Method on the Axial Compressive Strength of a Unidirectional Composite Material", *Experimental Mechanics*, Vol. 31, No. 1, 1991, pp. 14-20.

12. Xie, M. and Adams, D. F., "Effect of Loading Method on Compression Testing of Composite Materials", *Journal of Composite Materials*, Vol. 29, No. 12, 1995, pp. 1581-1600.

13. Adams, D. F. and Welsh, J. S., "The Wyoming Combined Loading Compression (CLC) Test Method", *Journal of Composites Technology & Research*, Vol. 19, No. 3, 1997, pp. 123-133.

14. Lagace, P. A. and Vizzini, A. j., "The Sandwich Column as a Compressive Characterization Specimen for Thin Laminates", *Composite Materials: Testing and Design (Eighth Conference), ASTM STP 972*, 1988, pp. 143-160.

15. "D 5467 Standard Test Method for Compressive Properties of Unidirectional Polymer Matrix Composite Materials Using a Sandwich Beam", *Annual Book of ASTM Standards*, Vol. 15.03, 1998.

16. "C 364 Standard Test Method for Edgewise Compressive Strength of Sandwich Constructions", *Annual Book of ASTM Standards*, Vol. 15.03, 1998.

17. Kim, R. Y. and Crasto, A. S., "A Longitudinal Compression Test for Composites Using a Sandwich Specimen", *Journal of Composite Materials*, Vol. 26, No. 13, 1992.

18. Welsh, J. W. and Adams, D. F., "An Experimental Investigation of the Mini-Sandwich Laminate as Used to Obtain Unidirectional Composite Compression Strengths", *Journal of Composite Materials*, Vol. 31, No. 3, 1997, pp. 293-314.

19. Welsh, J. S. and Adams, D. F., "Current Status of Compression test Methods for Composite Materials", *SAMPE Journal*, Vol. 33, No. 1, 1997, pp. 35-43.

20. Kwon, Y. W., Yoon, S. H., and Sistare, P. J., "Compressive Failure of Carbon-Foam Sandwich Composites With Holes and/or Partial Delamination", *Composite Structures*, Vol. 38, No. 1-4, 1997, pp. 573-580.

21. Berg, J. S. and Adams, D. F., "An Evaluation of Composite Material Compression Test Methods", *Journal of Composites Technology & Research*, Vol. 11, No. 2, 1989, pp. 41-46.

22. Schultheisz, C. R. and Waas, A. M., "Compressive Failure of Composites, Part I: Testing and Micromechanical Theories", *Progress in Aerospace Sciences*, Vol. 32, No. 1, 1996, pp. 1-42.

23. Hahn, H. T. and Williams, J. G., "Compression Failure Mechanisms in Unidirectional Composites", *Composite Materials: Testing and Design (Seventh Conference), ASTM STP 893*, ASTM, 1986, pp. 115-139.

24. Effendi, R. R., "Failure Mechanism Analysis Under Compression Loading of Unidirectional Carbon/Epoxy Composites Using Micromechanical Modelling", *Composite Structures*, Vol. 31, 1995, pp. 87-98.

25. Soutis, C., "Compressive Strength of Unidirectional Composites: Measurement and Prediction", *Composite Materials: Testing and Design, Thirteenth Volume, ASTM STP 1242*, ASTM, 1997, pp. 168-176.

26. Waas, A. M., JungHyun, A., and Khamseh, A. R., "Compressive Failure of Notched Uniply Composite Laminates", *Composites Part B-Engineering*, Vol. 29, No. 1, 1998, pp. 75-80.

27. Grandidier, J. C., Ferron, G., and Potier-Ferry, M., "Microbuckling and Strength in Long-Fiber Composites: Theory and Experiments", *International Journal of Solids and Structures*, Vol. 29, No. 14/15, 1992, pp. 1753-1761.

28. Wu, H. F. and Yeh, J. R., "Compressive Response of Kevlar-Epoxy Composites: Experimental Verification", *Journal of Materials Science*, Vol. 27, 1992, pp. 755-760.

29. Wei, Y. G., Yang, W., and Huang, K. Z., "Theoretical and Experimental Researches of Post-Microbuckling for Fiber-Reinforced Composites", *Science in China Series A-Mathematics Physics Astronomy*, Vol. 37, No. 9, September, 1994, pp. 1077-1087.

30. Jelf, P. M. and Fleck, N. A., "Compression failure Mechanisms in Unidirectional Composites", *Journal of Composite Materials*, Vol. 26, No. 18, 1992, pp. 2706-2726.

31. Moran, P. M., Liu, X. H., and Shih, C. F., "Kink Band Formation and Band Broadening in Fiber Composites Under Compressive Loading", *Acta Metallurgica Et Materialia*, Vol. 43, No. 8, 1995, pp. 2943-2958.

32. Moran, P. M. and Shih, C. F., "Kink Band Propagation and Broadening in Ductile Matrix Fiber Composites: Experiments and Analysis", *International Journal of Solids and Structures*, Vol. 35, No. 15, 1998, pp. 1709-1722.

33. Vogler, T. J. and Kyriakides, S., "Initiation and Axial Propagation of Kink Bands in Fiber Composites", *Acta Materialia*, Vol. 45, No. 6, 1997, pp. 2443-2454.

34. Sutcliffe, M. P. F. and Fleck, N. A., "Microbuckle Propagation in Carbon Fibre-Epoxy Composites", *Acta Metallurgica Et Materialia*, Vol. 42, No. 7, 1994, pp. 2219-2231.

35. Sivashanker, S., Fleck, N. A., and Sutcliffe, M. P. F., "Microbuckle Propagation in a Unidirectional Carbon Fibre-Epoxy Matrix Composite", *Acta Materialia*, Vol. 44, No. 7, 1996, pp. 2581-2590.

36. Fleck, N. A., Sutcliffe, M. P. F., Sivashanker, S., and Xin, X. J., "Compressive R-Curve of a Carbon Fibre-Epoxy Matrix Composite", *Composites Part B-Engineering*, Vol. 27, No. 6, 1996, pp. 531-541.

37. Sivashanker, S., "Damage Growth in Carbon Fibre-PEEK Unidirectional Composites Under Compression", *Materials Science and Engineering A-Structural Materials Properties Microstructure and Processing*, Vol. 249, 1998, pp. 259-276.

38. Guynn, E. G., "Micromechanics of Compression Failures in Open Hole Composite Laminates", Texas A&M University, M. S. Thesis, 1987.

39. Guynn, E. G., Bradley, W. L., and Elber, W., "Micromechanics of Compression Failures in Open Hole Composite Laminates", *Composite Materials: Fatigue and Fracture, Second Volume, ASTM STP 1012*, ASTM, 1989, pp. 118-136.

40. Guynn, E. G. and Bradley, W. L., "Measurements of the Stress Supported by the Crush Zone in Open Hole Composite Laminates Loaded in Compression", *Journal of Reinforced Plastics and Composites*, Vol. 8, 1989, pp. 133-149.

41. Guynn, E. G. and Bradley, W. L., "A Detailed Investigation of the Micromechanisms of Compressive Failure in Open-Hole Composite Laminates", *Journal of Composite Materials*, Vol. 23, 1989, pp. 479-504.

42. Soutis, C., "Compressive Failure of Notched Carbon Fibre-Epoxy Panels", Cambridge University, Ph.D. Thesis, 1989.

43. Soutis, C. and Fleck, N. A., "Static Compression Failure of Carbon Fibre T800/924C Composite Plate with a Single Hole", *Journal of Composite Materials*, Vol. 24, 1990, pp. 536-558.

44. Soutis, C., Fleck, N. A., and Smith, P. A., "Failure Prediction Technique for Compression Loaded Carbon Fibre-Epoxy Laminate with Open Holes", *Journal of Composite Materials*, Vol. 25, 1991, pp. 1476-1498.

45. Sutcliffe, M. P. F. and Fleck, N. A., "Effect of Geometry on Compressive Failure of Notched Composites", *International Journal of Fracture*, Vol. 59, 1993, pp. 115-132.

46. Camponeschi, E. T. J., Gillespie, J. W. J., and Wilkins, D. J., "Kink-Band Failure Analysis of Thick Composites in Compression", *Journal of Composite Materials*, Vol. 27, No. 5, 1993, pp. 471-490.

47. Fleck, N. A., Jelf, P. M., and Curtis, P. T., "Compressive Failure of Laminated and Woven Composites", *Journal of Composites Technology & Research*, Vol. 17, No. 3, July, 1995, pp. 212-220.

48. *Composites*, Engineered Materials Handbook, ed. Dostal, C. A. Vol. 1, ASM International, Metals Park, 1987, pp. 148-150.

49. Cox, B. N., Dadkhah, M. S., Morris, W. L., and Flintoff, J. G., "Failure Mechanisms of 3D Woven Composites in Tension, Compression, and Bending", *Acta Metallurgica Et. Materialia*, Vol. 42, No. 12, 1994, pp. 3967-3984.

50. Karayaka, M. and Kurath, P., "Deformation and Failure Behavior of Woven Composite Laminates", *Journal of Engineering Materials and Technology-Transactions of the ASME*, Vol. 116, No. 2, April, 1994, pp. 222-232.

51. Gupta, V., Anand, K., and Kryska, M., "Failure Mechanisms of Laminated Carbon-Carbon Composites-I. Under Uniaxial Compression", *Acta Metallurgica Et. Materialia*, Vol. 42, No. 3, 1994, pp. 781-795.

52. Alif, N. and Carlsson, L. A., "Failure Mechanisms of Woven Carbon and Glass Composites", *Composite Materials: Fatigue and Fracture (Sixth Volume), ASTM STP 1285*, ASTM, 1997, pp. 471-493.

53. Cox, B. N., Dadkhah, M. S., Inman, R. V., Morris, W. L., and Zupon, J., "Mechanisms of Compressive Failure in 3D Composites", *Acta Metallurgica Et. Materialia*, Vol. 40, No. 12, 1992, pp. 3285-3298.

54. Evans, A. G. and Adler, W. F., "Kinking as a Mode of Structural Degradation in Carbon Fiber Composites", *Acta Metallurgica*, Vol. 26, 1978, pp. 725-738.

55. "Honeycomb and Prepreg in Sandwich Construction", Technical Service Bulletin 100, Hexcel Corporation, 1974.

56. "Design Handbook for Honeycomb Sandwich Structures", Technical Service Bulletin 123, Hexcel Corporation, 1970.

57. Guy, T. A. and Lagace, P. A., "Compressive Residual Strength of Graphite/Epoxy Laminates After Impact", *Ninth DOD/NASA/FAA Conference on Fibrous Composites in Structural Design*, Lake Tahoe, Nevada, DOT/FAA/CT-92-25, 1992, pp. 253-274.

58. Rhodes, M. D., "Impact Fracture of Composite Sandwich Structures", AIAA Paper 75-748, 1975.

59. Kassapoglou, C., "Compression Strength of Composite Sandwich Structures After Barely Visible Impact Damage", *Journal of Composites Technology & Research*, Vol. 18, No. 4, October, 1996, pp. 274-284.

60. Vogler, T. J., "Compressive Behavior and Failure of Composite Sandwich Panels", Massachusetts Institute of Technology, TELAC Report 94-7, S. M. Thesis, 1994.

61. Minguet, P. J., "Buckling of Graphite/Epoxy Sandwich Plates", Massachusetts Institute of Technology, TELAC Report 86-16, S. M. Thesis, 1986.

62. Minguet, P., Dugundji, J., and Lagace, P. A., "Buckling and Failure of Sandwich Plates with Graphite/Epoxy Faces and Various Cores", TELAC Report 87-5, Massachusetts Institute of Technology, 1987.

63. Minguet, P., Dugundji, J., and Lagace, P. A., "Buckling and Failure of Sandwich Plates with Graphite-Epoxy Faces and Various Cores", *Journal of Aircraft*, Vol. 25, No. 4, April, 1988, pp. 372-379.

64. Lie, S. C., "Damage Resistance and Damage Tolerance of Thin Composite Facesheet Honeycomb Panels", Massachusetts Institute of Technology, TELAC Report 89-3, S. M. Thesis, 1989.

65. Marmorini, L., "The Contribution of Face Wrinkling to the Compressive Strength of Thin Composite Facesheet Sandwich Panels", TELAC Report 90-16, Massachusetts Institute of Technology, 1990.

66. Llorente, S., Weems, D., and Fay, R., "Evaluation of Advanced Sandwich Structure Designed for Improved Durability and Damage Tolerance", *46th Annual Forum of the American Helicopter Society*, Washington, D. C., 1990, pp. 825-831.

67. Kassapoglou, C., Fantle, S. C., and Chou, J. C., "Wrinkling of Composite Sandwich Structures Under Compression", *Journal of Composites Technology & Research*, Vol. 17, No. 4, October, 1995, pp. 308-316.

68. Kyriakides, S., Arseculeratne, R., Perry, E. J., and Liechti, K. M., "On the Compressive Response of Fiber Reinforced Composites", *International Journal of Solids and Structures*, Vol. 32, No. 6-7, 1995, pp. 689-738.

69.   Kyriakides, S. and Ruff, A. E., "Aspects of the Failure and Postfailure of Fiber Composites in Compression", *Journal of Composite Materials*, Vol. 31, No. 20, 1997, pp. 2000-2037.

70.   Wang, A. S. D., "A Non-Linear Microbuckling Model Predicting the Compressive Strength of Unidirectional Composites", *ASME Winter Annual Meeting*, ASME Paper 78-WA/Aero 1, San Francisco, 1978, pp. 1-8.

71.   Steif, P. S., "A Model for Kinking in Fiber Composites-I. Fiber Breakage Via Micro-Buckling", *International Journal of Solids and Structures*, Vol. 26, No. 5-6, 1990, pp. 549-561.

72.   Waas, A. M., Babcock, C. D. J., and Knauss, W. G., "A Mechanical Model for Elastic Fiber Microbuckling", *Journal of Applied Mechanics-Transactions of the ASME*, Vol. 57, No. 1, March, 1990, pp. 138-149.

73.   Swanson, S. R., "A Micro-Mechanics Model for In-Situ Compression Strength of Fiber Composite Laminates", *Journal of Engineering Materials and Technology-Transactions of the ASME*, Vol. 114, No. 1, January, 1992, pp. 8-12.

74.   Xu, Y. L. and Reifsnider, K. L., "Micromechanical Modeling of Composite Compressive Strength", *Journal of Composite Materials*, Vol. 27, No. 6, 1993, pp. 572-588.

75.   Williams, T. O. and Cairns, D. S., "A Model for the Compressive Failure of Composite Materials", *Journal of Composite Materials*, Vol. 28, No. 2, 1994, pp. 92-111.

76.   Chung, I. and Weitsman, Y., "A Mechanics Model For the Compressive Response of Fiber Reinforced Composites", *International Journal of Solids and Structures*, Vol. 31, No. 18, 1994, pp. 2519-2536.

77. Drapier, S., Gardin, C., Grandidier, J. C., and Pontier-Ferry, M., "Structure Effect and Microbuckling", *Composites Science and Technology*, Vol. 56, 1996, pp. 861-867.

78. Abu-Farsakh, G. A., Numayr, K. S., and Hamad, K. A., "A Micro-Mechanical Model for Predicting the Compressive Strength of Fibrous Composite Materials", *Composites Science and Technology*, Vol. 57, No. 9-10, 1997, pp. 1415-1422.

79. Budiansky, B., "Micromechanics", *Computers & Structures*, Vol. 16, No. 1-4, 1983, pp. 3-12.

80. Steif, P. S., "A Model for Kinking in Fiber Composites-II. Kink Band Formation", *International Journal of Solids and Structures*, Vol. 26, No. 5-6, 1990, pp. 563-569.

81. Budiansky, B. and Fleck, N. A., "Compressive failure of Fibre Composites", *Journal of the Mechanics and Physics of Solids*, Vol. 41, No. 1, 1993, pp. 183-211.

82. Lagoudas, D. C. and Saleh, A. M., "Compressive Failure Due to Kinking of Fibrous Composites", *Journal of Composites Materials*, Vol. 27, No. 1, 1993, pp. 83-106.

83. Chung, I. and Weitsman, Y., "On the Buckling/Kinking Compressive Failure of Fibrous Composites", *International Journal of Solids and Structures*, Vol. 32, No. 16, 1995, pp. 2329-2344.

84. Dao, M. and Asaro, R. J., "On the Critical Conditions of Kink Band Formation in Fiber Composites with Ductile Matrix", *Scripta Materialia*, Vol. 34, No. 11, June, 1996, pp. 1771-1777.

85. Christoffersen, J. and Jensen, H. M., "Kink Band Analysis Accounting for the Microstructure of Fiber Reinforced Materials", *Mechanics of Materials*, Vol. 24, 1996, pp. 305-315.

86. Christensen, R. M. and DeTeresa, S. J., "The Kink Band Mechanism for the Compressive Failure of Fiber Composite Materials", *Journal of Applied Mechanics*, Vol. 64, No. 1, 1997, pp. 1-6.

87. Jensen, H. M. and Christoffersen, J., "Kink Band Formation in Fiber Reinforced Materials", *Journal of the Mechanics and Physics of Solids*, Vol. 45, No. 7, 1997, pp. 1121-1136.

88. Liu, X. H., Moran, P. M., and Shih, C. F., "The Mechanics of Compressive Kinking in Unidirectional Fiber Reinforced Ductile Matrix Composites", *Composites Part B-Engineering*, Vol. 27, No. 6, 1996, pp. 553-560.

89. Budiansky, B., Fleck, N. A., and Amazigo, J. C., "On Kink-Band Propagation in Fiber Composites", *Journal of the Mechanics and Physics of Solids*, Vol. 46, No. 9, 1998, pp. 1637-1653.

90. Barbero, E. J. and Tomblin, J., "A Damage Mechanics Model for Compression Strength of Composites", *International Journal of Solids and Structures*, Vol. 33, No. 29, 1996, pp. 4379-4393.

91. Tomblin, J. S. and Barbero, E. J., "Statistical Microbuckling Propagation Model for Compressive Strength Prediction of Fiber-Reinforced Composites", *Composite Materials: Testing and Design, Thirteenth Volume, ASTM STP 1242*, ASTM, 1997, pp. 151-167.

92. Barbero, E. J., "Prediction of Compression Strength of Unidirectional Polymer Matrix Composites", *Journal of Composite Materials*, Vol. 32, No. 5, 1998, pp. 483-502.

93. Ishikawa, T. and Chou, T. W., "One-Dimensional Micromechanical Analysis of Woven Fabric Composites", *AIAA Journal*, Vol. 21, No. 12, 1983, pp. 1714-1721.

94. Guynn, E. G., "Experimental Observations and Finite Element Analysis of the Initiation of Fiber Microbuckling in Notched Composite Laminates", Texas A&M University, Ph.D. Thesis, 1990.

95. Guynn, E. G., Ochoa, O. O., and Bradley, W. L., "A Parametric Study of Variables That Affect Fiber Microbuckling Initiation in Composite Laminates: Part 1-Analysis", *Journal of Composite Materials*, Vol. 26, No. 11, 1992, pp. 1594-1616.

96. Fleck, N. A. and Shu, J. Y., "Microbuckle Initiation in Fibre Composites: A Finite Element Study", *Journal of the Mechanics and Physics of Solids*, Vol. 43, No. 12, 1995, pp. 1887-1918.

97. Shu, J. Y. and Fleck, N. A., "Microbuckle Initiation in Fibre Composites Under Multiaxial Loading", *Proceedings of the Royal Society of London Series A-Mathematical Physical and Engineering Sciences*, Vol. 453, No. 1965, October, 1997, pp. 2063-2083.

98. Whitney, J. M. and Nuismer, R. J., "Stress Fracture Criteria for Laminated Composites Containing Stress Concentrations", *Journal of Composite Materials*, Vol. 8, 1974, pp. 253-265.

99. Awerbuch, J. and Madhukar, M. S., "Notched Strength of Composite Laminates: Predictions and Experiments-A Review", *Journal of Reinforced Plastics and Composites*, Vol. 4, 1985, pp. 3-159.

100. Nuismer, R. J., "Applications of the Average Stress Failure Criterion: Part II-Compression", *Journal of Composite Materials*, Vol. 13, 1979, pp. 49-60.

101. Dharan, C. K. H., "Fracture Mechanics of Composite Materials", *Journal of Engineering Materials and Technology*, Vol. 100, 1978, pp. 233-247.

102. Waddoups, M. E., Eisenmann, J. R., and Kaminski, B. E., "Macroscopic Fracture Mechanics of Advanced Composite Materials", *Journal of Composite Materials*, Vol. 5, 1971, pp. 446-454.

103. Mar, J. W. and Lin, K. Y., "Fracture Mechanics Correlation for Tensile Failure of Filamentary Composites with Holes", *Journal of Aircraft*, Vol. 14, No. 7, July, 1977, pp. 703-704.

104. Mar, J. W. and Lin, K. Y., "Characterization of Splitting Process in Graphite/Epoxy Composites", *Journal of Composite Materials*, Vol. 13, October, 1979, pp. 278-287.

105. Dugdale, D. S., "Yielding of Steel Sheets Containing Slits", *Journal of the Mechanics and Physics of Solids*, 1960, pp. 118-136.

106. Backlund, J., "Fracture Analysis of Notched Composites", *Computers and Structures*, Vol. 13, 1981, pp. 145-154.

107. Backlund, J. and Aronsson, C. G., "Tensile Fracture of Laminates with Holes", *Journal of Composite Materials*, Vol. 20, May, 1986, pp. 259-287.

108. Aronsson, C. F. and Backlund, J., "Tensile Fracture of Laminates with Cracks", *Journal of Composite Materials*, Vol. 20, May, 1986, pp. 287-307.

109. Aronsson, C. G., "Strength of Carbon/Epoxy Laminates with Countersunk Hole", *Composite Structures*, Vol. 24, 1993, pp. 283-289.

110. Eriksson, I. and Aronsson, C. G., "Strength of Tensile Loaded Graphite/Epoxy Laminates Containing Cracks, Open and Filled Holes", *Journal of Composite Materials*, Vol. 24, May, 1990, pp. 456-482.

111. Afaghi-Khatibi, A., Ye, L., and Mai, Y. W., "An Effective Crack Growth Model for Residual Strength Evaluation of Composite Laminates with Circular Holes", *Journal of Composite Materials*, Vol. 30, No. 2, 1996, pp. 142-163.

112. Afaghi-Khatibi, A., Ye, L., and Mai, Y. W., "Effective Crack Growth and Residual Strength of Composite Laminates with a Sharp Notch", *Journal of Composite Materials*, Vol. 30, No. 3, 1996, pp. 333-355.

113. Eriksson, I., "Strength Prediction of Compressive Loaded Laminates Containing Circular Holes", *8th International Conference on Composite Materials*, Honolulu, HI, 1991, pp. 35-C-2-35-C-10.

114. Ashby, M. F., "Physical Modelling of Materials Problems", *Materials Science and Technology*, Vol. 8, No. 2, February, 1992, pp. 102-111.

115. Sullins, R. T., Smith, G. W., and Spier, E. E., "Manual for Structural Stability Analysis of Sandwich Plates and Shells", CR-1457, NASA, December, 1969.

116. Newman, J. C. J., "A Nonlinear Fracture Mechanics Approach to the Growth of Small Cracks", *AGARD Conference Proceedings No. 328*, France, 1982, pp. 6-1 - 6-26.

117. Zok, F. and Hom, C. L., "Large-Scale Bridging in Brittle Matrix Composites", *Acta Metallurgica et Materialia*, Vol. 38, No. 10, October, 1990, pp. 1895-1904.

118. Mikulas, M. M., "Failure Prediction Techniques for Compression Loaded Composite Laminates with Holes", NASA CP 2142, NASA, 1980.

APPENDIX A

SPECIMEN MEASUREMENTS

Figure A.1 illustrates the locations on each specimen at which measurements were made. Tables A.1-A.6 list the measurements.
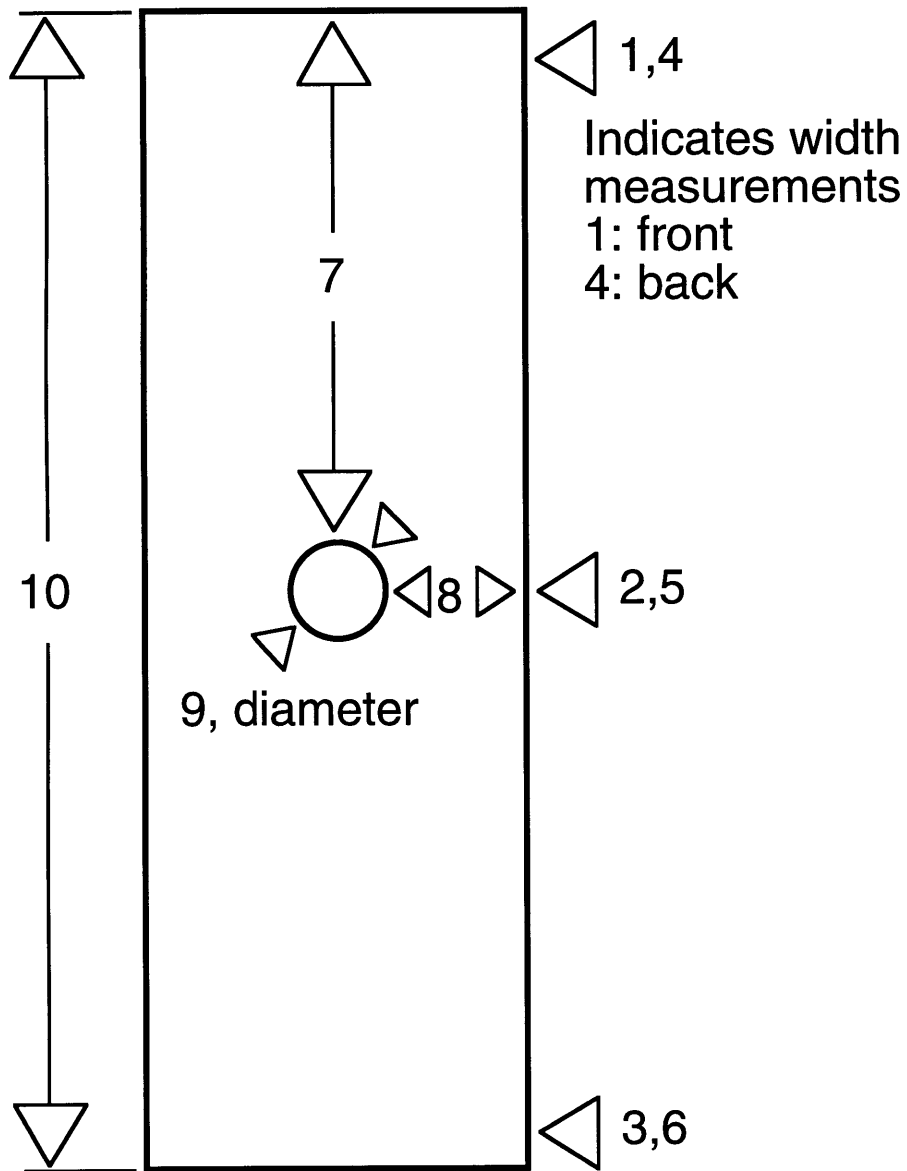
Arrows and associated numbers indicate
approximate measurement locations and
measurement identifier used in
Tables A.1-A.6.

Figure A.1   Specimen measurement locations.

Table A.1   Measurements for AAA Specimens

Measurement	Specimen	Value	Specimen	Value
	All measurements in mm			
1	AAA1	49.63	AAA2	49.45
2		49.63		49.45
3		49.66		49.43
4		49.63		49.48
5		49.63		49.45
6		49.66		49.45
7		69.62		69.52
8		18.44		18.01
9		12.70		12.67
10		152.3		152.3
1	AAA3	49.66	AAA4	49.51
2		49.58		49.51
3		49.58		49.45
4		49.61		49.40
5		49.61		49.43
6		49.61		49.43
7		69.85		70.00
8		18.21		17.98
9		12.78		12.73
10		152.3		152.3

Table A.2   Measurements for ABB Specimens

Measurement	Specimen	Value	Specimen	Value
		All measurements in mm		
1	ABB1	100.7	ABB2	100.7
2		100.7		100.7
3		100.8		100.4
4		100.7		100.8
5		100.7		100.5
6		100.8		100.7
7		139.0		139.1
8		37.36		37.34
9		25.55		25.43
10		304.8		304.8
1	ABB3	100.7	ABB4	100.5
2		100.8		100.4
3		100.8		100.4
4		100.7		100.5
5		100.7		100.6
6		100.7		100.7
7		139.8		139.6
8		38.23		37.47
9		25.55		25.50
10		305.2		304.9

Table A.3   Measurements for ADC Specimens

	All measurements in mm			
Measurement	Specimen	Value	Specimen	Value
1	ADC1	201.8	ADC2	202.0
2		202.1		201.7
3		201.7		201.9
4		201.7		202.0
5		202.0		201.7
6		201.7		201.9
7		178.0		178.6
8		75.39		74.85
9		50.93		50.93
10		407.1		406.9

Table A.4 Measurements for BAA Specimens

Measurement	Specimen	Value	Specimen	Value
		All measurements in mm		
1	BAA1	50.83	BAA2	50.75
2		50.85		50.90
3		50.75		50.75
4		50.93		50.80
5		50.90		50.93
6		50.83		50.90
7		69.65		69.49
8		18.64		18.57
9		12.70		12.73
10		152.7		152.4
1	BAA3	51.03	BAA4	50.55
2		51.00		50.57
3		50.93		50.65
4		51.05		50.39
5		50.90		50.52
6		50.80		50.47
7		70.08		69.95
8		18.92		19.08
9		12.88		12.80
10		152.5		152.4

Table A.5   Measurements for BBB Specimens

	All measurements in mm			
Measurement	Specimen	Value	Specimen	Value
1	BBB1	100.3	BBB3	101.1
2		100.0		100.7
3		99.64		100.2
4		100.3		101.2
5		100.1		101.1
6		99.70		100.6
7		140.4		140.3
8		37.21		37.59
9		25.58		25.48
10		304.8		304.8
1	BBB4	100.2		
2		100.4		
3		100.5		
4		100.3		
5		100.4		
6		100.6		
7		37.34		
8		141.1		
9		25.50		
10		305.2		

Table A.6   Measurements for BDC Specimens

Measurement	Specimen	Value	Specimen	Value
	All measurements in mm			
1	BDC1	202.6	BDC2	202.3
2		202.6		202.3
3		202.7		202.2
4		202.7		202.4
5		202.9		202.3
6		202.7		202.1
7		178.3		178.1
8		76.20		75.90
9		50.75		51.13
10		406.9		407.8

APPENDIX B

DAMAGE GROWTH MODEL

Damage Growth Code for M4 Large Panel

Mathematica Version 3.0

(*Note: Comments are enclosed by "(* *)" *)

Off[General::spell1]
  (*turns off warning for possible spelling errors*)

■ Panel physical variables

r = 1; (*hole radius; units: in*)
w = 4; (*half facesheet width; units: in*)
tk = 0.019; (*facesheet thickness; units: in*)
σun = 23565; (*unnotched strength; units: psi*)
e = 3.2 * 10^6; (*facesheet modulus; units: psi*)

■ Traction law / fracture variables

Ko = 1831.26; (*material fracture toughness; units: psi $\sqrt{in}$ *)

σc = 17500; (*traction law parameter/max stress; units: psi*)

vc = 0.025; (*traction law parameter/max COD; units: in*)

$$\sigma v = \sigma c * \left(1 - \frac{vx}{vc}\right);$$ (*the equation for the traction law*)

initial = 0.001; (*initial assumed crack length; units: in*)

Sincrement = 100; (*applied stress increment; units: psi*)

dmax = 2.8; (*maximum allowable

crack length governed by Newman equations; units: in*)

$$dincrement = \frac{(dmax - r)}{100};$$ (*the crack increment length,

number of increments is number in denominator; units: in*)

n = 10; (*number of crack discretizations*)

maxerror = 10^{-5};

(*maximum allowable error for crack profile convergence*)

   Orth = 1.35; (*orthotropic correction factor*)

■ Definitions

(*no specific comments are included in this section. the
definitions in this section follow the analysis presented in
chapter 4. the necessary equations for the stress intensity
factors and crack opening displacements are defined in this section*)

$$\lambda = \frac{r}{d};$$

f = 1 + 0.358 * λ + 1.425 * λ^2 - 1.578 * λ^3 + 2.156 * λ^4;

A1 = -0.02 λ^2 + 0.558 λ^4;

A2 = 0.221 λ^2 + 0.046 λ^4;

$$g\gamma\lambda = \left(1 + \frac{A1}{1 - \lambda} + \frac{3 * A2}{2 * (1 - \lambda)^2}\right) * ArcSin[\gamma] +$$

$$\left(\frac{A1}{1 - \lambda} + \frac{(4 - \gamma) * A2}{2 * (1 - \lambda)^2}\right) * \sqrt{1 - \gamma^2};$$

$$G\gamma\lambda = \left(g\gamma\lambda /. \gamma \to \frac{b2}{d}\right) - \left(g\gamma\lambda /. \gamma \to \frac{b1}{d}\right);$$

$$B1 = \frac{Sin[\frac{\pi * b1}{2 * w}]}{Sin[\frac{\pi * d}{2 * w}]};$$

$$B2 = \frac{Sin[\frac{\pi * b2}{2 * w}]}{Sin[\frac{\pi * d}{2 * w}]};$$

$$Fsh = \sqrt{1 - \frac{r}{d}} * f;$$

$$Foh = \frac{G\gamma\lambda}{ArcSin[\frac{b2}{d}] - ArcSin[\frac{b1}{d}]};$$

$$Fsw = \sqrt{Sec\left[\frac{\pi * r}{2 * w}\right] * Sec\left[\frac{\pi * d}{2 * w}\right]};$$

$$Fow = \left(\frac{ArcSin[B2] - ArcSin[B1]}{ArcSin[\frac{b2}{d}] - ArcSin[\frac{b1}{d}]}\right) * \sqrt{Sec\left[\frac{\pi * d}{2 * w}\right]};$$

$Ks = S \sqrt{\pi * d} * Fsh * Fsw * Orth;$

$Ga = soutis * Ks^2;$

$K\sigma =$

$$\frac{2 * \sigma}{\pi} * \sqrt{\pi * d} * \left(ArcSin\left[\frac{b2}{d}\right] - ArcSin\left[\frac{b1}{d}\right]\right) * Foh * Fow * Orth;$$

$$Vs = \frac{2 * S}{e} * \sqrt{d^2 - x^2} * Fsh * Fsw * Orth;$$

$$v = (b - x) * ArcCosh\left[\frac{d^2 - (b * x)}{d * Abs[b - x]}\right] + \sqrt{d^2 - x^2} * ArcSin\left[\frac{b}{d}\right];$$

$vb2 = v /. b -> (b2);$

$vb1 = v /. b -> (b1);$

$$V = \frac{2 * \sigma}{\pi * e} * (vb2 - vb1);$$

$Vneg = V /. x -> (-x);$

$Vtot = V + Vneg;$

$V\sigma = Vtot * Fow * Foh * Orth;$

■ Routines

(*this section defines routines that are called in t he main
   procedure. each routine is annotated prior to its definition.
  it should be noted that the counters,such as "c20, c30, etc."
  can be any variable; their value has no significance other than
  for identification purposes. the routines are called with
  dummy variables; i.e. the "1" in Converge[1] means nothing,
  it' s needed to start the routine*)

```
(*typically,
 the arrays store "discrete" values .  for example, σlist stores the
 "n" tractions at "n" locations along the crack, instead of the entire
 traction distribution.  this facilitates superposition of solutions*)

(*creates all of the arrays*)
CreateList[z_] := For[c3 = 1, c3 == 1,
  c3++, {VsList = Array[z, n], VxList = Array[z, n],
   Vxprev = Array[z, n], fi = Array[z, n], gi = Array[z, n],
   xi = Array[z, n], σList = Array[z, n], KσList = Array[z, n],
   VσEqns = Array[z, n], VσList = Array[z, n]}]


(*for a given crack length, discretizes the crack into
 "n" segements*)
Positions[z_] :=
```

$$\text{For}\Big[c4 = 1,\ c4 <= n,\ c4{+}{+},\ \Big\{fi[[c4]] = di - \Big(\frac{c4}{n}\Big) * (di - r),$$

$$gi[[c4]] = di - \Big(\frac{c4 - 1}{n}\Big) * (di - r),$$

$$xi[[c4]] = di - \Big(\frac{c4 - 0.5}{n}\Big) * (di - r)\Big\}\Big]$$

```
(*fills the VsList array which stores discrete CODs due to a remote
 stress*)
FindVsList[z_] := For[c20 = 1, c20 <= n, c20++,
  VsList[[c20]] = Vs /. {S -> Si, d -> di, x -> xi[[c20]]}]


(*fills VxList with the CODs due to the superposition of the two
 solutions*)
FindVxList[z_] := For[c5 = 1, c5 <= n,
  c5++, VxList[[c5]] = VsList[[c5]] - VσList[[c5]]]


(*fills σList with discrete tractions*)
FindσList[z_] := For[c6 = 1, c6 <= n,
  c6++, σList[[c6]] = Re[σv /. vx -> VxList[[c6]]]]


(*fills VσList with CODs due to the tractions*)
FindVσList[z_] :=
   (VσEqns = Array[z, n];
  For[c7 = 1, c7 <= n, c7++,
    VσEqns[[c7]] = (Vσ /. {σ -> σList[[c7]],
      b1 -> fi[[c7]], b2 -> gi[[c7]], d -> di})];
  VσSum = 0;
```

```
For[c7b = 1, c7b <= n, c7b++, VσSum = (VσSum + VσEqns[[c7b]])];
VσList = Array[z, n];
  For[c7c = 1, c7c <= n, c7c++,
  VσList[[c7c]] = Re[VσSum /. x -> xi[[c7c]]]])


(*fills Vxprev with the previous step's CODs*)
FillVxprev[z_] :=
 For[c30 = 1, c30 <= n, c30++, Vxprev[[c30]] = VxList[[c30]]]


(*determines KσSum, the SIF due to the tractions*)
FindKσList[z_] :=
 (For[c8 = 1, c8 <= n, c8++,
  KσList[[c8]] = Kσ /. {d -> di, σ -> σList[[c8]],
      b1 -> fi[[c8]], b2 -> gi[[c8]]}];
  KσSum = 0;
  For[c14 = 1, c14 <= n, c14++, KσSum = (KσSum + KσList[[c14]])])


(*converges on a consistent crack profile*)
Converge[z_] :=
(verge = False;
 posVx = False;
  (*the outer loop will not stop until CODs converge,
    or until vc is reached*)
For[con1 = 1, verge == False && kill == False, con1++,
    {For[con2 = 1, posVx == False, con2++,
     {FindVsList[1];
      For[con3 = 1, con3 <= n, con3++,
        σList[[con3]] = Re[σv /. vx -> VsList[[con3]]]];
        (*check if a traction is negative; if it is, vc reached!*)
          For[con4 = 1, con4 <= n, con4++, If[σList[[con4]] < 0,
          {Print["σ < 0"], kill = True, Break[]}]];
      FindVσList[1];
      FindVxList[1];
      (*check to see if all COD's are positive; if not,
        increment stress and repeat above until posVx=True*)
          switch = 0;
      For[con5 = 1, con5 <= n, con5++,
       If[VxList[[con5]] < 0,
        {Si = Si + Sincrement, switch = switch + 1}]];
       If[switch == 0, posVx = True, posVx = False]}];


    (*is error below limits?  if not, keep iterating below*)
      error = Array[er, n];
```

```
For[con6 = 1, con6 <= n, con6++,
 error[[con6]] = Re[(VxList[[con6]] - VsList[[con6]])]];
If[Abs[Min[error]] < maxerror,
If[Abs[Max[error]] < maxerror,
 verge = True, verge = False], verge = False];
```
(*continue only if not converged yet*)
```
        If[verge == False,
```
(*loop below will continue until convergence reached
   or vc reached. if a COD is negative, increment stress
   and go back up to get positive CODs*)

```
    For[con7 = 1, posVx == True && verge == False, con7++,
        {FillVxprev[1];
         FindσList[1];
         For[con8 = 1, con8 <= n, con8++, If[σList[[con8]] < 0,
        {Print["σ < 0"], kill = True, Break[]}]];
         FindVσList[1];
         FindVxList[1];
```
(*check to see if CODs are positive*)
```
                    switch = 0;
            For[con9 = 1, con9 <= n, con9++,
             If[VxList[[con9]] < 0,
        {Si = Si + Sincrement, switch = switch + 1}]];
                If[switch == 0, posVx = True, posVx = False];
```
(*check convergence error*)
```
                    error = Array[er, n];
            For[con10 = 1, con10 <= n, con10++,
             error[[con10]] =
        Re[(VxList[[con10]] - Vxprev[[con10]])]];
             If[Abs[Min[error]] < maxerror,
              If[Abs[Max[error]] < maxerror, verge = True,
        verge = False], verge = False]}]]}])
```

■ Procedure

```
Kapp = Array[a, 1]; (*used for storing the applied SIF vaues*)
delta = Array[a, 1]; (*used for storing the crack length values*)
(*the following three arrays are only needed for the net-section
   stress analysis*)
FFforce = Array[a, 1]; (*used for storing the applied force values*)
LDZforce = Array[a, 1]; (*used for storing the LDZ force values*)
Ligamentforce = Array[a, 1];
  (*used for storing the ligament force values*)
```

```
(*obtain the first point on the R-curve; no traction influence*)
Si = Extract[Solve[Ks == Ko, S] /. d -> (r + initial), {1, 1, 2}];
Kapp[[1]] = (Ks /. {S -> Si, d -> (r + initial)});
delta[[1]] = r + initial;
```

$$\text{FFforce}[[1]] = \left(\frac{Si}{2} * tk * 2 * w\right);$$

```
LDZforce[[1]] = 0;
Ligamentforce[[1]] = 0;
kill = False;
```

```
(*the governing program loop will continue until either dmax
    or vc is reached.  loop==true is a dummy condition to start the
    loop.  "break" indicates that the program will be terminated*)
For[loop = True; c1 = 1, loop == True && kill == False, c1++,
 {If[c1 == 1, di = (r + dincrement), di = (di + dincrement)];
  If[di > dmax, {Print["dmax reached"], Break[]}];
   CreateList[1];
   Positions[1];
  Si = Extract[Solve[Ks == Ko, S] /. d -> di, {1, 1, 2}];
   Converge[1];
  If[kill == True, Break[]];
  If[Re[VxList[[n]]] >= vc, {Print["Vc reached!"], Break[]}];
  FindσList[1];
  FindKσList[1];
  (*if crack growth condition is not satisfied,
   increment stress until it is*)
    If[(Ks /. {S -> Si, d -> di}) - KσSum < Ko,
    For[UpStress = True; c2 = 1, UpStress == True, c2++,
    If[(Ks /. {S -> Si, d -> di}) - KσSum < Ko,
      {Si = Si + Sincrement;
       Converge[1];
      If[kill == True, Break[]];
       If[Re[VxList[[n]]] >= vc,
       {Print["Vc reached!!"], Break[]}];
       FindσList[1];
       FindKσList[1]}, UpStress = False]]];
  (*loop will exit when crack growth condition is satisfied.  then,
  after obtaining plot information, it will start again and increment
  the crack length*)

    (*the following commands simply append to the arrays used
    for plotting. the new crack length and applied SIF are
```

```
        stored for plotting the R-curve*)
          (*get plot data- crack length and applied SIF*)
        AppendTo[delta, di];
      AppendTo[Kapp, Ks /. {S -> Si, d -> di}];
      (*get net-section stress data*)

      AppendTo[FFforce, (Si/2 * tk * 2 * w)];

      ldzforces = Array[z, n];
      segment = (gi[[1]] - fi[[1]]);
      For[c50 = 1, c50 <= n, c50++,
        ldzforces[[c50]] = (σList[[c50]] * tk * segment)];
      ldzforce = 0;
      For[c51 = 1, c51 <= n,
        c51++, (ldzforce = ldzforce + ldzforces[[c51]])];
      AppendTo[LDZforce, ldzforce];
      AppendTo[Ligamentforce, (2 * σun * (tk * (w - di)))];
      (*last check to see if vc reached before incrementing crack
        length*)
        If[VxList[[n]] >= vc, {Print["Vc reached"],
        Break[]}];}]
```

■ Plots

```
    (*create points array for R-curve plot; convert to SI units*)
    points = Array[a, {Length[delta], 2}];
    For[i = 1, i <= Length[delta],
      i++, {points[[i, 1]] = (delta[[i]] * 25.4);
      points[[i, 2]] = (Kapp[[i]] * 0.00109884349411)}]

    (*data from experiment; LDZ length and associated stress*)
    ADC2BR = {{0.001, 9480.6}, {0.222, 8652.7}, {0.264, 8622.9},
      {0.302, 8682.5}, {0.35, 8722.3}, {0.363, 8858},
      {0.441, 8940.8}, {0.477, 9225.6}, {0.535, 9778.6},
      {0.589, 9755.4}, {0.592, 9828.3}, {0.65, 9881.3},
      {0.8, 9828.3}, {0.85, 9818.3}, {0.895, 9947.5},
      {0.929, 9993.8}};

    (*add radius to LDZ length, convert stress to SIF*)
    adc2br = Array[a, {Length[ADC2BR], 2}];
    For[i = 1, i <= Length[ADC2BR], i++,
      {adc2br[[i, 1]] = (ADC2BR[[i, 1]] + r),
        adc2br[[i, 2]] =
        (Ks /. {d -> (ADC2BR[[i, 1]] + r), S -> ADC2BR[[i, 2]]})}];
```
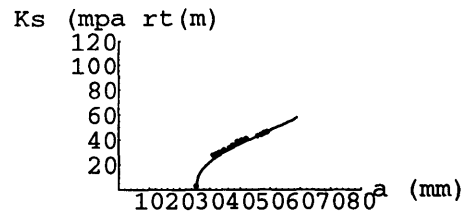
```
(*Conversion of Data Points to SI UNITS*)
For[i = 1, i <= Length[adc2br], i++,
  {adc2br[[i, 1]] = adc2br[[i, 1]] * 25.4,
   adc2br[[i, 2]] = adc2br[[i, 2]] * 0.00109884349411}];

plot1 = ListPlot[points,
  PlotRange -> {{0, 80}, {0, 400}}, PlotJoined -> True];
plot5 = ListPlot[adc2br, PlotRange -> {{0, 80}, {0, 400}},
  PlotStyle -> PointSize[0.02]];
```
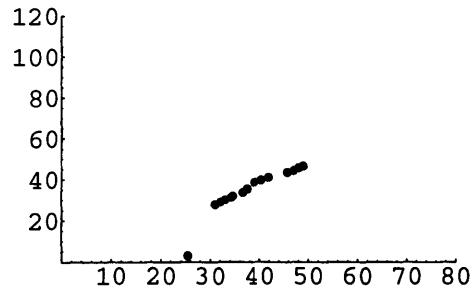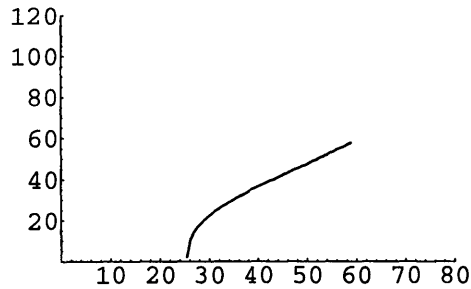


```
Show[plot1, plot5, AxesLabel -> {"a (mm)", "Ks (mpa rt(m)"},
  PlotRange -> {{0, 80}, {0, 400}}];
```
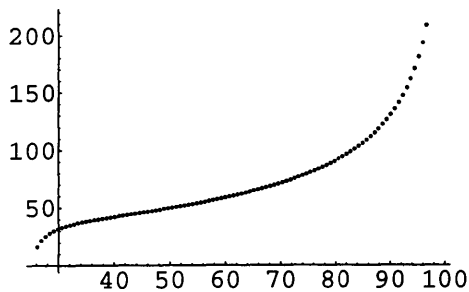

■ Driving Force Curve

```
(*choose one stress, and plug into applied SIF equation*)
Stress = 10500;
df = Ks /. S -> Stress;
```

```
(*create constant stress curve in SI units*)
steps = 100;
dfpoints = Array[a, {steps, 2}];
For[i = 1, i <= steps, i++,
 {dfpoints[[i, 1]] = (i * (2.9 / steps) + r),
  dfpoints[[i, 2]] = df /. d -> (i * (2.9 / steps) + r)}];
For[i = 1, i <= steps, i++,
 {dfpoints[[i, 1]] = dfpoints[[i, 1]] * 25.4,
  dfpoints[[i, 2]] = dfpoints[[i, 2]] * 0.00109884349411}]
```

```
plotg = ListPlot[dfpoints];
```



```
Show[plot1, plot5, plotg, PlotRange -> {{0, 80}, {0, 125}},
 AxesLabel -> {"a (mm)", "Ks (mpa rt(m)"},
 TextStyle -> {FontFamily -> "Helvetica"}];
```
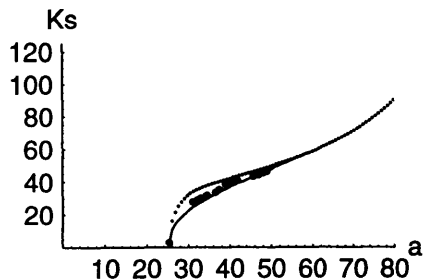
APPENDIX C

MODIFIED CONVERGENCE ALGORITHM

The crack profile convergence algorithm in the damage growth code (refer to Appendix B), as well as the traction assignment routine, are modified for use with the CTM. Tests showed that the modifications had no effect on R-curve predictions (no effect on damage growth or strength predictions).

(*the FindσList routine is changed: if a negative COD is found,
then σc is assigned*)

```
FindσList[z_] := For[c6 = 1, c6 <= n, c6++,
   If[VxList[[c6]] < 0, σList[[c6]] = σc,
     σList[[c6]] = Re[σv /. vx -> VxList[[c6]]]]]
```

(*the Converge routine is modified by allowing negative CODs to
 occur: the stress incrementation (refer to Appendix B to compare
 with old convergence routine) routines are removed*)

```
Converge[z_] :=
(verge = False;
For[con1 = 1, verge == False && kill == False, con1++,
     {FindVsList[1];
       For[con3 = 1, con3 <= n, con3++,
       σList[[con3]] = Re[σv /. vx -> VsList[[con3]]]];
       For[con4 = 1, con4 <= n, con4++,
         If[σList[[con4]] < 0,
         {Print["σ < 0"], kill = True, Break[]}]];
       FindVσList[1];
       FindVxList[1];
           error = Array[er, n];
     For[con6 = 1, con6 <= n, con6++,
       error[[con6]] = Re[((VxList[[con6]]) - (VsList[[con6]]))]];
     If[Abs[Min[error]] < maxerror,
       If[Abs[Max[error]] < maxerror,
         verge = True, verge = False], verge = False];
      If[verge == False,
      For[con7 = 1, verge == False, con7++,
           {FillVxprev[1];
            FindσList[1];
            For[con8 = 1, con8 <= n, con8++, If[σList[[con8]] < 0,
           {Print["σ < 0"], kill = True, Break[]}]];
            FindVσList[1];
            FindVxList[1];
            error = Array[er, n];
            For[con10 = 1, con10 <= n, con10++,
               error[[con10]] =
          Re[((VxList[[con10]]) - (Vxprev[[con10]]))]];
            If[Abs[Min[error]] < maxerror,
               If[Abs[Max[error]] < maxerror, verge = True,
          verge = False], verge = False]}]]}])
```